

The Pennsylvania State University

The Graduate School

Department of Aerospace Engineering

**OPTIMIZED DESIGN AND STRUCTURAL MECHANICS OF A SINGLE-PIECE
COMPOSITE HELICOPTER DRIVESHAFT**

A Dissertation in

Aerospace Engineering

by

Todd C. Henry

Submitted in Partial Fulfillment
of the Requirements
for the Degree of

Doctor of Philosophy

August 2014

The dissertation of Todd Henry was reviewed and approved* by the following:

Dr. Charles E. Bakis
Distinguished Professor of Engineering Science and Mechanics
Dissertation Advisor
Co-Chair of Committee

Edward C. Smith
Professor of Aerospace Engineering
Co-Chair of Committee

George A. Lesieutre
Professor and Head of the Department of Aerospace Engineering

Christopher D. Rahn
Professor of Mechanical Engineering

*Signatures are on file in the Graduate School

ABSTRACT

In rotorcraft driveline design, single-piece composite driveshafts have much potential for reducing driveline mass and complexity over multi-segmented metallic driveshafts. The single-piece shaft concept is enabled by the relatively high fatigue strain capacity of fiber reinforced polymer composites over metals. Challenges for single-piece driveshaft design lie in addressing the self-heating behavior of the composite due to the material damping, as well as, whirling stability, torsional buckling stability, and composite strength. Increased composite temperature due to self-heating reduces the composite strength and is accounted for in this research. The laminate longitudinal stiffness (E_x) and strength (F_x) are known to be heavily degraded by fiber undulation, however, both are not well understood in compression. The whirling stability (a function of longitudinal stiffness) and the composite strength are strongly influential in driveshaft optimization, and thus are investigated further through the testing of flat and filament wound composite specimens.

The design of single-piece composite driveshafts, however, needs to consider many failure criteria, including hysteresis-induced overheating, whirl stability, torsional buckling stability, and material failure by overstress. The present investigation uses multi-objective optimization to investigate the design space which visually highlights design trades. Design variables included stacking sequence, number of laminae, and number of hanger bearings. The design goals were to minimize weight and maximize the lowest factor of safety by adaptively generating solutions to the multi-objective problem. Several design spaces were investigated by examining the effect of misalignment, ambient temperature, and constant power transmission on the optimized solution. Several materials of interest were modeled using experimentally determined elastic properties and novel temperature-dependent composite strength. Compared to the baseline multi-segmented metallic driveline, weight reductions of 43% and 48% were obtained for single-piece flexible and

rigid matrix composite shafts. The rigid matrix weight reduction was slightly lower than that seen in the literature due to consideration of shaft misalignment.

In filament wound composites, the existence of fiber undulation introduces unique challenges in the prediction of compressive modulus and strength using traditional laminated composite theories. In the current investigation, novel full field strain measurements of compressively loaded specimens were used to evaluate local strain distributions in the region of a 0-deg. undulated lamina in a $[0_n/90_n]_s$ laminate ($n=2,4,6$) and a 30-deg. undulated lamina in a $[30_n/-60_n]_s$ laminate ($n=2,4$). Unique to this research, specimens were fabricated with carbon fibers, various amplitudes of undulation, and matrix materials with three different moduli of elasticity. Full-field strains were measured on the free edge and across the width of the compressively loaded specimens using two-dimensional digital image correlation (DIC). The observed strains were highly influenced by the undulation geometry. The longitudinal modulus of a $[0_n/90_n]_s$ laminate was more sensitive to reinforcement undulation when the matrix was flexible rather than rigid. An undulation with an amplitude/length ratio of 0.1 (low for a filament wound cylinder) reduces the average longitudinal modulus of elasticity in the undulation region by approximately 43% and 3% in laminates with flexible and rigid matrices, respectively, relative to a similar material without undulation. Observations of strain on the free edge revealed that fiber undulation caused elevated out-of-plane shear (γ_{xz}) and through-thickness normal (ϵ_{zz}) strains in regions eventually involved in the fiber microbuckling failure process.

A new three dimensional method was derived for the homogenization of a heterogeneous composite laminate consisting of individual anisotropic lamina for which structural coupling (B_{ij}) may occur due to in- and out-of-plane (undulation) fiber reinforcement orientation. Three-dimensional elastic constants were calculated by considering a representative volume element taken from the heterogeneous laminate. Three-dimensional elastic constant predictions were validated through comparison with established methods, both two- and three- dimensional. When

the new derived three dimensional theory was applied to experimental results, the modulus and strength predictions compared favorably.

A series of $[\pm\theta/89/\pm\theta]$ cylinders with multiple helical fiber angles, winding patterns, and matrix materials were fabricated and tested in compression. Digital image correlation was used for the first time to measure outside surface displacements and strains. Longitudinal and hoop direction strain fluctuations between the undulated and non-undulated regions were found to be of the order of 20-30% of the mean values throughout the cylinders. Qualitatively, these fluctuations can be related to non-classical elastic couplings (B_{ij}) in the anti-symmetric regions of the filament winding pattern. Failure of the cylinder occurred by fiber microbuckling, which initiated near the crossing of circumferential and helical cross-over bands. Based on a statistical analysis of surface strains in the local fiber coordinate system, it was determined that longitudinal compressive and in-plane longitudinal shear strains at incipient microbuckling were two to four times greater than their respective global counterparts. These results indicate the magnitude of strain concentration existing in the cylinders immediately before final failure (possibly during local failure) and highlight the importance of longitudinal compressive (ϵ_{11}) and in-plane longitudinal shear strains (γ_{12}) in the failure process.

A novel local-global approach was used in predicting the longitudinal modulus and strength of filament wound cylinders. Several representative volume elements were chosen to represent the filament winding rhombus, and were used as a basis for homogenization. Strength predictions were augmented with empirical critical distance factors. The average E_x and ν_{xy} prediction error for Conathane DPRN 30917 was 6.8 % and 21 % and the average error for EPON 862 was 9.7 % and 14 % respectively. The strength prediction error was approximately 7.7 % and 24 % for 30917 and EPON 862 with failure location typically at the circumferential undulation by mode σ_6 (τ_{12}). The failure mode prediction was consistent with experimental observations from filament

wound cylinders and flat-undulated specimens of similar lamination arrangement. Additional comparison with previous Adiprene LF750 filament wound cylinder testing produced prediction error of 11.8 % and 8.9 % for longitudinal modulus and strength respectively. The average absolute value of the error, considering every material, for modulus, strength, and Poisson's ratio was 14 %. Application of critical distance factors to flat undulated specimens was deemed inadvisable due to considerably higher strain intensity at failure compared to filament wound cylinders.

TABLE OF CONTENTS

List of Figures.....	ix
List of Tables.....	xiv
Nomenclature and Acronyms	xvi
Acknowledgements.....	xix
Chapter 1 Literature Review	1
1.1 Composite Helicopter Driveshaft Design	1
1.2 Undulated Composite Stiffness and Strength.....	8
1.3 Filament Wound Cylinders and Filament Winding Pattern	15
1.4 Analytical and FEA Methods for E_1 and F_{1C} Determination	18
1.5 Standards and Empirical Methods for E_1 and F_{1C} Determination	22
1.6 Opportunities for Research	27
1.7 Objectives	28
Chapter 2 Materials and Manufacturing.....	30
2.1 Matrix Materials	31
2.2 Manufacturing	33
2.2.1 <i>In-Plane Transverse Compression, F_{2C} and E_{2C}, Testing</i>	37
2.2.2 <i>Helically Wound Cylinder Testing</i>	38
2.2.3 <i>In-Plane Transverse Tension, F_{2T} and E_{2T}, Testing</i>	39
2.2.4 <i>Discrete Undulation Testing</i>	40
Chapter 3 Composite Helicopter Driveshaft Design.....	45
3.1 Temperature Controlled Tests: Neat Resin	46
3.2 Temperature Controlled Tests: Composite	50
3.3 Temperature Dependent Strength Prediction	55
3.4 Driveshaft Design Model	59
3.4.1 <i>Shaft Temperature Module</i>	61
3.4.2 <i>Whirling Module</i>	66
3.4.3 <i>Buckling Module</i>	69
3.4.4 <i>Structural Module</i>	74
3.4.5 <i>Factors of Safety</i>	77
3.5 ATSV Optimization Strategy	79
3.5.1 <i>Blackhawk Design Space</i>	80
3.5.2 <i>Chinook Design Space</i>	91
3.5.3 <i>Operating Frequency and Torque Variation</i>	93
Chapter 4 Discrete Undulation Two Dimensional DIC	96
4.1 Discrete Undulation Test Method.....	97
4.2 Discrete Undulation Test Results	99

4.3 Analytical Homogenized Stiffness for an RVE.....	112
4.4 Discrete Undulated Composite Modeling: Validation.....	125
4.5 Discrete Undulation Modulus and Strength Prediction	133
Chapter 5 Filament Wound Cylinder Three Dimensional DIC	143
5.1 Helically Wound Composite Cylinder Test Method	144
5.2 Experimental Results	147
5.3 Analytical Methodology for Modulus and Strength	159
5.4 Analytical Predictions for Modulus and Strength	170
5.5 Average Stress Criterion As Applied to DIC Imaging	175
Chapter 6 Conclusions	178
6.1 Composite Helicopter Driveshaft Design	178
6.2 Discrete Undulation Two Dimensional DIC	180
6.3 Filament Wound Cylinder Three Dimensional DIC	183
6.4 Recommendations for Future Work	185
Appendix	188
References	192

LIST OF FIGURES

Figure 1-1. Global and local coordinate systems for a composite	3
Figure 1-2. Schematic of traditional driveline (top) and proposed driveline (bottom) (Mayrides, 2005)	7
Figure 1-3. Schematic of filament wound cylinders: winding patterns of 2,5, and 10, showing repeating rhombic units (left); cross-section of undulated helical tow (right).....	8
Figure 1-4. Constitutive equations with varying degrees of fiber reinforcement rotation	11
Figure 1-5. Laminate compression failure modes (Naik et al., 1999).....	12
Figure 1-6. [90/0/90] Lamina waviness unit cell (Bogetti et al., 1992)	13
Figure 1-7. Interlaminar stress within the wavy 0-deg. lamina in AS4/PEEK: unilongitudinal compressive loading (Bogetti, et al., 1992)	14
Figure 1-8. Filament wound cylinder subjected to internal pressure; homogeneous, pattern of 2, pattern of 4 (Morozov, 2006)	16
Figure 1-9. Typical buckling mode shape of [± 30] filament wound cylinder (Hahn et al., 1994).....	17
Figure 1-10. Effect of circumferential crossover-band spacing (specimen length/circumferential undulation spacing) on the buckling stress of 57-mm diameter [± 30] filament-wound cylinders (Hahn et al., 1994)	18
Figure 1-11. Identification of representative volume element (RVE) for fiber tow crossover region (Pai and Jensen, 2001).....	19
Figure 1-12. FEA results and experimental observation (Zhou et al., 2009)	22
Figure 1-13. LF750/AS4D longitudinal modulus versus fiber angle θ_x —experiments and theory (Sollenberger, 2010)	24
Figure 1-14. Compression testing: specimen barreling and Poisson’s ratio.....	25
Figure 1-15. a) Shear strain measured during torsion test, b) longitudinal strain field during a test with a combination of traction and flexure, c) local radius (Crouzeix et al., 2009).....	26
Figure 1-16. Snapshots of longitudinal strain in rigid $\pm 45^\circ$ undamaged (left) and damaged, lower center (right) cylinders tested in tension (Sollenberger et al., 2010).....	26
Figure 2-1. Filament winder front view	35

Figure 2-2. Mandrel and ping ring	35
Figure 2-3. Mandrel with shrink tape and final part ready for heating	36
Figure 2-4. 25.4 cm x 25.4 cm paddle mandrel and schematic of unidirectional pre-preg sectioning (Sollenberger, 2010)	40
Figure 2-5. Undulated specimen layup sequence	41
Figure 2-6. Discrete undulated specimen location diagram	42
Figure 2-7. Photographs of polished edges of flat $[0_n/90_n]_s$ specimens showing undulation (scale: cm). Dimension “ L_u ” indicates the length of the undulation.....	42
Figure 3-1. Neat resin specimen test set-up: CMTC.....	47
Figure 3-2. Longitudinal stress vs. average longitudinal strain: neat resin tension	47
Figure 3-3. Normalized modulus (all resins) vs. chamber ambient temperature, line fit to 30757	49
Figure 3-4. Normalized storage modulus vs. temperature, EPON 862 neat resin DMA test in flexure.....	50
Figure 3-5. Experimental composite test set-up: CMTC.....	51
Figure 3-6. Transverse stress vs. Transverse strain: 30917 composite	52
Figure 3-7. Average modulus, strength and ultimate strain vs. temperature: transverse-tension tests: 30917	53
Figure 3-8. Average modulus, strength, and ultimate strain vs. temperature: transverse-compression specimen: 30917	55
Figure 3-9. Lamina strength vs. resin modulus, E_m (Henry, 2012).....	56
Figure 3-10. Temperature controlled experimental and empirical predictions: 30917	58
Figure 3-11. Flow chart for calculating equilibrium temperature for the composite shaft (Shan, 2006).....	66
Figure 3-12. Orientation of axes in the middle surface of cylindrical shell (Cheng and Ho, 1963).....	70
Figure 3-13. Cylinder under study and applied loads (Jolicouer and Cardou, 1993).....	75
Figure 3-14. Flowchart of composite driveline optimization strategy	80
Figure 3-15. Design space with Pareto frontier: EPON 862, Blackhawk ,40°C, 1500 $\mu\epsilon$	81

Figure 3-16. Blackhawk design considerations: four bearings, $\pm\theta 4$ laminate, 1500 $\mu\epsilon$, 30757, 40°C	83
Figure 3-17. Blackhawk design analysis: 1500 $\mu\epsilon$, EPON 862, 20-40-60°C	84
Figure 3-18. S_{min} vs. various S : Blackhawk, 1500 $\mu\epsilon$, EPON 862, 20-40-60°C	85
Figure 3-19. S_{min} vs. various S : Blackhawk, 60°C, EPON 862, 0-750-1500 $\mu\epsilon$	86
Figure 3-20. S_{min} vs. various S : Blackhawk, 1500 $\mu\epsilon$, 30757, 20-40-60°C	87
Figure 3-21. S_{min} vs. various S : Blackhawk, 60°C, 30757, 0-750-1500 $\mu\epsilon$	88
Figure 3-22. Three dimensional design space: Blackhawk, 20°C, 30757, 1500 $\mu\epsilon$	89
Figure 3-23. Most preferred Blackhawk driveline weight and S_{min}	91
Figure 3-24. Most preferred Chinook driveline weight and S_{min}	93
Figure 4-1. Undulated specimen compression test set-up	98
Figure 4-2. Longitudinal normal strain, ϵ_{xx} , in $[0_n/90_n]_s$ specimens at 50% of ultimate (thickness-side view)	100
Figure 4-3. Out-of-plane normal strain, ϵ_{zz} , in $[0_n/90_n]_s$ specimens at 50% of ultimate (thickness-side view).	101
Figure 4-4. Out-of-plane tensor shear strains, ϵ_{xz} , in $[0_6/90_6]_s$ and $[30_4/-60_4]_s$ specimens at 50% of ultimate (thickness-side view).	102
Figure 4-5. Longitudinal normal strains, ϵ_{xx} , in $[30_n/-60_n]_s$ specimens at 50% of ultimate.	103
Figure 4-6. Out-of-plane normal strains, ϵ_{zz} , in $[30_n/-60_n]_s$ specimens at 50% of ultimate (thickness-side view).	103
Figure 4-7. Longitudinal stress vs. longitudinal strain results: LF750, 30917, EPON 862.....	104
Figure 4-8. Compressive modulus and strength versus undulation amplitude-to-length ratio.....	107
Figure 4-9. Strains at Stages A, B, and C in an LF750 $[0_6/90_6]_s$ specimen (thickness-side view).....	108
Figure 4-10. Longitudinal strain in width-side view for $[30_n/-60_n]_s$ specimens and a filament wound cylinder for comparison.	110
Figure 4-11. Transverse and shear strains in the x - y plane for $[30_n/-60_n]_s$ specimens.....	111
Figure 4-12. Micro-buckling failure in a 30917 $[30_n/-60_n]_s$ specimen and a 30917 filament wound cylinder.....	112

Figure 4-13. RVE of a heterogeneous laminate.....	113
Figure 4-14. In-plane displacement continuity	114
Figure 4-15. Traction continuity through the laminate thickness	114
Figure 4-16. Example undulated heterogeneous RVE, $[\theta_1/\theta_2/\theta_1/\theta_2/\theta_1]$	126
Figure 4-17. Homogenized modulus convergence vs. longitudinal discretization: EPON 862.....	130
Figure 4-18. Homogenized longitudinal modulus vs. undulation height/ length: [90/0/90/0/90] laminate, anisotropic solutions	133
Figure 4-19. Flat undulated three dimensional modulus experimental and theoretical results.....	134
Figure 4-20. Flat undulation two and three dimensional sensitivity: longitudinal modulus ...	136
Figure 4-21. Lamina level stress calculation diagram.....	137
Figure 4-22. Flat undulated longitudinal strength experimental and theoretical results	139
Figure 4-23. Flat undulated longitudinal experimental strength and MST predictions.....	140
Figure 4-24. Flat undulation two and three dimensional sensitivity: longitudinal strength by MST	142
Figure 5-1. Unpainted (left) and painted (right) specimen	144
Figure 5-2. Helically wound cylinder compression test set-up	145
Figure 5-3. Outer radius measurement of $[\pm 31/89/\pm 31]$ {10/10} cylinders with no applied stress.....	148
Figure 5-4. Global longitudinal strains, ε_{yy} , in cylinders prior to fiber microbuckling.	149
Figure 5-5. Global hoop strains, ε_{xx} , in cylinders prior to fiber microbuckling.	150
Figure 5-6. Out-of-plane displacement according to DIC data and theory for an FMC [$\pm 31/89/\pm 31$] {5/5} specimen.	151
Figure 5-7. Longitudinal strain along path A-A' in an RMC $[\pm 45/89/\pm 45]$ {5/5} specimen, highlights reduced longitudinal strain magnitude in undulated vs. laminated regions of FWP	152
Figure 5-8. Strains in FMC specimens in the lamina longitudinal direction, ε_{11} , immediately before failure. Un-shaded regions have fibers in the 1-direction shown. ..	153

Figure 5-9. DIC data for an FMC $[\pm 45/89/\pm 45]$ $\{5/5\}$ specimen near failure (a-e) and after failure (f). Un-shaded regions shown in (b-e) have fibers in the 1-direction shown.....	154
Figure 5-10. Average normalized modulus results, GPa, scatter bars indicate the range of replicate test results	156
Figure 5-11. Average normalized ultimate strength results, MPa, scatter bars indicate the range of replicate test results.....	157
Figure 5-12. Example analysis of strain components in microbuckled region of interest in a $[\pm 45/89/\pm 45]$ $\{5/5\}$ FMC cylinder.....	158
Figure 5-13. Various percentile strains, ε_{11} and γ_{12} , in FMC cylinders in the region of strain localization immediately prior to failure. Also shown are strains computed using CLT.	159
Figure 5-14. Filament wound rhombus RVE and coordinate system	161
Figure 5-15. RVE undulation sample extraction	163
Figure 5-16. Undulation polishing.....	164
Figure 5-17. Polished undulated cross-sections highlighting measured parameters.....	165
Figure 5-18. Rhombus RVE sectioning and ratio of contribution to stiffness with respect to longitudinal location: ± 45 -deg., FWP=10	167
Figure 5-19. Local-global laminate stiffness construction mixed boundary conditions, laminate $[\pm \theta/89/\pm \theta]$	168
Figure 5-20. MST stress intensity profile along RVE C, laminate $[\pm 31/89/\pm 31]$ $\{5/5\}$	170
Figure 5-21. E_x and ν_{xy} predictions for $[\pm \theta/89/\pm \theta]$ cylinders various FWP	171
Figure 5-22. F_x predictions for $[\pm \theta/89/\pm \theta]$ cylinders various FWP.....	173
Figure 5-23. E_x and F_x predictions for $[\pm \theta/89/\pm \theta]$ LF750 cylinders	174
Figure 5-24. Physical size of $2a_0$ with respect to strain concentrations in 3D DIC: 30917.....	175
Figure 5-25. Strain intensity comparison of cylindrical specimens with a_0	176
Figure 5-26. Strain intensity comparison of flat undulated specimens with a_0	177

LIST OF TABLES

Table 1-1. Mechanical lamina properties needed for analysis and design	3
Table 2-1. Neat resin tensile properties (mean and coefficient of variation, C_v), room temperature and resin mix ratios	32
Table 2-2. Description of specimens for evaluating F_{2C} and E_{2C} of cylinders: 30917	37
Table 2-3. Description of specimens for compressively loaded filament wound cylinder testing	39
Table 2-4. Description of 30917 specimens for evaluating F_{2T} and E_{2T} of plates: 30917	40
Table 2-5. Measured flat undulated material details	43
Table 3-1. Neat resin modulus summary.....	48
Table 3-2. Transverse-tension specimen temperature controlled test summary: 30917	53
Table 3-3. Transverse-compression specimen temperature controlled test summary: 30917	54
Table 3-4. Transverse-tension modulus and strength, experiment and prediction: 30917	57
Table 3-5. Transverse-compression modulus and strength, experiment and prediction: 30917	57
Table 3-6. Driveshaft geometric parameters	59
Table 3-7. Quasi-static composite material properties	60
Table 3-8. Fractional derivative model fit constants, transverse and shear (Henry, 2012)	64
Table 3-9. Pareto frontier designs: EPON 862, Blackhawk, 40°C, 1500 $\mu\epsilon$	82
Table 3-10. Most preferred Blackhawk driveline design results	90
Table 3-11. Most preferred Chinook driveline design results	92
Table 3-12. Blackhawk most preferred design with and without allowed variation in ξ : 1500 $\mu\epsilon$, 60°C	95
Table 4-1. Specimen gage lengths utilizing ASTM D 3410.....	98
Table 4-2. Average compressive modulus (E_x) and Strength (σ_x) results	105
Table 4-3. Lamina elastic material properties: discrete undulation (Henry, 2012).....	129
Table 4-4. Homogenized elastic predictions: EPON 862 non-undulated.....	131

Table 4-5. Three-dimensional homogenized elastic predictions: EPON 862 undulated.....	132
Table 4-6. Lamina strength properties: discrete undulation (Henry, 2012)	137
Table 4-7. Flat undulated failure mode and transition undulation amplitude over length: [2D/3D].....	140
Table 5-1. Normalized compression test results for RMC cylinders	155
Table 5-2. Normalized compression test results for FMC cylinders.....	155
Table 5-3. Lamina properties: filament wound cylinder (Henry, 2012)	162
Table 5-4. Undulation characterization measurements	166
Table 5-5. Analytical failure location prediction and major stress component	172
Table 5-6. Prediction Error, (Theory-Experiment)/Theory*100	174
Table A-1. Discrete undulation modulus and ultimate strength test results: LF750, [30 _n /- 60 _n] _s	188
Table A-2. Discrete undulation modulus and ultimate strength test results: 30917, [30 _n /- 60 _n] _s	188
Table A-3. Discrete undulation modulus and ultimate strength test results: LF750, [0 _n /90 _n] _s	189
Table A-4. Discrete undulation modulus and ultimate strength test results: 30917, [0 _n /90 _n] _s	190
Table A-5. Discrete undulation modulus and ultimate strength test results: EPON 862	191

NOMENCLATURE AND ACRONYMS

1,2,3	principal lamina coordinate directions
a_o	average stress distance
a_s, b_s, c_s	structural bending equation constants
b_w	tow bandwidth
c_b	buckling polynomial coefficients
c_w	whirling polynomial coefficients
d_o	critical stress distance
dx	longitudinal location increment
dR_f	change in radius from test start to end
f	angular frequency
f_{crit}	first driveshaft natural frequency
g	structural bending coefficients
h_{89}	circumferential lamina thickness
h_f	undulating lamina thickness
h_i	lamina height location
h_t	laminar thickness
h_u	undulation height
$h_{\pm\theta}$	helical lamina thickness
k	lamina index
\bar{m}	ratio of inner to outer radius of a shaft
m	structural bending equation roots
m_b	longitudinal buckling mode number
m_w	whirling mode number
n	number of lamina in a laminate
n_b	circumferential buckling mode number
q'''	energy dissipated per unit volume
r_m	mean radius of the shaft
u, v, w	displacements in the x, y, z directions
x, y, z	global coordinate directions
x, θ, z	cylindrical coordinates
A^*, B^*, C^*, D^*	fractional derivative series expansion coefficients
A_{ij}, B_{ij}, D_{ij}	two dimensional stiffness matrices
$\bar{A}_{ij}, \bar{B}_{ij}, \bar{D}_{ij}$	$1/A_{22}(A_{ij}, B_{ij}/r_m, D_{ij}/r_m^2)$, adjusted membrane stiffness matrices
A_r	cross-sectional area of the shaft
C_{ij}	three dimensional stiffness coefficients
C_B	effective bending stiffness
C_{BT}	effective bending-twist coupling stiffness
C_S	effective transverse shear stiffness
C_T	effective torsional stiffness
$D^\beta[\]$	fractional derivative
D_f	fiber diameter
D_o	orifice diameter
E, G, a_i, b_i, β_i	fractional derivative constants
E'	storage modulus of elasticity
E''	loss modulus of elasticity

E_1	longitudinal modulus and elasticity
E_2	in-plane transverse modulus of elasticity
E_3	out-of-plane transverse modulus of elasticity
E_m	neat resin modulus of elasticity
$F[]$	Fourier transform
F_{1T}	longitudinal tensile strength
F_{2T}	in-plane transverse tensile strength
F_{3T}	out-of-plane transverse tensile strength
F_{1C}	longitudinal compressive strength
F_{2C}	in-plane transverse compressive strength
F_{3C}	out-of-plane transverse compressive strength
F_4	out-of-plane transverse shear strength
F_5	out-of-plane longitudinal shear strength
F_6	in-plane longitudinal shear strength
F_x	longitudinal laminate strength
G_{12}	in-plane longitudinal shear modulus of elasticity
G_{13}	out-of-plane longitudinal shear modulus of elasticity
G_{23}	out-of-plane transverse shear modulus of elasticity
I	second area moment of inertia
J	polar area moment of inertia
K'	structural bending constant
K	buckling shear correction coefficient
L	driveshaft segment length
L_u	undulation length
$M_x, M_\theta, M_{x\theta}$	resultant moment per unit width of the laminate
$N_x, N_\theta, N_{x\theta}$	resultant force per unit width of the laminate
N_f	number of fibers
N_l	effective lamina number
P	longitudinal load
Q_{crit}	critical buckling torque
Q_{ij}	two dimensional lamina stiffness matrix
Q_s	external torsional force per unit width
R	initial radius DIC radius
R_i	inner radius of the shaft
R_o	outer radius of the shaft
S	factor of safety
S_b	factor of safety for buckling
S_h	factor of safety for heating
S_{ij}	three dimensional compliance matrix
S_{min}	minimum factor of safety
S_w	factor of safety for whirling
S_σ	factor of safety for stress
$T_{ij}(\alpha)$	out-of-plane transformation matrix
$T_{ij}(\theta)$	in-plane transformation matrix
T_{amb}	ambient temperature
T_{cal}	calculated temperature
T_{mat}	material temperature
T_r	reference temperature

V_f	actual fiber volume fraction
V_{ft}	target volume fraction
V^k	lamina volume fraction
$W_{curative}$	curative weight
α	out-of-plane orientation angle
α_t	temperature shift factor
β_{ij}	reduced elastic constants
γ	shear strain
ε	normal strain
η	loss factor
θ	in-plane orientation angle
$\kappa_x, \kappa_\theta, \kappa_{x\theta}$	curvature
λ_b	$m^b \pi r_m / L$, buckling dimensionless parameter
λ_w	$m^w \pi / L$, whirling dimensionless parameter
μ	particular solution to structural bending coefficients
ν_{12}	in-plane longitudinal Poisson's ratio
ν_{13}	out-of-plane longitudinal Poisson's ratio
ν_{23}	out-of-plane transverse Poisson's ratio
ρ	density
σ	normal stress
τ	shear stress
ϕ	stress intensity
ψ_x, ψ_y, ψ_z	rotations in the x, y, z directions
Γ	gamma function
Γ_i	homogenization constants
Λ, Π	Airy stress function
ΔW	dissipated energy
ATSV	ARL trade space visualizer
CLT	classical lamination theory
DIC	digital image correlation
DMA	dynamic mechanical analysis
FMC	flexible matrix composite
FEA	finite element analysis
FWP	filament winding pattern
MST	maximum stress theory
NCO	nitrogen-carbon-oxygen group
PAN	polyacrylonitrile
PTFE	polytetrafluoroethylene
PVC	polyvinyl chloride
RMC	rigid matrix composite
RoM	rule of mixtures
RVE	representative volume element
TDI	toluene diisocyanate

ACKNOWLEDGEMENTS

I would like to thank Dr. Charles E. Bakis and Dr. Edward C. Smith for taking time out of their weeks to assist me in my research. Both of my advisors gave valuable direction that aided in the completion of this research while having considerable patience.

Chemtura and Cytec Corporations are thanked for supplying materials on a free sample basis. Dr. Thomas Juska of Penn State University is thanked for valuable technical discussions on processing. Mr. Simon Miller is thanked for help with creating batch files and other communication coding between Matlab and ATSV. The assistance I have received from Mr. Miller through the entirety of the time I've known him has always been of exceptional caliber. I would like to thank my family for their continued kind words and support as I complete my time at Penn State.

I wish to acknowledge the mentorship of Dr. Jaret C. Riddick. I would like to thank Dr. Ryan Emerson of WMRD for advice and for putting me into contact with experts of varying fields. Additionally my lab POC's at Aberdeen Proving Ground, David Gray, Bob Kaste, and Paul Moy were enormously helpful in experimentation set-up and image correlation. I wish to thank the Army Research Lab, Vehicle Technology Directorate and United States Department of Defense for financial support through the SMART Fellowship.

Chapter 1

Literature Review

This chapter reviews relevant literature on the subject of filament wound composite helicopter driveshaft design as it relates to problems including, but not limited to, torsional buckling stability, whirling stability, driveshaft self-heating, and lamina material failure. Further investigation into micromechanical material failure is warranted because of unique weaving constructs (such as out-of-plane fiber undulation) created during the filament winding manufacturing process which present unique design challenges for filament wound cylinders. Significant degradation of composite modulus and strength are recognized to be caused by fiber undulation. Various experimental and modeling techniques for modulus and strength prediction which take into account fiber undulation are surveyed with more advanced techniques, including complex finite element analysis models and full-field strain measurement by digital image correlation.

1.1 Composite Helicopter Driveshaft Design

Rotary wing aircraft, such as a helicopter or tiltrotor, are essential to many various mission profiles because they can perform tasks that their fixed wing counterparts cannot. They aerially pursue criminals, fight fires, report the news, rescue civilians in danger, transport personnel/equipment, and support the Armed Services. Two common limitations that affect a helicopter's ability to complete these objectives are the time it can remain on station, and downtime incurred through regularly scheduled maintenance of the helicopter. Structural engineers strive to minimize the weight of helicopters to increase flight time or gross payload,

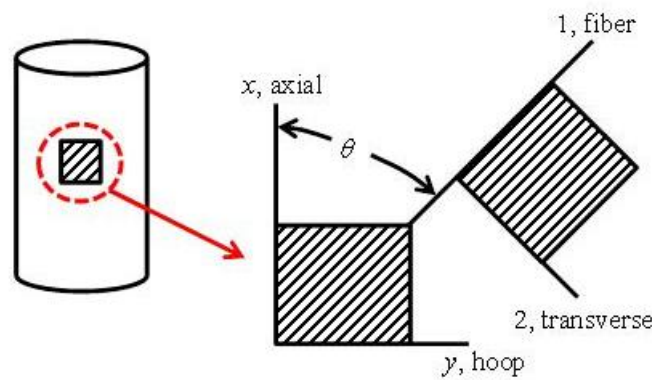
and to minimize the number of parts to decrease design complexity as well as maintenance downtimes.

Power transmission driveline components, such as tail rotor driveshafts and interconnects, have been the focus of on-and-off research in recent years. Current helicopter driveshafts are made of multiple, short-metal segments that are connected together via flexible couplers that accommodate inevitable driveshaft misalignment. Flexible couplers ensure that bending strain is not imparted to segments of the helicopter driveshaft, keeping the metal, usually aluminum, from developing cracks associated with fully reversed cyclic fatigue loading during operation. Driveshaft bending is generated by tailboom flexure from crosswinds, downwash, and/or regular maneuvering. Mid-span hanger bearings are evenly spaced along the driveshaft to hold the bearings and couplers to the airframe, while restricting the driveshaft segments from contacting the airframe. The current multi-segmented driveline concept “gets the job done”, but leaves much to be desired in terms of weight, complexity, and maintenance.

Composites are attractive in lightweight structural design because they are easily tailored and have high specific modulus and strength compared to conventional isotropic materials such as metals. A relatively new class of composites known as flexible matrix composites (FMCs), consisting of high strength fibers such as glass or carbon and an elastomeric matrix such as polyurethane or silicone, are particularly well suited for structural applications requiring ultra-high anisotropy in modulus or strength. E_1 divided by E_2 is 20-100 and F_{1c} divided by F_{2T} is 10-30 for carbon/polyurethane composites of practical interest (**Table 1-1, Figure 1-1**). A possible application for a carbon/polyurethane composite is a one-piece filament wound helicopter driveshaft that can accommodate driveline misalignment (soft in bending) while transmitting power (stiff in torsion) (**Figure 1-2**). The composite rotorcraft driveshaft must additionally transmit high torque, resist buckling and whirling instabilities, and spin in a misaligned configuration without overheating or experiencing fatigue failure.

Table 1-1. Mechanical lamina properties needed for analysis and design

Lamina Property	Symbol
Longitudinal Modulus of Elasticity	E_1
In-Plane Transverse Modulus of Elasticity	E_2
In-Plane Longitudinal Shear Modulus of Elasticity	G_{12}
In-Plane Longitudinal Poisson's Ratio	ν_{12}
Longitudinal Tensile and Compressive Strengths	F_{1t}, F_{1c}
In-Plane Transverse Tensile and Compressive Strengths	F_{2t}, F_{2c}
In-Plane Longitudinal Strength	F_6

**Figure 1-1.** Global and local coordinate systems for a composite

The advantages of composite use over metals received attention due to the former's high specific modulus and strength, allowing for longer driveshaft segments between hanger bearings. Replacement of metal driveshaft segments with boron/epoxy segments was investigated by Zinberg (1970). Based on measured elastic and strength properties, a $[90/\pm 45/0_6/90]$ (plies listed inside to outside) was calculated to exist in the viable design space considering whirling instability, torsional buckling instability, and torsional strength. The critical speed was calculated assuming pinned supports and the buckling torque and average shear stress were calculated with thin-walled shaft assumptions. In comparison to the aluminum driveline, the boron/epoxy driveline had reduced weight by virtue of longer shaft segments (fewer hanger bearings) and less weight in the segments themselves.

Lim and Darlow (1986) applied optimization to the design composite shafts of varying fiber type, segment length, and outer radius, with constraints based on whirl speed, torsional buckling, torsional strength via the maximum strain criterion at the ply level, and torsional vibration. Shear deformation and rotary inertia were included in the whirl analysis. The shaft was allowed to vary in terms of laminate arrangement, average radius, length of unsupported segments, and operating speed. The optimization scheme adopted for this design exercise is considered a sequential one, where the speed and number of segments are initially specified, the wall thickness is determined based on torsional and lateral vibration requirements, and the optimization routine determines the best laminate arrangement given the previous steps. Significant weight reductions were obtained with composite shafts versus the aluminum baseline, with larger reductions associated with supercritical operation and a minimum number of shaft segments.

Darlow and Creonte (1995) designed minimum weight carbon/epoxy composite drivelines using a generalized reduced gradient algorithm. Supercritical shafts were included in this work to demonstrate the weight saving potential of this operational regime. Whirling stability, torsional buckling, torsional strength, and torsional vibration stability were used as constraints in the analysis. Elastic and strength properties at the ply level were specified. Lamination arrangement, ply thickness, and the inside diameter of the shaft comprised the design variables, while operating speed, transmitted power, and overall length were held constant. Shear deformation and rotary inertia were included in the whirl analysis. The investigators observed that torsional buckling and whirling were the dominant constraints. For subcritical and supercritical operation, significant weight reductions were realized by varying the wall thickness and ply orientation along the length of the shaft segments.

A relatively little-known class of fiber reinforced composite that has been under investigation since the mid-1980s for driveshaft applications (Hannibal et al., 1985) is flexible matrix composites (FMCs). These materials combine the high strength and stiffness of typical

reinforcement fibers and the high elongation characteristics of certain polymer matrix systems such as polyurethane. This combination enables the design of structures that are relatively strong, stiff, and of low ultimate strain in the fiber-dominated directions while being relatively compliant and of high ultimate strain in directions not aligned with the fibers. In the context of driveshafts, laminated FMCs may be designed with high torsional strength and stiffness coupled with compliant bending properties, which could eliminate or reduce the number of flexible couplers and bearings along the length of a helicopter driveline. In a limited study of thick-walled glass/polyurethane $[\pm 45]_s$ shafts that were designed to match the torsional strength of a baseline glass/epoxy shaft, Hannibal et al., (1985) identified potential issues with overheating and whirling of the FMC shaft. The overheating was attributed to material damping while whirling was attributed to flexural compliance. It was mentioned that these issues could potentially be mitigated with additional material development and shaft optimization.

Ocalan (2002) was the first to apply a wide range of criteria to the design of FMC helicopter drivelines. A finite element modeling approach accounted for the dynamics of a super-critically spinning shaft attached through active magnetic bearings to a tail boom. The design constraints were ply-level strength, torsional buckling, shaft temperature due to external environment and internal dissipation, shaft displacement, and external damping requirements. Torsional vibration was neglected. Classical lamination theory was employed to calculate ply stresses and strains along with shaft stiffness parameters for the whirl and buckling analyses. The design variables were the lamination arrangement and wall thickness, which were constant along the length of the shaft, and the bearing control parameters. Carbon fiber FMC ply properties included constant storage and loss moduli in the longitudinal, transverse, and shear directions. That is, the storage and loss moduli did not vary with rate or temperature. Similarly, the ply-level strengths were independent of rate and temperature. Although not all the design constraints were applied concurrently, the possibility of weight reduction versus an aluminum shaft was demonstrated.

Shin et al. (2003) utilized an analysis akin to Ocalan (2002) and included more materials and laminate arrangements, which allowed a broader range of conclusions to be drawn on the effects of shaft design parameters on allowable misalignment, shaft temperature, and the amount of external damping needed in the bearings for stability in supercritical operation. Torsional buckling and vibration were not considered in this work. The material properties included the same carbon FMC system as used by Ocalan, a conventional carbon reinforced rigid matrix composite (RMC), and two imaginary intermediate carbon composites with properties interpolated from the FMC and RMC properties. No rigorous optimization was attempted in this work. It was concluded that ply orientation had the most important effect on system performance and that the design space was rather complicated, with several sets of shaft design parameters providing satisfactory system performance.

Mayrides et al. (2005) continued the work by Ocalan (2002) and Shin et al. (2003) by including additional laminate types, focusing on subcritical operation, and adopting a more rigorous optimization approach to overcome the complicated design space. Torsional buckling was reintroduced to the analysis and the candidate materials were limited to FMC and RMC. To address torsional vibration issues, a new constraint on torsional stiffness was added to the analysis. Once again, the ply level storage and loss moduli and strengths did not vary with rate or temperature. The recommended laminates for maximum weight reduction without undue layup complexity were of the $[\pm\theta/\mp\theta]$ type (mixed angle ply). All previous research on driveshaft design was able to reduce number of bearings, shaft wall thickness, and with FMC flexible couplers (**Figure 1-2**) using quasi-static modulus and strength properties neglecting the effects of strain rate and temperature on material properties.

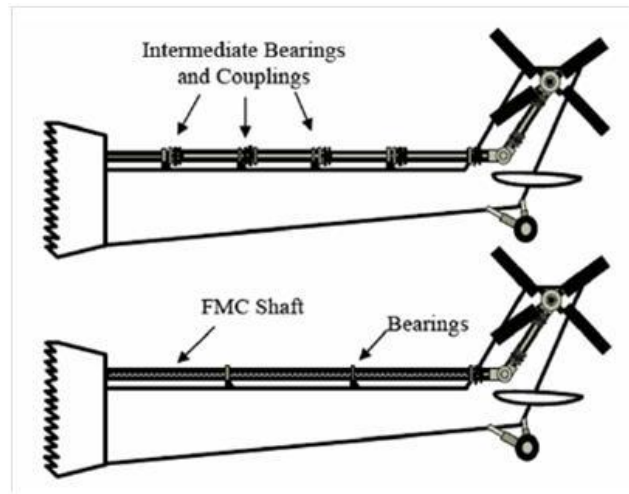


Figure 1-2. Schematic of traditional driveline (top) and proposed driveline (bottom) (Mayrides, 2005)

Shan and Bakis (2009) developed an analytical model for the prediction of the self-heating of a FMC driveshaft spinning with misalignment to fill the gap in rate and temperature dependent properties of FMCs. Model validation was done for a FMC system with temperature and frequency dependent properties and simple angle-ply cylinders of $[\pm\theta]_s$ lamination. Bakis et al. (2011) improved the analysis by including mixed angle-ply cylinders $[\pm\theta_1/\pm\theta_2/\dots\pm\theta_n]$ consisting of a new FMC system. Mixed angle-ply analysis was vital because previous driveshaft analysis (Ocalan, 2002; Mayrides et al., 2005) showed that optimized laminates contain more than one fiber angle. Roos and Bakis (2011) utilized genetic algorithm based optimization to design a $[\pm\theta_1/\pm\theta_2/\dots\pm\theta_n]$ subcritical laminate with the Bakis et al. (2011) frequency and temperature dependent FMC moduli. The analysis evaluated torsional buckling stability, driveshaft self-heating, whirling stability, and static-room temperature lamina strength, while neglecting torsional vibration stability as well as tailboom vibration interaction. Roos and Bakis (2011) used a sequential approach to design by first optimizing for the minimum number of hanger bearings (with number of lamina constant) and subsequently optimizing for the minimum number of

composite lamina (with number of hanger bearings constant). Weight reduction was primarily due to elimination of flexible couplers and material density reduction.

1.2 Undulated Composite Stiffness and Strength

Driveshafts and other cylindrical composites are often fabricated by the filament winding process, wherein tows of fiber are wrapped onto the cylindrical mandrel helically at $\pm\theta$ angles relative to the longitudinal axis. In a single helically wound layer, $-\theta$ tows pass under and over $+\theta$ tows and vice versa, resulting in triangular regions of $\pm\theta$ and $\mp\theta$ laminated material. The triangular regions repeat around the circumference of the cylinder by an integer number known as the filament winding pattern, FWP (**Figure 1-3**). At the helical and circumferential borders of these triangles, fibers undulate as they switch from the top layer to the bottom layer and vice versa (**Figure 1-3**).

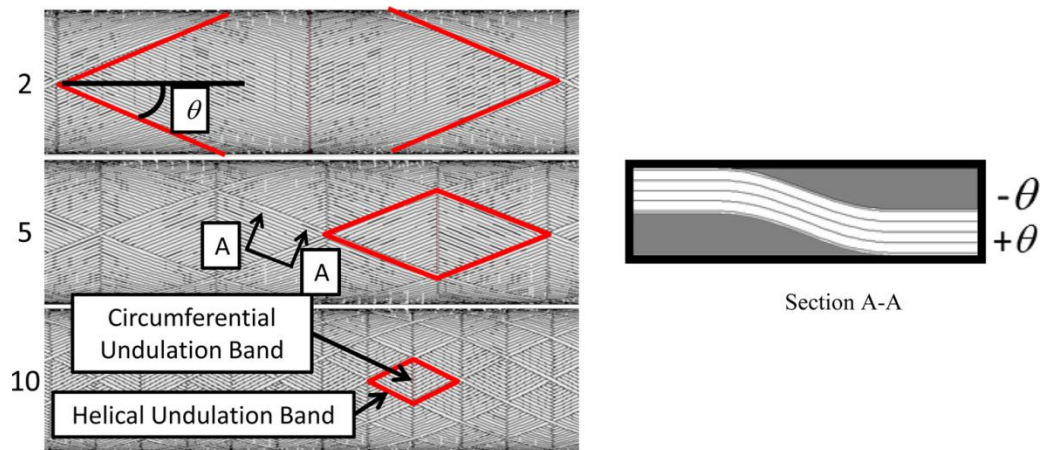


Figure 1-3. Schematic of filament wound cylinders: winding patterns of 2,5, and 10, showing repeating rhombic units (left); cross-section of undulated helical tow (right).

The out-of-plane fiber orientation creates local reduction of modulus and strength (Adams and Hyer, 1992). Heterogeneous composite laminates consist of several lamina that may have different elastic properties depending on their respective orientations. All available

micromechanical methods to homogenize such a laminate make assumptions about the nature of individual heterogeneous lamina and boundary conditions. Homogenization is generally applied at the representative volume element (RVE) level, a repeatable small fraction of the heterogeneous volume. The RVE is assumed to contain all of the necessary geometric information for the heterogeneous laminate. Many micromechanical approaches have been developed to homogenize composite laminates.

A well known model for unidirectional composites is the rule of mixtures (RoM). The RoM is used to determine homogenized properties utilizing a volume weighted average of each constituent (Daniel and Ishai, 2006). Two variations on the RoM exist, namely the iso-strain model (Voight model) and the iso-stress model (Reuss model), and are considered the RoM and inverse RoM respectively. These two models predict the upper and lower bound for homogenized elastic property prediction respectively. Additional prediction methods, such as the modified RoM and the Halpin-Tsai models, include semi-empirical factors for increased prediction accuracy with results lying between RoM and inverse RoM (Daniel and Ishai, 2006).

Laminate homogenization was initially considered for a heterogeneous laminate consisting of individual isotropic lamina. Several researchers (White and Angona, 1955; Postma, 1955; Rytov, 1956; Behrens, 1967) used a dispersion technique and elastic wave propagation theory to predict the homogenized elastic properties for a heterogeneous RVE element, determining the homogeneous laminate response to be transversely isotropic (simplified **Figure 1-4a**). Chu et al. (1972) increased the solution complexity by considering a heterogeneous laminate consisting of monoclinic lamina (**Figure 1-4b**). A monoclinic lamina has a plane of symmetry parallel to the plane containing the fibers. The method finds a solution, namely the homogeneous elastic properties, for non-undulated composites. The procedure was similar to classical lamination theory (CLT) but has the additional capability of three-dimensional stress calculation. Chou et al. (1972) makes use of the assumptions of the Voight and Reuss hypothesis. The normal and shear

in-plane strains, as well as the normal and shear out-of-plane stresses, are uniform in each lamina, while the remaining stresses and strains are averaged in order to predict homogenized elastic properties.

Several other researchers predicted the homogenized elastic properties considering monoclinic lamina. Pagano (1974) predicted the three-dimensional elastic response of an RVE that encompassed the entire thickness of the laminate. The stress-strain response includes the moment and curvature effects that are evident in unbalanced laminates. Sun and Li (1988) presented a simplification to the earlier work of Chou et al. (1972) by considering only balanced laminates, e.g., filament wound composites. The reduced homogenized elastic constants were in good agreement with previous work and allowed for a simplified analysis. These monoclinic procedures are meant for in-plane rotation only, neglecting out-of-plane rotation terms (**Figure 1-4c** or **Figure 1-4d**)

Ishikawa and Chou (1982) introduced several composite textile models for addressing fiber undulation of two-dimensional, orthogonally woven fabrics. The fiber crimp model assumed that CLT was valid at discrete points along the undulation. The stiffness response of the composite was then integrated along those points to estimate the undulated region stiffness. Several researchers (Zhang et al., 2008; Hipp and Jensen, 1992; Jensen and Pai, 1993; Pai and Jensen, 2001; Bogetti et al., 1992) expanded upon Ishikawa and Chou (1982) by including non-orthogonal fibers. Three-dimensional fiber orientation was considered, taking into account in-plane orientation as well as out-of-plane orientation caused by weaving (anisotropic lamina, **Figure 1-4d**). The analysis of the woven composite was truncated to two dimensions for use with CLT assuming a state of plane stress. The undulated fiber architecture was predicted to create complex elastic coupling (Zhang et al., 2008; Hipp and Jensen, 1992; Jensen and Pai, 1993; Pai and Jensen 2001) and stress distributions (Morozov, 2006; Bogetti et al., 1992) at the lamina level, which have been shown analytically and experimentally to reduce the longitudinal

modulus of elasticity (Hipp and Jensen, 1992; Jensen and Pai, 1993; Pai and Jensen, 2001, Bogetti et al., 1992). Any 2D model can only predict in-plane elastic properties.

$$\{\sigma\} = \begin{bmatrix} C_{11} & C_{12} & C_{13} & 0 & 0 & 0 \\ & C_{22} & C_{23} & 0 & 0 & 0 \\ & & C_{33} & 0 & 0 & 0 \\ & & & C_{44} & 0 & 0 \\ & sym & & & C_{55} & 0 \\ & & & & & C_{66} \end{bmatrix} \{\varepsilon\}$$

(a) Orthotropic, unidirectional

$$\{\sigma\} = \begin{bmatrix} C_{11} & C_{12} & C_{13} & 0 & 0 & C_{16} \\ & C_{22} & C_{23} & 0 & 0 & C_{26} \\ & & C_{33} & 0 & 0 & C_{36} \\ & & & C_{44} & C_{45} & 0 \\ & sym & & & C_{55} & 0 \\ & & & & & C_{66} \end{bmatrix} \{\varepsilon\}$$

(b) Monoclinic, in-plane rotation

$$\{\sigma\} = \begin{bmatrix} C_{11} & C_{12} & C_{13} & 0 & C_{15} & 0 \\ & C_{22} & C_{23} & 0 & C_{25} & 0 \\ & & C_{33} & 0 & C_{35} & 0 \\ & & & C_{44} & 0 & C_{46} \\ & sym & & & C_{55} & 0 \\ & & & & & C_{66} \end{bmatrix} \{\varepsilon\}$$

(c) Monoclinic, out-of-plane rotation

$$\{\sigma\} = \begin{bmatrix} C_{11} & C_{12} & C_{13} & C_{14} & C_{15} & C_{16} \\ & C_{22} & C_{23} & C_{24} & C_{25} & C_{26} \\ & & C_{33} & C_{34} & C_{35} & C_{36} \\ & & & C_{44} & C_{45} & C_{46} \\ & sym & & & C_{55} & C_{56} \\ & & & & & C_{66} \end{bmatrix} \{\varepsilon\}$$

(d) Anisotropic, in- and out-of-plane rotation

Figure 1-4. Constitutive equations with varying degrees of fiber reinforcement rotation

Compressive strength of composites is difficult to predict and measure. True material compressive failure in experimental testing can be preempted by global or local (microbuckling) buckling of the fiber reinforcement. Analytical and semi-empirical models used for strength prediction of unidirectional composites loaded in compression were stated as for microbuckling or kinking of fibers. Microbuckling is the local buckling of fibers embedded within a polymer matrix foundation (**Figure 1-5a**). Kinking is the process by which bands of material experience plastic deformation in regions where the fiber reinforcement has broken (**Figure 1-5b**). FMC materials are hypothesized to fail by fiber microbuckling due to the material returning to its undeformed shape when compressive load is removed after microbuckling has occurred, as well as a lack of bifurcation stress-strain response.

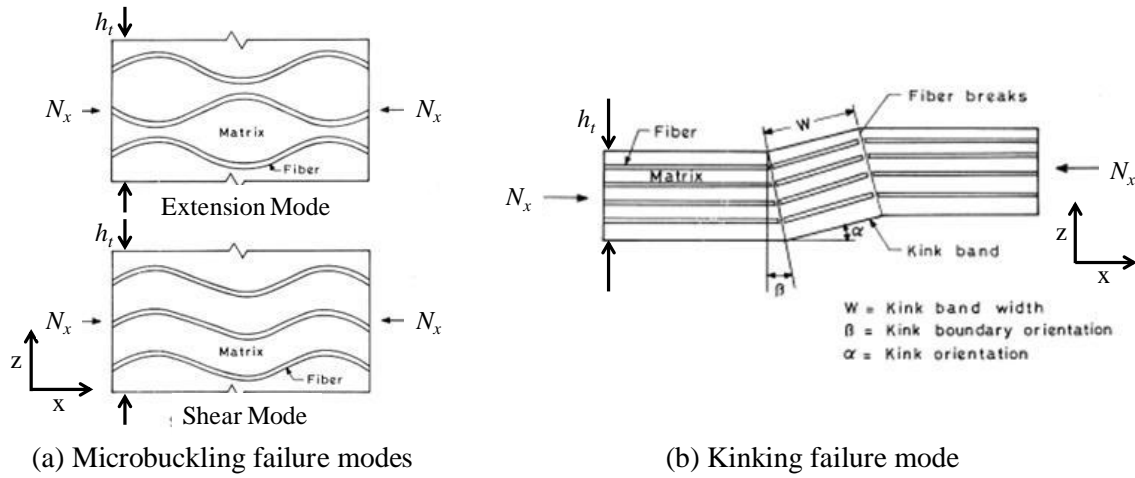


Figure 1-5. Laminate compression failure modes (Naik et al., 1999)

Analytical models for unidirectional laminate compressive strength generally rely on assumed mechanisms of failure. For example, Rosen (1965) assumed that fibers buckle with in-phase or out-of-phase modes (**Figure 1-5a**). Experimental strengths are often below those predicted by Rosen's models due to imperfect fiber spacing and orientation, as well as various flaws such as voids. Improvements to Rosen's models stemmed from the understanding that fiber misalignment (Yugartis, 1987; Lo and Chim, 1992) and waviness (Adams and Bell, 1995) were important factors in compressive strength modeling. Misalignment and waviness can be due to manufacturing related defects such as thermal gradients and improper layup or manufacturing method such as weaving, braiding, or filament winding. Micromechanical models (Bogetti et al., 1992) predicted that out-of-plane undulation creates significant shear stress in the plane of the undulation and suggested that accurate knowledge of the geometry of the undulation was critical to accurate strength prediction. Bogetti et al. (1992) approached modulus prediction of undulated composites by using Ishikawa and Chou's (1982) 2D method. The laminate $[[90/0/90]]$ was analyzed; the 0-deg. lamina was assumed to have a half sine wave undulation (**Figure 1-6**). The height of the undulation, h_u , is primarily a function of fiber tow parameters such as tension, fiber count, width, and through-the-thickness direction compaction.

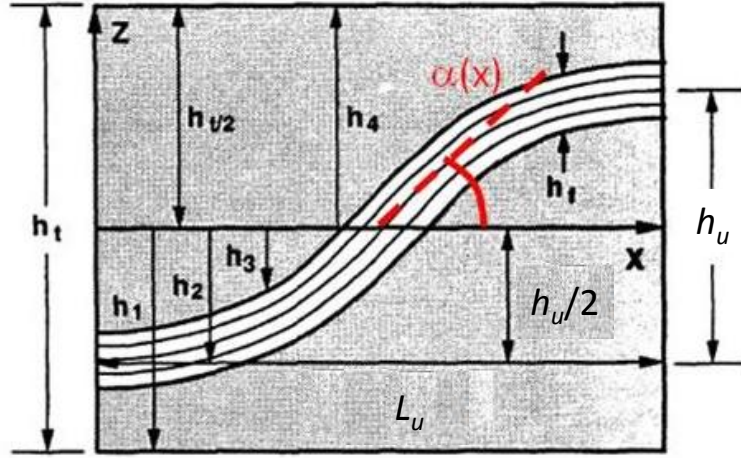


Figure 1-6. [90/0/90] Lamina waviness unit cell (Bogetti et al., 1992)

The undulation geometry was used to calculate the modulus of the undulating lamina (Q_{ij}) which could then be used to calculate the effective stiffness matrix of the laminate (A_{ij} , B_{ij} , D_{ij}) (Gibson, 2007). Bogetti et al. (1992) investigated the effect of undulation amplitude on the failure mode of the composite by applying a stress in the x -direction that would cause compressive failure in the fiber direction (F_{1c}) if the composite material was non-undulated. Failure was detected when any principal stress component in any lamina at any segment dx along the undulation exceeded the strength allowable (maximum stress theory, MST). Lamina level stresses were non-dimensionalized by their corresponding strength allowable and distance along the undulation was non-dimensionalized by the undulation length. The 0-deg. lamina made up one third the laminate thickness ($h_1/h_f=3$) and the undulation length was five times the 0-deg. thickness ($L_u/h_f=5$). **Figure 1-7** shows that for a non-undulated composite ($h_u=0$) out-of-plane transverse stress σ_3 and out-of-plane longitudinal shear stress τ_{13} were zero. σ_3 can be seen to just exceed the strength allowable, while τ_{13} far exceeds the allowable for an undulated composite ($h_u=0.01$), indicating that τ_{13} becomes the dominant failure mode. The 2D nature of this approach neglects coupling between various in-plane and out-of-plane stress components (essentially a

lower order approximation compared to 3D) which may increase or decrease the influence of individual stress components changing the laminate failure strength.

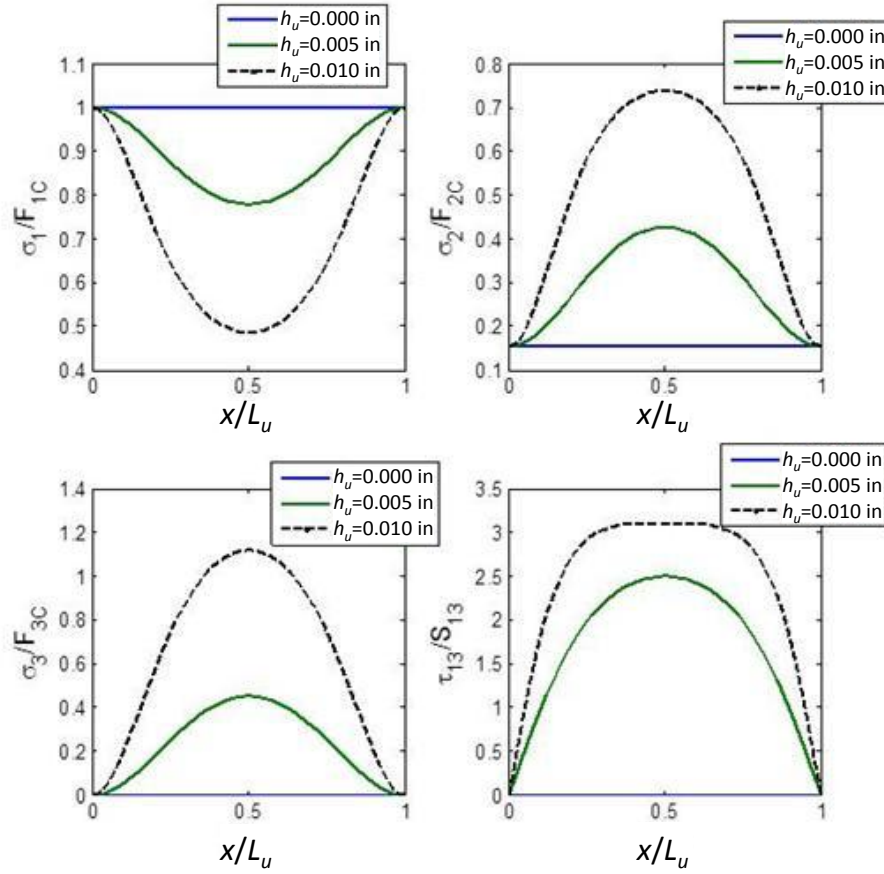


Figure 1-7. Interlaminar stress within the wavy 0-deg. lamina in AS4/PEEK: unilongitudinal compressive loading (Bogetti, et al., 1992)

Guyann et al, (1992a) created a finite element analysis (FEA) model of an infinite fiber/matrix series of initially wavy fibers from manufacturing defects. The model simplified the fiber undulation to a half sine wave. The unit cell consisted of a single fiber with matrix elements along side, creating a doubly symmetric model constrained with multi-point symmetry to approximate an infinite two dimensional series of fibers. The left and right sides of the model were subjected to boundary conditions such that the distance between points at any longitudinal station along the undulation stays constant. Non-linear shear constitutive behavior was

considered for the resin elements. The FEA model predicted that the compression strength at microbuckling failure (defined as increases in displacement with no corresponding increase in load) would decrease with increasing resin shear compliance and fiber misalignment amplitude. Guynn et al., 1992b chose a woven fabric instead of creating a laminate of the type used in the FEA analysis barring direct comparison; however, observations supported the conclusions of the analytical work. Undulated composites were commonly evaluated using plain or harness satin weaves to approximate discrete misalignment.

1.3 Filament Wound Cylinders and Filament Winding Pattern

A single helically wound layer creates adjacent laminated triangular regions of $\pm\theta$ and $\mp\theta$ stacking sequence in a cylinder, where the borders of the triangles comprise regions of out-of-plane fiber undulation (**Figure 1-3**). The filament winding pattern (FWP) refers to the integer number of highlighted rhombic regions that can be placed side-by-side around the circumference of the cylinder. Helically wound cylinders of the same geometric size and fiber angle can be made with a user-selected pattern of one or larger by varying fiber bandwidth (width of a single tow of fibers as they are laid down in manufacturing) or by varying the circuits to pattern (number of tows per rhombus). Circumferentially wound 89-deg. layers had no winding pattern, as the tow was laid spirally alongside itself along the length of the mandrel.

Previous research efforts have shown that winding patterns of different sizes lead to different heterogeneous distributions of stresses and strains at the lamina-level in filament wound cylinders (Morozov, 2006; Zhang et al. 2008) (**Figure 1-8**). It had been hypothesized this was due to lamina level stiffness changes in regions where the reinforcement was undulated, as well as the introduction of material stiffness coupling where the laminate was not symmetric. The effect of the FWP on internal (Rousseau et al., 1999) or external (Moon et al., 2010) pressure at failure has

been shown to be insensitive to FWP. Rousseau et al. (1999) observed, however, that filament wound cylinders manufactured with higher values of FWP were found to begin weeping (leaking) at lower pressures and hypothesized the cause to be a larger number of initiation sites (more undulation by volume). Classical theories and finite element approaches have been shown to be dependable in predicting external or internal pressure at failure for carbon/epoxy filament wound cylinders (Cohen, 1997; Rousseau et al., 1999).

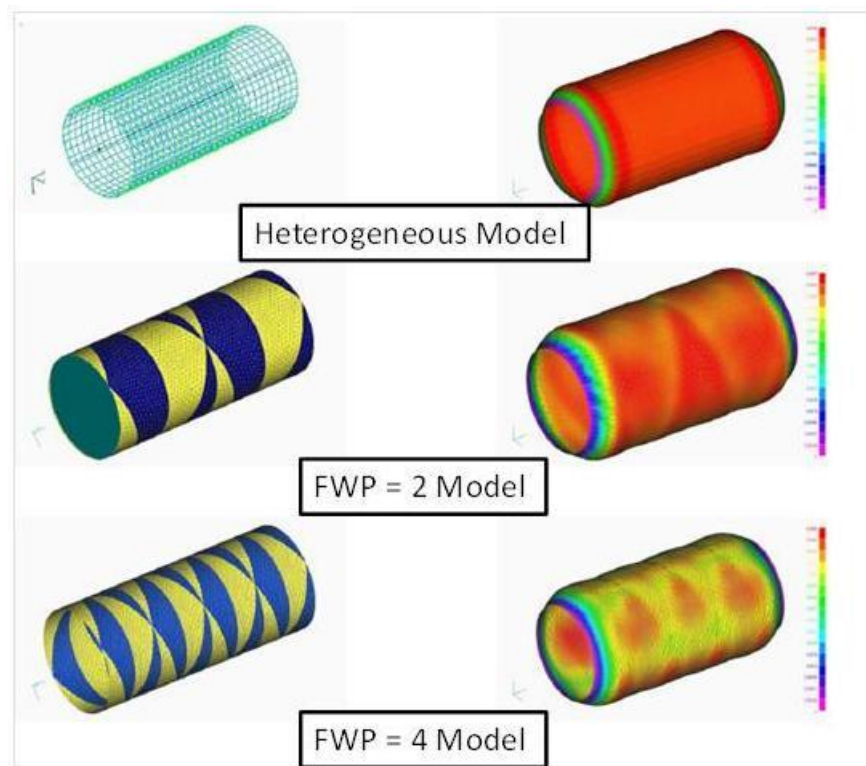


Figure 1-8. Filament wound cylinder subjected to internal pressure; homogeneous, pattern of 2, pattern of 4 (Morozov, 2006)

Filament wound composite cylinders subjected to excessive longitudinal compressive loading (σ_x) were shown to exhibit rhombic shaped longitudinal buckling instabilities that occur along the length and around the circumference of the cylinder (**Figure 1-9**) (Hahn et al., 1994; Card, 1966; Hillburger and Starnes, 2002).

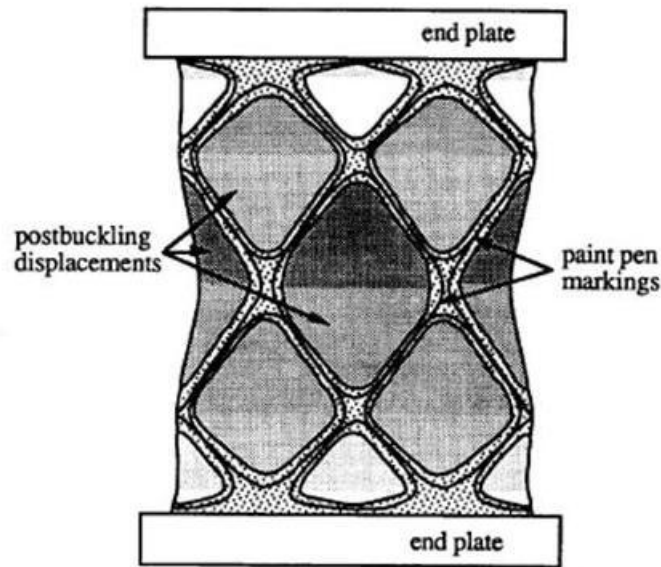


Figure 1-9. Typical buckling mode shape of $[\pm 30]$ filament wound cylinder (Hahn et al., 1994)

A longitudinal buckling failure was more likely to occur when the tested filament wound cylinder has a large diameter compared to thickness (“thin walled”). Experimental results from Hahn et al. (1994), (57 mm and 152 mm diameter, 0.5 and 2 mm thickness cylinders) showed that changing the FWP from 5 ($AR = 3$ in **Figure 1-10**) to 23 ($AR = 12.5$ in **Figure 1-10**) in angle-ply filament wound cylinders increased the compression strength by 27 %. Changing the FWP through the thickness, using winding patterns of 10 and 5 in a two layer laminate, increased the ultimate compression strength by up to 25 %, compared to cylinders of winding pattern of 5 and 5 (Hahn et al., 1994). It has been hypothesized that when the FWP is of similar size to the longitudinal buckling instability the sample will have a lower strength (Claus, 1994) (**Figure 1-10**).

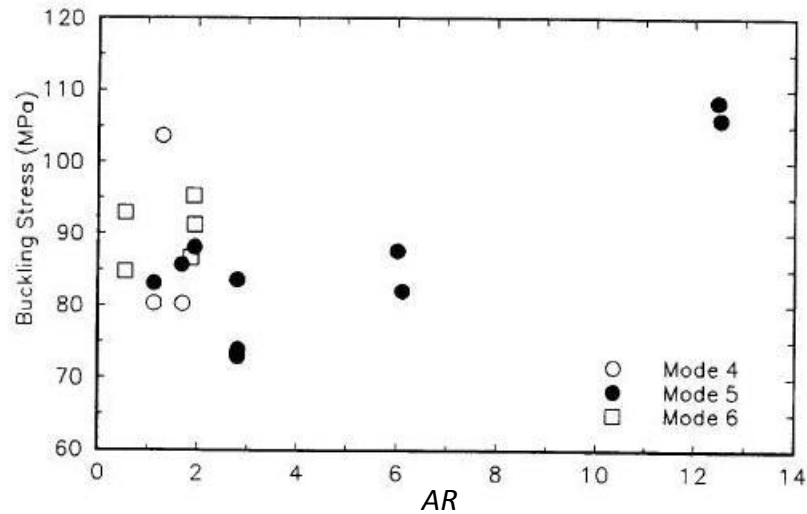


Figure 1-10. Effect of circumferential crossover-band spacing (specimen length/circumferential undulation spacing) on the buckling stress of 57-mm diameter [± 30] filament-wound cylinders (Hahn et al., 1994)

1.4 Analytical and FEA Methods for E_1 and F_{1C} Determination

The combination of undulated fiber architecture inherent in filament wound composites and a compliant matrix produces unique challenges in the prediction of modulus (E_1) and strength (F_{1C}) using traditional laminated composite theories. Particularly inaccurate was the RoM micromechanical equation for fiber-direction modulus (excluding tension) and CLT for the modulus of multi-directionally reinforced cylinders (Daniel and Ishai, 2006). Previous research asserts that the cause of the prediction error was structural regions containing out-of-plane fiber undulation or anti-symmetric lamination arrangement creating elastic structural couplings such as extension-twist, bend-twist, etc. (Hipp and Jensen, 1992; Jensen and Pai, 1993; Zhang et al., 2008; Zindel and Bakis, 2011).

Jensen and Pai (1993), acknowledging the efforts of Ishikawa and Chou (1982), attempted to modify the fiber crimp model for application in modeling the modulus and longitudinal buckling

load of filament wound RMC cylinders. The stiffness Q_{ij} for each lamina was rotated with respect to the out-of-plane fiber misalignment angle. The stiffness was then rotated to the global coordinate system (xy system) through the off-axis filament winding angle (**Figure 1-11**). The mean value theorem was used to numerically integrate the laminate constitutive properties A_{ij} , B_{ij} , and D_{ij} along half of the undulation to ensure nonzero bending-extension coupling due to anti-symmetry of the undulated area. Jensen and Pai (1993) concluded that inclusion of the bending-membrane stiffness coupling effects in the various regions of the composite (B_{ij} matrix) increased longitudinal modulus and buckling strength prediction accuracy compared to other available analytical methods.

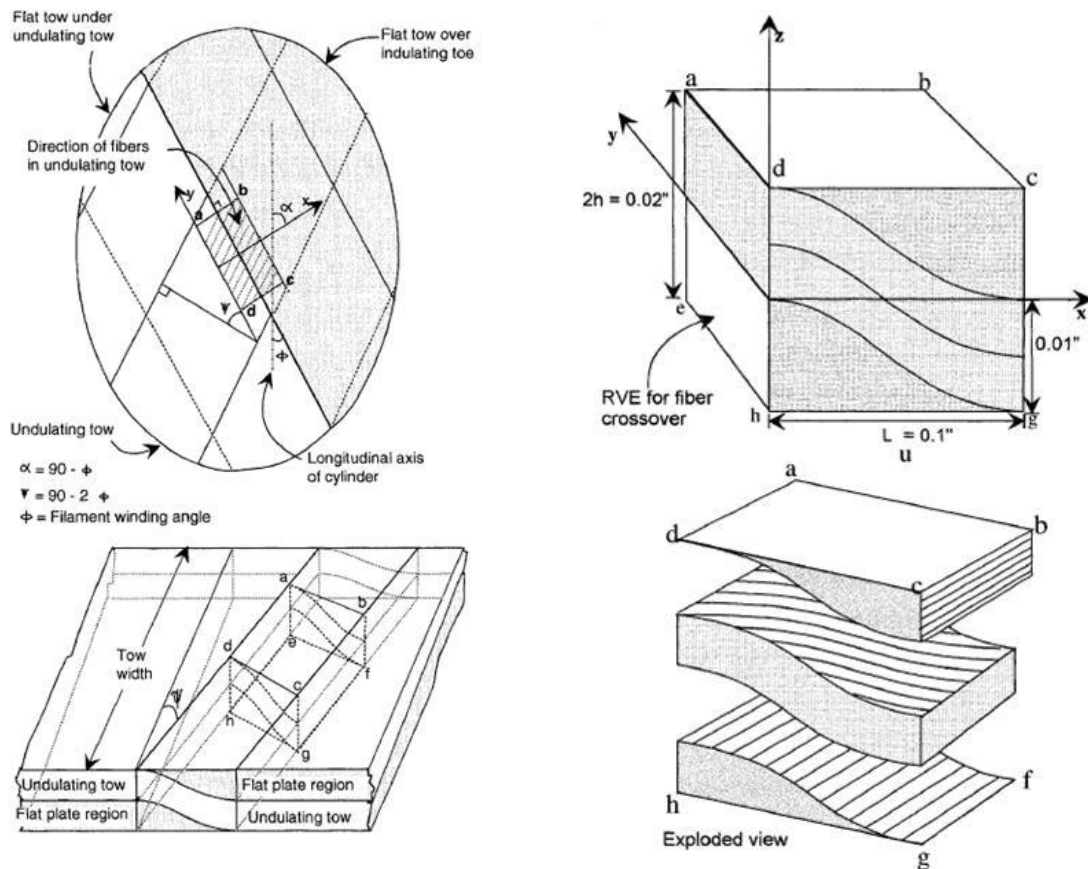


Figure 1-11. Identification of representative volume element (RVE) for fiber tow crossover region (Pai and Jensen, 2001)

Pai and Jensen (2001) advanced their previous work by attempting to recreate the filament wound architecture with FEA using separate elements with non-undulated or undulated elastic properties for corresponding regions to predict the buckling strength of RMC-filament-wound cylinders. The stiffness matrix of the RMC was rotated three dimensionally through the out-of-plane rotation angle caused by the fiber undulation and through the in-plane filament winding angle to the local lamina coordinate system to avoid some of the simplifying assumptions of Jensen and Pai (1993). The three dimensional stiffness matrix was then converted to a two dimensional effective stiffness matrix which was used to calculate the homogenized laminate stiffness. The FEA modeling effort was supported by experimentally tested cylinders of dimension $152.4 \times 228.6 \times 0.5$ mm (diameter, length, thickness) considered “thin-walled”. The peak longitudinal buckling load prediction from eigenvalue analysis increased with undulation by volume (increasing the FWP) while experimentally the longitudinal buckling load decreased. The model was able to capture the strength reducing effect of stretch-twist/bend-shear and bend-twist coupling introduced in the laminate by undulation.

Pai and Jensen (2001) as well as Zhang et al. (2008) predicted that the filament winding pattern has only a small effect (less than 10%) on the membrane stiffness coefficients of RMC cylinders. Zindel and Bakis (2011), however, predicted reductions of 15-30 % in the longitudinal modulus of FMC helically wound cylinders as FWP was increased. Therefore, it was believed that modulus of the matrix material may be important when evaluating the degenerative effect of FWP on the mechanical properties of helically wound composite cylinders. The lamina level micromechanical models (Jensen and Pai, 1993; Zhang et al., 2008; Zindel and Bakis, 2011) appeared to be capable of quantifying the influence of modulus-reducing out-of-plane fiber undulation and FWP. Similar to the undulated microbuckling models for two dimensional woven composites, cylindrical models require accurate measurements of a number of geometric parameters as well as three-dimensional elastic properties, and lack extensive experimental

validation. In addition, excluding a refined finite element analysis that captures the geometry of every tow in the repeating FWP rhombic RVE (Zhang et al. 2008), the published models were not universally suited for the accurate calculation of stress and prediction of filament wound cylinder modulus and micromechanical strength. Additionally, the models developed by Hipp and Jensen (1992), Jensen and Pai (1993), and Pai and Jensen (2001) were developed to predict the structural buckling of thin-walled filament wound cylinders loaded solely by longitudinal compression.

Complex FEA models for textile composites account for two and three dimensional fiber alignment. Textile simulation has been used in understanding crack initiation and growth, ballistic damage response, and mechanizations for three dimensionally reinforced fabrics and braids consolidation during manufacturing. Multi-chain digital elements (which consist of multiple elements paired together using pinned boundary conditions) were used to model fiber yarns, which consist of several thousand individual fibers, with realistic weaving architecture such as fiber crimping and non-constant yarn cross-section (Wang et al., 2010). Model simulations for the verification of compaction and microstructure was shown (Miao et al., 2008) to be very realistic for various tri-axis weaves as processed via vacuum assisted resin transfer molding (**Figure 1-12**).

Crack propagation (Kurashiki et al., 2007) and ballistic damage textile models (Hur, 2006) utilized yarn level meshing in conjunction with a FEA package such as Abaqus to conduct structural analysis of the FEA mesh. Importation of full textile models into a structural FEA package, including lamina level stiffness and strength, could yield more accurate predictions of cylinder modulus and strength as the fiber yarn was modeled as a continuous artifact instead of using separate undulated and non-undulated elements in analysis (Pai and Jensen, 2001). The main weakness of such an approach was the excessive number of elements required to accurately capture the manufacturing complexity.

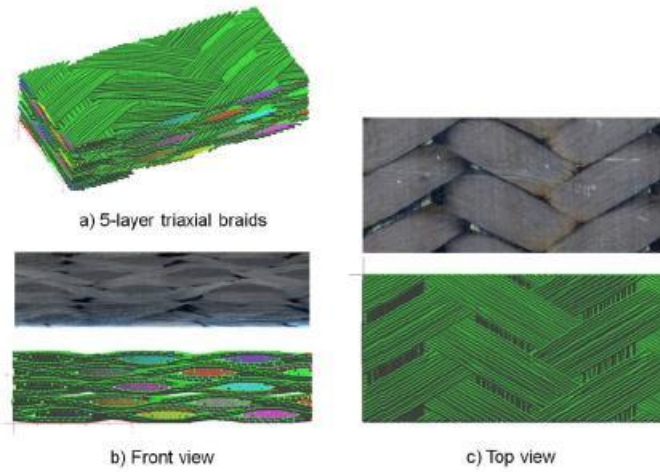


Figure 1-12. FEA results and experimental observation (Zhou et al., 2009)

1.5 Standards and Empirical Methods for E_1 and F_{1C} Determination

Commonly, compressive properties of polymer matrix composites such as E_1 and F_{1C} are experimentally determined through testing of unidirectional non-undulated specimens. Non-undulated specimens can be compressively tested through pure end loading (ASTM D 685), combined end loading and shear (ASTM D6641), or longitudinal loading through shear traction (ASTM D3410). True fiber compression failures are difficult to achieve experimentally due to relatively low longitudinal shear strength (F_5 , F_6) and transverse strength (F_{2C} or F_{2T} , F_{3C} or F_{3T}) compared to the longitudinal strength (F_{1C}).

A method was developed by Adams and Welsh (1997) to overcome the difficulties involved in testing unidirectional flat composites by using a multi-directional laminate where individual 0-deg. lamina were exchanged for 90-deg. lamina. The use of a specially orthotropic laminate (equal number of 0-deg. lamina and 90-deg. lamina) for compressive testing reduced grip related failures and at the same time allowed a value of F_{1C} to be obtained. This method requires prior measurement of all unidirectional lamina elastic properties so that CLT could be utilized in back-

calculation of F_{1C} for the load supporting 0-deg. lamina of the laminate. Adams and Welsh (1997) demonstrated that the in-situ compressive strength of fibers in the laminate was dependent on the degree of constraint provided by adjoining lamina. The in-situ compressive strength of fibers in most practical multi-directionally reinforced laminates (can't exceed F_{1C}) significantly exceeded that in 0-deg. unidirectional specimens due to imperfections. Unidirectional test specimens were unsuitable for determining compressive modulus or strength of filament wound cylinders due to a lack fiber weaving (undulation), which will cause a measured unidirectional value to far exceed an in-situ filament wound cylinder measurement. Available standards are unsuitable due to the short gage length (much smaller than the FWP), as well as the high anisotropy of the FMC leading to undesirable matrix related failures.

Previous research by Sollenberger (2010) aimed to interpolate, based on the R^2 fit, the in-situ fiber-direction modulus of FMC material in filament wound cylinders using an empirical approach. Cylinders of various angle-ply lamination arrangements ranging from ± 20 -deg. to almost 90-deg. (a circumferential winding pattern) were manufactured and loaded in longitudinal compression and tension to failure. Cylinders with ± 45 -deg. lamina provided the lamina level longitudinal shear modulus, G_{12} , while circumferentially-wound cylinders loaded in compression provided the transverse modulus of the lamina, E_2 . The longitudinal Poisson's ratio of the lamina, ν_{12} , was calculated using the RoM and the longitudinal modulus E_1 was back calculated with CLT to match the longitudinal modulus of the laminated cylinder experiments, E_x .

As can be seen in **Figure 1-13**, the extrapolated longitudinal modulus of cylinders with a hypothetical winding angle of 0-deg. (i.e., all longitudinally oriented fibers), which actually provides the value of E_1 at the lamina level, ranges between 43 GPa and 59 GPa, depending on the sign of stress applied to the cylinders. As expected due to the low modulus of the matrix (~245 MPa), the backed out E_1 is less in compression than in tension. More important, however, was the discrepancy between either of these E_1 values and the predicted value of 145 GPa that

one obtains using the RoM, with the known fiber volume fraction and constituent properties (Sollenberger, 2010; Shan and Bakis, 2009). Sollenberger's (2010) approach for experimentally determining a value for E_1 was unique because it accounted for the fiber undulation and FWP of a filament wound cylinder. Clearly, classical analytical models which ignore FWP and fiber reinforcement undulation cannot be used to model the modulus of these cylinders.

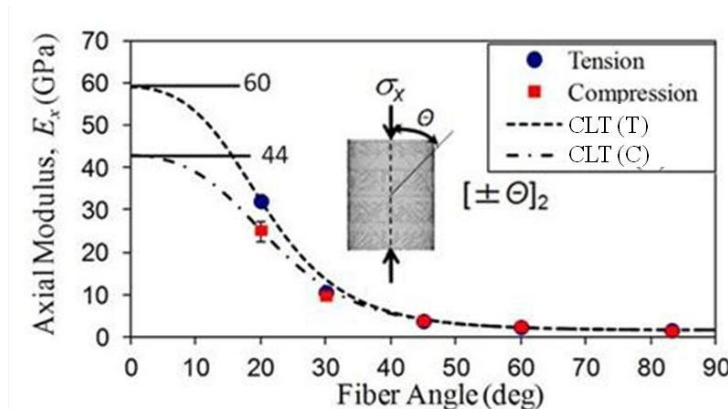


Figure 1-13. LF750/AS4D longitudinal modulus versus fiber angle θ_x —experiments and theory (Sollenberger, 2010)

Low-single-angle FMC cylinders tested in compression by Sollenberger (2010) were observed to take on a barrel shape due to the transverse constraint provided by the potted end caps (**Figure 1-14a**). It is hypothesized that this barrel shape detracts from the compressive modulus and strength of the specimen, potentially biasing the backed out modulus E_1 and strength F_{1c} of the laminate downwards, as well. This barreling should therefore be eliminated by redesigning the laminate. Using the FMC lamina properties of Sollenberger (2010), CLT was used to estimate the longitudinal Poisson's ratio, ν_{xy} , of the entire spectrum of possible $[\pm\theta]_2$ angle-ply cylinders, where θ was measured relative to the longitudinal direction of the cylinder. ν_{xy} can be as high as 4 for a fiber angle near 20 degrees. A simple improvement to reduce barreling in a $[\pm\theta]_2$ cylinder was to add a circumferentially wound lamina to the laminate – similar to the approach of Adams and Welsh (1997) for preventing undesirable failure modes in

flat unidirectional reinforced specimens. **Figure 1-14b** shows v_{xy} for $[\pm\theta/89/\pm\theta]$ laminates, where 89 deg. was the closest possible angle to 90 deg. because of the way a tow was wound with a finite bandwidth. The Poisson's ratio of an FMC cylinder with 20-deg. angle lamina was reduced by nearly a factor of 10 with the addition of the 89-deg. layer, suggesting that barreling should be mitigated in a compression test.

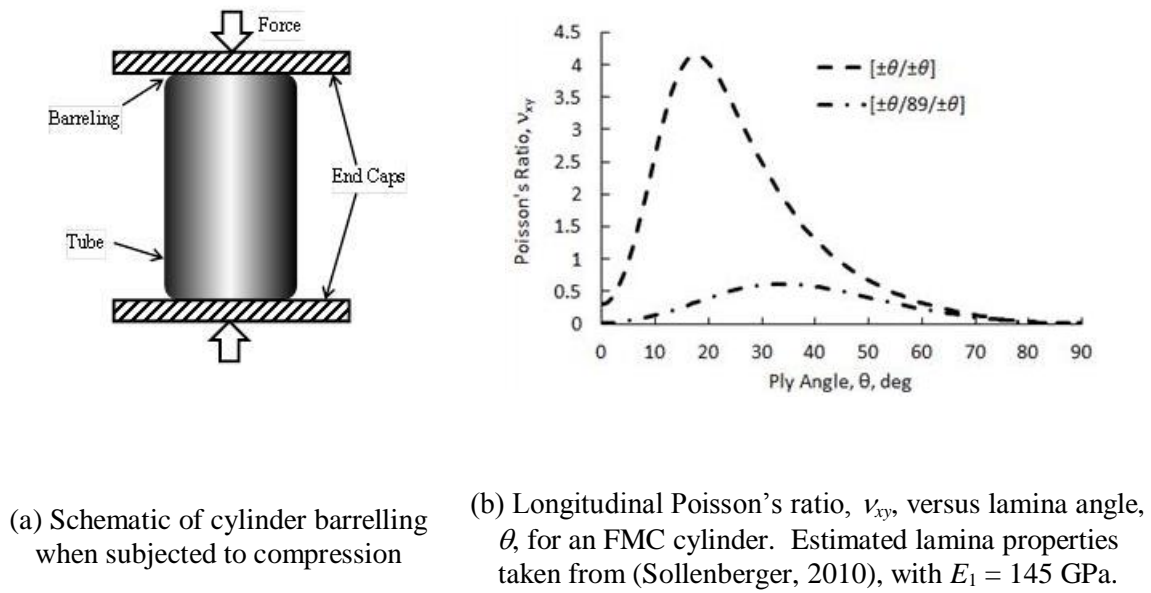


Figure 1-14. Compression testing: specimen barreling and Poisson's ratio

Recently developed experimental methods allow for the improved characterization of not only complex strain fields but also failure mechanisms in filament wound cylinders, with the undulated fibers of particular interest. For example, the digital image correlation (DIC) method (made practical by the advent of measurement-grade digital cameras and high speed computers) has been used to measure full-field strains in filament wound cylinders under internal pressure (Scheuer et al., 2009), combined tension, torsion, and bending loads (Crouzeix et al., 2009) (**Figure 1-15**), and in compression before and after ballistic impact damage (Sollenberger et al., 2010) (**Figure 1-16**). DIC results were able to resolve the FWP in the correlated images of the

radial locations of a cylindrical surface as well as in the various strain fields. Clarity of the correlated results was largely dependent on the resolution of the digital cameras used in capturing the images. Failure mechanisms such as excessive local yielding and strain localization were captured visually with specific interest around areas of concentrated-localized strain (**Figure 1-16**). DIC has also been used to evaluate flat tensile coupons manufactured with fiber tows woven in a FWP (Torres et al., 2010). Torres et al. (2010) observed that FWP was important in determining locations of potential crack initiation and growth with future application in internal pressurization tests. Makeev et al. (2009) observed the complex strain state and delamination failure process near wavy fibers in a shear-loaded composite beam using DIC, noting the significance of the fiber undulation.

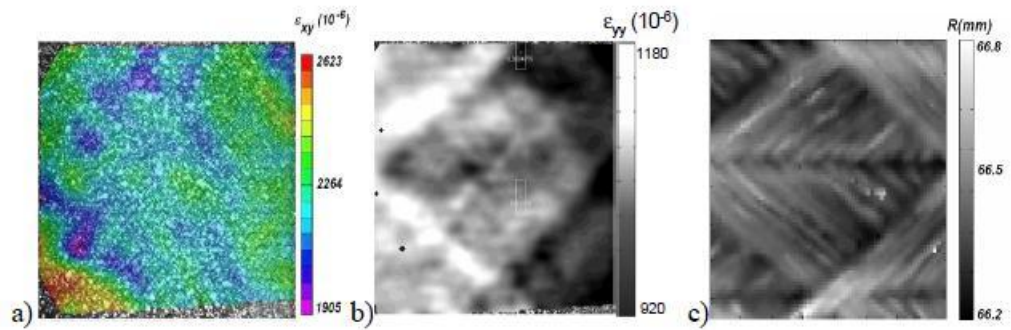


Figure 1-15. a) Shear strain measured during torsion test, b) longitudinal strain field during a test with a combination of traction and flexure, c) local radius (Crouzeix et al., 2009)

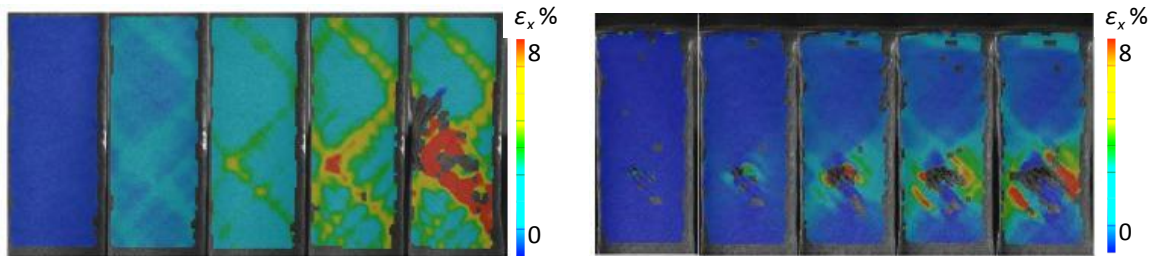


Figure 1-16. Snapshots of longitudinal strain in rigid $\pm 45^\circ$ undamaged (left) and damaged, lower center (right) cylinders tested in tension (Sollenberger et al., 2010)

1.6 Opportunities for Research

Available literature on filament wound driveshaft design leaves areas of opportunity with respect to multi-objective design trades and inclusion of temperature-dependent composite strength. Previous investigations estimated composite strength at room temperature to determine failure of homogeneous, orthotropic, cylindrical driveshafts of fixed or variable multi-angle laminates. Implementation of a multi-objective optimization tool allows for the visualization of the design space and the observation of trades for the optimization problem. Additionally the lamination arrangement should be unrestricted unlike many previous efforts. Rate and temperature effects were modeled for resin dominated moduli only. Estimates of F_{1C} and E_1 in particular are known to be optimistic for filament wound driveshafts as they rarely take into account fiber undulation and neglect material softening due to increased operating temperatures. Composite materials with undulation have a lack of tandem experimental-analytical support for implementation in modeling. All of these points were exceptionally true for FMCs, for which the literature was lacking compared to RMCs.

Analytical micromechanical models of undulated composites were rarely supported by extensive experimental testing. Only two dimensional models were created to analyze lamina with in- and out-of-plane rotation (anisotropic lamina) but are only able to determine in-plane elastic properties and neglect out-of-plane stress components. Available three dimensional models were developed for non-undulated composites (monoclinic lamina) and must be corrected for out-of-plane orientation. Opportunities for research exist in developing a three dimensional model which homogenizes a laminate containing anisotropic lamina. Such a model would be able to determine all three dimensional properties as well as predict the homogenized stress state at a higher level of analysis (i.e. including all coupling terms).

Experimentally, methods for determination of a suitable value of E_1 and F_{1C} for use in driveshaft optimization codes were lacking in the literature. ASTM standard methods, used with composites made from unidirectional tape, ignore out-of-plane fiber undulation and FWP. As such, measured values of E_1 and F_{1C} far exceed (30 % and 60 % higher respectively) practical in-situ values for filament wound cylinders. Empirical methods in the literature require extensive testing to determine suitable empirical constants. Opportunities for research exist in advanced techniques such as DIC, which may yield insight into failure mechanisms such as excessive local yielding and strain localization that happen concurrently with fiber microbuckling by capturing these phenomena visually as well as possibly analyzing them critically.

FWP was shown to affect the strain distributions in filament wound cylinders. This phenomenon was not well understood, but was hypothesized to be related to the longitudinal buckling shape of the cylinder. Composite failure mechanisms in filament wound cylinders pose an opportunity for research in the literature, especially for a new class of material such as FMC for which bifurcation was not present in the stress-strain curve, suggesting a micromechanical failure. Simple FEA methods employed homogenized elements for undulated and non-undulated regions to some success. Intensive exploration required excessive numbers of elements.

1.7 Objectives

The objective of the current investigation is to:

1. Elucidate trades in the multi-objective design of a misaligned filament wound composite driveline using a wide range of candidate matrix materials that are differentiated by their temperature-dependent mechanical properties.
2. Observe the effects of out-of-plane fiber undulation on the full-field strain and structural behavior of flat undulated composites under compression for which modulus and strength

measurements can be used to validate a 3D derived micromechanical model for anisotropic lamina.

3. Observe the effects of filament winding parameters and matrix modulus of elasticity on the full-field strain and structural behavior of composite cylinders under compression and develop a local-global approach for predicting experimentally measured modulus and strength.

The completion of these objectives requires the following tasks:

- Characterize the relationship between lamina level composite strength and temperature
- Develop an optimization strategy for the design of a composite helicopter driveshaft
- Experimentally evaluate the effect of undulation height and neat resin modulus on composite compression modulus and strength with two dimensional DIC
- Derive and validate a three-dimensional approach for analytically predicting the modulus and strength of composites with half-sine undulation
- Investigate the surface strain field response due to longitudinal compression of filament wound cylinders with varying neat resin modulus, FWP, and fiber angles using 3D DIC
- Develop a local-global approach for predicting filament wound cylinder modulus and strength

Chapter 2

Materials and Manufacturing

This chapter focuses on the materials and manufacturing methods used in this research. Flat and cylindrical transverse test specimens were manufactured for determining transverse composite modulus and strength dependence on temperature. Previously developed quasi-static composite modulus-neat resin modulus and composite strength-neat resin modulus relationships (Henry, 2012) were created using multiple resins of varying neat resin modulus at room temperature. It was hypothesized that if the neat resin modulus of any singular resin was controlled through temperature changes, the modulus and strength of the corresponding composite would continue to follow this relationship. To this end, neat resin specimens were subjected to temperature controlled tests to develop relationships between neat resin modulus and temperature. Flat and cylindrical transverse composite specimens were evaluated for modulus and strength at the same temperatures to validate the previous relationships with neat resin modulus now known at various temperatures. Such a validated tool would allow for novel strength and modulus dependent temperature relationships that could be integrated into an optimization scheme for a composite driveshaft.

Flat and cylindrical undulated composite specimens were made to investigate the implications of fiber undulation on longitudinal modulus and strength. The presence of the undulation is known in the literature to be degenerative. Flat composite specimens with discrete undulation were made to investigate a simplified undulation case for which analytical models could be validated with respect to undulated composite modulus and strength prediction. Cylindrical undulated specimens made by filament winding expand upon the flat specimen experiments by introducing a larger, more complex structure for which modulus and strength predictions are

poorly understood. Flat and cylindrical undulated specimens were observed using DIC with the express purpose of understanding the complex strain states and failure mechanisms associated with undulated composites for which experimental measurements will be validated analytically.

2.1 Matrix Materials

Four polyurethane resins and one epoxide resin were evaluated in this investigation. Polyurethane toluene diisocyanate (TDI) terminated polyether prepolymers representing FMCs include Adiprene LF750D (Chemtura, Middlebury CT), Conathane DPRN 30748, Conathane DPRN 30757, and Conathane DPRN 30917 (all from Cytec Industrices, Olean NY). Conathane resins 30748, 30757, and 30917 contain polytetramethylene ether glycol in addition to TDI with 30917 also containing 10 % triol. All polyurethane prepolymers were cured with a delayed-action diamine curing agent Duracure C3LF (Chemtura, Middlebury CT: equivalent weight 247 g). A delayed action curative is designed to activate only when “unblocked” by the addition of heat to the mixture of prepolymer and curative facilitating cross linking and solidification of the material. All polyurethane prepolymers were cured at 140 °C for 2 hours, followed by a post cure at 100 °C for 16 hours. EPON 862, a bisphenol F epoxide, cured with an aromatic amine curing agent, Curative W (both from Momentive Specialty Chemicals, Columbus OH) were used as the RMC material in this investigation. The cure schedule was 121 °C for 1 hour followed by 177 °C for 2 hours for epoxy. The amount of parts curative per 100 parts prepolymer for polyurethanes, by mass, was calculated using **Equation 2-1**.

$$W_{curative} = (\%NCO \text{ of polymer}) \left(\frac{\text{equivalent weight of curing agent}}{42} \right) (.95) \quad (2-1)$$

Three neat resin specimens of each type were manufactured by liquid casting in an open “dogbone” mold (25.4 cm length, 1.3 cm width, 1.0 cm thickness) and tested in tension at room

temperature. The mold was prepared by first abrading the open surfaces with Scotch-Brite 7440 heavy duty hand pads (3M, St. Paul, MN), removing dirt and other foreign contaminants. The mold was then wiped clean with acetone leaving a smooth, contaminant-free surface. A layer of silicone release agent, Ease Release 200™ (Mann Formulated Products, Easton PA), was then applied liberally to the open surfaces of the mold, and the mold was placed in a convection heat oven at 140 °C (248 °F) to evaporate the solvents from the silicone. This was done two times for a period of thirty minutes each time. The prepolymer of interest was then mixed with the associated curative thoroughly at 50 °C. The resin was placed in a vacuum chamber under 30 inches of mercury (in Hg) to remove all air bubbles from within the resin which would become trapped after curing, leaving voids and reducing quality. When all air bubbles have been removed from the resin, the resin was poured into the preheated specimen mold (to the first respective resin cure temperature).

Average longitudinal strain was measured on the front and back of the specimen. Previously measured Young's modulus and Poisson's ratio in the 1000-2000 $\mu\epsilon$ strain range for neat resin tensile tests are shown in **Table 2-1** (Henry, 2012). The softest polyurethane resin (LF750) had a modulus approximately one order of magnitude more compliant than that of the epoxy resin. The selected resins represent a wide range of possible neat resin moduli for use in a composite driveshaft. One specimen of each selected resin was tested (tension) in this investigation at 21, 32, 43, 54, and 66 °C ambient temperature.

Table 2-1. Neat resin tensile properties (mean and coefficient of variation, C_v), room temperature and resin mix ratios

Resin Material	Equivalent Weight, g	Mix Ratio with Curative	Pre-polymer NCO, %	Young's modulus, MPa (C_v)
LF750	472	100:49.7	8.9	245 (2%)
30748	420	100:55.9	10	510 (2%)
30757	350	100:67.0	12	887 (1%)
30917	350	100:67.0	12	976 (5%)
EPON 862		100:26.4		2950 (2%)

2.2 Manufacturing

Composite specimens were fabricated in this investigation using a McClean Anderson Super Hornet filament winder (Schofield, WI). Only one type of fiber reinforcement was used, AS4D-GP-12K, a high strength polyacrylonitrile (PAN) carbon fiber made by Hexcel Corporation (Stamford, CT). The carbon tow of 12,000 individual fibers was saturated with the resin through the use of a resin bath. The resin bath controls the areal percentage of resin and fiber through the use of an orifice with a carefully chosen inner bore. The target fiber volume fraction, V_{ft} , and the diameter of the front orifice, D_o , are related by **Equation 2-2**,

$$V_{ft} = \frac{D_f^2 N_f}{D_o^2} \quad (2-2)$$

In **Equation 2-2**, D_f is the diameter of one fiber (6.7 μm) (Hexcel, 2010), and N_f is the number of fibers in a tow (12,000). In this investigation, the bore of the front orifice was 0.97 mm (0.038 in) for filament wound cylinders and 1.07 mm (0.042 in) for discrete undulated specimens, controlling the amount of fiber by volume in the wet tow to 58% and 50% respectively. During filament winding, the resin bath was kept at 50 °C to lower the resin viscosity. Actual fiber volume fraction of a cured part was dependent on the amount of resin that drips off during manufacturing (exacerbated by lower viscosity). The geometric measurements of the cured part can be used to find the approximate fiber volume fraction, V_f using **Equation 2-3**.

$$V_f = \frac{N_l N_f \pi D_f^2}{2 b_w h_t} \quad (2-3)$$

In **Equation 2-3** N_l was the number of effective lamina, with each helical pair ($\pm\theta$) counting as one lamina and each circumferential layer counting as one half lamina, b_w was the bandwidth, the width of the tow when placed on the mandrel, and h_t was the thickness of the cured part. When designing a winding program the input bandwidth, b_w , was selected to be slightly smaller than the

natural bandwidth of the tow to take into account the uneven spreading of the tow on the mandrel. For this research bandwidth was defined as 2.54 mm (0.1 in) in all filament winding.

The carbon fiber tow leaves the resin bath and was deposited on the mandrel in a calculated way through the filament winder's four degrees of motion. For helical and circumferential winding programs, mandrel (angular displacement and velocity), carriage (longitudinal displacement and velocity), and payout eye (angular rotation of the payout eye) motion were utilized. Tow tension was kept to 4.5-9 N. The filament winding technique uses a metal cylinder as the inner mold for the composite, also known as a mandrel. A helical winding program deposits the saturated fiber tow at a user chosen angle, $\pm\theta$, relative to the centerline axis of the mandrel through the aforementioned control of motion (**Figure 2-1**). Circumferential winding programs wrap saturated fiber tows at approximately 90 degrees. The actual winding angle was related to the bandwidth as tows are placed beside one another along the length of the mandrel, in this research at 89.5°. Use of a smaller bandwidth or larger diameter mandrel will cause the winding angle to more closely approach 90°. During filament winding of helical and circumferential programs the mandrel rotates at a constant velocity. The carriage reverses direction at the end of the mandrel, with fiber placement secured using pin rings, placing the saturated tow at negative the initial angle creating the characteristic woven architecture (**Figure 2-2**). Pin rings should be of the same diameter as the mandrel with as many pins as there are strokes, or passages of the mandrel from start to end. In this case, 1.5 times as many pins as strokes were used in three rows spaced ¼ inch apart. The material of the pin ring does not influence the quality of filament winding or the finished product. If possible, an easily machined material such as PVC should be chosen, lowering machine shop costs and delivery time.

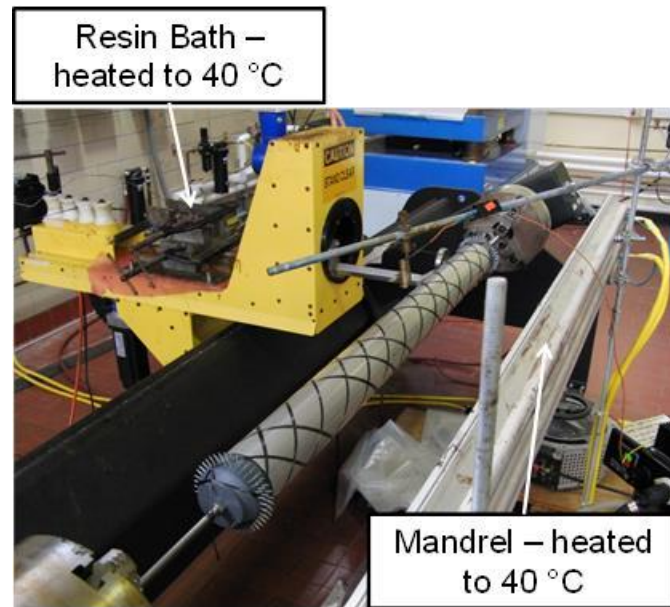


Figure 2-1. Filament winder front view

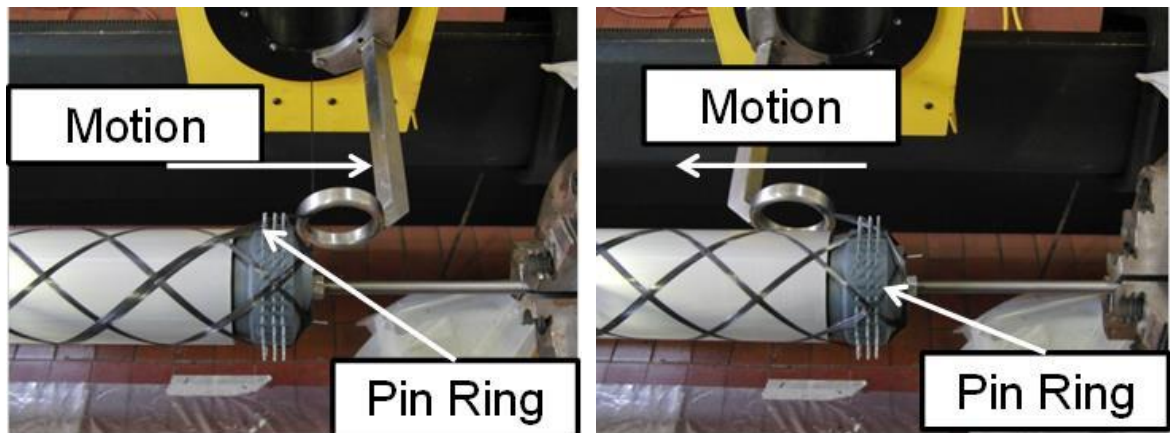
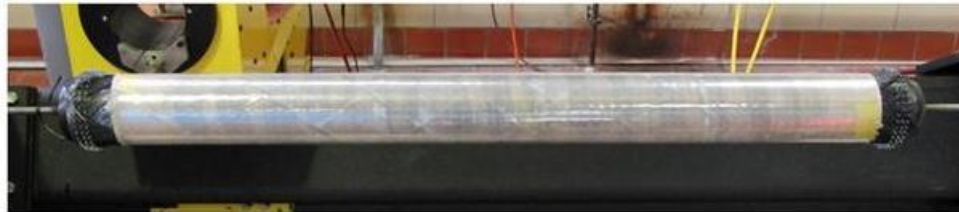


Figure 2-2. Mandrel and ping ring

The mandrel itself was lightly abraded to remove dirt and surface scarring. The surface was additionally wiped down with acetone removing oil and other contaminants. Two layers of Mann Ease Release 200 were baked onto the mandrel, evaporating solvents, for around thirty minutes at around 140 °C, twice. Extraction of the finished part was ensured with careful preparation of the mandrel surface. Additional consideration should be given to mandrel preparation as the resin compliance and filament winding angle increase. It may be necessary to use additional release

agent layers or a different mandrel type if the resin is sufficiently compliant. Difficulty in composite removal from the mandrel may be mitigated by freezing both, as aluminum will contract more than the composite. On several occasions reducing the temperature of the part and mandrel to below freezing allowed for part removal which was not possible at room temperature.

Finished parts were wrapped in two layers of release-coated heat-shrinking tape called Hi-Shrink Tape: Release Coated (25 mm wide, 0.05 mm thick, 80°C activation temperature) from Dunstone Inc. (Charlotte, NC). The ends of the shrink tape were secured with Flashbreaker II high temperature tape (Airtech, CA). After the shrink tape was applied, excess fiber was cut from the ends of the part and it was ready to be placed into a preheated oven (**Figure 2-3**). Helical winding patterns which place reinforcement at $\pm\theta$ create a FWP. Circumferentially wound layers have no helical winding pattern and no undulation bands, as the tow was laid spirally beside itself along the length of the mandrel.



(a) Mandrel with composite on pin rings, wrapped with shrink tape



(b) Final part with pin rings freed ready for heating

Figure 2-3. Mandrel with shrink tape and final part ready for heating

2.2.1 In-Plane Transverse Compression, F_{2C} and E_{2C} , Testing

A circumferential winding program was used on a 48.3 mm diameter aluminum mandrel for manufacturing Conathane 30917 specimens for in-plane transverse compression testing. Conathane 30917 was chosen for temperature controlled testing because the measured value of neat resin modulus lies near the mean of the range previously used to find trends for composite strength versus neat resin modulus (Henry, 2012). It was expected that as the material was heated, the neat resin modulus would decrease as would the composite strength, following the previously determined relationships. During manufacturing the circumferential winding program was restarted when the carriage finished one stroke and returned to the head end of the mandrel. The fiber angle, therefore, was always +89-deg. (rather than ± 89 in a typical helical pattern) creating a final laminate of $[89]_4$. The part was covered with two layers of shrink tape for consolidation and placed in a convection oven at the appropriate cure schedule. The average specimen height was 76.2 mm (cut by water cooled circular diamond saw) with V_f calculated using **Equation 2-3**. Specimens were tested at 21, 32, 43, 54, and 66 °C ambient temperature for evaluating strength degradation due to softening.

Table 2-2. Description of specimens for evaluating F_{2C} and E_{2C} of cylinders: 30917

Test Temperature, °C	Inner Diameter, mm	Number Tested	Avg. Radial Thickness, mm	N_l	V_f , %
21.1	48.3	3	1.13	2	59
32.2	48.3	3	1.14	2	59
43.3	48.3	3	1.15	2	58
54.4	48.3	3	1.12	2	59
65.6	48.3	3	1.12	2	60

2.2.2 Helically Wound Cylinder Testing

Composite cylinders for longitudinal compression were made by wet filament winding onto a 48.3 mm diameter aluminum mandrel. The various types of specimens made for the investigation are summarized in **Table 2-3**, where specimens are described in terms of lamination arrangement in square brackets [-] and FWP in curved braces {-}. The $[\pm\theta/89/\pm\theta]$ laminate was selected to reduce the Poisson's ratio of the cylinder in comparison to a pure angle-ply laminate, thus reducing stress concentrations at the restrained ends. Further details on end effects in filament wound cylindrical specimens are presented in Henry (2012) for longitudinal compression tests and Mertiny et al. (2004) for internal pressurization tests. The fiber angles and FWP in **Table 2-3** are listed in order from the inside of the cylinder to the outside. The helical $\pm\theta$ layers were wound with FWPs of 2, 5, or 10 with a nominal thickness of 0.5 mm. The 89-deg. layer represents a single circumferential layer (no FWP) of nominally 0.25 mm thickness. The total laminate thickness for all specimens was roughly 1.25 mm. The geometry of the cylinder and fiber orientation of the helical layers was selected with insight gained from a previous investigation (Henry, 2012) so that a fiber microbuckling mode of failure could be obtained, rather than longitudinal buckling.

When filament winding was finished, two layers of release coated shrink tape (Hi-Shrink, Dunstone Inc., Charlotte, NC) were applied to the part to promote consolidation. Shrink tape was secured with Flashbreaker II tape (Airtech, CA). The part and mandrel were then placed into a forced-air oven for the appropriate cure schedule. After the part was removed from the mandrel, specimens were machined to a 76 mm length using a water cooled circular diamond saw. Four or five replicates for each type of specimen were tested, as shown in **Table 2-3** with volume fraction information. Modulus and strength results were normalized to a fiber volume fraction, V_f , of 58% by dividing the experimentally measured result by the actual fiber volume fraction (%) and

multiplying by 58%. Normalization was used to compare the influence of undulation across various material systems and laminates.

Table 2-3. Description of specimens for compressively loaded filament wound cylinder testing

Material	Stacking Sequence	Number of Replicate Tests and Actual Fiber Volume Fraction (%) for each FWP arrangement {-/-}				
		{2/2}	{5/5}	{10/10}	{10/5}	{5/10}
EPON 862	[±16/89/±16]	4 (69%)	5 (68%)	4 (69%)	5 (70%)	5 (67%)
	[±31/89/±31]	5 (66%)	5 (67%)	5 (69%)	5 (68%)	5 (68%)
	[±45/89/±45]	5 (66%)	5 (65%)	5 (67%)	5 (65%)	5 (64%)
30917	[±16/89/±16]	4 (57%)	5 (56%)	4 (62%)	5 (58%)	0
	[±31/89/±31]	4 (58%)	5 (56%)	5 (61%)	5 (58%)	4 (57%)
	[±45/89/±45]	5 (56%)	5 (57%)	5 (59%)	5 (59%)	4 (59%)

2.2.3 In-Plane Transverse Tension, F_{2T} and E_{2T} , Testing

Impregnated sheets of unidirectional reinforced material were manufactured by passing carbon fiber tow through a resin bath and winding the tow onto a flat paddle mandrel with a target fiber volume fraction of 50 % (**Figure 2-4**). The paddle mandrel was covered by non-porous PTFE coated glass fabric from Airtech (Huntington Beach, CA). The unidirectional material was cut from the paddle mandrel and used in fabricating panels for later use in further processing through hot pressing. When circumferentially winding on a paddle mandrel, the mandrel diameter input to the filament winder was found by equating the perimeter of the plate to a faux cylinder circumference. Tow tension was set to zero and the bath temperature was at room temperature for this specific procedure.

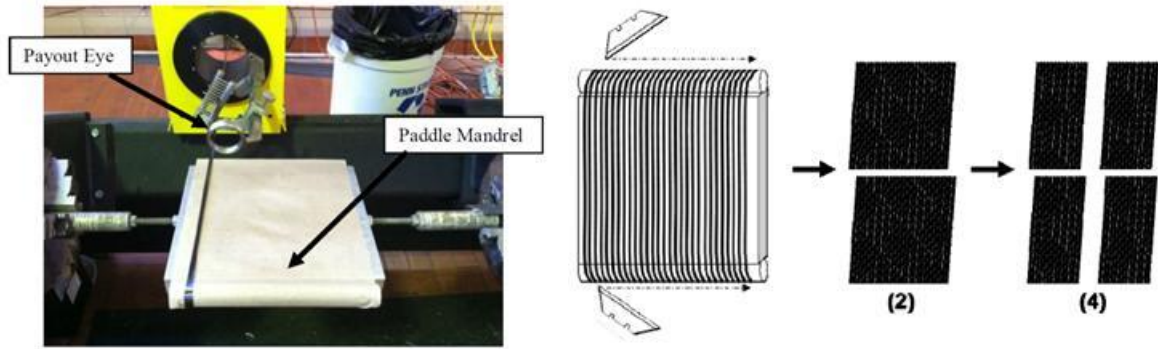


Figure 2-4. 25.4 cm x 25.4 cm paddle mandrel and schematic of unidirectional pre-preg sectioning (Sollenberger, 2010)

Sixteen carbon/30917 unidirectional strips were stacked on top one another and placed into a pre-heated mold with PTFE coated fiberglass still attached to the top and bottom of the stack. A pre-heated silicone slab was placed on top of the stack and the mold was closed, ensuring even pressure on the composite. The closed mold was placed into a smart press under 241 kPa of pressure. The smart press can be scheduled to heat the platens according to the necessary cure schedule. Specimens were tested at 21, 32, 43, 54, and 66 °C ambient temperatures. Dimensions are available in **Table 2-4**.

Table 2-4. Description of 30917 specimens for evaluating F_{2T} and E_{2T} of plates: 30917

Test Temperature, °C	Width, mm	Number Tested	Thickness, mm	N_l	V_f , %
21.1	12.8	3	3.8	8	71
32.2	12.5	3	3.7	8	72
43.3	12.6	3	3.7	8	73
54.4	12.5	3	3.7	8	72
65.6	12.5	3	3.7	8	72

2.2.4 Discrete Undulation Testing

Impregnated sheets of unidirectionally reinforced material were manufactured by circumferentially winding onto a paddle mandrel. Upon cutting the completed unidirectional

layer along the edges of the mandrel, two impregnated sheets were obtained. To create each laminate, four sheets of n layers were used. Laminates of larger undulation amplitude were created by winding a larger number of layers (n). For example, four sheets comprised of two layers make $[0_2/90_2]_s$ and four sheets comprised of four layers make $[0_4/90_4]_s$ etc. All other manufacturing conditions were kept approximately constant for the various thickness laminates.

The manufacture of specimens with controlled undulation involves the hand layup of 0- and 90-deg. lamina. The unidirectional sheets serving as the 90-deg. lamina were first cut in half. Next, a half-sheet of 90-deg. material was laid in a closed mold (**Figure 2-5a**). Then, a whole 0-deg. sheet was laid over the first half-layer of 90-deg. material (**Figure 2-5b**), and another half-sheet of 90-deg. material was added to complete half of the laminate thickness. These steps were repeated in reverse order to create a symmetric laminate with a nearly-sinusoidal undulation in the 0-deg. layers (**Figure 2-5c**). Care was taken to overlap the 90-deg. layers by approximately one millimeter to obtain a constant laminate thickness in the undulated region. Two layers of porous PTFE coated glass fabric (Airtech, CA) were placed at the top and bottom of the laminate, and the mold and part were consolidated in a computer-controlled press set for 241 kPa of pressure while the materials were heated according their respective cure schedules.

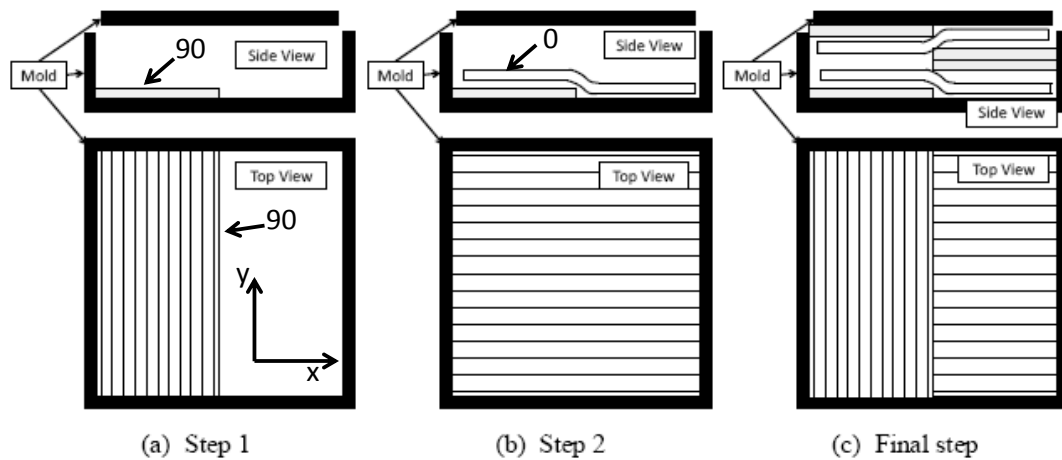


Figure 2-5. Undulated specimen layup sequence

After the laminate was removed from the mold, specimens with and without undulations were cut to a length of 140-155 mm and a width of 25.4 mm (**Figure 2-6**). The specimens without undulations were referred to as “non-undulated” specimens. The undulation was placed near the mid-length position of the specimen. Visual inspection revealed that, for nearly identical manufacturing conditions, materials with a higher viscosity resin at room temperature had a shorter undulation wavelength. This result was illustrated in **Figure 2-7a** with EPON 862 (lowest viscosity), **Figure 2-7b** with LF750 (intermediate viscosity) and **Figure 2-7c** with 30917 (highest viscosity). In all cases the manufactured undulations followed a nearly ideal half-sine shape and were nearly symmetric about the laminate midplane.

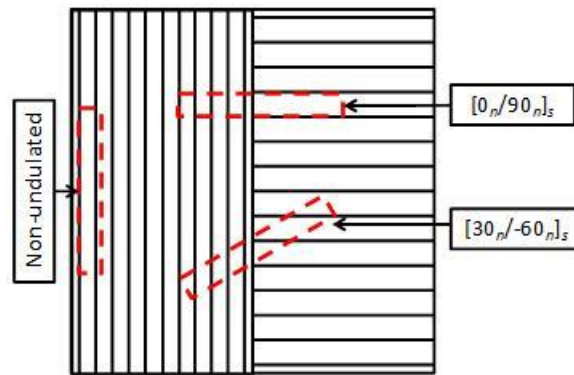


Figure 2-6. Discrete undulated specimen location diagram

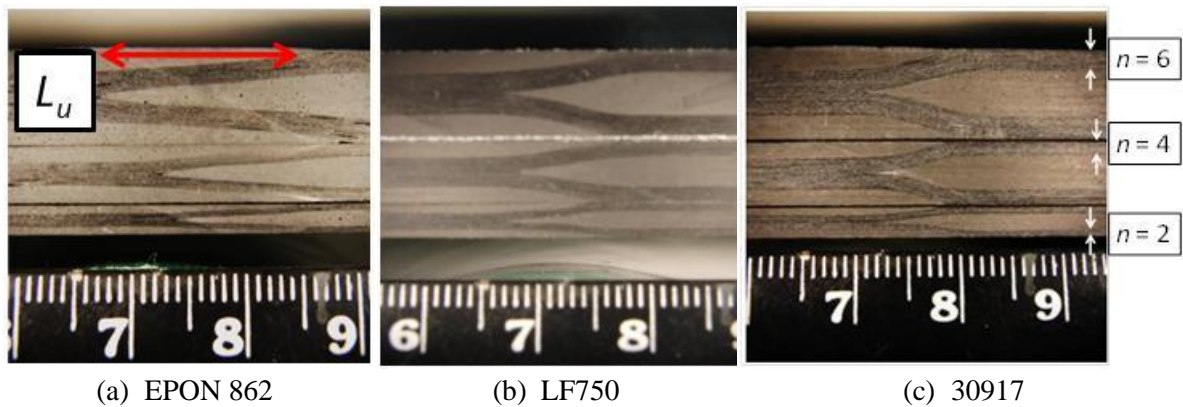


Figure 2-7. Photographs of polished edges of flat $[0_n/90_n]_s$ specimens showing undulation (scale: cm). Dimension “ L_u ” indicates the length of the undulation

Geometric parameters of the undulations based on the photographs in **Figure 2-7** were tabulated in **Table 2-5**. The parameters were presumably identical in the $[0_n/90_n]_s$ and $[30_n/-60_n]_s$ specimens since they were all cut from the same laminate. Distances were measured in pixels using an image analysis tool and converted to millimeters. The amplitudes under investigation vary from approximately 0.6 mm to 1.8 mm, which translates to approximately 5- to 20-deg. of out-of-plane inclination of the fibers. The amplitude of the sine wave was approximately equal to 25% of the laminate thickness since all lamina are of roughly equal thickness.

Table 2-5. Measured flat undulated material details

Material	Number of lamina, n	Pixels per mm	Undulation amplitude, h_u (pixels)	Undulation length, L_u (pixels)	Undulation amplitude, h_u (mm)	Undulation length, L_u (mm)	h_u/L_u	Lamina thickness, mm	Estimated fiber volume content, V_f , %
LF750	2	46	34	291	0.73	6.33	0.10	0.36	48
	4	46	61	319	1.32	6.93	0.17	0.33	
	6	46	87	395	1.89	8.59	0.23	0.32	
DPRN 30917	2	48	32	236	0.67	4.92	0.12	0.33	47
	4	48	66	261	1.36	5.44	0.19	0.34	
	6	48	90	320	1.88	6.67	0.26	0.31	
EPON 962	2	33	19	345	0.58	10.45	0.06	0.29	59
	4	33	37	435	1.11	13.18	0.08	0.28	
	6	33	58	574	1.74	17.39	0.10	0.29	

Compressive modulus and strength results were normalized to a fiber volume fraction, V_f , of 50% by dividing the experimentally measured property by the actual V_f and multiplying by 0.50. Normalization facilitates the comparison of properties across the three material systems which, as shown in **Table 2-5**, had different fiber volume fractions. The estimated V_f values in **Table 2-5** were determined based on the known fiber areal weight and the cured laminate thickness (Henry, 2012). The epoxy-based systems had the highest V_f due to relatively abundant resin loss during

processing. The number of specimens of each type tested in longitudinal compression was at minimum five.

Chapter 3

Composite Helicopter Driveshaft Design

This chapter focuses on improvements to the state-of-the-art in filament wound composite driveshaft optimization. Driveshaft optimization herein focuses on tradeoffs between five aspects: driveshaft weight, shaft operating temperature, whirling stability, torsional buckling stability, and lamina-level material failure. This chapter excludes shaft eccentricity, torsional vibration stability, and coefficient of thermal expansion in the longitudinal direction. Incorporation of shaft operating temperature in determination of lamina-level ultimate strengths was identified as an important improvement over existing design models which utilized quasi-static room temperature values.

Empirical relationships for neat resin modulus (E_m) and composite strength (F_{1C} , etc.) were previously determined at room temperature (Henry, 2012). Additional neat resin and composite specimen tests were conducted at several temperatures. Neat resin tests determined Young's modulus with respect to temperature. Hypothetically, along with the previous empirical relationships, the composite strength at any temperature could be calculated. To validate this hypothesis, temperature controlled composite tests for strength were conducted and compared to the empirical relationship. Sources of composite helicopter driveshaft operating temperature include ambient temperature and driveshaft self-heating. Higher operating temperatures soften the composite and reduce the strength.

The Applied Research Laboratory Trade Space Visualizer (ATSV, Stump et al., 2009) was used in conjunction with MATLAB for generating a composite helicopter driveshaft optimization strategy. ATSV implementation advances the state of the art through the Pareto optimization technique and visual representations of the driveshaft design space. Visualization of the design

space allows for a quantitative analysis and understanding of composite helicopter design tradeoffs and highlights areas of potential future improvement.

3.1 Temperature Controlled Tests: Neat Resin

Neat resin specimens were tested on an Instron Model 1331 test frame with a 15 kN electronic load cell. Displacement control tests were run in tension at a nominal strain rate of 380 $\mu\text{ε/s}$. Two extensometers, a 2.5 cm strain gage based extensometer and a laser extensometer (target gage length 2.5 cm), were used to measure longitudinal strain on opposite faces of the specimen to compensate for bending (**Figure 3-1**). Three loading cycles were undertaken with measurements on the last loading cycle to eliminate Mullin's effect, or the tendency of a polymer to have a stiffer response on first loading. The stiffness response of the material was observed to be convergent after approximately three loading cycles. The temperature of the specimen was controlled through a heat gun, which warmed the ambient air surrounding the specimen in a Lexan chamber to 21.1, 32.2, 43.3, 54.4, and 65.6 °C. The chamber was kept at the target temperature for fifteen minutes to ensure temperature equilibrium of the specimen.

Neat resin specimens were loaded in displacement control at a target of approximately 1.2 % strain. The modulus of each test was measured as a linear fit in the 1000 – 2000 $\mu\text{ε}$ strain range (highlighted in **Figure 3-2a**). The stress-strain response was approximately linear within the strain range of investigation becoming increasingly compliant as the ambient temperature of the chamber was increased (**Figure 3-2b**). The highest stress level reached does not represent the failure of the tested specimen.

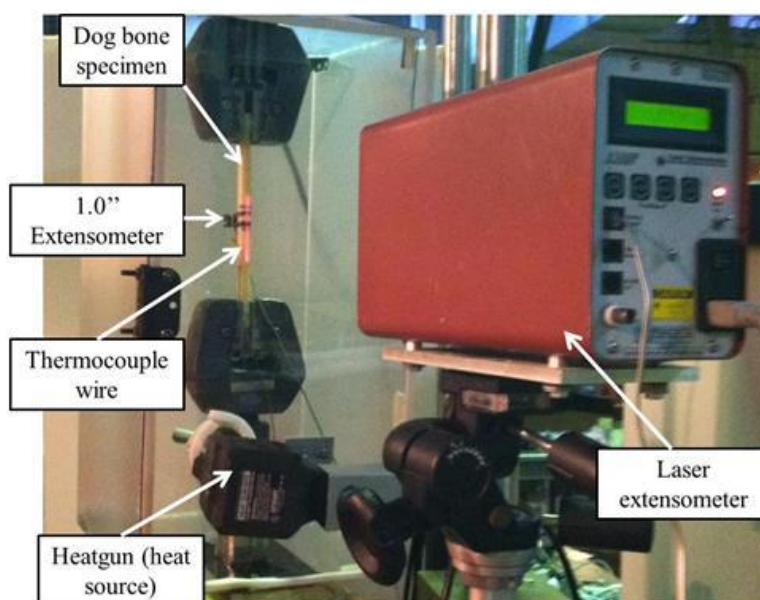


Figure 3-1. Neat resin specimen test set-up: CMTC

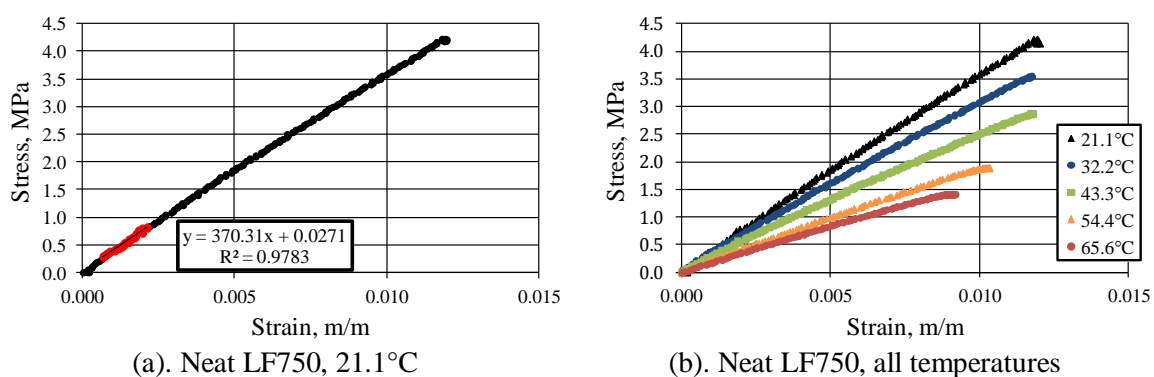


Figure 3-2. Longitudinal stress vs. average longitudinal strain: neat resin tension

All neat resins exhibited an approximately linear response with a modulus decrease at higher temperatures (**Table 3-1**). The modulus obtained at each temperature was normalized to the 21.1 °C to further illustrate the reduction in modulus as a penalty. A value of one-half therefore would represent a 50 % modulus reduction at that temperature compared to room temperature.

Table 3-1. Neat resin modulus summary

Material	Temperature, °C	Modulus, MPa	Modulus Normalized to 21.1°C
LF750	21.1	370	1.00
	32.2	305	0.82
	43.3	271	0.73
	54.4	183	0.49
	65.6	174	0.47
30748	21.1	545	1.00
	32.2	461	0.84
	43.3	375	0.69
	54.4	314	0.58
	65.6	242	0.44
30757	21.1	741	1.00
	32.2	626	0.84
	43.3	460	0.62
	54.4	322	0.43
	65.6	224	0.30
30917	21.1	800	1.00
	32.2	721	0.90
	43.3	515	0.64
	54.4	335	0.42
	65.6	200	0.25

The sensitivity of the normalized modulus to increasing temperature was approximately linear (**Figure 3-3**). Therefore, a line was fit to the experimental data points with an R^2 of 0.96 or higher for each neat resin. A linear regression allows for the estimation of the neat resin modulus at any intermediate temperature. EPON 862 was insensitive to temperatures under 70 °C (Henry, 2012). It should also be noted in **Figure 3-3** that polyurethane resins of the highest neat resin modulus at 21.1 °C (30757 and 30917, hollow points) experience the largest reductions in modulus at temperatures above 40 °C. This result is interesting when considering the composite driveshaft application. It has been shown (Henry, 2012) that the neat resin modulus has a positive correlation with composite modulus and strength. When optimizing a composite helicopter

driveshaft operating at elevated temperatures, the neat resin with the highest modulus at 21.1 °C may not yield the lightest design due to the significant softening at elevated temperatures.

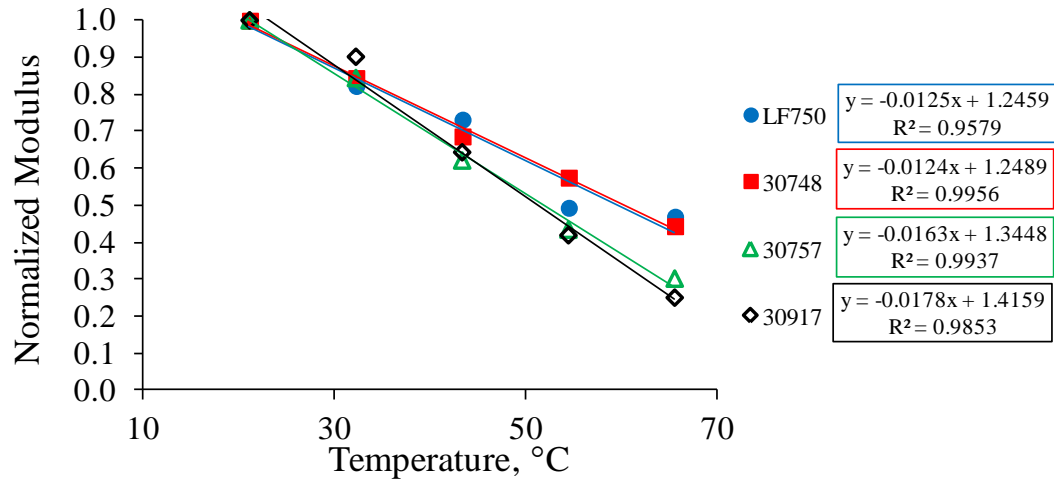


Figure 3-3. Normalized modulus (all resins) vs. chamber ambient temperature, line fit to 30757

EPON 862 neat resin response with respect to temperature was quantified using a dynamic mechanical analysis test in flexure (DMA details in Henry, 2012) due to material availability (**Figure 3-4**). A linear equation was fit to the normalized storage modulus with respect to temperature in the range of 50°C to 80°C (highlighted in **Figure 3-4**). The fit equation allows for the estimation of the neat resin modulus at any temperature that the material might experience. A linear fit for each resin under investigation is presented as **Equations 3-1—3-5**, where T_{mat} in deg. C is the tested temperature of the material, and E_m in MPa is the room temperature value of neat resin modulus. The small amplitude of the linear equation slope showed that EPON 862 was largely insensitive to temperature.

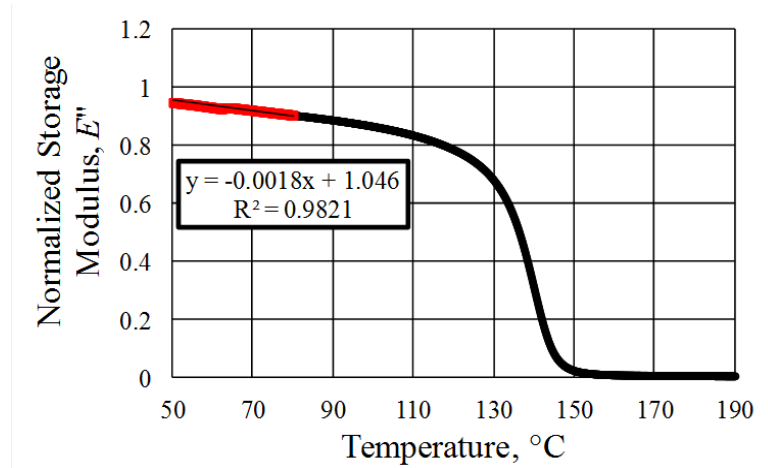


Figure 3-4. Normalized storage modulus vs. temperature, EPON 862 neat resin DMA test in flexure

$$\text{LF750} \quad E_{m(T_{mat})} = E_{m(21.1^{\circ}\text{C})}(-0.0125T_{mat} + 1.2459) \quad (3-1)$$

$$30748 \quad E_{m(T_{mat})} = E_{m(21.1^{\circ}\text{C})}(-0.0124T_{mat} + 1.2489) \quad (3-2)$$

$$30757 \quad E_{m(T_{mat})} = E_{m(21.1^{\circ}\text{C})}(-0.0163T_{mat} + 1.3448) \quad (3-3)$$

$$30917 \quad E_{m(T_{mat})} = E_{m(21.1^{\circ}\text{C})}(-0.0178T_{mat} + 1.4159) \quad (3-4)$$

$$\text{EPON 862} \quad E_{m(T_{mat})} = E_{m(21.1^{\circ}\text{C})}(-0.0018T_{mat} + 1.0460) \quad (3-5)$$

3.2 Temperature Controlled Tests: Composite

30917 transverse composite specimens for tension and circumferentially wound cylinders for compression were tested on an Instron Model 1331 test frame with a 15 kN electronic load cell. Displacement control tests were run for both tests at a strain rate of 350 $\mu\text{ε/s}$ to failure. Two 2.5 cm extensometers were used to measure longitudinal strain on opposite sides of the specimens to compensate for bending. The specimen temperature was controlled through a heat gun which warmed the ambient air surrounding the specimen in a Lexan chamber to 21.1, 32.2, 43.3, 54.4, and 65.6 $^{\circ}\text{C}$. A thermocouple was placed directly onto the specimen far away from the heat

source. The chamber equilibrated for 15 minutes at the target temperature. Transverse-compression specimens were potted into end platens to prevent the specimen ends from “brooming” during testing (**Figure 3-5**). A hemispherical bearing was placed in the load train to minimize the transmission of moments to the specimen due to misalignment. Transverse-tension specimens were tested in tension by the hydraulic wedge grips directly with an identical set-up sans platens and bearing.

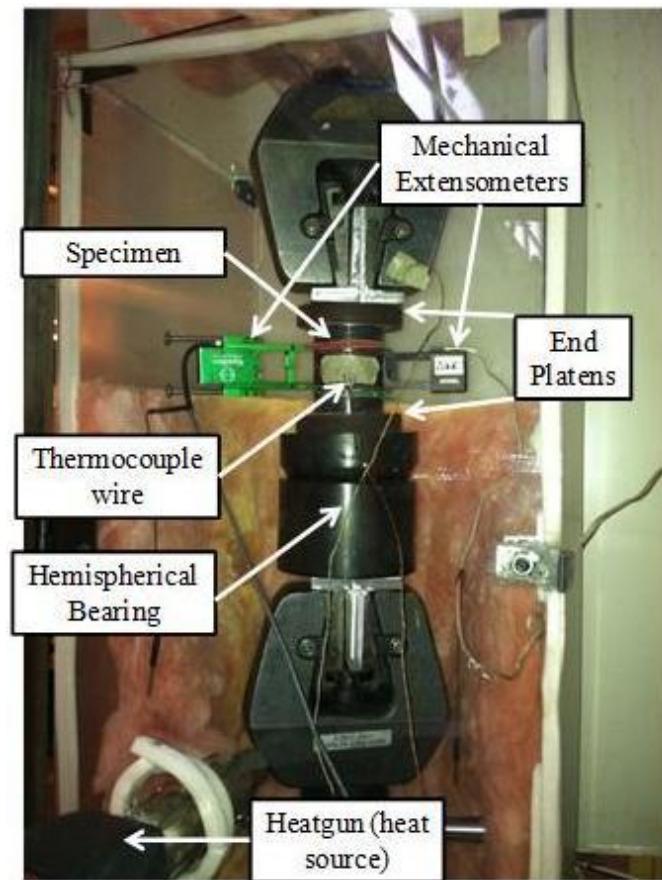


Figure 3-5. Experimental composite test set-up: CMTC

Composite specimens were loaded in displacement control until specimen failure. The modulus of each test was measured as a linear fit in the $1000 - 2000 \mu\epsilon$ strain range. The response of the composite was increasingly non-linear with higher ambient temperature (**Figure**

3-6). For the transverse-tension tests (**Figure 3-6a**) and transverse-compression tests (**Figure 3-6b**), higher ambient temperatures decreased the modulus and strength of the composite.

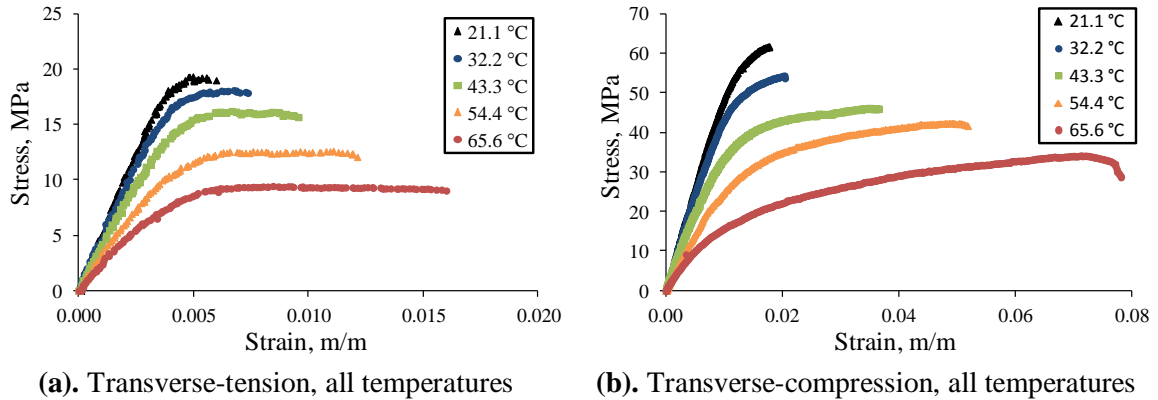
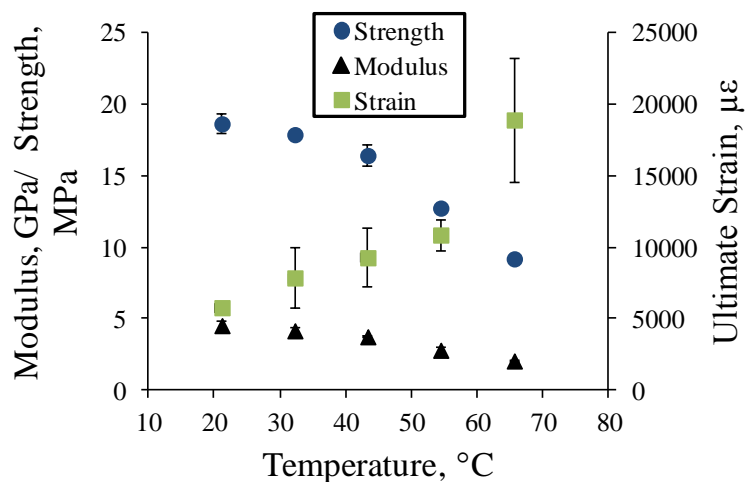


Figure 3-6. Transverse stress vs. Transverse strain: 30917 composite

Transverse-tension test results are summarized in **Table 3-2**. Ultimate strength was defined as the largest stress achieved during the test. Modulus and strength results were observed to fall to less than 50 % of their room temperature values when heated to 65.6 °C (**Figure 3-7**). Error bars show the minimum and maximum of the set. Subsequently, the failure strain increased to approximately four times the value at 21.1 °C when the specimen was heated to 65.6 °C. The transverse-tension modulus at 65.6 °C compared to the value at 21.1 °C (0.46) was higher than the respective neat resin ratio (0.25).

Table 3-2. Transverse-tension specimen temperature controlled test summary: 30917

Temperature, °C	Modulus, GPa	Average, GPa	C _v , %	Ultimate Strength, MPa	Average, MPa	C _v , %	Failure Strain, µε	Average, µε	C _v , %
21.1	4.30			18.7			5791		
	4.41	4.55	7.5	17.9	18.7	3.8	5629	5801	3.0
	4.93			19.4			5983		
32.2	4.50			17.6			6124		
	4.07	4.18	6.7	18.1	17.9	1.3	7363	7882	26
	3.98			18.0			10158		
43.3	3.81			17.3			11196		
	3.78	3.77	1.3	16.2	16.4	4.6	9564	9293	22
	3.71			15.8			7119		
54.4	2.58			12.6			12130		
	3.00	2.82	7.8	13.1	12.8	2.3	10393	10882	10
	2.89			12.6			10123		
65.6	2.01			8.9			23887		
	2.10	2.07	2.6	9.3	9.2	3.4	16894	18928	23
	2.11			9.5			16002		

**Figure 3-7.** Average modulus, strength and ultimate strain vs. temperature: transverse-tension tests: 30917

Transverse-compression test results are summarized in **Table 3-3**. Ultimate strength was defined as the largest stress achieved during the test. Similar to transverse tensile tests, modulus and strength results were observed to fall to less than 50 % of their room temperature values when heated to 65.6 °C (**Figure 3-8**). Ultimate failure strain increased to approximately six times the value at room temperature when the specimen was heated to 65.6 °C. The composite was also more resistant to temperature increases with respect to percentage of modulus or strength retained compared to the neat resin.

Table 3-3. Transverse-compression specimen temperature controlled test summary: 30917

Temperature, °C	Modulus, GPa	Average, GPa	C _v , %	Strength, MPa	Average, MPa	C _v , %	Failure Strain, µε	Average, µε	C _v , %
21.1	5.20 5.38 5.37	5.31	1.9	51.3 61.8 58.6	57.2	9.4	16152 17742 13237	15710	14.5
32.2	5.00 4.94 4.82	4.92	1.8	45.1 48.1 54.4	49.2	9.6	14572 20494 20441	18502	18.4
43.3	3.92 3.83 3.90	3.88	1.2	47.1 47.7 46.2	47.0	1.5	44560 43213 36576	41450	10.3
54.4	2.87 2.82 3.13	2.94	5.6	42.4 44.0 39.6	42.0	5.2	51855 55732 47527	51705	7.9
65.6	2.17 2.30 2.09	2.19	4.8	34.2 42.2 36.9	37.8	10.8	78159 74788 94336	82428	12.7

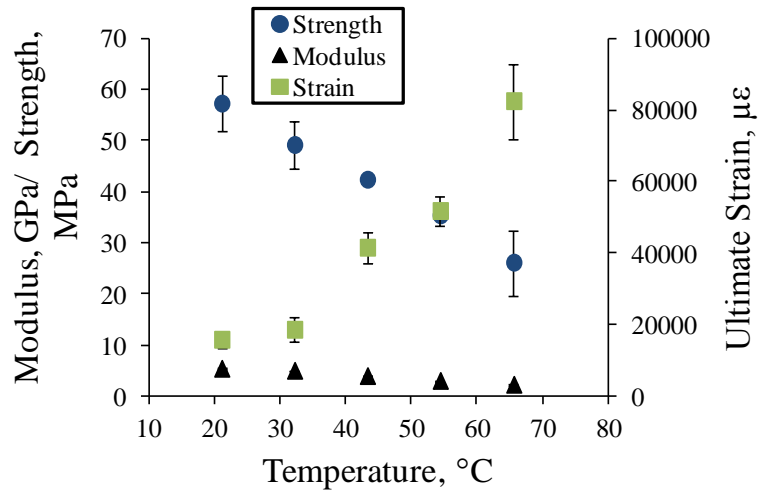


Figure 3-8. Average modulus, strength, and ultimate strain vs. temperature: transverse-compression specimen: 30917

3.3 Temperature Dependent Strength Prediction

Previous research (Henry, 2012) developed an empirical power law relationship between neat resin modulus, E_m , and composite strength. These relationships were developed in order to mitigate future experimental testing that would need to be accomplished in order to evaluate a new potential resin for design. A power law was fit to experimental data for four resins representing a range of neat resin moduli from 300 to 3000 MPa (LF750, 30748, 30917, EPON 862) at 21.1 °C (**Figure 3-9**).

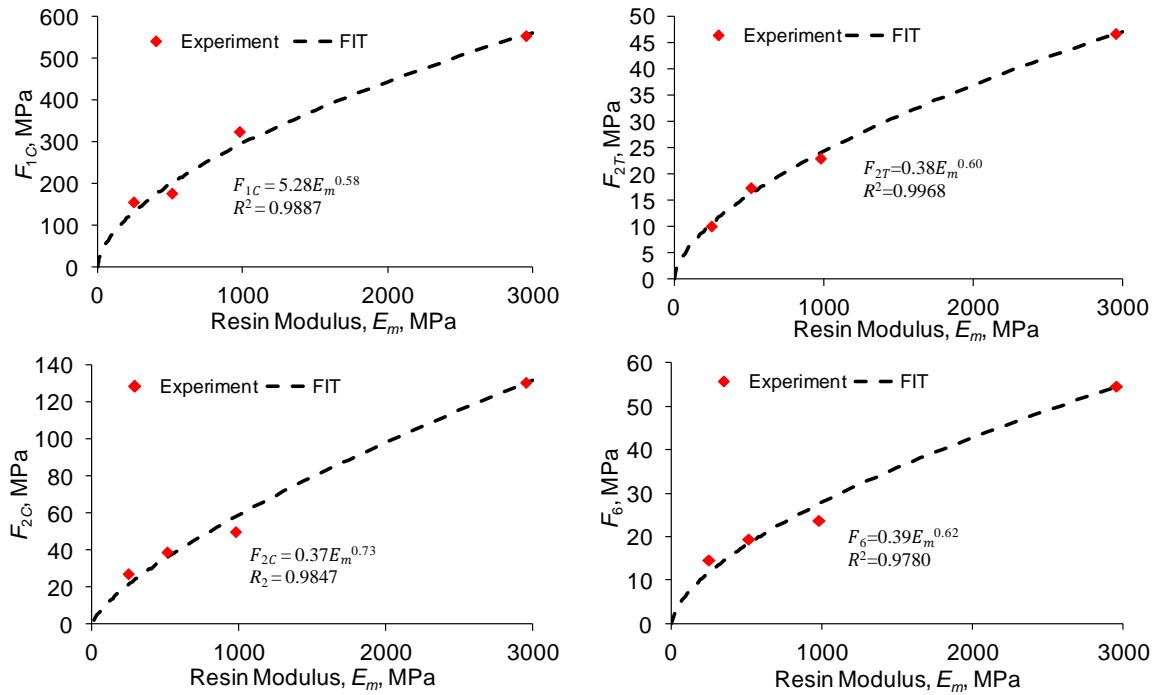


Figure 3-9. Lamina strength vs. resin modulus, E_m (Henry, 2012)

For a resin material to be used in a composite driveshaft optimization code, the lamina level material properties and strengths would need to be determined at any operating temperature. An empirical prediction such as **Figure 3-9** could be utilized if the response of a composite was shown to follow the prediction as the composite was heated. The modulus, E_{2T} , and strength, F_{2T} , found experimentally, as well as the empirical prediction, are shown in **Table 3-4** for the transverse-tension tests. The modulus, E_{2C} , and strength, F_{2C} , found experimentally, as well as the empirical prediction, are shown in **Table 3-5** for the transverse-compression composite tests (**Figure 3-6**). Significantly increased failure strain at high testing temperatures leads to proportionately higher strengths, creating increased error compared to the empirical prediction. Prediction accuracy would increase if a limit on strain was chosen ($\sim 5000\mu\epsilon$ for tension, $\sim 20000\mu\epsilon$ for compression).

Table 3-4. Transverse-tension modulus and strength, experiment and prediction: 30917

Temperature, °C	Resin Modulus, MPa	Experiment		Prediction		Abs(Error, %)	
		E_{2T} , GPa	F_{2T} , MPa	E_{2T} , GPa	F_{2T} , MPa	E_{2T} , GPa	F_{2T} , MPa
21.1	800	4.6	18.7	3.9	21.2	16.7	12.1
32.2	721	4.2	17.9	3.6	20.0	15.1	10.3
43.3	515	3.8	16.4	2.9	16.3	30.1	1.0
54.4	335	2.8	12.8	2.2	12.6	30.2	1.5
65.6	200	2.1	9.2	1.5	9.2	35.5	0.0

Table 3-5. Transverse-compression modulus and strength, experiment and prediction: 30917

Temperature, °C	Resin Modulus, MPa	Experiment		Prediction		Abs(Error, %)	
		E_{2C} , GPa	F_{2C} , MPa	E_{2C} , GPa	F_{2C} , MPa	E_{2C} , GPa	F_{2C} , MPa
21.1	800	5.3	57.2	3.6	50.0	46.8	14.3
32.2	721	4.9	49.2	3.4	46.4	45.8	6.1
43.3	515	3.9	47.0	2.7	36.2	44.7	29.8
54.4	335	2.9	42.0	2.0	26.4	46.4	59.0
65.6	200	2.2	37.8	1.4	18.1	54.2	108.8

The experimental modulus and strength were paired with the value of neat resin modulus for 30917 at each respective temperature and plotted against the empirical prediction in **Figure 3-10** (new testing-triangle, previous testing-diamond). The modulus and strength found previously experimentally, as well as the empirical prediction, are shown in **Figure 3-10a,b** for the transverse-tension composite tests and **Figure 3-10c,d** for transverse-compression composite tests. The current data for 30917 temperature controlled testing is overlaid to demonstrate the correlation. Note that the transverse modulus here is quasi-static and used for empirical prediction validation only. The design model uses temperature-frequency dependent values of E_2 .

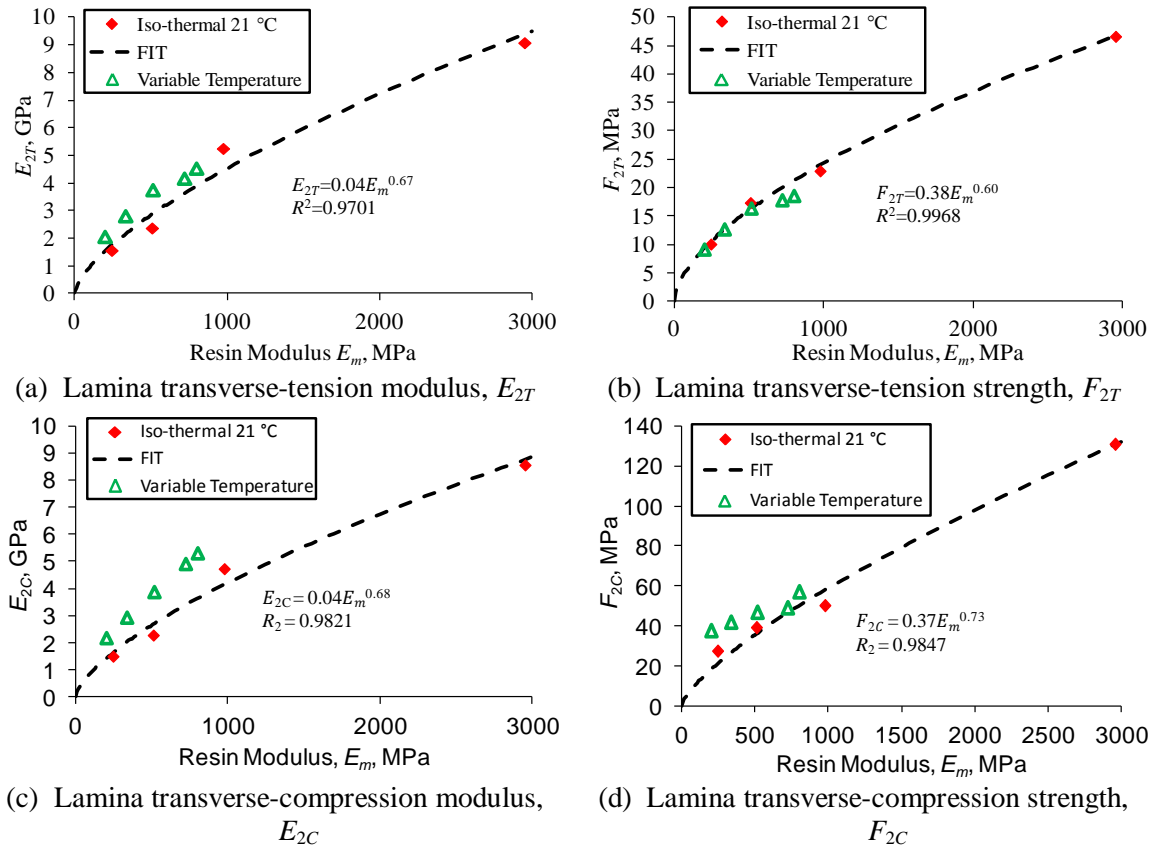


Figure 3-10. Temperature controlled experimental and empirical predictions: 30917

Each discrete temperature evaluated experimentally showed good correlation between the softening of the neat resin, and the reduction in both modulus and strength. The good correlation between the experimental modulus and strength in transverse-tension and compression supports the use of the empirical predictions in an optimization design code. The neat resin modulus can be predicted for any operating temperature of the driveshaft using **Equations 3-1:3-5**. Composite strength can then be determined using the empirical relationships (**Figure 3-9**). The fiber direction tensile strength F_{1T} was determined using RoM assuming that the property was insensitive to temperature.

3.4 Driveshaft Design Model

The driveshaft design model utilizes four modules:

- Shaft Temperature Module —driveshaft operating temperature while misaligned
- Whirling Module — critical driveshaft operating frequency for a subcritical driveshaft
- Buckling Module — critical driveshaft buckling torque
- Structural Module — maximum lamina coordinate system (1-2) stress components

The UH-60 Blackhawk and CH-47 Chinook driveshafts were considered for potential redesign (**Table 3-6**). The current design employs a multi-piece segmented metallic driveline with weight contributions from the aluminum shaft, flexible couplers, and four and six midspan hanger bearings respectively. The driveshaft design model seeks to minimize the weight of the driveline. Use of a single piece composite driveshaft negates the need for flexible couplers, eliminating the weight source. The remaining weight sources, the midspan hanger bearings and the shaft's laminate design, are input variables captured and manipulated, either by optimization or by exploration, through ARL Trade Space Visualizer (ATSV). The number of hanger bearings in an optimized composite design was constrained to not exceed the number for the existing driveshaft.

Table 3-6. Driveshaft geometric parameters

Parameter	Blackhawk	Chinook
Shaft Length, m	7.544	8.598
Shaft Outer Diameter, m	0.0889	0.1143
Operating Frequency, rpm	4116	6912
Applied Torque, N-m	734	4067
Midspan Bearing Weight, kg	3.84	5.20
Original Driveshaft Weight, kg	31.3	60.1

The driveshaft, as a composite, is made up of multiple $\pm\theta$ helically wound lamina represented as $+\theta$ and $-\theta$ unidirectional layers. The optimized composite design was constrained to have no less than three lamina and no more than eight. The reinforcement angle

for each lamina may be no less than 10-deg. and no more than 85-deg. at an interval of 5-deg.

Additional parameters include:

- Lamina thickness, 0.25 mm
- Maximum operating temperature, 85 °C
- Composite density, 1489 kg/m³
- Longitudinal loading, 0 N

Quasi-static material properties as determined by Henry (2012) are listed in **Table 3-7**. These properties are assumed to be independent of testing frequency or temperature. The analysis uses linear viscoelastic material properties and assumes transverse isotropy in the 23-plane. E_2 and G_{12} are found dynamically through DMA testing. The out-of-plane transverse Poisson's ratio, ν_{23} , is estimated in terms of the quasi-static E_2 (GPa), using the empirical relationship developed by Sollenberger (2010) (**Equation 3-6**).

$$\nu_{23} = 0.0397E_2 + 0.9322 \quad (3-6)$$

The out-of-plane transverse shear modulus, G_{23} , was calculated using **Equation 3-7** with known E_2 and ν_{23} .

$$G_{23} = \frac{E_2}{2(1 + \nu_{23})} \quad (3-7)$$

In this case, E_2 was dynamic while ν_{23} was treated as a constant. Therefore, G_{23} has rate- and temperature-dependence similar to that of the transverse modulus.

Table 3-7. Quasi-static composite material properties

Parameter	LF750	30748	30757	30917	EPON 862
E_1 , GPa	101	103	113	114	134
ν_{12}	0.30	0.32	0.32	0.30	0.32
ν_{13}	0.30	0.32	0.32	0.30	0.32
ν_{23}	0.87	0.84	0.78	0.74	0.58
η_1	0.0015 (Gibson, 2007)				

3.4.1 Shaft Temperature Module

The advantage of replacing a multiple piece, segmented, metallic driveline with a single piece composite driveshaft was in the composite's ability to operate in a misaligned condition. The misaligned driveshaft experiences cyclic bending strain as it spins. The internal damping of the material experiences the hysteretic strain by dissipating energy through heat generation (Shan and Bakis, 2009). Lamina level normal strains in all directions as well as in-plane shear strain were assumed the only contributors.

Dynamic tests were carried out on the properties of the composite material that are most dominated by the viscoelastic behavior of the matrix—i.e. the transverse and shear moduli. The viscoelastic response of the composite was evaluated over a large range of temperatures and frequencies. Based on the temperature-frequency superposition principal (Ferry, 1970) a viscoelastic property such as the storage, loss modulus, or the loss factor can be plotted versus the logarithm of loading frequency for a given test temperature. A series of such curves at discrete temperatures can be shifted horizontally to create one smooth curve known as a master curve. The horizontal shift distance on the logarithmic scale was a multiplicative shift factor, α_T , for the loading frequency, which varies with test temperature. In the present investigation, the shift factors were determined by eye. The variation of shift factor, α_T , with test temperature, T_{mat} , relative to a reference temperature, T_r , has been found previously and was known to follow the well-known Williams-Landel-Ferry (WLF) equation (**Equation 3-8**).

$$\log [\alpha_T] = \frac{-C_1(T_{mat} - T_r)}{C_2 + (T_{mat} - T_r)} \quad (3-8)$$

Constants C_1 and C_2 were found by curve fitting $\log[\alpha_T]$ versus T data.

Temperature- and frequency-dependent viscoelastic behaviors in the transverse and longitudinal shear directions of the unidirectionally reinforced (transversely isotropic) lamina were characterized using a fractional derivative constitutive model. The model was originally

developed for neat polymers by Bagley and Torvick (1979) and was subsequently applied to the transverse and shear directions of unidirectionally reinforced composites by Shan and Bakis (2009). The fractional derivative viscoelastic model is given by **Equation 3-9**,

$$\sigma[t] + \sum_{k=1}^n a_k D^{\beta_k} \sigma[t] = E \varepsilon[t] + E \sum_{k=1}^n b_k D^{\beta_k} \varepsilon[t] \quad (3-9)$$

where σ , ε , and E respectively refer to the stress, engineering strain, and elastic modulus and D^{β_k} are fractional derivatives of order β_k ($0 < \beta_k < 1$), defined as

$$D^{\beta_k} [x[t]] = \frac{1}{\Gamma[1 - \beta_k]} \frac{d}{dt} \int_0^t \frac{x[\tau]}{(t - \tau)^{\beta_k}} d\tau \quad (3-10)$$

where Γ is the gamma function,

$$\Gamma[x] = \int_0^\infty t^{x-1} e^{-t} dt, \quad (x > 0) \quad (3-11)$$

The constitutive behavior is purely elastic when β_k equals 0 and purely viscous when β_k equals 1. Following Bagley and Torvick (1983), the Fourier transform of a time dependent variable $x[t]$ is

$$F[x[t]] = \int_{-\infty}^{\infty} x[t] e^{i\omega t} dt = x^*[if] \quad (3-12)$$

where $i = \sqrt{-1}$ and the superscript * represents a complex variable which is a function f —the cyclic frequency in Hz. The fractional derivative operator (**Equation 3-10**) has a special property in the Fourier domain such that the Fourier transform of the fractional derivative of order β_k of $x[t]$ is given by **Equation 3-13**

$$F[D^{\beta_k} [x[t]]] = (if)^{\beta_k} F[x[t]] \quad (3-13)$$

Thus, the Fourier transform of the fractional derivative viscoelastic model (**Equation 3-9**) is

$$\sigma^*[if] + \sum_{k=1}^n a_k (if)^{\beta_k} \sigma^*[if] = E \varepsilon^*[if] + E \sum_{k=1}^n b_k (if)^{\beta_k} \varepsilon^*[if] \quad (3-14)$$

Collecting complex stress, $\sigma^*[if]$, and complex strain, $\varepsilon^*[if]$, terms and rearranging,

$$\sigma^*[if] = E \varepsilon^*[if] \frac{1 + \sum_{k=1}^n b_k (if)^{\beta_k}}{1 + \sum_{k=1}^n a_k (if)^{\beta_k}} \quad (3-15)$$

The storage modulus, loss modulus, and loss factor are then defined by **Equations 3-16:18**

$$E' = \text{Re} \left\{ \frac{1 + \sum_{k=1}^n b_k (if)^{\beta_k}}{1 + \sum_{k=1}^n a_k (if)^{\beta_k}} \right\} E = \frac{A^* C^* + B^* D^*}{C^{*2} + D^{*2}} E \quad (3-16)$$

$$E'' = \text{Im} \left\{ \frac{1 + \sum_{k=1}^n b_k (if)^{\beta_k}}{1 + \sum_{k=1}^n a_k (if)^{\beta_k}} \right\} E = \frac{B^* C^* - A^* D^*}{C^{*2} + D^{*2}} E \quad (3-17)$$

$$\eta = \frac{E''}{E'} = \frac{B^* C^* - A^* D^*}{A^* C^* + B^* D^*} \quad (3-18)$$

Constants A^* , B^* , C^* , and D^* can be defined using only two terms in the series expansion ($n=2$), according to the findings of Shan and Bakis (2009). Using the identity $i^{\beta_k} = \cos\left(\frac{\pi\beta_k}{2}\right) + i\sin\left(\frac{\pi\beta_k}{2}\right)$, one can express the four constants as in **Equations 3-19:22**.

$$A^* = 1 + b_1 f^{\beta_1} \cos\left[\frac{\pi\beta_1}{2}\right] + b_2 f^{\beta_2} \cos\left[\frac{\pi\beta_2}{2}\right] \quad (3-19)$$

$$B^* = b_1 f^{\beta_1} \sin\left[\frac{\pi\beta_1}{2}\right] + b_2 f^{\beta_2} \sin\left[\frac{\pi\beta_2}{2}\right] \quad (3-20)$$

$$C^* = 1 + a_1 f^{\beta_1} \cos\left[\frac{\pi\beta_1}{2}\right] + a_2 f^{\beta_2} \cos\left[\frac{\pi\beta_2}{2}\right] \quad (3-21)$$

$$D^* = a_1 f^{\beta_1} \sin\left[\frac{\pi\beta_1}{2}\right] + a_2 f^{\beta_2} \sin\left[\frac{\pi\beta_2}{2}\right] \quad (3-22)$$

The seven viscoelastic parameters E , b_1 , β_1 , b_2 , β_2 , a_1 , and a_2 take on two distinct sets of values: one set for the transverse (E_2 and E_3) moduli of the lamina and a second set for the longitudinal shear moduli (G_{12} and G_{13}) of the lamina. Temperature-frequency superposition was implemented by replacing the cyclic frequency f by the cyclic frequency multiplied by the shift factor, $\alpha_t f$, utilizing the unique α_t for each data set and respective temperature (**Equation 3-8**). The storage and loss factor functions (**Equation 3-16** and **Equation 3-18**, respectively) were fitted by an

optimization algorithm to their respective experimental master curves to determine the optimal viscoelastic parameters of E , b_1 , β_1 , b_2 , β_2 , a_1 , and a_2 to thereby characterize E_2 , E_3 , G_{12} , and G_{13} in the tested ranges of temperature and loading frequency.

Table 3-8. Fractional derivative model fit constants, transverse and shear (Henry, 2012)

Parameter	LF750	30748	30757	30917	EPON 862
E (GPa)	5.58E-01	6.52E-01	7.29E-02	1.60E-01	1.44E+00
$a_1 \left(\frac{1}{\text{Hz}}\right)^{\beta_1}$	7.35E-01	3.81E+01	1.31E+03	4.85E+00	3.71E+01
$b_1 \left(\frac{1}{\text{Hz}}\right)^{\beta_1}$	-2.51E+01	-1.08E+01	-6.96E-03	1.58E-07	6.11E-03
β_1	2.81E-01	6.25E-01	-1.14E-01	2.45E-01	1.14E-01
$a_2 \left(\frac{1}{\text{Hz}}\right)^{\beta_2}$	2.18E+00	1.66E+01	1.34E+03	2.95E-12	2.02E-05
$b_2 \left(\frac{1}{\text{Hz}}\right)^{\beta_2}$	3.05E+01	1.27E+02	8.05E+04	8.54E+01	1.58E+02
β_2	3.24E-01	7.61E-01	4.83E-02	2.72E-01	1.27E-01
C_1	-6.34E+00	-2.35E+08	-3.13E+02	-4.15E+12	-7.91E+11
C_2	1.15E+02	4.49E+09	3.77E+03	2.64E+13	1.01E+13
G (GPa)	7.28E-02	1.83E-01	4.35E-02	3.43E00	7.27-01
$a_1 \left(\frac{1}{\text{Hz}}\right)^{\beta_1}$	9.32E-01	1.47E+00	4.62E+00	7.24E+01	-2.89E-00
$b_1 \left(\frac{1}{\text{Hz}}\right)^{\beta_1}$	2.76E+01	2.52E-02	2.90E+02	-4.79E+01	9.57E+01
β_1	2.49E-01	1.84E-01	2.61E-01	2.31E-01	3.20E-01
$a_2 \left(\frac{1}{\text{Hz}}\right)^{\beta_2}$	2.27E+00	4.92E-02	7.02E+00	8.96E+01	1.48E+01
$b_2 \left(\frac{1}{\text{Hz}}\right)^{\beta_2}$	8.81E-04	7.94E+00	8.82E-04	1.68E+02	-4.10E-01
β_2	1.62E-01	2.18E-01	2.33E-01	2.95E-01	3.08E-01
C_1	-1.31E+02	-2.46E+01	-6.70E+01	-9.30E+01	-4.57E+10
C_2 (°C)	1.10E+03	2.47E+02	5.43E+02	8.95E+02	4.64E+11

The analytical self-heating model (Shan and Bakis, 2009), augmented for mixed angle-ply laminates (Bakis et. al 2011), predicts the steady-state operating temperature of a spinning shaft subjected to time-invariant, uniform bending strain via four computational steps (**Figure 3-11**). First, the lamina-level temperature- and frequency-dependent properties are calculated at a material temperature, T_{mat} , initially set equal to the ambient temperature, T_{amb} , operating at a

cyclic frequency f . Second, the three-dimensional shaft stresses and strains, assuming a state of pure bending, are calculated using the quasi-static analysis of laminated, thick-walled composite shafts developed by Jolicoeur and Cardou (1994). This analysis determines the lamina-level stresses and strains by treating each filament wound $\pm\theta$ layer as two unidirectionally reinforced lamina. Details of the stress analysis are omitted here for brevity. Third, using the strain energy method developed by Adams and Bacon (1973), the energy dissipated per unit volume in each unidirectional lamina in a single load cycle, ΔW , is given by **Equation 3-23**,

$$\Delta W = \pi(\eta_1\sigma_1\varepsilon_1 + \eta_2\sigma_2\varepsilon_2 + \eta_3\sigma_3\varepsilon_3 + \eta_{12}\tau_{12}\gamma_{12}) \quad (3-23)$$

where ε and γ are strains in extension and shear, respectively. Contributions to energy dissipation due to out-of-plane shear strains (γ_{13} and γ_{23}) were assumed to be negligible for shafts undergoing flexural strain but no torque, according to findings in Shan and Bakis (2009). It was assumed that all the energy dissipated in the material was converted to thermal energy. Thus, for a shaft loaded at a cyclic frequency f , the energy dissipated per unit volume and time, q''' , was found using **Equation 3-24**.

$$q''' = f\Delta W \quad (3-24)$$

Linear strain variation through the wall thickness of the shaft was assumed when calculating the heat generation. In the fourth step, the average temperature of the spinning shaft under uniform bending was calculated using a one-dimensional finite difference heat transfer model with three elements per lamina in the composite shaft. The heat generation per unit volume in each element, q''' , was calculated using **Equation 3-24**. The inner radius of the shaft was assumed to be insulated and the outer radius was allowed to lose heat through forced convection and radiation to the ambient environment. The radial thermal conductivity of the shaft was assumed to be $0.72 \text{ W}\cdot\text{m}^{-1}\cdot\text{K}^{-1}$, the emissivity was assumed to be 1, and the surface convection

was based on a horizontal shaft spinning in air of temperature 20°C. The average shaft temperature predicted by a pass through the four steps, T_{cal} , was then used to update the material properties by changing the material temperature in the viscoelastic model, T_{mat} . This process is repeated until convergence is achieved ($T_{mat}=T_{cal}$) within a tolerance of 0.001 °C. Additional details of the heat transfer model are reported in Shan and Bakis (2009).

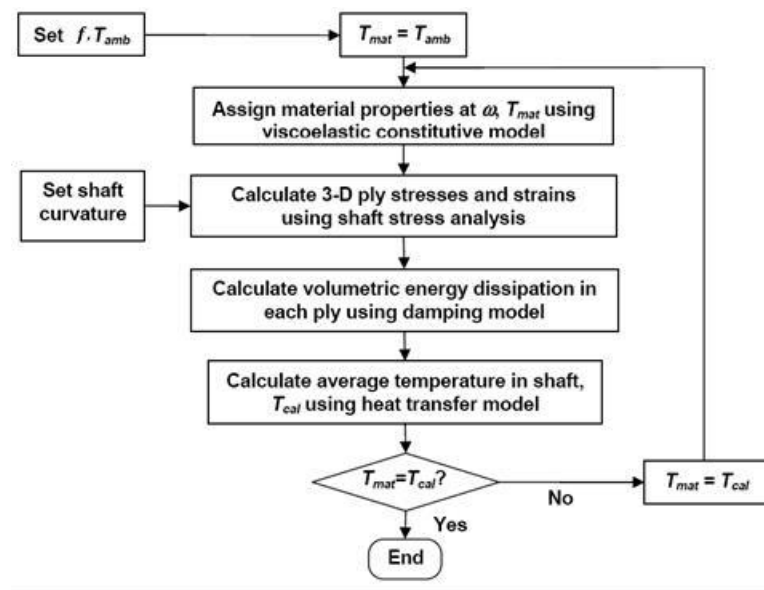


Figure 3-11. Flow chart for calculating equilibrium temperature for the composite shaft (Shan, 2006)

3.4.2 Whirling Module

The Whirling Module calculates the first critical frequency of the operating driveshaft using the shaft geometry and lamina properties. This module assumes that the shaft has a uniform circular cross-section operating with pinned-pinned boundary conditions at a constant speed. A Cartesian coordinate system fixed in space was aligned such that the x -direction was parallel to the longitudinal axis of the shaft. Applying Hamilton's principle to the equations of motion for a rotating anisotropic Bresse-Timoshenko beam yields **Equations 3-25** (Bert and Kim, 1995a),

$$\begin{aligned}
C_S \left(\frac{\partial^2 v}{\partial x^2} - \frac{\partial \psi_z}{\partial x} \right) &= \rho A_r \frac{\partial^2 v}{\partial t^2} \\
C_S \left(\frac{\partial^2 w}{\partial x^2} - \frac{\partial \psi_y}{\partial x} \right) &= \rho A_r \frac{\partial^2 w}{\partial t^2} \\
C_B \frac{\partial^2 \psi_y}{\partial x^2} + \frac{C_{BT}}{2} \frac{\partial^2 \psi_x}{\partial x^2} + C_S \left(\frac{\partial w}{\partial x} - \psi_y \right) &= \rho I \frac{\partial^2 \psi_y}{\partial t^2} - 2\rho I f_{oper} \frac{\partial \psi_z}{\partial t} \\
C_B \frac{\partial^2 \psi_z}{\partial x^2} + \frac{C_{BT}}{2} \frac{\partial^2 \psi_x}{\partial x^2} + C_S \left(\frac{\partial v}{\partial x} - \psi_z \right) &= \rho I \frac{\partial^2 \psi_z}{\partial t^2} - 2\rho I f_{oper} \frac{\partial \psi_y}{\partial t} \\
C_T \frac{\partial^2 \psi_x}{\partial x^2} + \frac{C_{BT}}{2} \left(\frac{\partial^2 \psi_y}{\partial x^2} + \frac{\partial^2 \psi_z}{\partial x^2} \right) &= \rho J \frac{\partial^2 \psi_x}{\partial t^2}
\end{aligned} \tag{3-25}$$

where A_r , I , and J are the cross-sectional area, the area moment of inertia, and the polar area moment of inertia respectively, f is the angular frequency (Hz), and ρ is the density of the material. The material parameters C_S , C_B , C_{BT} , and C_T are the transverse shear, bending, bending-twisting coupling, and torsional stiffnesses respectively. The displacements in the coordinate directions x-y-z are represented by u - v - w while the rotations are ψ_x - ψ_y - ψ_z .

The three dimensional effective elastic constants were calculated using a method developed by Sun and Li (1988) (at the steady state temperature from the Shaft Temperature Module and the operating frequency) and used in calculating the factor K (**Equation 3-26**) where $\bar{m} = \frac{R_i}{R_o}$.

$$K = \frac{\frac{6}{7}(1 - \bar{m}^4)(1 + \bar{m}^2)}{1 + \frac{27}{7}\bar{m}^2(1 - \bar{m}^2) - \bar{m}^6 - 2\left(\frac{\nu_{xy}G_{xy}}{7E_x}\right)(1 + 9 * \bar{m}^2(1 - \bar{m}^2) - \bar{m}^6)} \tag{3-26}$$

The material stiffness terms are given by **Equations 3-27** where each, excluding C_S , involves terms summed over all lamina k in the laminate with n representing the total number of lamina. Q terms are found using the well-known CLT equations.

$$C_S = K A_r G_{xy} \tag{3-27}$$

$$C_B = \frac{\pi}{4} \sum_{k=1}^n Q_{11}^k (R_o^4 - R_i^4)^k$$

$$C_{BT} = \sum_{k=1}^n Q_{16}^k (R_o^4 - R_i^4)^k$$

$$C_T = \frac{\pi}{2} \sum_{k=1}^n Q_{66}^k (R_o^4 - R_i^4)^k$$

Assuming modes of vibration i.e. $u(x, t) = U(x)e^{ift}$ and substituting them into the equations of motions yields three coupled ordinary differential equations in x . A set of three homogeneous equations results from applying pinned-pinned boundary conditions (**Equation 3-28**).

$$\begin{bmatrix} X_{11} & iX_{12} & X_{13} \\ -iX_{12} & X_{11} & X_{13} \\ X_{31} & X_{31} & X_{33} \end{bmatrix} \begin{Bmatrix} \bar{U} \\ \bar{V} \\ \bar{W} \end{Bmatrix} = \begin{Bmatrix} 0 \\ 0 \\ 0 \end{Bmatrix} \quad (3-28)$$

Each term X (**Equations 3-29**) is defined by the material stiffnesses (**Equations 3-27**) as well as the vibration mode number m_w , free length of the shaft between supports $\lambda_w = \frac{m_w \pi}{L}$, and f_{oper} the operating angular frequency of the driveshaft (Hz).

$$X_{11} = C_B \lambda_w^4 - \left(\rho I + \frac{C_B}{C_S} \rho A_r \right) f \lambda_w^2 + \left(\frac{\rho^2 I A_r}{C_S} f^2 - \rho A_r f^2 \right)$$

$$X_{12} = 2\rho I f_{oper} f \left(\lambda_w^2 - \frac{\rho A_r}{C_S} f^2 \right)$$

$$X_{13} = \frac{C_{BT}}{2} \lambda_w^3 \quad (3-29)$$

$$X_{31} = X_{13} - \frac{C_{BT}}{2} \frac{\rho A_r}{C_S} \lambda_w f^2$$

$$X_{33} = C_T \lambda_w^2 - \rho J f^2$$

The critical frequencies of the driveshaft are the solutions to the determinant of the left hand side of **Equation 3-28**. A fifth order polynomial ($c_{5w}(f^2)^5 + c_{4w}(f^2)^4 + c_{3w}(f^2)^3 + c_{2w}(f^2)^2 + c_{1w}(f^2) + c_{0w} = 0$) in f^2 is solved (terms in **Equation 3-30**) where the first natural frequency, f_{crit} , is the square root of the smallest root f^2 .

$$\begin{aligned}
 c_{0w} &= C_B \pi^{10} (-C_{BT}^2 + 2C_B C_T) \left(\frac{1}{2L^{10}} \right) \\
 c_{1w} &= \pi^6 \rho \{ C_S (C_{BT}^2 I - 2C_B (2C_T I + C_B J)) \pi^2 \\
 &\quad + A_r [(-4C_B C_T (C_S L^2 + C_B \pi^2 - IL^2 \rho) \\
 &\quad + C_{BT}^2 (C_S L^2 + 2C_B \pi^2 - IL^2 \rho))] \} \left(\frac{1}{2C_S L^8} \right) \\
 c_{2w} &= \pi^2 \rho^2 \{ 2C_S^2 I (-3C_T I + 2C_B J) \pi^4 \\
 &\quad + A_r^2 (C_S L^2 + C_B \pi^2 - IL^2 \rho) (2C_S C_T L^2 - C_{BT}^2 \pi^2 + 2C_B C_T \pi^2 - 2C_T IL^2 \rho) \\
 &\quad + A_r C_S \pi^2 [4C_S (C_T I + C_B J) L^2 - C_{BT}^2 I \pi^2 \\
 &\quad + 4(C_T I + C_B J) (C_B \pi^2 - IL^2 \rho)] \} \left(\frac{1}{2C_S^2 L^6} \right) \tag{3-30}
 \end{aligned}$$

$$\begin{aligned}
 c_{3w} &= -\rho^3 [-3C_S^2 I^2 J \pi^4 + A_r^2 J (C_S L^2 + C_B \pi^2 - IL^2 \rho)^2 \\
 &\quad + 2A_r C_S I \pi^2 (C_S J L^2 - 4C_T I \pi^2 + C_B J \pi^2 - IJ L^2 \rho)] \left(\frac{1}{C_S^2 L^4} \right)
 \end{aligned}$$

$$c_{4w} = \frac{-4A_r I^2 (A_r C_T + 2C_S J) \pi^2 \rho^4}{C_S^2 L^2}$$

$$c_{5w} = \frac{4A_r^2 I^2 J \rho^5}{C_S^2}$$

3.4.3 Buckling Module

The Buckling Module calculates the lowest buckling torque of a thin-walled, very long shaft (Cheng and Ho, 1963). Additional assumptions include small displacements relative to the

thickness, and an element perpendicular to the middle surface remains so after deformation. The cylindrical coordinate system used by Cheng and Ho (1963) is shown in **Figure 3-12**.

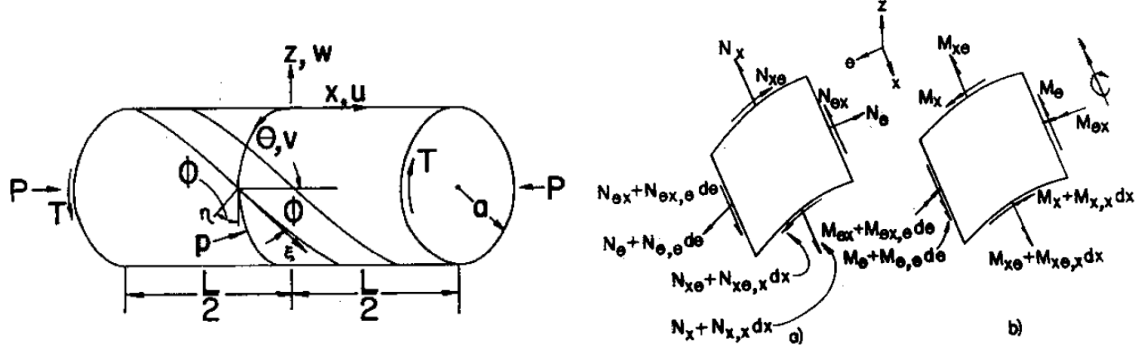


Figure 3-12. Orientation of axes in the middle surface of cylindrical shell (Cheng and Ho, 1963)

Using these assumptions the stress-strain relationships relations become

$$\begin{Bmatrix} \sigma_x \\ \sigma_\theta \\ \tau_{x\theta} \end{Bmatrix} = \begin{bmatrix} C_{11} & C_{12} & C_{16} \\ C_{12} & C_{22} & C_{26} \\ C_{16} & C_{26} & C_{66} \end{bmatrix} \begin{Bmatrix} \varepsilon_x \\ \varepsilon_\theta \\ \gamma_{x\theta} \end{Bmatrix} \quad (3-31)$$

The resultant force and moment stress relations can be established from **Figure 3-12** where r_m is the mean radius.

$$\begin{aligned} N_x &= \int_{-\frac{h_t}{2}}^{\frac{h_t}{2}} \sigma_x \left(1 + \frac{z}{r_m}\right) dz \\ N_\theta &= \int_{-\frac{h_t}{2}}^{\frac{h_t}{2}} \sigma_\theta dz \\ N_{x\theta} &= \int_{-\frac{h_t}{2}}^{\frac{h_t}{2}} \tau_{x\theta} \left(1 + \frac{z}{r_m}\right) dz \\ N_{\theta x} &= \int_{-\frac{h_t}{2}}^{\frac{h_t}{2}} \tau_{\theta x} dz \end{aligned} \quad (3-32)$$

$$M_x = \int_{-\frac{h_t}{2}}^{\frac{h_t}{2}} \sigma_x \left(1 + \frac{z}{r_m}\right) z dz$$

$$M_\theta = \int_{-\frac{h_t}{2}}^{\frac{h_t}{2}} \sigma_\theta z dz$$

$$M_{x\theta} = \int_{-\frac{h_t}{2}}^{\frac{h_t}{2}} \tau_{x\theta} \left(1 + \frac{z}{r_m}\right) z dz$$

$$M_{\theta x} = \int_{-\frac{h_t}{2}}^{\frac{h_t}{2}} \tau_{\theta x} z dz$$

The strains-displacement relations for a cylindrical element at the middle surface neglecting terms much smaller than 1 are

$$\begin{aligned} \varepsilon_x &= u_{,x} - z w_{,xx} = \varepsilon_x^o - z \kappa_x \\ \varepsilon_\theta &= \frac{v_{,\theta}}{r_m} - \frac{z}{r_m} \frac{w_{,\theta\theta}}{(r_m + z)} + \frac{w}{r_m + z} = \varepsilon_\theta^o + z \left(1 - \frac{z}{r_m}\right) \kappa_\theta \\ \gamma_{x\theta} &= \frac{u_{,\theta}}{r_m + z} + \left(1 + \frac{z}{r_m}\right) v_{,x} - w_{,x\theta} \left(\frac{z}{r_m} + \frac{z}{r_m + z}\right) \\ &= \left[1 + \left(\frac{z^2}{2r_m^2}\right)\right] \varepsilon_{x\theta}^o + z \left[1 - \left(\frac{z}{2r_m}\right)\right] \kappa_{x\theta} \end{aligned} \quad (3-33)$$

Substituting **Equation 3-31** and **Equation 3-33** into **Equation 3-32** results in **Equation 3-34**

where the terms A_{ij} , B_{ij} , and D_{ij} for $i, j = 1, 2, 6$ are given by the well-known CLT relationship

$$(A_{ij}, B_{ij}, D_{ij}) = \int_{-\frac{h_t}{2}}^{\frac{h_t}{2}} Q_{ij}(1, z, z^2) dz.$$

$$\begin{Bmatrix} N_x \\ N_\theta \\ N_{x\theta} \\ N_{\theta x} \\ M_x \\ M_\theta \\ M_{x\theta} \\ M_{\theta x} \end{Bmatrix} = \begin{bmatrix} A_{11} + \frac{B_{11}}{r_m} & A_{12} + \frac{B_{12}}{r_m} & A_{16} + \frac{B_{16}}{r_m} + \frac{D_{16}}{2r_m^2} \\ A_{12} & A_{22} & A_{26} + \frac{D_{26}}{2r_m^2} \\ A_{16} + \frac{B_{16}}{r_m} & A_{26} + \frac{B_{26}}{r_m} & A_{66} + \frac{B_{66}}{r_m} + \frac{D_{66}}{2r_m^2} \\ A_{16} & A_{26} & A_{66} + \frac{D_{66}}{2r_m^2} & \dots \\ B_{11} + \frac{D_{11}}{r_m} & B_{12} + \frac{D_{12}}{r_m} & B_{16} + \frac{D_{16}}{r_m} \\ B_{12} & B_{22} & B_{26} \\ B_{16} + \frac{D_{16}}{r_m} & B_{26} + \frac{D_{26}}{r_m} & B_{66} + \frac{D_{66}}{r_m} \\ B_{16} & B_{26} & B_{66} \end{bmatrix} \begin{Bmatrix} \varepsilon_x^o \\ \varepsilon_\theta^o \\ \gamma_{x\theta}^o \\ \kappa_x \\ \kappa_\theta \\ \kappa_{x\theta} \end{Bmatrix} \quad (3-34)$$

The deformation of a cylindrical element of the structure is governed by the following differential equations (**Equations 3-35**) of equilibrium during buckling, where Q_S is the external torsional force per unit length. For this analysis external radial pressure and external longitudinal compression force per unit length are assumed to be zero.

$$\begin{aligned} r_m N_{x,x} + N_{\theta x,\theta} - 2Q_S u_{x\theta} &= 0 \\ r_m N_{\theta,\theta} + r_m^2 N_{x\theta,x} + M_{\theta,\theta} + a M_{x\theta,x} - 2r_m Q_S (v_{x\theta} + w_{,x}) &= 0 \\ M_{\theta,\theta\theta} + r_m (M_{x\theta} + M_{\theta x})_{,x\theta} + r_m^2 M_{x,xx} - r_m N_\theta + 2r_m Q_S (v_{,x} - w_{,x\theta}) &= 0 \end{aligned} \quad (3-35)$$

Substituting **Equation 3-33** and **Equation 3-34** into **Equation 3-35** allows for the differential equations of equilibrium to be expressed in terms of the middle surface shell displacements. Cheng and Ho (1963) acknowledged the difficulty of solving the resulting sets of partial

differential equations exactly and proposed a particular solution via the inverse method. The displacements at the middle shell surface were assumed to be of the form

$$\begin{aligned} u &= U \sin\left(\frac{\lambda x}{r_m} + n_b \theta\right) \\ v &= V \sin\left(\frac{\lambda x}{r_m} + n_b \theta\right) \\ w &= W \cos\left(\frac{\lambda x}{r_m} + n_b \theta\right) \end{aligned} \quad (3-36)$$

where the longitudinal half-wavelength $\lambda_b = \frac{m_b \pi r_m}{L}$ with m_b being the number of half waves in the longitudinal direction and n_b being the number of waves in the circumferential direction. U , V , and W are constants. It should be recognized that **Equations 3-36** cannot satisfy any boundary conditions. It is for this reason that the shaft was assumed to be “very long” such that the boundary conditions do not greatly affect the critical stress magnitude. Substituting **Equation 3-36** into the partial differential equations allows one to obtain **Equation 3-37**.

$$\begin{bmatrix} H_{11} - 2n_b \lambda_b \frac{1}{A_{22}} Q_s & H_{12} & H_{13} \\ & H_{22} - 2n_b \lambda_b \frac{1}{A_{22}} Q_s & H_{23} - 2\lambda_b \frac{1}{A_{22}} Q_s \\ \text{sym} & & H_{33} - 2n_b \lambda_b \frac{1}{A_{22}} Q_s \end{bmatrix} \begin{Bmatrix} U \\ V \\ W \end{Bmatrix} = \begin{Bmatrix} 0 \\ 0 \\ 0 \end{Bmatrix} \quad (3-37)$$

where H_{ij} are given by,

$$\begin{aligned} H_{11} &= (\bar{A}_{11} + \bar{B}_{11})\lambda_b^2 + 2n_b \bar{A}_{16} \lambda_b + n_b^2 (\bar{A}_{66} - \bar{B}_{66} + \bar{D}_{66}) \\ H_{12} &= (\bar{A}_{16} + 2\bar{B}_{16} + \bar{D}_{16})\lambda_b^2 + n_b (\bar{A}_{12} + \bar{A}_{66} + \bar{B}_{12} + \bar{B}_{66})\lambda_b + n_b^2 \bar{A}_{26} \\ H_{13} &= (\bar{B}_{11} + \bar{D}_{11})\lambda_b^3 + n_b (3\bar{B}_{16} + \bar{D}_{16})\lambda_b^2 + [n_b^2 (\bar{B}_{12} + 2\bar{B}_{66} - \bar{D}_{66}) + \bar{A}_{12}]\lambda_b \\ &\quad + n_b^3 (\bar{B}_{26} - \bar{D}_{26}) + n_b (\bar{A}_{26} - \bar{B}_{26} + \bar{D}_{26}) \\ H_{22} &= (\bar{A}_{66} + 3\bar{B}_{66} + 3\bar{D}_{66})\lambda_b^2 + 2n_b (\bar{A}_{26} + 2\bar{B}_{26} + \bar{D}_{26})\lambda_b + n_b^2 (1 + \bar{B}_{22}) \end{aligned} \quad (3-38)$$

$$H_{23} = (\bar{B}_{16} + 2\bar{D}_{16})\lambda_b^2 + n_b(\bar{B}_{12} + 2\bar{B}_{66} + \bar{D}_{12} + 3\bar{D}_{66})\lambda_b^2 \\ + [n_b^2(3\bar{B}_{26} + 2\bar{D}_{26}) + \bar{A}_{26} + \bar{B}_{26}]\lambda_b + n_b^3\bar{B}_{22} + n_b$$

$$H_{33} = \bar{D}_{11}\lambda_b^4 + 4n_b\bar{D}_{16}\lambda_b^3 + 2[n_b^2(\bar{D}_{12} + 2\bar{D}_{66}) + \bar{B}_{12}]\lambda_b^2 \\ + 2n_b(2n_b^2\bar{D}_{26} + 2\bar{B}_{26} - \bar{D}_{26})\lambda_b + (n_b^2 - 1)^2\bar{D}_{22} + (2n_b^2 - 1)\bar{B}_{22} \\ + 1$$

The terms $(\bar{A}_{ij}, \bar{B}_{ij}, \bar{D}_{ij}) = \frac{1}{A_{22}}(A_{ij}, \frac{B_{ij}}{r_m}, \frac{D_{ij}}{r_m^2})$. The critical buckling torque of the driveshaft is the lowest solution to the determinant of the left-hand side of **Equation 3-37**. A third order polynomial $(c_{3b}(\frac{1}{A_{22}}Q_s)^3 + c_{2b}(\frac{1}{A_{22}}Q_s)^2 + c_{1b}(\frac{1}{A_{22}}Q_s) + c_{0b} = 0)$ in $\frac{1}{A_{22}}Q_s$ is solved (terms in **Equation 3-38**) for an array of chosen longitudinal (m_b) and circumferential (n_b) wave numbers with the lowest root related to the critical buckling torque, Q_{crit} .

$$c_{3b} = 8L^3n_b - 8L^3n_b^3 \\ c_{2b} = -4H_{11}L^2 - 8H_{23}L^2n_b + 4H_{11}L^2n_b^2 + 4H_{22}L^2n_b^2 + 4H_{33}L^2n_b^2 \\ c_{1b} = -4H_{12}H_{13}L + 4H_{11}H_{23}L + 2H_{12}^2Ln_b + 2H_{13}^2Ln_b - 2H_{11}H_{22}Ln_b + 2H_{23}^2Ln_b \\ - 2H_{11}H_{33}Ln_b - 2H_{22}H_{33}Ln_b \quad (3-39)$$

$$c_{0b} = -H_{13}^2H_{22} + 2H_{12}H_{13}H_{23} - H_{11}H_{23}^2 - H_{12}^2H_{33} + H_{11}H_{22}H_{33}$$

Once the lowest root of the polynomial was found, the critical buckling torque was calculated using **Equation 3-40**.

$$Q_{crit} = 2\pi r_m^2 Q_s \quad (3-40)$$

3.4.4 Structural Module

The *Structural Module* calculates the highest stresses in each of the lamina coordinate directions. The stresses were found using an approach by Jolicouer and Cardou (1993) which

assumes a bent hollow cylinder of constant curvature under small strains with no shear resultant.

The coordinate system used by Jolicouer and Cardou (1993) is shown in **Figure 3-13**.

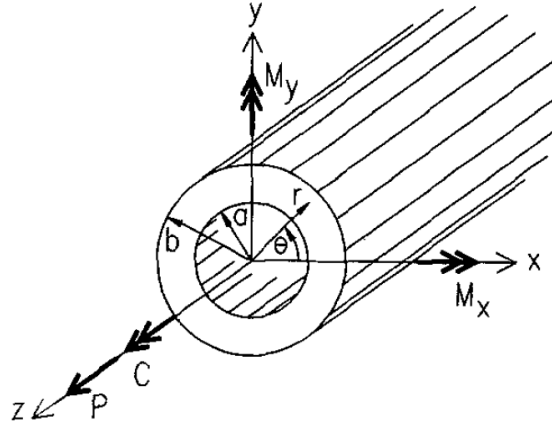


Figure 3-13. Cylinder under study and applied loads (Jolicouer and Cardou, 1993)

The three dimensional effective elastic constants, C_{ij} , were calculated using a method developed by Sun and Li (1988) (at the steady state temperature from the *Shaft Temperature Module* and the operating frequency) with reduced elastic constants (Lekhnitskii, 1981).

$$\beta_{ij} = C_{ij} - \frac{C_{i3}C_{3j}}{C_{33}} \quad (3-41)$$

The strain-displacement compatibility relations and stress functions developed by Lekhnitskii (1981) were used in developing a general solution to a problem of pure bending and pure longitudinally symmetric loading using separation of variables. Jolicouer and Cardou (1993) assume a stress function of the form $\Lambda_1 = K'r^{m+1}$ and $\Pi_1 = K'gr^m$ for which K' represents an arbitrary constant applied to the pure bending problem. Substitution of this solution into the homogeneous system of equations for the pure bending problem (Lekhnitskii, 1981) yields **Equation 3-42**

$$g = \frac{\beta_{24}m^3 + (\beta_{14} + \beta_{24})m^2 - \beta_{56}}{\beta_{44}m^2 - \beta_{55}} \quad (3-42)$$

for which the characteristic equation is

$$a_s m^6 + b_s m^4 + c_s m^2 = 0 \quad (3-43)$$

with

$$\begin{aligned} a_s &= \beta_{22}\beta_{44} - \beta_{24}^2 \\ b_s &= \beta_{24}(2\beta_{14} + \beta_{24} + 2\beta_{56}) - \beta_{44}(\beta_{11} + 2\beta_{12} + \beta_{22} + \beta_{66}) - \beta_{22}\beta_{55} + \beta_{14}^2 \\ c_s &= \beta_{55}(\beta_{11} + 2\beta_{12} + \beta_{22} + \beta_{66}) \end{aligned} \quad (3-44)$$

The characteristic equation **Equation 3-43** has four roots defined as

$$m_i = \pm \frac{\sqrt{-b_s \pm \sqrt{b_s^2 - 4a_s c_s}}}{2a_s}, i = 1 \text{ to } 4 \quad (3-45)$$

A particular solution for the non-homogeneous system of equations (Lekhnitskii, 1981) of the form $\Lambda_1 = \left(\frac{\mu_1}{2}\right)r^3$ and $\Pi_1 = \mu_2 r^2$ gives an additional pair of linear equations,

$$\begin{Bmatrix} \mu_1 \\ \mu_2 \end{Bmatrix} = \begin{bmatrix} -2\beta_{14} - 6\beta_{24} + \beta_{56} & 4\beta_{44} - \beta_{55} \\ -\beta_{11} - 2\beta_{12} + 3\beta_{22} - \beta_{66} & 2\beta_{14} - 2\beta_{24} + \beta_{56} \end{bmatrix}^{-1} \frac{1}{C_{33}} \begin{Bmatrix} 2C_{34} \\ C_{13} - C_{23} \end{Bmatrix} \quad (3-46)$$

Additionally four constants g_i (**Equation 3-42**) are obtained through using the values from **Equation 3-45**

$$g_i = \frac{\beta_{24}m_i^2 + (\beta_{14} + \beta_{24})m_i - \beta_{56}}{\beta_{44}m_i^2 - \beta_{55}}, i = 1 \text{ to } 4 \quad (3-47)$$

The general solution to the longitudinally symmetric problem published by Lekhnitskii (1981) has the roots m' to the characteristic equation

$$\begin{aligned} m'_i &= \pm \sqrt{\frac{\beta_{11}\beta_{44} - \beta_{14}^2}{\beta_{22}\beta_{44} - \beta_{24}^2}}, i = 1, 2 \\ g'_i &= \frac{\beta_{14} + \beta_{24}m'_i}{\beta_{44}}, i = 1, 2 \end{aligned} \quad (3-48)$$

$$\begin{Bmatrix} \mu_3 \\ \mu_4 \end{Bmatrix} = \begin{bmatrix} \beta_{14} + 2\beta_{24} & -\beta_{44} \\ 4\beta_{22} - \beta_{11} & \beta_{14} - 2\beta_{24} \end{bmatrix}^{-1} \begin{Bmatrix} 1 \\ 0 \end{Bmatrix}$$

$$\mu_5 = \frac{C_{34}(\beta_{24} - \beta_{14}) + \beta_{44}(C_{13} - C_{23})}{C_{33}[\beta_{14}^2 - \beta_{24}^2 + \beta_{44}(\beta_{22} - \beta_{11})]}$$

Equations 3-45, 3-46, 3-47, and 3-48 are substituted into the state equations (Lekhnitskii, 1981) with no-slip boundary conditions between lamina and solved simultaneously returning the global stiffness in the laminate coordinates (**Equation 3-49**).

$$\begin{Bmatrix} P \\ Q_s \\ M \end{Bmatrix} = \begin{bmatrix} EA_r & B_{12} & 0 \\ B_{21} & GJ & 0 \\ 0 & 0 & EI \end{bmatrix} \begin{Bmatrix} \varepsilon \\ \theta \\ \kappa \end{Bmatrix} \quad (3-49)$$

Applying the stress state of the composite shaft via the external forces and moments (bending moment and operating torque) in **Equation 3-49** yields the laminate coordinate direction strains. Stress and strain in the lamina coordinate directions can be determined through transformation using well known equations. The maximum stress amplitude for each stress component was found by evaluating the stress state for every lamina.

3.4.5 Factors of Safety

The maximum allowable operating temperature of the composite driveshaft was selected to be 85°C based on the guidance of extreme conditions by Mayrides (2005). Additionally, neat resin testing at temperatures above 85°C showed that the modulus of an FMC material was too compliant to be a viable above 85°C. The operating temperature of the driveshaft was calculated by the *Shaft Temperature Module*. The factor of safety (*S*) for heating is **Equation 3-50**.

$$S_h = \frac{85^\circ\text{C}}{T_{mat}} \quad (3-50)$$

The critical whirling speed was found by the *Whirling Module* to be the first natural frequency of vibration. This speed was an absolute maximum for the design of a sub-critically operating driveshaft. The factor of safety for whirling is **Equation 3-51**.

$$S_w = \frac{f_{crit}}{f_{oper}} \quad (3-51)$$

The critical buckling torque, Q_{crit} , was found by the *Buckling Module*. Q_{crit} was the absolute maximum torque that the driveshaft can carry. The length of the shaft segments between bearings compared to the diameter is approximately 15, considered *very long* suggesting assumed boundary conditions are unimportant. The factor of safety for buckling is **Equation 3-52** where Q_s is the applied torque.

$$S_b = \frac{Q_{crit}}{Q_s} \quad (3-52)$$

MST failure criterion was applied to predict lamina failure. The stress components in the lamina coordinate directions were determined in the *Structural Model* for every lamina. The maximum value of each stress component in the laminate (checked for each lamina) was compared against the corresponding strength. Material strength was calculated with dependence on temperature. **Equation 3-1:3-5** allow for neat resin modulus prediction, $E_m(T_{mat})$, at varying temperature, T_{mat} (°C), which can be used to calculate each strength component **Equations 3-53**.

$$\begin{aligned} F_{1T} &= [2247, 2249, 2250, 2252, 2265] \text{ MPa} \\ F_{1C} &= -5.2752e6 * E_m(T_{mat})^{0.5830} \text{ MPa} \\ F_{2T} &= 0.3786e6 * E_m(T_{mat})^{0.6024} \text{ MPa} \\ F_{2C} &= -0.3714e6 * E_m(T_{mat})^{0.7335} \text{ MPa} \\ F_6 &= 0.3919e6 * E_m(T_{mat})^{0.6175} \text{ MPa} \end{aligned} \quad (3-53)$$

The factor of safety for stress was defined as the minimum of all of the strength components each divided by the corresponding lamina strength component (**Equation 3-54**).

$$S_\sigma = MIN \left\{ \frac{F_{1T}}{\sigma_{11t}^{max}}, \left| \frac{F_{1C}}{\sigma_{11c}^{max}} \right|, \frac{F_{2T}}{\sigma_{22t}^{max}}, \left| \frac{F_{2C}}{\sigma_{22c}^{max}} \right|, \frac{F_6}{\tau_{12}^{max}} \right\} \quad (3-54)$$

F_{1T} , fiber direction strength in tension, was assumed to not be dependent on temperature (listed by material LF750, 30748, 30757, 30917, EPON 862). No knockdowns were applied to

account for fatigue. Previous testing showed material resistance to fatigue failure at misalignment strains up to 1500 $\mu\epsilon$ for several million cycles.

3.5 ATSV Optimization Strategy

ATSV is a multidimensional data visualization interface that supports trade space exploration of complex design problems (Stump et al., 2009). The interface includes 3D glyph plots, 2D scatter plots, 2D scatter matrices, parallel coordinates, and histogram plots to visualize data. Users can dynamically filter designs based on user-defined limits as well as apply preference shading and Pareto frontiers to highlight preferred designs in the trade space. ATSV was used to generate, record, and investigate the design space using a Pareto optimization procedure with differential evolution as the underlying heuristic search strategy to guide the optimization process. The selection strategy used by the differential algorithm allows the user to specify population size, crossover probability, and mutation factor (40, 0.5, and 0.5 respectively). Pareto sampling seeks to generate new designs along a Pareto frontier that was identified by one or more directions of preference specified by the user (minimizing or maximizing two or more variables). Determining the set of Pareto optimal designs was done using ATSVs visualization and analysis tools.

The Driveshaft Design Model was written in the numerical programming language MATLAB. A batch file facilitates communication between ATSV and MATLAB. Inputs are separated into two groups, composite design and scenario (**Figure 3-14**). Scenario options include material choice, ambient temperature, misalignment strain, helicopter platform; one selection from each defines a design case (highlighted). The shaft is loaded by the corresponding torque and misalignment strain. Composite design variables were manipulated by ATSV at every simulation iteration. Inputs were read by MATLAB and passed into the Design Model. The

Design Model simulates the design and then writes outputs to ATSV; which then applies design constraints on the design space, implements a sampling bias, stores the design variables, and mutates variables for subsequent calls to the Design Model. In this investigation, the preference of the sampling bias was to maximize the smallest factor of safety (S_{min}) and to minimize weight (reduce number of bearings and number of lamina). The optimization program was assumed to converge when all S were traded off, such that S_{min} cannot be increased further, and no additional bearings or lamina can be eliminated. Such a state can be recognized when multiple S are the same value for a given number of lamina and bearings. Some experience and insight from the user was required for recognition.

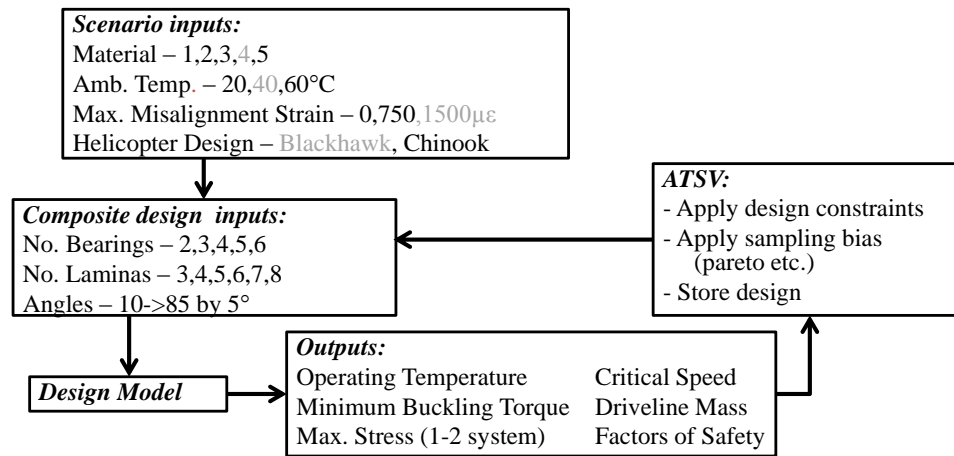


Figure 3-14. Flowchart of composite driveline optimization strategy

3.5.1 Blackhawk Design Space

The design space was constrained such that $S_{min} > 1.1$. The optimal designs in the design space were determined by the Pareto frontier, which represents the “best” designs for the multi-objective problem defined by the preference directions (maximize the S_{min} and minimize the weight). The preference direction can be observed as the arrow in **Figure 3-15**, with Pareto

designs marked by a solid circle. Pareto designs are those that trade off S_{min} and driveline weight such that no other design was lighter or the same weight with a higher S_{min} .

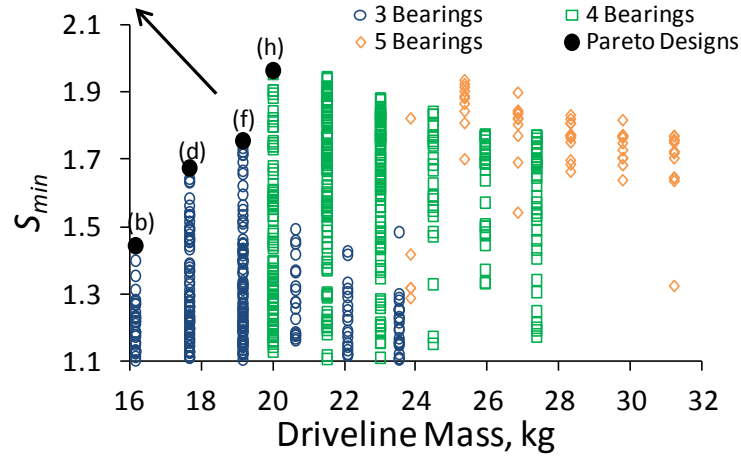


Figure 3-15. Design space with Pareto frontier: EPON 862, Blackhawk ,40°C, 1500 $\mu\epsilon$

Pareto designs from the design space (**Figure 3-15**) are shown in **Table 3-9** with the design immediately less desirable at the same driveline weight. Designs with the largest S_{min} for a given number of bearings or lamina (b,d,f,h: Pareto) illustrate the Pareto frontier tradeoffs between S_{min} and driveline weight. For a given design case (a & b or c & d, etc.), an increase in S_w corresponds to a decrease in S_b . Consider a Blackhawk driveline of laminate $[\pm\theta_4]$ with arbitrary constant geometric parameters. When the longitudinal stiffness was relatively high (lamina angle was low), S_w was high while S_b was low (**Figure 3-16a**). The opposite can be said when the lamina angle was high. In general, for a constant number of lamina, lower angles increase longitudinal stiffness and S_w , while higher angles increase circumferential stiffness and S_b . S_h was also dependent on lamina angle. Lamina angles near 15-30-deg. (**Figure 3-16a**) generate the most heat. Dynamic material response will affect the damping of the composite (self-heating), potentially varying the range of lamina angles which cause the most heating.

Table 3-9. Pareto frontier designs: EPON 862, Blackhawk, 40°C, 1500 $\mu\epsilon$

Design (b,d,f,h: Pareto)	a	b	c	d	e	f	g	h
Number of Bearings	4	4	3	3	3	3	3	3
Number of Lamina	3	3	5	5	4	4	3	3
Laminate	[$\pm 75/\pm 25/\pm 35$]	[$\pm 80/\pm 20/\pm 30$]	[$\pm 20/\pm 15/\pm 15/\pm 10/\pm 15$]	[$\pm 10/\pm 10/\pm 10/\pm 10/\pm 10$]	[$\pm 20/\pm 55/\pm 10/\pm 20$]	[$\pm 35/\pm 10/\pm 10/\pm 10$]	[$\pm 70/\pm 15/\pm 25$]	[$\pm 85/\pm 10/\pm 20$]
Temperature, °C	44	43	49	46	46	47	44	43
Critical Speed, rpm	7850	8400	7060	7200	6320	6900	5760	5940
Buckling Torque, N-m	1680	1440	1670	1460	1200	1200	1220	1060
$S_{\sigma_{1T}}$	9.34	8.52	9.67	9.07	9.73	9.59	8.39	6.96
$S_{\sigma_{1C}}$	2.25	2.05	2.32	2.18	2.34	2.30	2.02	1.68
$S_{\sigma_{2T}}$	4.62	4.51	5.19	7.86	5.89	5.82	4.18	4.38
$S_{\sigma_{2C}}$	13.0	12.7	14.4	21.9	17.0	16.2	11.9	12.4
$S_{\tau_{12}}$	3.13	2.9	2.51	2.48	2.99	2.49	2.82	2.18
S_h	1.94	1.97	1.72	1.85	1.85	1.79	1.96	1.98
S_w	1.91	2.04	1.71	1.76	1.53	1.68	1.40	1.44
S_b	2.28	1.97	2.28	2.00	1.63	1.68	1.66	1.45
S_{σ}	2.25	2.05	2.32	2.18	2.34	2.30	2.02	1.68
S_{min}	1.91	1.97	1.71	1.76	1.53	1.67	1.40	1.44
Driveline Weight, kg	19.9	19.9	19.1	19.1	17.7	17.7	16.2	16.2

S_{σ} commonly has an inverse relationship with S_b and S_w . Note that the misalignment strain of the shaft was prescribed. Use of lower angles increases the component of stress which is in the fiber direction due to misalignment, while use of higher angles causes the same result due to applied torque. The relationship between lamina angle and S_{σ} (which is rarely not σ_{1C}) can be visualized in **Figure 3-16b**, increasing from low angles and then decreasing from approximately 50-deg. This is a problem for polymer composites for which support of the reinforcing fibers in compression is a known limitation. Designs which incorporate intermediate angles such as 45-65-deg. will have a larger S_{σ} than designs which utilize 10-25-deg. or 65-85-deg. lamina. The exact range for which S_{σ} will be a maximum depends on the material properties and stress state. A design could be said to be “fully utilized” if S_{σ} , S_w , and S_b were approximately identical. This

case arises when laminate variation was able to balance all S through intelligent lamina angle choice. A design space that was not “fully utilized” could carry higher applied torque or sustain larger misalignment, with the same S_{min} through laminate variation.

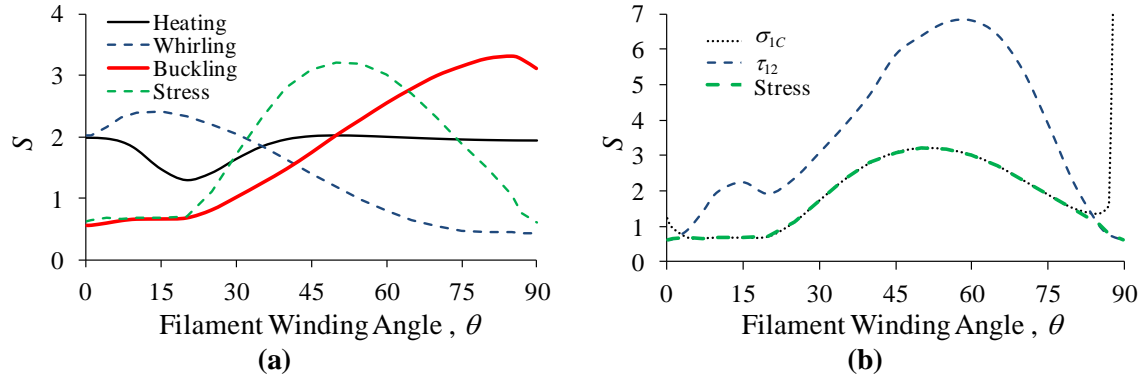


Figure 3-16. Blackhawk design considerations: four bearings, $[\pm\theta_4]$ laminate, $1500 \mu\epsilon$, 30757, 40°C

Blackhawk design analysis at $1500 \mu\epsilon$ for an EPON 862 shaft varying ambient temperature is presented in **Figure 3-17a**. S_h can be seen to decrease with increasing ambient temperature and with increasing number of layers. Ambient temperature defines the initial condition used for shaft equilibrium calculation and therefore a higher value will decrease S_h . The number of layers defines the shaft volume exposed to convective and conductive cooling. S_b decreases as the number of layers decreases. This results from a decrease in the torsional buckling stability of the shaft as the wall thickness is lessened. S_w decreases as the number of bearings are decreased (**Figure 3-17b**). The number of bearings defines the free length of the shaft used in calculating the whirl instability frequency. If the free length of the shaft is increased, the first natural frequency for the shaft is lessened or vice versa.

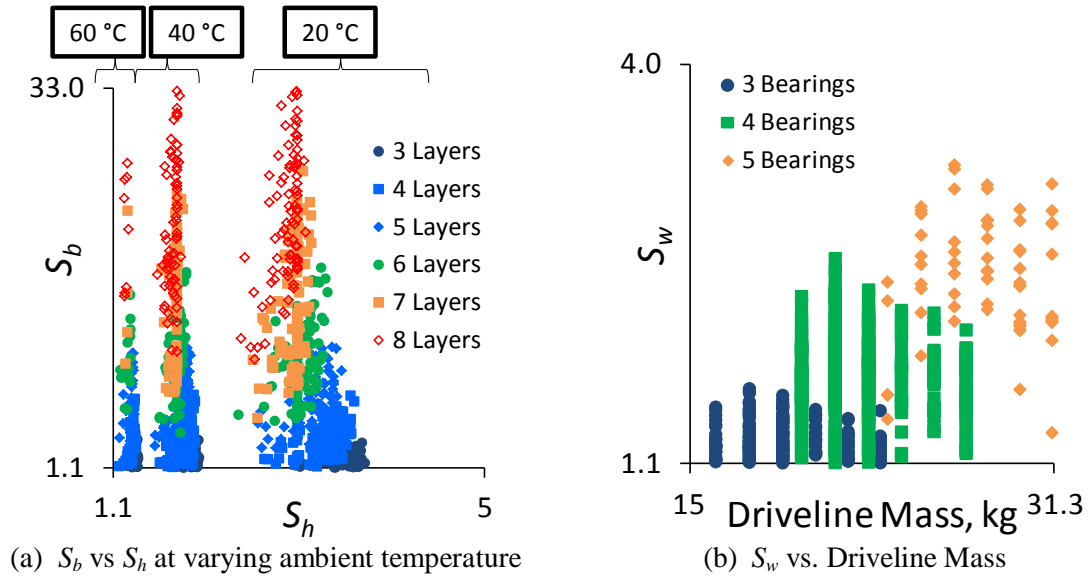


Figure 3-17. Blackhawk design analysis: 1500 $\mu\epsilon$, EPON 862, 20-40-60°C

Two parametric design studies were conducted in this investigation. The first fixes the misalignment strain to 1500 $\mu\epsilon$ and varies the ambient temperature (20-40-60°C) of an EPON 862 Blackhawk driveshaft. In order to determine which of the S was the limit on the design space, S_{min} for each design has been plotted against each S with misalignment strain held constant (**Figure 3-18**). A point representing unity (1:1) in any plot means that the specific S was S_{min} . At low ambient temperature (dark points), S_σ and S_w were the most common limiting factors, meaning that they were traded off. A laminate in this design space requires additional longitudinal stiffness to increase S_w , which decreases S_σ . The design space for high ambient temperatures (light points) was limited by S_h and S_w . S_h is limiting because of the high starting point for temperature equilibrium calculation while operating misaligned. S_b is rarely a limiting factor, suggesting that the EPON 862 Blackhawk driveline design space could be made to carry higher applied torque.

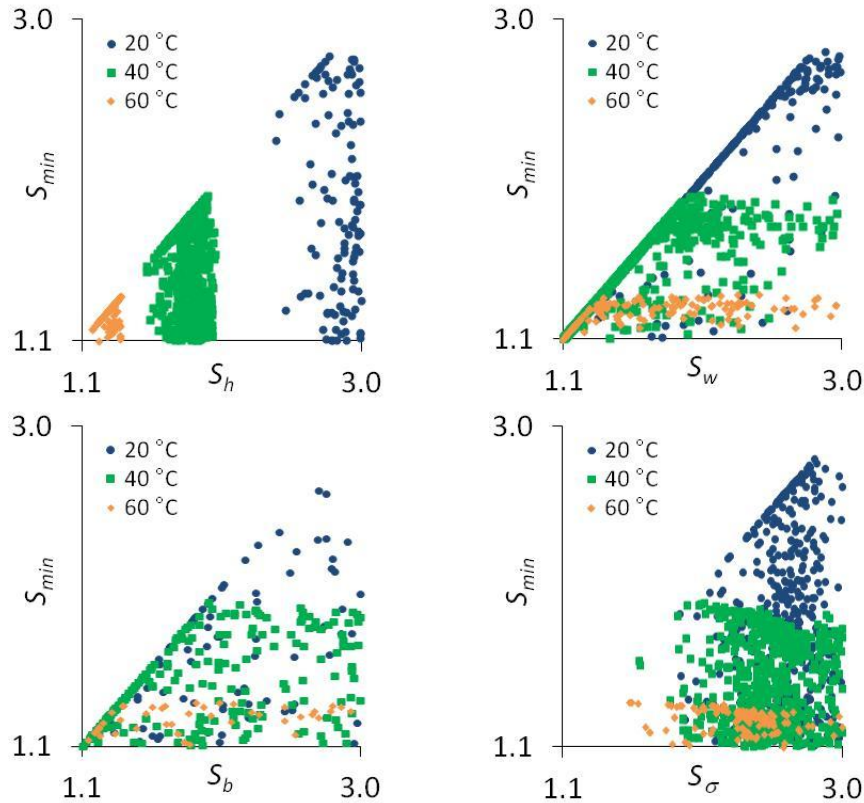


Figure 3-18. S_{min} vs. various S : Blackhawk, 1500 $\mu\epsilon$, EPON 862, 20-40-60°C

The second parametric design study fixes the ambient temperature at 60°C while the misalignment strain was varied (0-750-1500 $\mu\epsilon$) for an EPON 862 Blackhawk driveshaft (**Figure 3-19**). When the shaft misalignment was low, S_h , S_w , and S_b were limiting factors in design. RMC strength was shown to be insensitive to temperature increases leading to S_σ not being a limiting factor, instead S_w and S_b were traded off. When the misalignment was high, S_h and S_w are the limiting factors. Lower angles have been shown to increase shaft operating temperature; while in a misaligned condition, more than higher angles (**Figure 3-16a**). S_w , which desires low angles, and S_h , which desires high angles, must be traded off. S_{min} was observed to be more sensitive to the range of ambient temperature than range of misalignment.

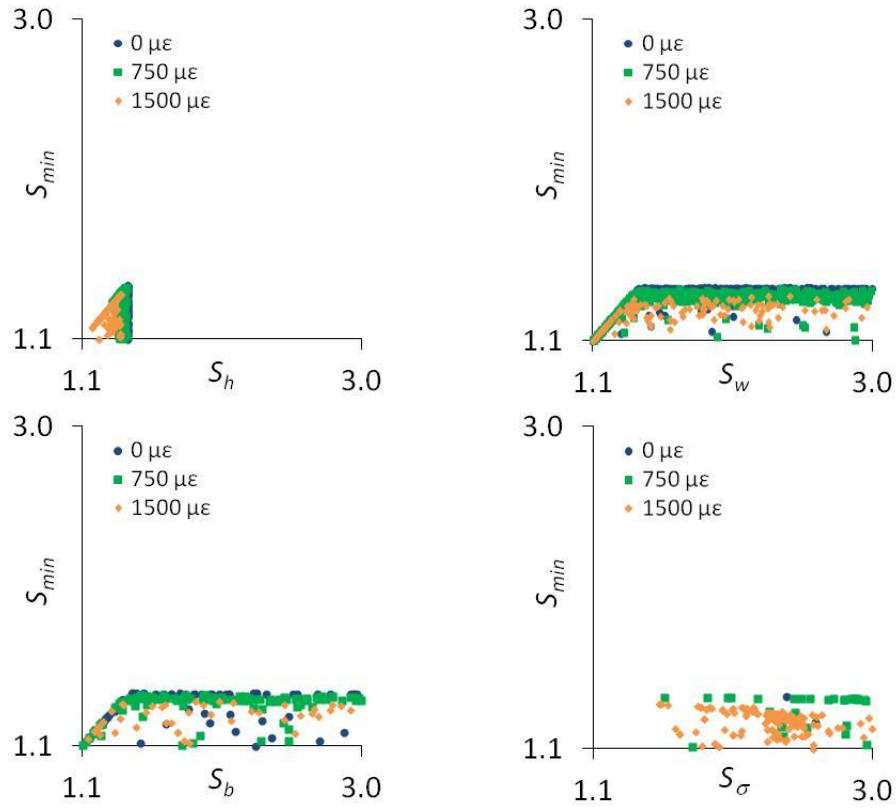


Figure 3-19. S_{min} vs. various S : Blackhawk, 60°C, EPON 862, 0-750-1500 $\mu\epsilon$

The parametric study results for a 30757 Blackhawk driveline operating at 1500 $\mu\epsilon$ varying ambient temperature (20-40-60°C) can be seen in **Figure 3-20**. At low and high ambient temperatures the design space is “fully utilized”, S_σ , S_w , and S_b are equally limiting factors. This result was not unlike the RMC design space (**Figure 3-18**), however, the low modulus and strength of FMC materials as well as their sensitivity to temperature results in S_σ being a limiter in design.

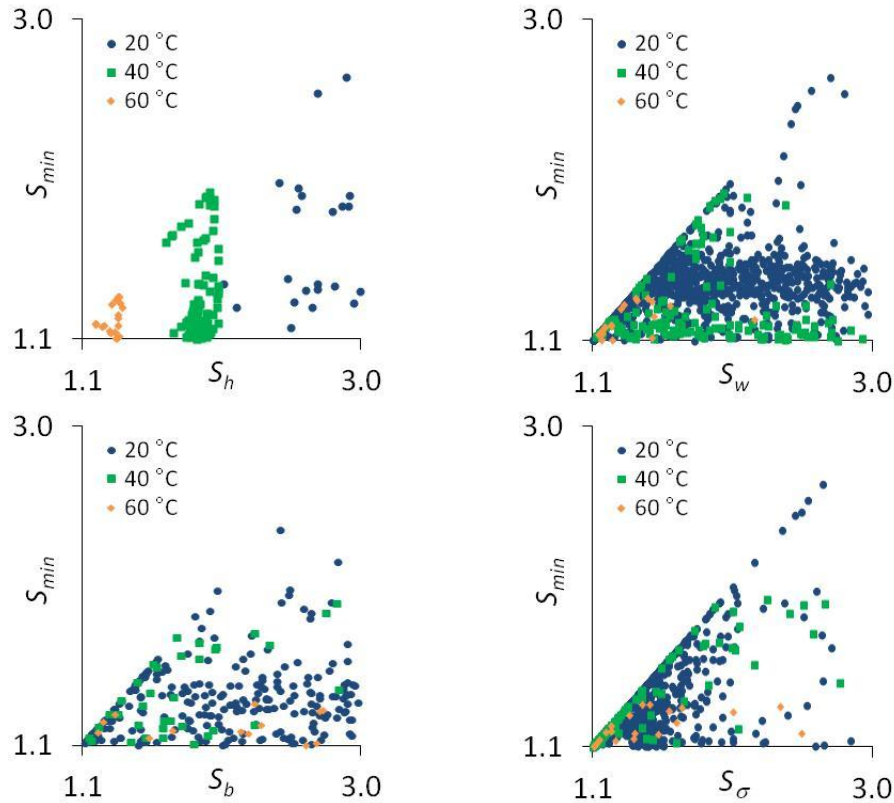


Figure 3-20. S_{min} vs. various S : Blackhawk, 1500 $\mu\epsilon$, 30757, 20-40-60°C

The parametric study results for a 30757 Blackhawk driveline operating at 60°C ambient temperature varying misalignment strain (0-750-1500 $\mu\epsilon$) can be seen in **Figure 3-21**. The design space was “fully utilized” when the misalignment strain was zero. Compared to the RMC parametric studies (**Figure 3-19**) which were rarely “fully utilized”, FMC materials have considerably lower strength at elevated temperature. S_w and S_b were traded off with S_σ when choosing laminate angles, but the feasible angle choices were limited due to low strength (angles cannot be very low or high). At high misalignment, S_w and S_σ were traded off (longitudinal stiffness, E_x , with fiber direction compression strength, F_{1c}). Compared to the RMC design case, S_h was rarely a limiter on the design space for both parametric studies. The FMC design space at high misalignment and high ambient temperature was also considerably smaller than the RMC design space. This can also be attributed to relatively lower stiffness and strength of FMCs.

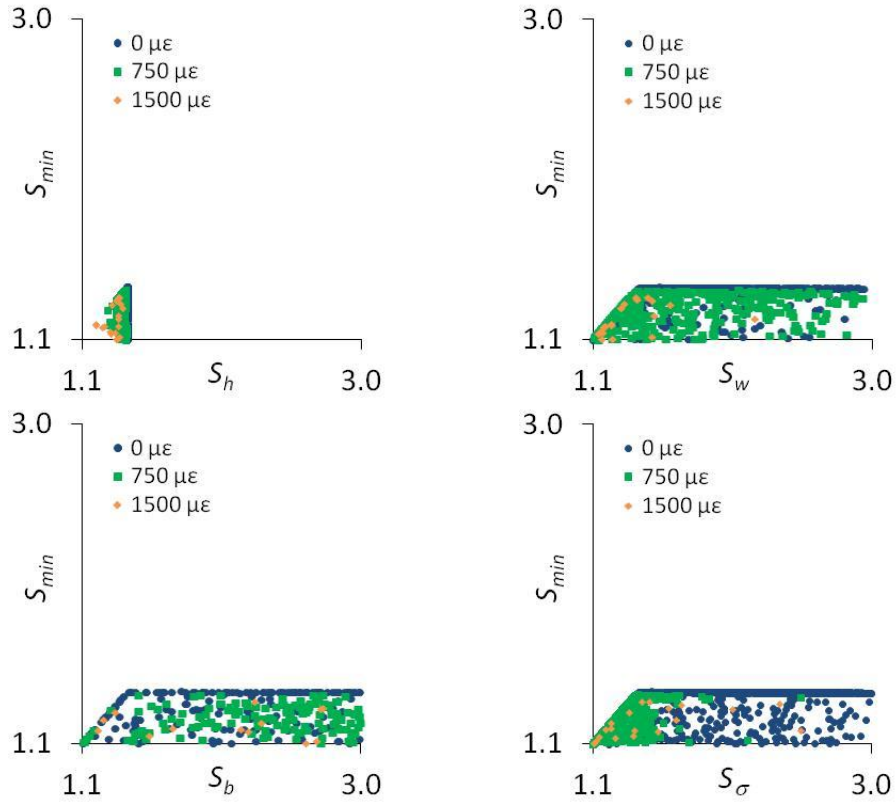


Figure 3-21. S_{min} vs. various S : Blackhawk, 60°C, 30757, 0-750-1500 $\mu\epsilon$

A three dimensional representation of the design space for a 30757 Blackhawk driveline operating at 1500 $\mu\epsilon$ and 20°C was generated with S_w vs. S_b vs. S_σ (**Figure 3-22**). The size of each block is related to the driveline mass where smaller blocks are lighter designs. The color of each block represents the operating temperature (dark to light, cold to warm). Designs that were “fully utilized” (all S traded off equally) have the lowest driveline weight (origin (1,1,1)). These designs also commonly have a lower operating temperature (darker, higher strength).

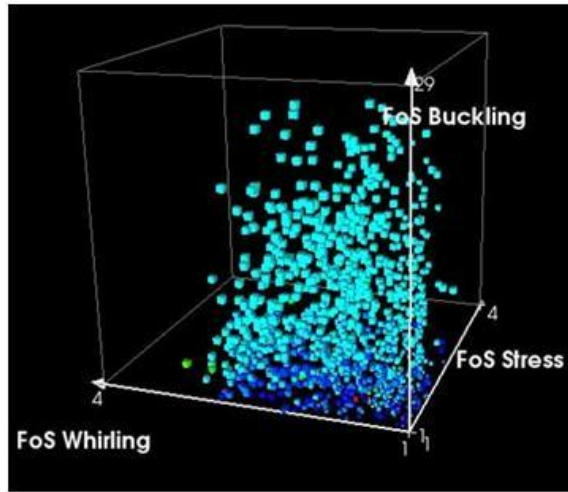


Figure 3-22. Three dimensional design space: Blackhawk, 20°C, 30757, 1500 $\mu\epsilon$

The “most preferred design”, or a design representing primarily the largest reduction in weight and secondarily the largest S_{min} for each material and parametric study are listed in **Table 3-10**. For the range of ambient temperatures and misalignment strains analyzed in this investigation, RMCs generate lighter designs with a higher S_{min} compared to the FMCs. FMC designs were less desirable due to significant strength reduction at high temperatures. The most common limiting factor was S_w and to a lesser extent S_b . When considering the driveshaft design space, S_w was a common limiting factor because of the design preference towards a lower number of bearings. The same can be said for S_b and the bias towards a lower number of lamina. S_w was the limiting factor more often than S_b because one bearing weighs more than one lamina and so bearings were more prioritized with respect to weight reduction. The weight of the most preferred driveline had an inverse relationship with increased misalignment or ambient temperature. If the driveline weight cannot be decreased, S_{min} can be seen to increase (**Figure 3-23**).

Note that stiffer FMC resins (30757 and 30917) generate lighter driveline designs than more compliant FMC resins (LF750 and 30748). Higher neat resin modulus at elevated temperatures correlates to higher lamina strength, resulting in the lightest FMC driveline being 30757 instead

of 30917 which is stiffer at room temperature. It should be noted that a “better” matrix material will have a large neat resin modulus at 21.1 °C, which does not degrade at higher temperatures. Self-heating of a composite driveshaft is known to be highly influenced by lamina damping behavior (Shan and Bakis, 2009; Henry, 2012). A “more desirable” material should exhibit less damping to avoid unstable heating, further lowering the operating temperature (raising lamina strength). Higher strength components (σ_{1C} specifically) will result in designs of reduced weight.

Table 3-10. Most preferred Blackhawk driveline design results

Material	Misalignment Strain, $\mu\epsilon$	Ambient Temperature, °C	Number of Bearings	Number of Lamina	Laminate	Operating Temperature, °C	S_{min}	Weight, kg	Limiting S
LF750	1500	60	4	4	[$\pm 45_4$]	65	1.18	21.49	(W/B/S)
	1500	40	3	5	[$\pm 35_5$]	57	1.11	19.14	(W/S)
	1500	20	3	5	[$\pm 35_5$]	40	1.15	19.14	(W/S)
	750	60	3	5	[$\pm 35/\pm 30/\pm 35_3$]	65	1.13	19.14	(W/S)
	0	60	3	4	[$\pm 40/\pm 30_3$]	60	1.17	17.65	(W/B/S)
30748	1500	60	4	3	[$\pm 55/\pm 45_2/\pm 35$]	64	1.19	19.99	(W/B/S)
	1500	40	3	4	[$\pm 40/\pm 30_3$]	55	1.19	17.65	(W/S)
	1500	20	3	4	[$\pm 40/\pm 25/\pm 30/\pm 25$]	36	1.25	17.65	(W/B/S)
	750	60	3	4	[$\pm 40/\pm 20_2/\pm 35$]	64	1.17	17.65	(W/S)
	0	60	3	4	[$\pm 40/\pm 15/\pm 20/\pm 30$]	60	1.31	17.65	(W/S)
30757	1500	60	3	4	[$\pm 35_4$]	68	1.18	17.65	(W/B)
	1500	40	3	4	[$\pm 35/\pm 25/\pm 40/\pm 35$]	47	1.21	17.65	(W/B)
	1500	20	3	3	[$\pm 60/\pm 25_2$]	26	1.21	16.15	(W/B/S)
	750	60	3	3	[$\pm 45/\pm 20/\pm 45$]	62	1.15	16.15	(W/B/S)
	0	60	3	3	[$\pm 55/\pm 15/\pm 30$]	60	1.25	16.15	(W/B/S)
30917	1500	60	4	3	[$\pm 55/\pm 50_2$]	66	1.17	19.99	(W/S)
	1500	40	3	4	[$\pm 30_2/\pm 40_2$]	57	1.19	17.65	(W/B)
	1500	20	3	3	[$\pm 60/\pm 25_2$]	26	1.21	16.15	(W/B)
	750	60	3	3	[$\pm 45/\pm 20/\pm 45$]	62	1.15	16.15	(W/S)
	0	60	3	3	[$\pm 55/\pm 15/\pm 30$]	60	1.25	16.15	(W/B)
EPON 862	1500	60	3	3	[$\pm 80/\pm 30/\pm 10$]	64	1.34	16.15	(H)
	1500	40	3	3	[$\pm 85/\pm 10/\pm 20$]	46	1.44	16.15	(W/B)
	1500	20	3	3	[$\pm 50/\pm 10/\pm 30$]	26	1.45	16.15	(W/B)
	750	60	3	3	[$\pm 75/\pm 10/\pm 25$]	61	1.39	16.15	(H/W)
	0	60	3	3	[$\pm 50/\pm 10/\pm 30$]	60	1.41	16.15	(H/W/B)
Al	0	-	4	5	-	-	-	31.3	

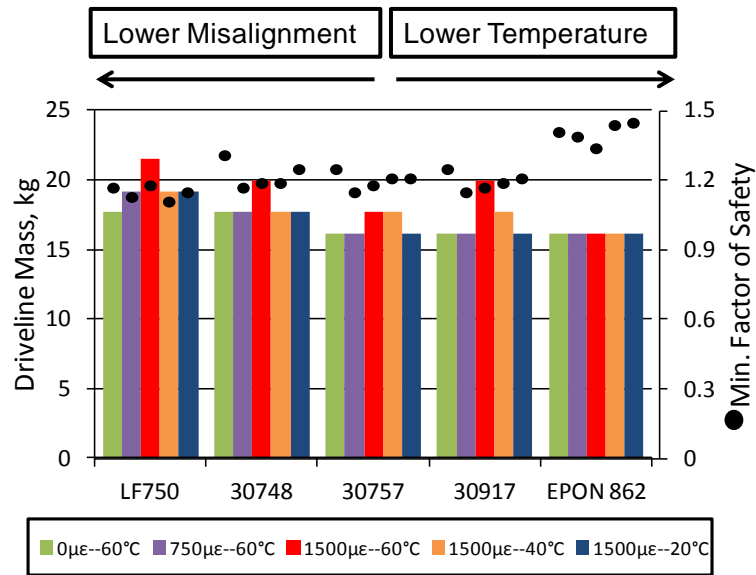


Figure 3-23. Most preferred Blackhawk driveline weight and S_{min}

3.5.2 Chinook Design Space

The most preferred design for each material and parametric study are listed in **Table 3-11** and presented graphically in **Figure 3-24** for the Chinook driveline. The Chinook driveshaft carries 5.5 times as much torque as the Blackhawk driveshaft and is approximately 15 % larger in diameter and length. Several FMC materials were unable to generate a Chinook driveline design that was lighter than the current metal driveline. Materials that are excessively compliant (LF750 or 30917 at elevated temperature) do not have the necessary strength or stiffness to increase S_{min} above 1.1. Viable FMC driveshaft designs utilize intermediate angles, which do not contribute large amounts of fiber compressive strain from shaft misalignment or applied torque. Use of RMCs reduces the weight of the composite driveline due to increased composite strength compared to FMCs, which is traded off with longitudinal and circumferential stiffness.

Table 3-11. Most preferred Chinook driveline design results

Material	Misalignment Strain, $\mu\epsilon$	Ambient Temp., $^{\circ}\text{C}$	Number of Bearings	Number of Lamina	Laminate	Operating Temperature, $^{\circ}\text{C}$	S_{min}	Weight, kg	Limiting S
LF750	1500	60			No Solution				(W/S)
	1500	40			No Solution				(W/S)
	1500	20			No Solution				(W/S)
	750	60			No Solution				(W/S)
	0	60			No Solution				(W/S)
30748	1500	60			No Solution				(S)
	1500	40	6	7	$[\pm 50_7]$	50	1.15	46.8	(W/S)
	1500	20	5	7	$[\pm 40_7]$	42	1.23	41.6	(W/B/S)
	750	60	5	8	$[\pm 45_8]$	64	1.12	43.8	(W/S)
	0	60	5	8	$[\pm 40_4/\pm 50_3/\pm 40]$	61	1.16	43.8	(W/S)
30757	1500	60	6	8	$[\pm 50_8]$	67	1.10	49.0	(S)
	1500	40	5	6	$[\pm 55/\pm 45_5]$	45	1.14	39.4	(W/S)
	1500	20	4	7	$[\pm 35_3/\pm 30_4]$	38	1.15	36.4	(W/B)
	750	60	5	8	$[\pm 40_4/\pm 50_4]$	62	1.17	43.8	(W/S)
	0	60	5	7	$[\pm 40/\pm 45_6]$	61	1.21	41.6	(W/S)
30917	1500	60			No Solution				(W/S)
	1500	40			No Solution				(W/S)
	1500	20	5	5	$[\pm 60/\pm 45_4]$	35	1.15	37.2	(W/B/S)
	750	60	6	8	$[\pm 55_8]$	65	1.12	49.0	(W/S)
	0	60	4	8	$[\pm 65/\pm 30/\pm 20/\pm 30/\pm 25/\pm 30_3]$	61	1.16	38.6	(W/S)
EPON 862	1500	60	4	4	$[\pm 70/\pm 15_2/\pm 55]$	66	1.21	29.8	(W/B)
	1500	40	4	4	$[\pm 75/\pm 10_2/\pm 55]$	46	1.24	29.8	(W/B/S)
	1500	20	4	4	$[\pm 75/\pm 10_2/\pm 55]$	26	1.24	29.8	(W/B/S)
	750	60	4	4	$[\pm 65/\pm 10_2/\pm 60]$	62	1.23	29.8	(W/B/S)
	0	60	4	4	$[\pm 70/\pm 10_2/\pm 55]$	60	1.24	29.8	(W/B/S)
Al	0	-	6	6	-	-	-	60.1	

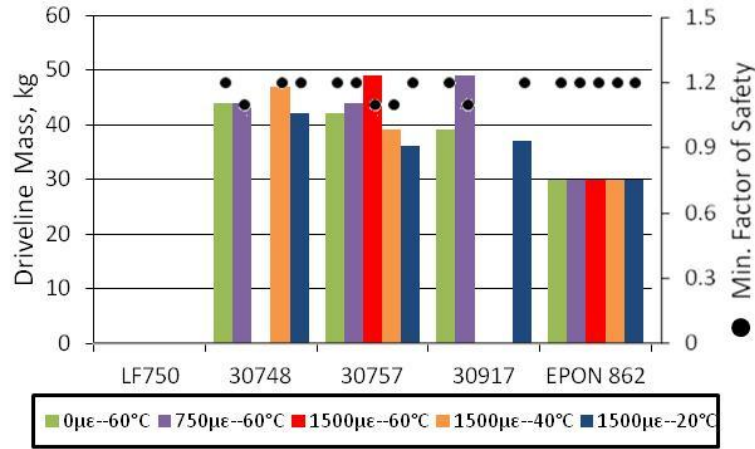


Figure 3-24. Most preferred Chinook driveline weight and S_{min}

3.5.3 Operating Frequency and Torque Variation

S_w was very often a limiting factor for the investigated design spaces (**Table 3-10** and **Table 3-11**). Each design with this restraint could be made to have a higher S_w by operating at a slower speed. If the driveshaft operates at a sufficiently reduced speed, additional bearings may be potentially eliminated. The secondary effect of reducing the driveshaft speed, however, is that the transmitted power through the driveshaft to the tail rotor is reduced because power is a linear function of applied torque (Q_b , N-m) and operating frequency (f , Hz). If the applied torque was increased by the same linear factor (ξ) that operating frequency was reduced by, the transmitted power could be kept constant (**Equation 3-55**)

$$\text{Power} = Q_b 2\pi f = \left(\frac{Q_b}{\xi}\right) (2\pi f \xi) \quad (3-55)$$

Formulation of a new design space was done for a Blackhawk driveline operating at 1500 µε misalignment and 60°C ambient temperature. For each material, the constraint $0.5 \leq \xi \leq 1.5$ was implemented allowing the operating frequency to vary between 50 and 150 % of the baseline value (at which the applied torque was adjusted inversely). Allowing flexibility in the operating

frequency and applied torque of the driveshaft allows for a different most preferred design by either increasing the S_{min} or by decreasing the driveline weight (**Table 3-12**). In most cases, the operating frequency of the driveshaft was reduced, facilitating a reduction in the number of bearings. Interestingly, LF750 was unable to decrease the number of bearings or lamina by decreasing operating frequency (due to low stiffness and strength). Instead the applied torque was decreased, raising S_{σ} by decreasing fiber direction stress amplitude.

A number of driveline changes occurred to compensate for the increased torque of the remaining materials under investigation. The increased stress-state in the material was accommodated through use of intermediate lamina angles, and critical buckling torque was raised by higher wall thickness. Fully utilized designs, such as that for 30757 and EPON 862, were able to reduce the number of bearings to two, significantly reducing the driveline weight. The 30748 and 30917 driveline design space, for which the neat resin modulus was severely reduced at elevated temperatures, was not fully utilized. The considerable reduction in strength and longitudinal modulus limited the viable lamina angles to only those which produce the smallest magnitude fiber direction stress (~50-deg.).

Table 3-12. Blackhawk most preferred design with and without allowed variation in ξ : 1500 $\mu\epsilon$, 60°C

Material	LF750		30748		30757		30917		EPON 862	
ξ	1	1.1	1	0.5	1	0.5	1	0.6	1	0.5
No. of Bearings	4	4	4	3	3	2	4	3	3	2
No. of Lamina	4	4	3	5	4	5	3	5	3	3
Laminate	$[\pm 45_4]$	$[\pm 45_4]$	$[\pm 55/\pm 45_2/\pm 35]$	$[\pm 55_5]$	$[\pm 35_4]$	$[\pm 40_4/\pm 45]$	$[\pm 55/\pm 50/\pm 50]$	$[\pm 50_5]$	$[\pm 80/\pm 30/\pm 10]$	$[\pm 85/\pm 15/\pm 45]$
Temp., °C	65	66	64	64	68	64	66	68	63	63
f_{crit} , rpm	5430	5450	5000	2400	4850	2330	4830	3220	5660	2810
Q_{crit} , N-m	1050	1030	870	2230	887	1840	990	3190	1010	2000
$S \sigma_{1T}$	33.2	36.2	21.1	20.6	25.9	18.9	22.0	23.3	7.77	6.01
$S \sigma_{1C}$	1.18	1.28	1.19	1.16	1.38	1.18	1.22	1.20	1.83	1.42
$S \sigma_{2T}$	6.15	6.60	4.30	3.19	2.16	3.91	2.79	2.96	4.27	3.01
$S \sigma_{2C}$	13.5	14.4	9.48	7.25	4.28	8.40	5.96	6.34	12.0	8.78
$S \tau_{12}$	3.46	3.43	4.45	4.84	2.31	3.24	1.41	1.34	2.71	1.83
S_h	1.30	1.29	1.34	1.33	1.25	1.34	1.28	1.25	1.34	1.36
S_w	1.32	1.20	1.22	1.16	1.18	1.13	1.17	1.30	1.37	1.37
S_b	1.43	1.57	1.19	1.52	1.21	1.26	1.35	2.61	1.38	1.36
S_σ	1.18	1.28	1.19	1.16	1.38	1.18	1.22	1.20	1.83	1.42
S_{min}	1.18	1.20	1.19	1.16	1.18	1.13	1.17	1.20	1.34	1.36
Driveline Weight, kg	21.5	21.5	20.0	19.1	17.7	15.3	20.0	19.1	16.2	12.3

Chapter 4

Discrete Undulation Two Dimensional DIC

This chapter focuses on studying the effect of discrete undulation in flat specimens. Fiber direction compressive strength (σ_{1C}) was shown to be a common limiting factor in driveshaft design (**Chapter 3**). The combination of undulated fiber architecture inherent in filament wound composites and compliant matrix (especially at high temperatures) produces unique challenges in the prediction of modulus and strength using laminated composite theories. In order for an appropriate value of fiber direction compressive strength to be applied in an optimization strategy, the micromechanical mechanisms related to compressive failure should be well understood.

In the current investigation, full field strain measurements were used to evaluate local strain distributions in the region of a 0-deg. undulated lamina in a $[0_n/90_n]_s$ laminate ($n=2,4,6$) and a 30-deg. undulated lamina in a $[30_n/-60_n]_s$ laminate ($n=2,4$). Specimens were manufactured with carbon fibers, various amplitudes of undulation, and matrix materials with three different moduli of elasticity. Full-field strains were measured on the free edge and across the width of the compressively loaded specimens using two-dimensional digital image correlation (DIC). Based on these measurements, the onset of material failure could be observed in many cases.

Experimental measurements of composite longitudinal modulus and strength were used to validate several modeling approaches. A two and three dimensional analytical homogenization approach based on CLT was used to model composite modulus. Composite strength was determined with stress based micromechanics analyzing lamina level stress at every location in the laminate. Investigating composite laminates which contain two planes of rotation (anisotropic lamina) where the fiber reinforcement is rotated in- and out-of-plane required the development of

a novel three dimensional homogenization scheme. Included equations fill that gap in the literature.

4.1 Discrete Undulation Test Method

Specimens were tested in stroke control on a servo-hydraulic test frame at an actuator rate of 1.27 mm/min. A 89-kN load cell was used to measure load. Two dimensional DIC (Vic-2D Correlated Solutions) was used to measure surface displacements. Two Point Grey Research (Richmond, B.C. Canada) GRAS-50S5M digital cameras were used to acquire images simultaneously on opposite sides of the specimen (either thickness or width). A step size of 15 and a subset of 30 were used during image correlation. A strain filter size of 5 and Lagrange tensor type were used. The area of interest was nominally 25.4 mm wide by 25.4 mm tall. For the GRAS-50S5M (2448×2048 px) the spatial resolution was 96×81 px/mm.

Model 647.10A hydraulic wedge grips were used to compressively load specimens through combined shear traction and end loading. The upper and lower hydraulic wedge grips were kept aligned by a bracket attached via tapped ports on the side of each wedge grip. The alignment bracket restrained the wedge grips from rotating with respect to one another, imparting undesirable torsional loading to the specimen. Glass/epoxy buffer strips were placed between the specimen and the grips (i.e., not bonded to the specimen) to prevent grip damage from being induced in the specimen. ASTM D 3410 was referenced in determining the minimum specimen gage length to avoid global buckling of the specimen. Laminate properties for gage length estimations were taken from Henry (2012) (**Table 4-1**). A florescent lamp was used to provide area illumination to the speckled surface of the sample in the area of interest. Cameras were placed approximately 50 cm from the test sample, away from common walkways. Nikon 28 mm – 105 mm focal length lenses were used in focusing the image of the sample. Photographs of the

set-up for thickness-side measurements and a schematic of width-side measurements are provided in **Figure 4-1**. Special care was taken to place the undulated region at the exact center of the gage length. The undulation in $[30_n/-60_n]_s$ specimens can be seen to traverse the width side of the specimen diagonally. Care should be taken in specimen design such that the gage length calculation takes into account the extra length necessary for the undulated region to remain not gripped during testing.

Table 4-1. Specimen gage lengths utilizing ASTM D 3410.

Material system	Gage length, mm				
	$[0_2/90_2]_s$	$[0_4/90_4]_s$	$[0_6/90_6]_s$	$[+30_2/-60_2]_s$	$[+30_4/-60_4]_s$
LF750	12.7	13.9	17.2	25.2	28.5
DPRN 30917	9.8	10.9	13.3	24.5	25.5
EPON 862	17.4	22.0	29.0	32.1	36.6

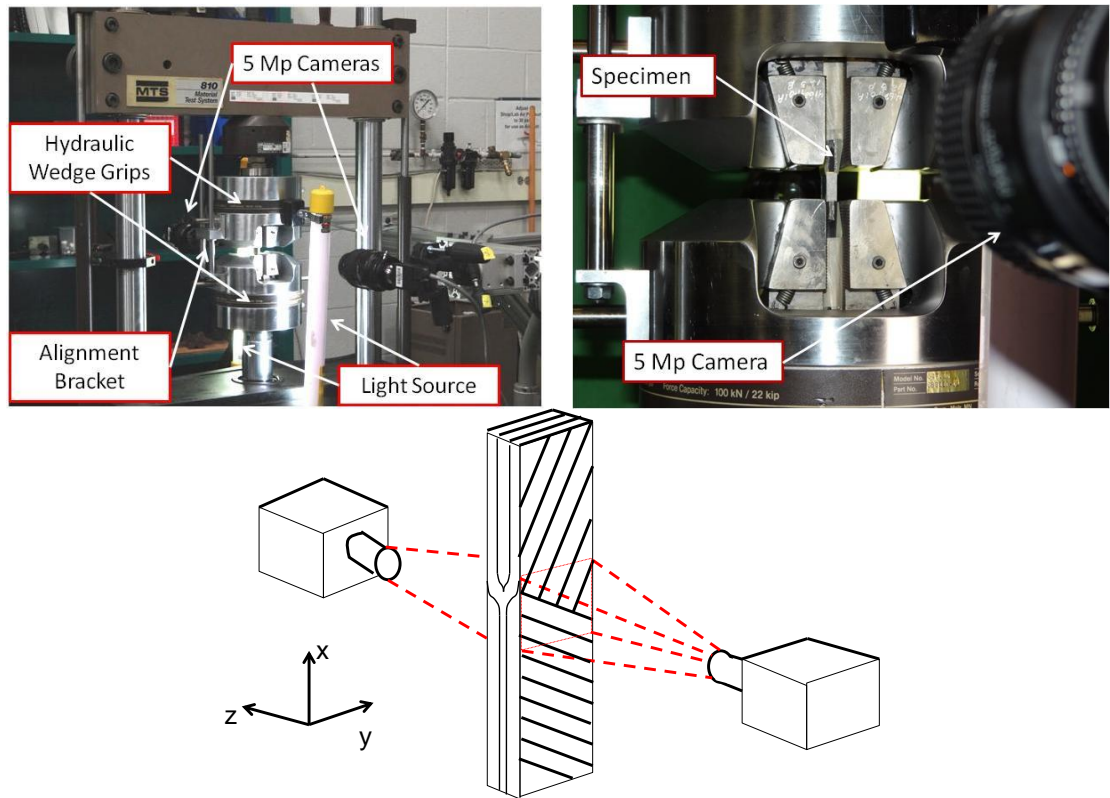


Figure 4-1. Undulated specimen compression test set-up

4.2 Discrete Undulation Test Results

Figure 4-2 shows representative longitudinal strain fields for compressively loaded $[0_n/90_n]_s$ specimens with various undulation amplitudes. In all the DIC images, the loading direction is horizontal, and the longitudinal stress at which the images were obtained was roughly 50% of the ultimate strength. The dark dashed line represents the path of the undulating 0-deg. lamina (inner lamina of the laminate on the left and the outer lamina of the laminate on the right). The location of the highest longitudinal strain (i.e., largest negative strain, highlighted with a light dashed circle) typically coincides with the location where the 0-deg. lamina begins to subduct under the 90-deg. lamina, in the underlying 90-deg. lamina. The region of lowest longitudinal strain (i.e., least negative or sometimes positive strain, highlighted with a light dashed rectangle) is typically located in the 90-deg. lamina near the point where the 0-deg. lamina meet at the laminate midplane.

Specimens with the largest undulation amplitude (i.e., $n=6$) show the variations in the longitudinal strain field with the best clarity. It was observed that there was high strain in the 0-deg. lamina where the 0-deg. lamina begin to subduct under the 90-deg lamina. As will be discussed later in this paper, such strain concentrations are important to the failure process of $[0_n/90_n]_s$ specimens. FMC specimens show this feature most readily because the unsupported length was about two times the undulation length. This places the undulated material sufficiently far away from the wedge grips to ensure no influence by grip-related strain disturbances. Due to the considerable compressive strength of RMCs, the unsupported length was reduced to a value that superposed grip-related strain disturbances with undulation-related strain disturbances.

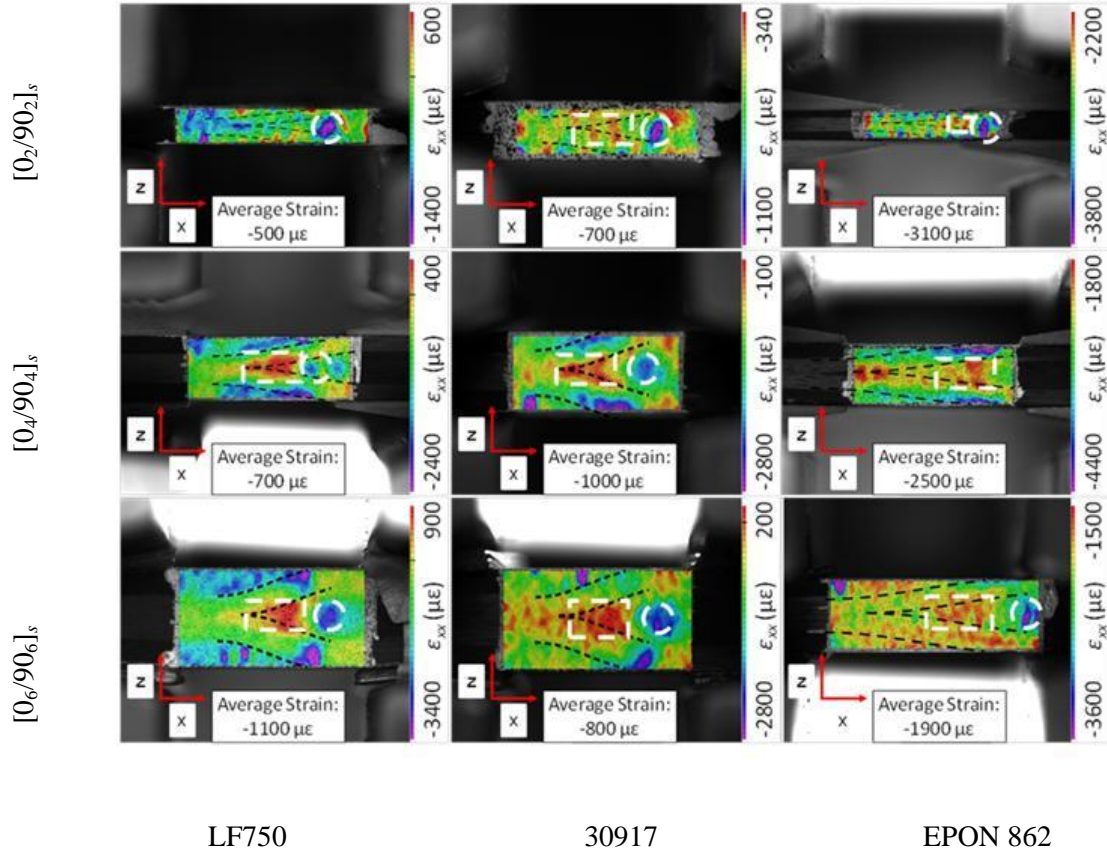


Figure 4-2. Longitudinal normal strain, ϵ_{xx} , in $[0_n/90_n]_s$ specimens at 50% of ultimate (thickness-side view)

Similar trends can be seen in the out-of-plane normal strain, ϵ_{zz} , where the highest strain (i.e., most positive strain; highlighted by light dashed circle) occurs in the middle 90-deg lamina where the 0-deg lamina begin to subduct (**Figure 4-3**). The lowest strain (negative strain; light dashed rectangle) also occurs in the middle 90-deg. lamina, near where the 0-deg. lamina meet at the midplane. Further increase in compressive load causes the localization of high out-of-plane strains, ϵ_{zz} , near the interface between the 0-deg. and 90-deg. lamina. Even in laminates without undulated lamina, the existence of strain concentrations where lamina interfaces intersect free edges is well known (Herakovich et al., 1985). The 30917 $[0_4/90_4]_s$ out-of-plane strain field in

Figure 4-3 features an early manifestation of this phenomenon. In general, specimens with larger undulation amplitude experience greater out-of-plane strains.

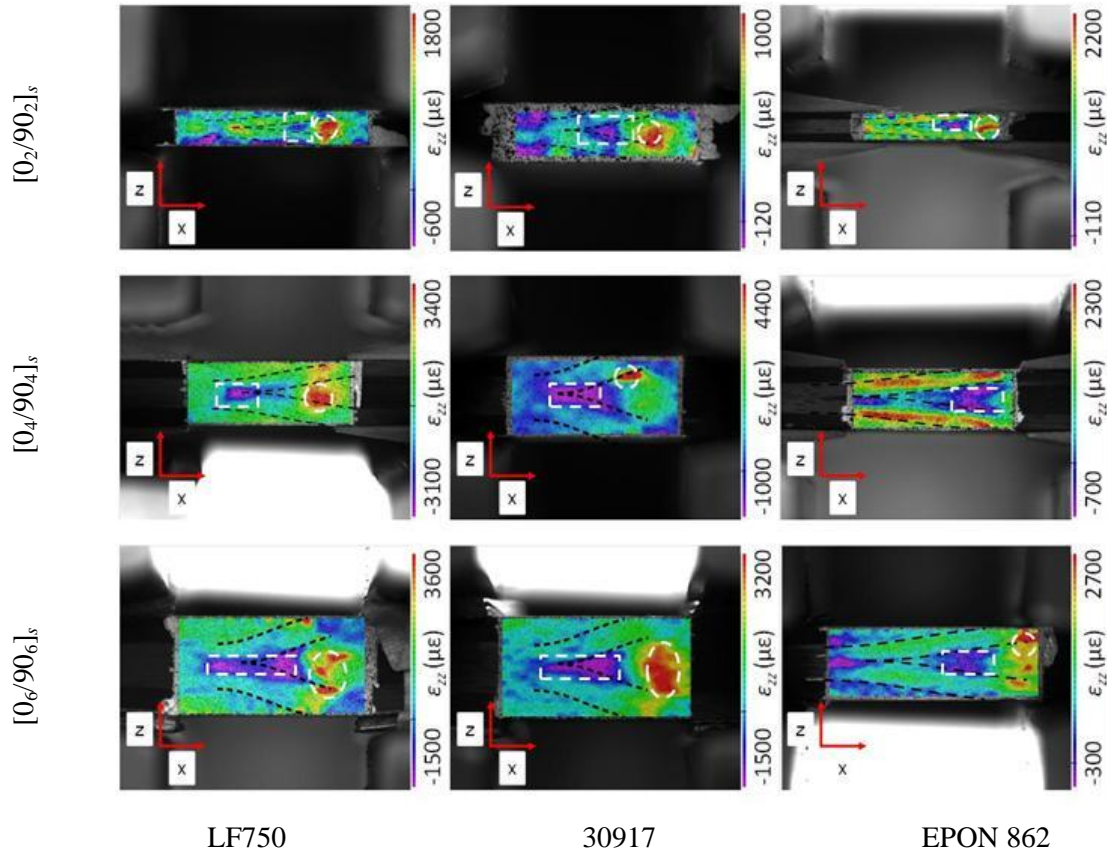


Figure 4-3. Out-of-plane normal strain, ϵ_{zz} , in $[0_n/90_n]_s$ specimens at 50% of ultimate (thickness-side view).

Out-of-plane tensor shear strain, ϵ_{xz} , was anti-symmetric about the midplane of the laminates, as may be expected, shown for $[0_6/90_6]_s$ and $[30_4/-60_4]_s$ specimens in **Figure 4-4** for brevity. This shear strain component was highest along the lamina interfaces, where mismatched lamina properties can be expected to cause high strains. The shear strain was higher in the $[30_4/-60_4]_s$ laminate than in the $[0_6/90_6]_s$ laminate, and was higher in softer resins than in stiffer resins. The latter result was expected, as a more compliant composite material will have a larger strain response at a given fraction of ultimate.

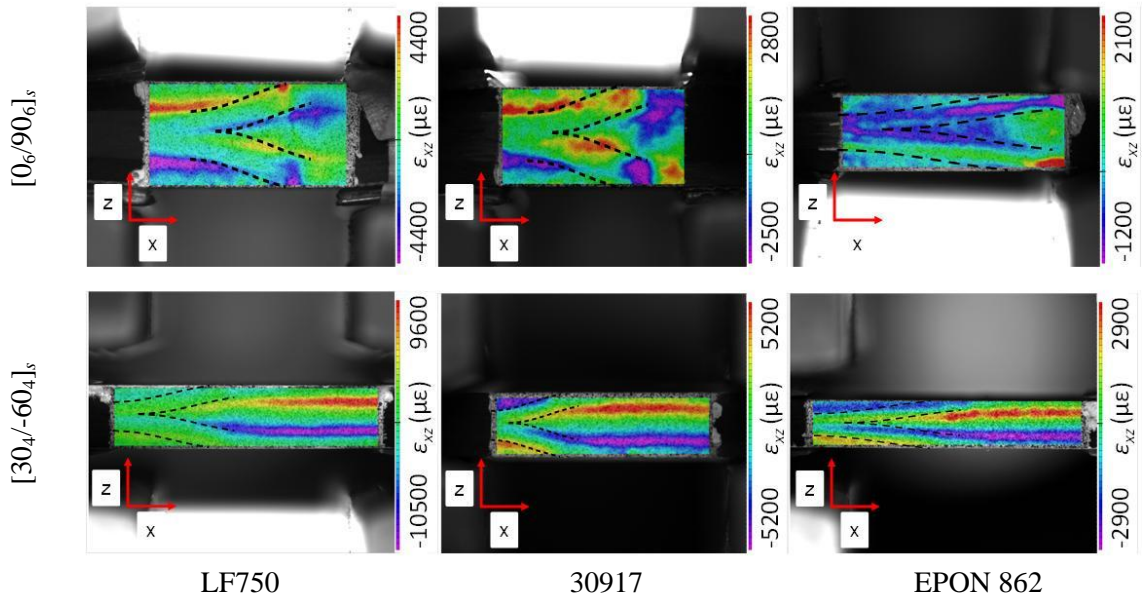


Figure 4-4. Out-of-plane tensor shear strains, ϵ_{xz} , in $[0_6/90_6]_s$ and $[30_4/-60_4]_s$ specimens at 50% of ultimate (thickness-side view).

DIC results for $[30_n/-60_n]_s$ laminates showed similar longitudinal (**Figure 4-5**) and out-of-plane normal (**Figure 4-6**) strain field response compared to the $[0_n/90_n]_s$ tests. That is, the highest magnitude strains were observed in the middle 60-deg. lamina where the 30-deg. surface lamina begin to subduct (light dashed circle). The lowest magnitude strains were seen in a broad area near where the 30-deg. lamina meet at the midplane (light dashed rectangle). As expected, greater undulation amplitude and matrix material compliance increase the strain amplitude in both the longitudinal and out-of-plane directions. The out-of-plane normal strain field also shows high magnitude concentrations at the lamina interfaces, as seen in the $[0_n/90_n]_s$ specimens.

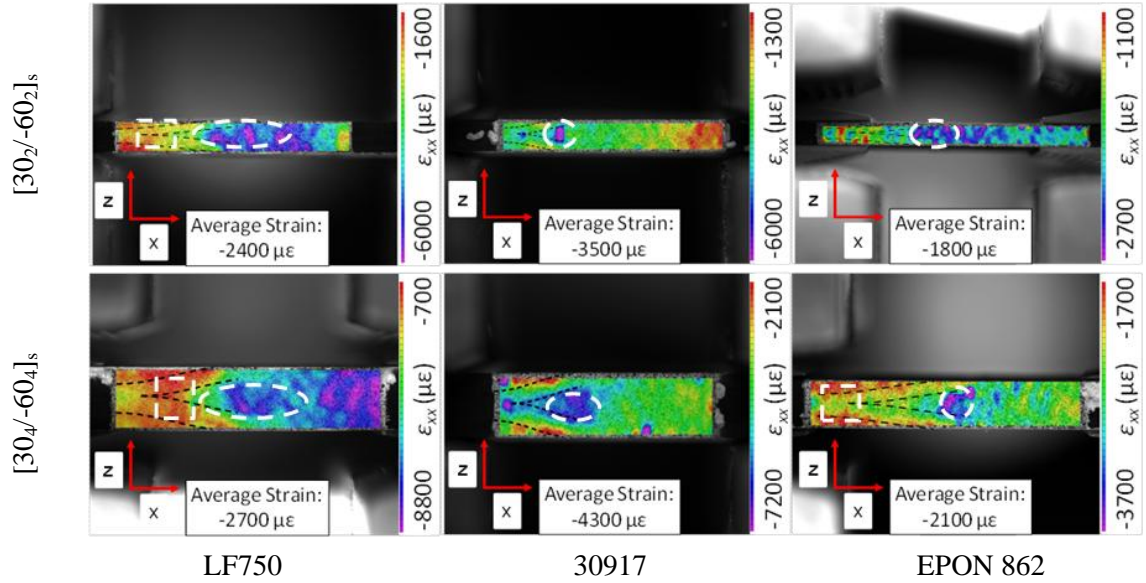


Figure 4-5. Longitudinal normal strains, ϵ_{xx} , in $[30_n/-60_n]_s$ specimens at 50% of ultimate.

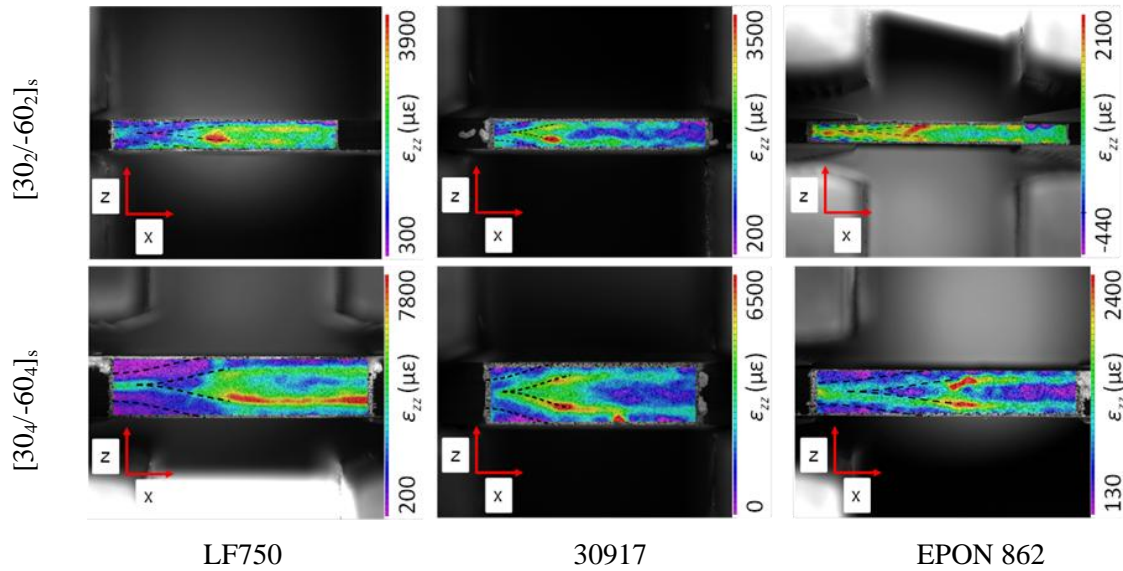


Figure 4-6. Out-of-plane normal strains, ϵ_{zz} , in $[30_n/-60_n]_s$ specimens at 50% of ultimate (thickness-side view).

Longitudinal stress-strain curves were observed to be approximately linear for specimens without undulation (**Figure 4-7**). Each point plotted in the stress-strain graphs represents the average value of strain across the undulated region of the specimen. The highest value of stress

plotted for the non-undulated specimens corresponded with failure near the grip for non-undulated specimens. For the undulated specimens, the highest value of longitudinal stress plotted corresponded to fiber microbuckling away from the grips. Increasing the undulation amplitude ($n=2 \rightarrow 6$) decreases both the strength and the modulus compared to the non-undulated case. Several differences between FMC and RMC response due to fiber undulation can be observed in **Figure 4-7**. The strength difference between specimens with and without undulation can be seen to be greater for FMC specimens compared to RMC specimens. The difference in modulus and strength between no undulation and $n=2$ was also much greater than the difference between $n=4$ and $n=6$, suggesting a diminishing effect of undulation amplitude beyond $n=2$. Fiber undulation also causes moderate non-linearity in the stress strain curves in FMCs but not in RMCs.

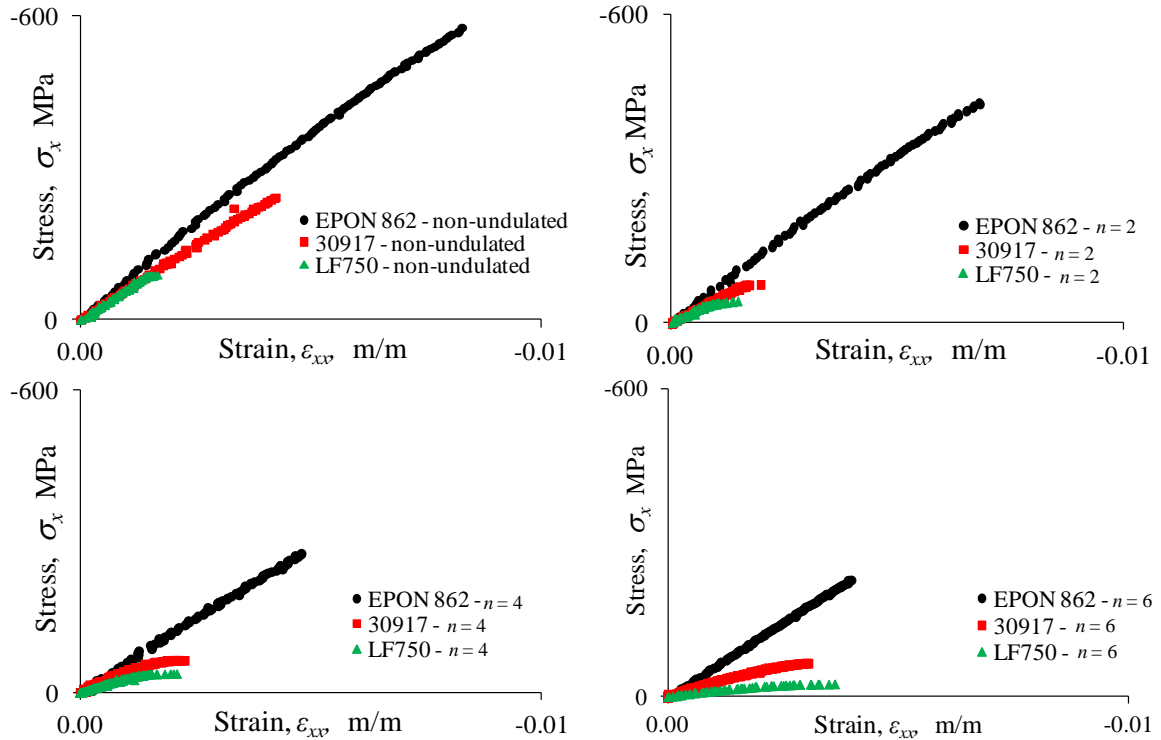


Figure 4-7. Longitudinal stress vs. longitudinal strain results: LF750, 30917, EPON 862

Average test results are summarized in **Table 4-2**. The longitudinal modulus, E_x , is based on a linear fit to the 1000 – 2000 $\mu\epsilon$ strain range and the longitudinal strength, σ_x , is the highest stress level achieved. E_x and σ_x results were normalized to a fiber volume fraction, V_f , of 50% based on thickness. Considering all cases with an undulation amplitude/length ratio of 0.1, the average longitudinal modulus of elasticity in the undulation region decreases by approximately 43%, 28%, and 3% in laminates with LF750, 30917, and EPON 862 matrices, respectively, relative to the corresponding non-undulated materials. The out-of-plane Poisson's ratio, ν_{xz} , increased with undulation amplitude.

Table 4-2. Average compressive modulus (E_x) and Strength (σ_x) results

Material	Laminate	$h_u L_u$	E_x , GPa	C_v , %	σ_x , MPa	C_v , %	ν_{xz}	C_v , %
LF750 – Non-undulated	$[0_2/90_2]_s$	-	56	8.6	-82*	18	0.47	14
	$[0_2/90_2]_s$	0.10	32	17	-42	12	0.77	7.3
LF750 – Undulated	$[0_4/90_4]_s$	0.17	25	9.0	-37	14	0.89	24
	$[0_6/90_6]_s$	0.23	12	20	-28	5.0	0.99	18
	$[30_2/-60_2]_s$	0.10	3.8	10	-26	3.6	0.70	10
	$[30_4/-60_4]_s$	0.17	3.8	19	-26	7.3	0.69	9.4
	$[30_4/-60_4]_s$	0.17	3.8	19	-26	7.3	0.69	9.4
30917 – Non-undulated	$[0_2/90_2]_s$	-	61	1.5	-244*	0.9	0.40	5.9
	$[0_2/90_2]_s$	0.12	44	5.2	-70	8.2	0.66	1.6
30917 – Undulated	$[0_4/90_4]_s$	0.19	30	14	-67	6.9	0.87	4.7
	$[0_6/90_6]_s$	0.26	26	12	-60	9.0	0.76	8.1
	$[30_2/-60_2]_s$	0.12	9.7	9.1	-55	5.2	0.42	6.3
	$[30_4/-60_4]_s$	0.19	7.2	18	-55	2.9	0.45	7.9
	$[30_4/-60_4]_s$	0.19	7.2	18	-55	2.9	0.45	7.9
EPON 962 – Non-undulated	$[0_2/90_2]_s$	-	60	1.6	-490*	7.7	0.27	21
	$[0_2/90_2]_s$	0.06	59	3.5	-324	8.0	0.49	11
EPON 962 – Undulated	$[0_4/90_4]_s$	0.08	54	6.7	-258	13.4	0.49	5.0
	$[0_6/90_6]_s$	0.10	51	1.9	-211	4.9	0.46	7.0
	$[30_2/-60_2]_s$	0.06	22	8.0	-83	6.2	0.41	56
	$[30_4/-60_4]_s$	0.08	23	9.8	-81	8.2	0.38	8.0
	$[30_4/-60_4]_s$	0.08	23	9.8	-81	8.2	0.38	8.0

*Strength influenced by grip failure.

The longitudinal modulus of unidirectional specimens is commonly considered a fiber dominated property. Thus, as expected, specimens with no fiber undulation (undulation amplitude/ length=0) had approximately the same modulus regardless of the matrix material (**Figure 4-8**). In the presence of undulation, specimens with a stiffer matrix material retained a larger percentage of the non-undulated modulus. This result suggests that fiber undulation causes

E_x to be more highly influenced by the matrix, possibly through the contributions of the out-of-plane shear modulus of the material and the out-of-plane fiber orientation in the undulation (Jensen and Pai, 1993; Bogetti et al., 1992).

For the range of undulation amplitude/length ratios investigated, both polyurethane resins showed little change in compressive strength. It is hypothesized that changes in strength come from a change in the failure mode caused by the introduction of undulation (Bogetti et al., 1992). In the non-undulated case, the failure mode is likely to be fiber microbuckling or kinking. As undulation is introduced in increasing amplitudes, the failure mode is increasingly influenced by out-of-plane shear, which reduces the longitudinal strength of the material. The undulation amplitude/length ratios obtained in the FMC materials appear to be too large to observe the transition in failure mode.

The $[30_n/-60_n]_s$ longitudinal modulus and strength are largely independent of the undulation geometry (**Figure 4-8**). This result suggests that the off-axis orientation of the fibers in the plane of the laminate (30-60 deg.) was more detrimental to the longitudinal properties when compared to the additional off-axis orientation of the fibers (5-20 deg.) in the undulated region. For the same undulation size and fiber volume fraction, stiffer matrix systems are stiffer and stronger than their more compliant counterparts.

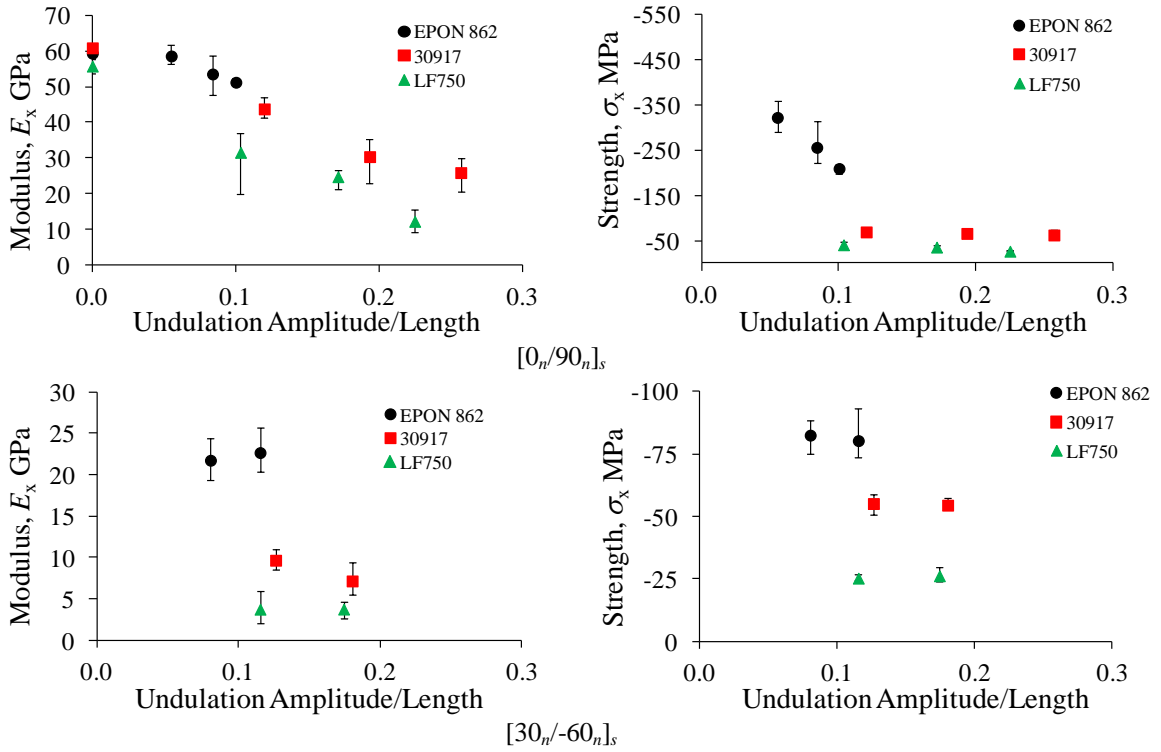


Figure 4-8. Compressive modulus and strength versus undulation amplitude-to-length ratio

DIC data obtained from the thickness-side view also facilitated understanding of the failure mode associated with undulated fibers. A typical stress strain curve for an LF750 $[0_6/90_6]_s$ specimen along with thickness-side DIC images at three stages of loading (Stage A, B, C) are shown in **Figure 4-9**. At the approximate onset of non-linearity (Stage A), the strain fields resemble those shown previously.

Stage B represents a significant change in the stress-strain behavior of the specimen. Damage onset was indicated by large out-of-plane normal strain, ε_{zz} , which signifies delamination in the regions highlighted by a light dashed circle. This damaged area increases the longitudinal strain, ε_{xx} , in the undulating fiber. With the out-of-plane stiffness now reduced due to delamination, the misalignment of the fiber increases until microbuckling occurs. Microbuckling can be observed at Stage C where the undulating fibers have displaced in the positive z -direction within the light

dashed circle. Strain components ϵ_{xx} , ϵ_{zz} , and ϵ_{xz} are approximately 4, 10, and 8 times higher, respectively, near the microbuckled area at Stage C versus the same area at Stage A.

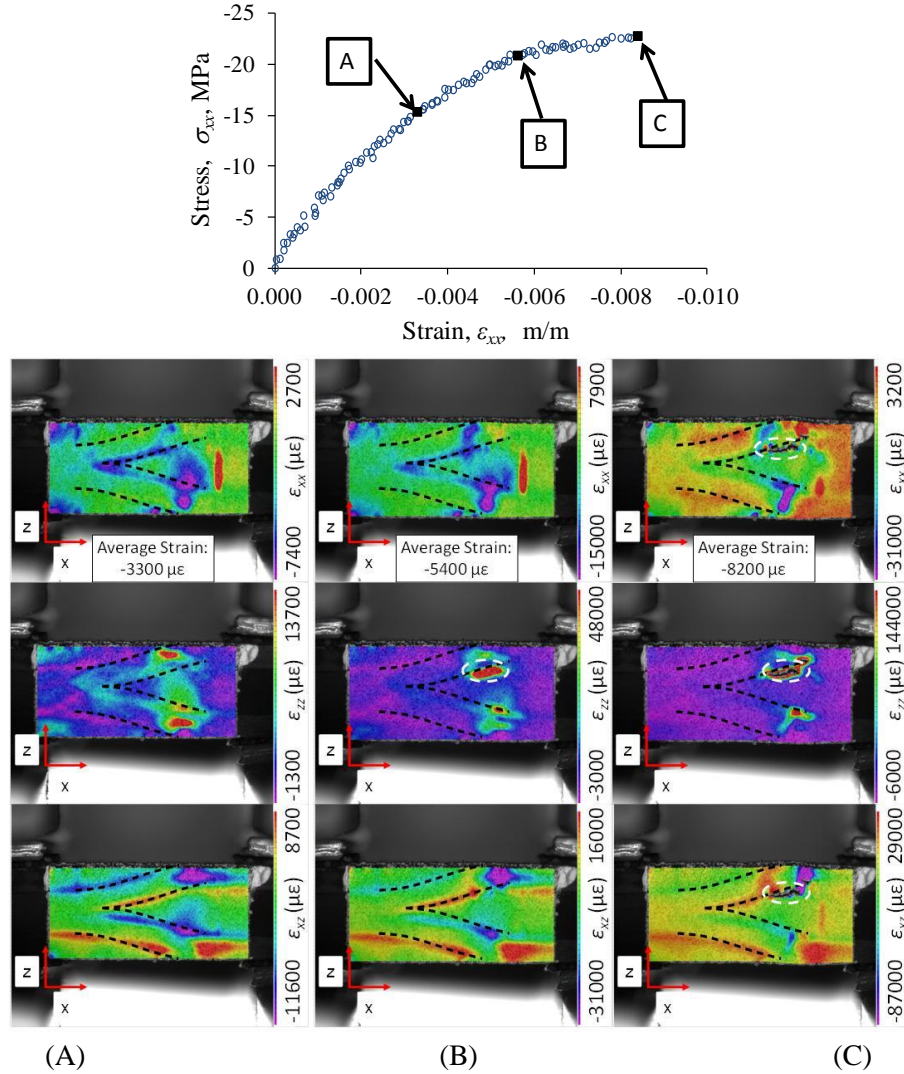


Figure 4-9. Strains at Stages A, B, and C in an LF750 $[0_6/90_6]_s$ specimen (thickness-side view).

Figure 4-10 shows width-side DIC results from $[30_n/-60_n]_s$ specimens. The loading direction for DIC images of the width-side is again horizontal. The average value of strain reported in the images is the average of the field over the undulation region (which in this case is the entire field of view). The DIC images were captured at 50% of ultimate strength. Arrows on the tabs (right side) indicate the $[30_n/-60_n]_s$ side of the laminate. The dashed dark lines highlight the start and

end of the undulated region in which the 30-deg. lamina undulates from the outer layer to the inner layer. The laminate is then $[-60_n/30_n]_s$ on the opposite side of the undulation. The peak and average values of the longitudinal strain field increased with increasing resin compliance. An interesting result was the decrease in longitudinal strain magnitude across the undulation. The lowest longitudinal strain (red) of the field was most distinct for stiffer resins. This result was counter-intuitive, knowing that the undulation reduces the stiffness of the specimen. Therefore, it was expected that the strain amplitude would be higher in the undulated region.

For comparison, the longitudinal strain field of a 30917 filament wound cylinder of winding sequence $[\pm 45/89/\pm 45]$ and a filament winding pattern of 5 in each of the helical layers is shown in **Figure 4-10**. Reduced longitudinal strain across the undulated regions can be seen to occur in the cylinder as well (dark dashed rectangle). Reduced compressive strains across the undulated region could be due to a few factors. Local buckling of the material near the width-side surface of the specimen, as seen in the thickness-size view of **Figure 4-9**, creates local curvature which could cause lower values of compressive strain to be measured in the width-side view due to the “convex” shape of the microbuckled fiber. Consistent with this microbuckled curvature explanation, concentrations of negative longitudinal strain were also commonly observed at the concave side of microbuckled region of the undulating fiber in the thickness-side view. Thus, the longitudinal strain measured in the width-side view (x - y plane) may be a potentially misleading representation of the average longitudinal strain through-the-thickness (x - z plane) which was observed to be non-uniform in the thickness-side view.

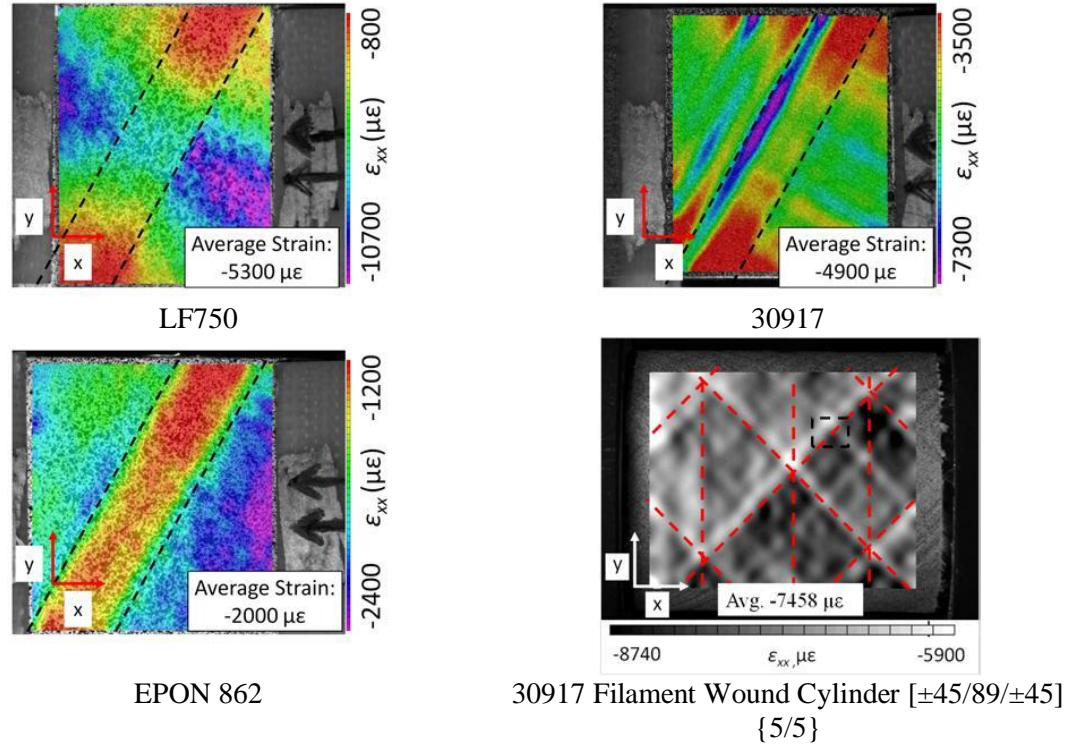


Figure 4-10. Longitudinal strain in width-side view for $[30_n/-60_n]_s$ specimens and a filament wound cylinder for comparison.

Besides the longitudinal strain, the transverse (ϵ_{yy}) and shear (ϵ_x) strain components can be seen to decrease across the undulated region as well (**Figure 4-11**). **Figure 4-10** and **Figure 4-11** might suggest that the undulated region of the specimen is not a likely failure location due to the low strains visible in the width-side view. This conclusion would be incorrect, however, as significant strain concentrations connected with failure onset were visible in the thickness-side view.

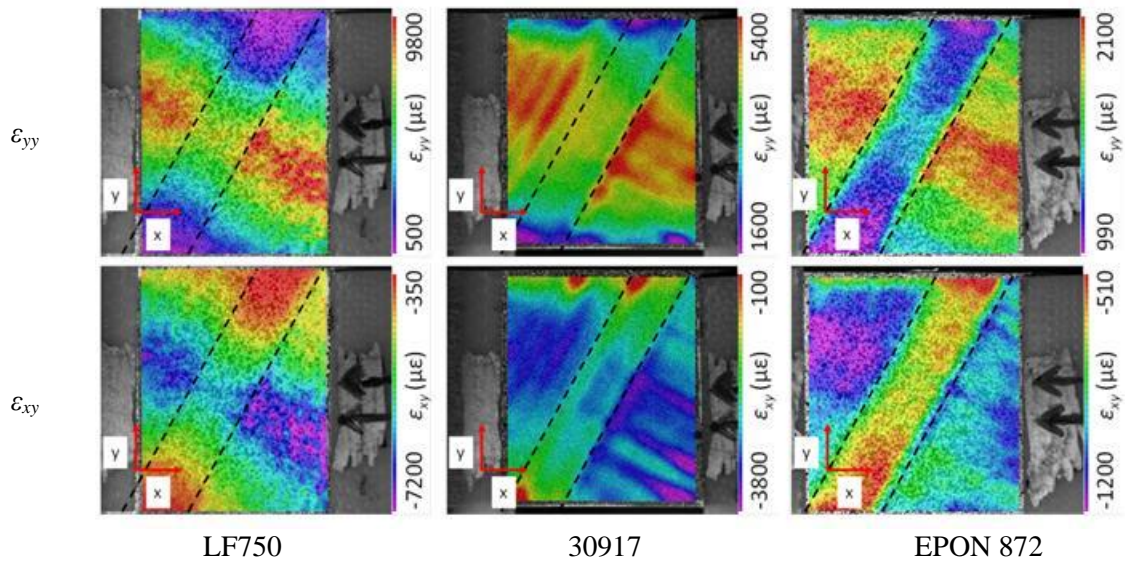


Figure 4-11. Transverse and shear strains in the x - y plane for $[30_n/-60_n]_s$ specimens.

An uncorrelated width-side image of a 30917 $[30_n/-60_n]_s$ flat specimen at failure is shown in **Figure 4-12**. The compressive loading direction is horizontal, again. The 30-deg. surface lamina subducts from the surface of the laminate on the left side of the image to the inside of the laminate on the right side (light dashed lines). Splitting of the matrix parallel to the 30-deg. fibers is indicative of a matrix-related failure mode in this lamina. An uncorrelated image of a 30917 filament wound cylinder is shown in **Figure 4-12** for comparison. The location and type of failure is identical in both cases. The undulated region can be seen to micro-buckle across the surface, characterized by a visually obvious displacement of material out-of-plane. The micro-buckling failure location was coincident with the start of the undulation subduction, where all the xz -plane strain components were shown in the present investigation to be of greatest magnitude.

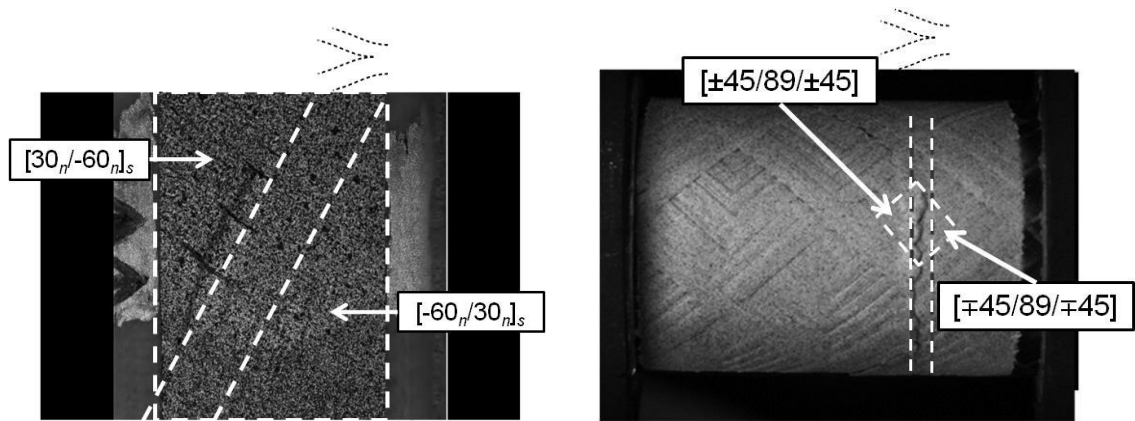


Figure 4-12. Micro-buckling failure in a 30917 $[30_n/-60_n]_s$ specimen and a 30917 filament wound cylinder.

4.3 Analytical Homogenized Stiffness for an RVE

An approach is given here for the derivation of equations which facilitate the determination of the three dimensional stiffness matrix (or, if inverted, the compliance matrix) for an equivalent homogeneous representative volume element, RVE, made up of anisotropic layered laminas (**Figure 4-13**). This approach is similar to that developed by Chou et al. (1972) with anisotropic laminas instead of monoclinic laminas. The novel contribution of anisotropic laminas allows for the inclusion of out-of-plane undulation terms which are not present in a monoclinic assumption. **Figure 4-13** represents a slice of the composite volume through-the-thickness for which the individual laminas may have in-plane ($k=n$) or out-of-plane ($k=1$) orientations.

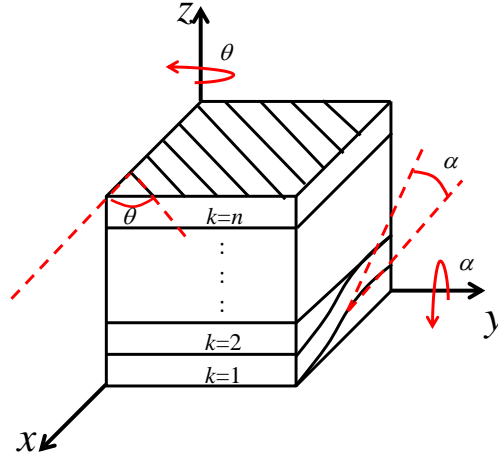


Figure 4-13. RVE of a heterogeneous laminate

For ease of use in contracted notation, the effective homogenized RVE coordinates x, y, z are replaced with 1,2,3, in **Equation 4-1** for this section only. The coordinate system used here should not be confused with the principal material coordinates of each lamina. The in-plane angle θ and out of-plane-angle are zero along the x -axis. The composite laminas were assumed to have an anisotropic material response. The generalized Hooke's law response for each anisotropic lamina, k , is given by,

$$\begin{Bmatrix} \sigma_1 \\ \sigma_2 \\ \sigma_3 \\ \sigma_4 \\ \sigma_5 \\ \sigma_6 \end{Bmatrix}^k = \begin{bmatrix} C_{11} & C_{12} & C_{13} & C_{14} & C_{15} & C_{16} \\ C_{21} & C_{22} & C_{23} & C_{24} & C_{25} & C_{26} \\ C_{31} & C_{32} & C_{33} & C_{34} & C_{35} & C_{36} \\ C_{41} & C_{42} & C_{43} & C_{44} & C_{45} & C_{46} \\ C_{51} & C_{52} & C_{53} & C_{54} & C_{55} & C_{56} \\ C_{61} & C_{62} & C_{63} & C_{64} & C_{65} & C_{66} \end{bmatrix}^k \begin{Bmatrix} \varepsilon_1 \\ \varepsilon_2 \\ \varepsilon_3 \\ \varepsilon_4 \\ \varepsilon_5 \\ \varepsilon_6 \end{Bmatrix}^k \quad (4-1)$$

Assuming iso-strain at the lamina interfaces ensures the normal strains in the 1- and 2- directions (ε_1 and ε_2) as well as the shear strain in the 1-2 plane (ε_6) are equivalent in each lamina. This assumption ensures that each face of the RVE in the 1-2 plane remains planar and continuous (**Figure 4-14**).

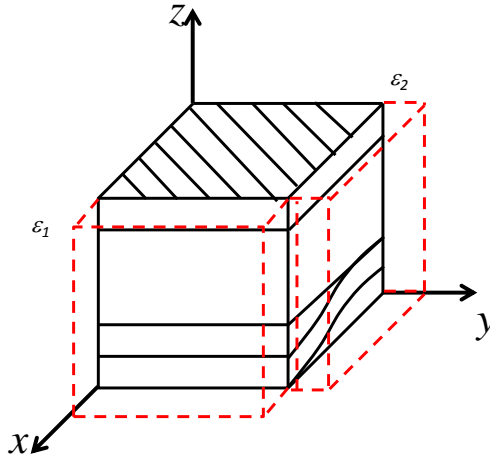


Figure 4-14. In-plane displacement continuity

Iso-stress was assumed through the thickness of the laminate, the out-of-plane transverse stress (σ_3) as well as the out-of-plane shear stresses (σ_4 and σ_5) are equivalent in each lamina (**Figure 4-15**).

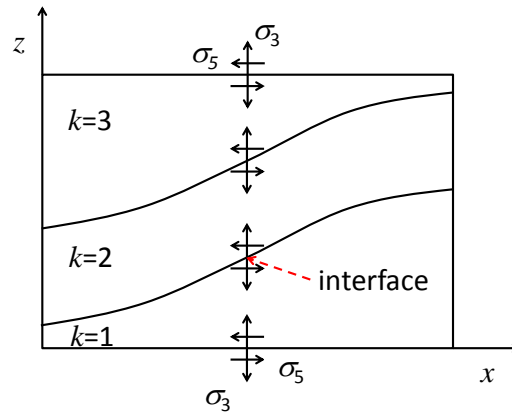


Figure 4-15. Traction continuity through the laminate thickness

The strain and stress assumptions of **Figure 4-14** and **Figure 4-15** in each lamina (total of n lamina) are then considered equal to those of the equivalent homogenized material.

$$\varepsilon_i = \varepsilon_i^k \text{ for } i = 1, 2, 6, k = 1, 2, \dots, n; \quad \sigma_i = \sigma_i^k \text{ for } i = 3, 4, 5, k = 1, 2, \dots, n \quad (4-2)$$

Remaining components of strain and stress for the equivalent homogenized RVE are assumed to be the average of those for each lamina where V^k is the ratio of the k^{th} lamina thickness to the laminate thickness.

$$\varepsilon_i = \sum_{k=1}^n V^k \varepsilon_i^k \text{ for } i = 3,4,5, k = 1,2, \dots, n; \sigma_i = \sum_{k=1}^n V^k \sigma_i^k \text{ for } i = 1,2,6, k = 1,2, \dots, n \quad (4-3)$$

Applying the assumption of **Equation 4-2** and **Equation 4-3** in **Equation 4-1** yields,

$$\begin{Bmatrix} \sigma_1^k \\ \sigma_2^k \\ \sigma_3 \\ \sigma_4 \\ \sigma_5 \\ \sigma_6^k \end{Bmatrix} = \begin{bmatrix} C_{11} & C_{12} & C_{13} & C_{14} & C_{15} & C_{16} \\ C_{21} & C_{22} & C_{23} & C_{24} & C_{25} & C_{26} \\ C_{31} & C_{32} & C_{33} & C_{34} & C_{35} & C_{36} \\ C_{41} & C_{42} & C_{43} & C_{44} & C_{45} & C_{46} \\ C_{51} & C_{52} & C_{53} & C_{54} & C_{55} & C_{56} \\ C_{61} & C_{62} & C_{63} & C_{64} & C_{65} & C_{66} \end{bmatrix}^k \begin{Bmatrix} \varepsilon_1 \\ \varepsilon_2 \\ \varepsilon_3^k \\ \varepsilon_4^k \\ \varepsilon_5^k \\ \varepsilon_6 \end{Bmatrix} \quad (4-4)$$

The goal of this approach is to solve for all of the homogenized RVE stresses σ_i in terms of the homogenized RVE strains ε_i . The equivalent homogenized RVE will have the generalized

Hooke's Law response $\sigma_i = C_{ij} \varepsilon_j$. Expanding the third through fifth rows of **Equation 4-4**,

$$\sigma_3 = C_{31}^k \varepsilon_1 + C_{32}^k \varepsilon_2 + C_{33}^k \varepsilon_3^k + C_{34}^k \varepsilon_4^k + C_{35}^k \varepsilon_5^k + C_{36}^k \varepsilon_6 \quad (4-5)$$

$$\sigma_4 = C_{41}^k \varepsilon_1 + C_{42}^k \varepsilon_2 + C_{43}^k \varepsilon_3^k + C_{44}^k \varepsilon_4^k + C_{45}^k \varepsilon_5^k + C_{46}^k \varepsilon_6 \quad (4-6)$$

$$\sigma_5 = C_{51}^k \varepsilon_1 + C_{52}^k \varepsilon_2 + C_{53}^k \varepsilon_3^k + C_{54}^k \varepsilon_4^k + C_{55}^k \varepsilon_5^k + C_{56}^k \varepsilon_6 \quad (4-7)$$

Rearranging **Equation 4-5**, **Equation 4-6**, and **Equation 4-7** for ε_i^k

$$\varepsilon_3^k = \frac{1}{C_{33}^k} \sigma_3 - \frac{C_{31}^k}{C_{33}^k} \varepsilon_1 - \frac{C_{32}^k}{C_{33}^k} \varepsilon_2 - \frac{C_{34}^k}{C_{33}^k} \varepsilon_4^k - \frac{C_{35}^k}{C_{33}^k} \varepsilon_5^k - \frac{C_{36}^k}{C_{33}^k} \varepsilon_6 \quad (4-8)$$

$$\varepsilon_4^k = \frac{1}{C_{44}^k} \sigma_4 - \frac{C_{41}^k}{C_{44}^k} \varepsilon_1 - \frac{C_{42}^k}{C_{44}^k} \varepsilon_2 - \frac{C_{43}^k}{C_{44}^k} \varepsilon_3^k - \frac{C_{45}^k}{C_{44}^k} \varepsilon_5^k - \frac{C_{46}^k}{C_{44}^k} \varepsilon_6 \quad (4-9)$$

$$\varepsilon_5^k = \frac{1}{C_{55}^k} \sigma_5 - \frac{C_{51}^k}{C_{55}^k} \varepsilon_1 - \frac{C_{52}^k}{C_{55}^k} \varepsilon_2 - \frac{C_{53}^k}{C_{55}^k} \varepsilon_3^k - \frac{C_{54}^k}{C_{55}^k} \varepsilon_4^k - \frac{C_{56}^k}{C_{55}^k} \varepsilon_6 \quad (4-10)$$

Equation 4-8, **Equation 4-9**, and **Equation 4-10** must be solved simultaneously such that each ε_i^k is in terms of only homogenized parameters (ε_i and σ_i). Substituting **Equation 4-8** into **Equation 4-9** and solving for ε_4^k yields,

$$\begin{aligned} \varepsilon_4^k = & \frac{\frac{1}{C_{44}^k}}{\left[1 - \frac{C_{43}^k}{C_{44}^k} \frac{C_{34}^k}{C_{33}^k}\right]} \sigma_4 - \frac{\frac{C_{43}^k}{C_{44}^k} \frac{1}{C_{33}^k}}{\left[1 - \frac{C_{43}^k}{C_{44}^k} \frac{C_{34}^k}{C_{33}^k}\right]} \sigma_3 + \frac{\left[\frac{C_{43}^k}{C_{44}^k} \frac{C_{31}^k}{C_{33}^k} - \frac{C_{41}^k}{C_{44}^k}\right]}{\left[1 - \frac{C_{43}^k}{C_{44}^k} \frac{C_{34}^k}{C_{33}^k}\right]} \varepsilon_1 + \frac{\left[\frac{C_{43}^k}{C_{44}^k} \frac{C_{32}^k}{C_{33}^k} - \frac{C_{42}^k}{C_{44}^k}\right]}{\left[1 - \frac{C_{43}^k}{C_{44}^k} \frac{C_{34}^k}{C_{33}^k}\right]} \varepsilon_2 \\ & + \frac{\left[\frac{C_{43}^k}{C_{44}^k} \frac{C_{35}^k}{C_{33}^k} - \frac{C_{45}^k}{C_{44}^k}\right]}{\left[1 - \frac{C_{43}^k}{C_{44}^k} \frac{C_{34}^k}{C_{33}^k}\right]} \varepsilon_5 + \frac{\left[\frac{C_{43}^k}{C_{44}^k} \frac{C_{36}^k}{C_{33}^k} - \frac{C_{46}^k}{C_{44}^k}\right]}{\left[1 - \frac{C_{43}^k}{C_{44}^k} \frac{C_{34}^k}{C_{33}^k}\right]} \varepsilon_6 \end{aligned} \quad (4-11)$$

Substituting **Equation 4-8** into **Equation 4-10** and solving for ε_5^k yields,

$$\begin{aligned} \varepsilon_5^k = & \frac{\frac{1}{C_{55}^k}}{\left[1 - \frac{C_{53}^k}{C_{55}^k} \frac{C_{35}^k}{C_{33}^k}\right]} \sigma_5 - \frac{\frac{C_{53}^k}{C_{55}^k} \frac{1}{C_{33}^k}}{\left[1 - \frac{C_{53}^k}{C_{55}^k} \frac{C_{35}^k}{C_{33}^k}\right]} \sigma_3 + \frac{\left[\frac{C_{53}^k}{C_{55}^k} \frac{C_{31}^k}{C_{33}^k} - \frac{C_{51}^k}{C_{55}^k}\right]}{\left[1 - \frac{C_{53}^k}{C_{55}^k} \frac{C_{35}^k}{C_{33}^k}\right]} \varepsilon_1 + \frac{\left[\frac{C_{53}^k}{C_{55}^k} \frac{C_{32}^k}{C_{33}^k} - \frac{C_{52}^k}{C_{55}^k}\right]}{\left[1 - \frac{C_{53}^k}{C_{55}^k} \frac{C_{35}^k}{C_{33}^k}\right]} \varepsilon_2 \\ & + \frac{\left[\frac{C_{53}^k}{C_{55}^k} \frac{C_{34}^k}{C_{33}^k} - \frac{C_{54}^k}{C_{55}^k}\right]}{\left[1 - \frac{C_{53}^k}{C_{55}^k} \frac{C_{35}^k}{C_{33}^k}\right]} \varepsilon_4 + \frac{\left[\frac{C_{53}^k}{C_{55}^k} \frac{C_{36}^k}{C_{33}^k} - \frac{C_{56}^k}{C_{55}^k}\right]}{\left[1 - \frac{C_{53}^k}{C_{55}^k} \frac{C_{35}^k}{C_{33}^k}\right]} \varepsilon_6 \end{aligned} \quad (4-12)$$

Substituting **Equation 4-11** into **Equation 4-12** and collecting and isolating ε_5^k terms yields,

$$\varepsilon_5^k = \Gamma_2^k \sigma_5 + \Gamma_3^k \sigma_4 + \Gamma_4^k \sigma_3 + \Gamma_5^k \varepsilon_1 + \Gamma_6^k \varepsilon_2 + \Gamma_7^k \varepsilon_6 \quad (4-13)$$

where,

$$\Gamma_1^k = 1 - \frac{\left[\frac{C_{53}^k}{C_{55}^k} \frac{C_{34}^k}{C_{33}^k} - \frac{C_{54}^k}{C_{55}^k}\right] \left[\frac{C_{43}^k}{C_{44}^k} \frac{C_{35}^k}{C_{33}^k} - \frac{C_{45}^k}{C_{44}^k}\right]}{\left[1 - \frac{C_{53}^k}{C_{55}^k} \frac{C_{35}^k}{C_{33}^k}\right] \left[1 - \frac{C_{43}^k}{C_{44}^k} \frac{C_{34}^k}{C_{33}^k}\right]} \quad (4-14)$$

$$\Gamma_2^k = \left(\frac{1}{\Gamma_1^k} \right) \left\{ \frac{\frac{1}{C_{55}^k}}{\left[1 - \frac{C_{53}^k C_{35}^k}{C_{55}^k C_{33}^k} \right]} \right\} \quad (4-15)$$

$$\Gamma_3^k = \left(\frac{1}{\Gamma_1^k} \right) \left\{ \frac{\left[\frac{C_{53}^k C_{34}^k}{C_{55}^k C_{33}^k} - \frac{C_{54}^k}{C_{55}^k} \right] \frac{1}{C_{44}^k}}{\left[1 - \frac{C_{53}^k C_{35}^k}{C_{55}^k C_{33}^k} \right] \left[1 - \frac{C_{43}^k C_{34}^k}{C_{44}^k C_{33}^k} \right]} \right\} \quad (4-16)$$

$$\Gamma_4^k = - \left(\frac{1}{\Gamma_1^k} \right) \left\{ \frac{\frac{C_{53}^k}{C_{55}^k} \frac{1}{C_{33}^k}}{\left[1 - \frac{C_{53}^k C_{35}^k}{C_{55}^k C_{33}^k} \right]} + \frac{\left[\frac{C_{53}^k C_{34}^k}{C_{55}^k C_{33}^k} - \frac{C_{54}^k}{C_{55}^k} \right] \frac{C_{43}^k}{C_{44}^k} \frac{1}{C_{33}^k}}{\left[1 - \frac{C_{53}^k C_{35}^k}{C_{55}^k C_{33}^k} \right] \left[1 - \frac{C_{43}^k C_{34}^k}{C_{44}^k C_{33}^k} \right]} \right\} \quad (4-17)$$

$$\Gamma_5^k = \left(\frac{1}{\Gamma_1^k} \right) \left\{ \frac{\left[\frac{C_{53}^k C_{31}^k}{C_{55}^k C_{33}^k} - \frac{C_{51}^k}{C_{55}^k} \right]}{\left[1 - \frac{C_{53}^k C_{35}^k}{C_{55}^k C_{33}^k} \right]} + \frac{\left[\frac{C_{53}^k C_{34}^k}{C_{55}^k C_{33}^k} - \frac{C_{54}^k}{C_{55}^k} \right] \left[\frac{C_{43}^k C_{31}^k}{C_{44}^k C_{33}^k} - \frac{C_{41}^k}{C_{44}^k} \right]}{\left[1 - \frac{C_{53}^k C_{35}^k}{C_{55}^k C_{33}^k} \right] \left[1 - \frac{C_{43}^k C_{34}^k}{C_{44}^k C_{33}^k} \right]} \right\} \quad (4-18)$$

$$\Gamma_6^k = \left(\frac{1}{\Gamma_1^k} \right) \left\{ \frac{\left[\frac{C_{53}^k C_{32}^k}{C_{55}^k C_{33}^k} - \frac{C_{52}^k}{C_{55}^k} \right]}{\left[1 - \frac{C_{53}^k C_{35}^k}{C_{55}^k C_{33}^k} \right]} + \frac{\left[\frac{C_{53}^k C_{34}^k}{C_{55}^k C_{33}^k} - \frac{C_{54}^k}{C_{55}^k} \right] \left[\frac{C_{43}^k C_{32}^k}{C_{44}^k C_{33}^k} - \frac{C_{42}^k}{C_{44}^k} \right]}{\left[1 - \frac{C_{53}^k C_{35}^k}{C_{55}^k C_{33}^k} \right] \left[1 - \frac{C_{43}^k C_{34}^k}{C_{44}^k C_{33}^k} \right]} \right\} \quad (4-19)$$

$$\Gamma_7^k = \left(\frac{1}{\Gamma_1^k} \right) \left\{ \frac{\left[\frac{C_{53}^k C_{36}^k}{C_{55}^k C_{33}^k} - \frac{C_{56}^k}{C_{55}^k} \right]}{\left[1 - \frac{C_{53}^k C_{35}^k}{C_{55}^k C_{33}^k} \right]} + \frac{\left[\frac{C_{53}^k C_{34}^k}{C_{55}^k C_{33}^k} - \frac{C_{54}^k}{C_{55}^k} \right] \left[\frac{C_{43}^k C_{36}^k}{C_{44}^k C_{33}^k} - \frac{C_{46}^k}{C_{44}^k} \right]}{\left[1 - \frac{C_{53}^k C_{35}^k}{C_{55}^k C_{33}^k} \right] \left[1 - \frac{C_{43}^k C_{34}^k}{C_{44}^k C_{33}^k} \right]} \right\} \quad (4-20)$$

ε_4^k is determined by substituting **Equation 4-13** into **Equation 4-11** and collecting terms,

$$\varepsilon_4^k = \Gamma_8^k \sigma_5 + \Gamma_9^k \sigma_4 + \Gamma_{10}^k \sigma_3 + \Gamma_{11}^k \varepsilon_1 + \Gamma_{12}^k \varepsilon_2 + \Gamma_{13}^k \varepsilon_6 \quad (4-21)$$

where,

$$\Gamma_8^k = \frac{\left[\frac{C_{43}^k C_{35}^k}{C_{44}^k C_{33}^k} - \frac{C_{45}^k}{C_{44}^k} \right]}{\left[1 - \frac{C_{43}^k C_{34}^k}{C_{44}^k C_{33}^k} \right]} \Gamma_2^k \quad (4-22)$$

$$\Gamma_9^k = \frac{\frac{1}{C_{44}^k}}{\left[1 - \frac{C_{43}^k C_{34}^k}{C_{44}^k C_{33}^k}\right]} + \frac{\left[\frac{C_{43}^k C_{35}^k}{C_{44}^k C_{33}^k} - \frac{C_{45}^k}{C_{44}^k}\right]}{\left[1 - \frac{C_{43}^k C_{34}^k}{C_{44}^k C_{33}^k}\right]} \Gamma_3^k \quad (4-23)$$

$$\Gamma_{10}^k = \frac{\left[\frac{C_{43}^k C_{35}^k}{C_{44}^k C_{33}^k} - \frac{C_{45}^k}{C_{44}^k}\right]}{\left[1 - \frac{C_{43}^k C_{34}^k}{C_{44}^k C_{33}^k}\right]} \Gamma_4^k - \frac{\frac{C_{43}^k}{C_{44}^k} \frac{1}{C_{33}^k}}{\left[1 - \frac{C_{43}^k C_{34}^k}{C_{44}^k C_{33}^k}\right]} \quad (4-24)$$

$$\Gamma_{11}^k = \frac{\left[\frac{C_{43}^k C_{31}^k}{C_{44}^k C_{33}^k} - \frac{C_{41}^k}{C_{44}^k}\right]}{\left[1 - \frac{C_{43}^k C_{34}^k}{C_{44}^k C_{33}^k}\right]} + \frac{\left[\frac{C_{43}^k C_{35}^k}{C_{44}^k C_{33}^k} - \frac{C_{45}^k}{C_{44}^k}\right]}{\left[1 - \frac{C_{43}^k C_{34}^k}{C_{44}^k C_{33}^k}\right]} \Gamma_5^k \quad (4-25)$$

$$\Gamma_{12}^k = \frac{\left[\frac{C_{43}^k C_{32}^k}{C_{44}^k C_{33}^k} - \frac{C_{42}^k}{C_{44}^k}\right]}{\left[1 - \frac{C_{43}^k C_{34}^k}{C_{44}^k C_{33}^k}\right]} + \frac{\left[\frac{C_{43}^k C_{35}^k}{C_{44}^k C_{33}^k} - \frac{C_{45}^k}{C_{44}^k}\right]}{\left[1 - \frac{C_{43}^k C_{34}^k}{C_{44}^k C_{33}^k}\right]} \Gamma_6^k \quad (4-26)$$

$$\Gamma_{13}^k = \frac{\left[\frac{C_{43}^k C_{36}^k}{C_{44}^k C_{33}^k} - \frac{C_{46}^k}{C_{44}^k}\right]}{\left[1 - \frac{C_{43}^k C_{34}^k}{C_{44}^k C_{33}^k}\right]} + \frac{\left[\frac{C_{43}^k C_{35}^k}{C_{44}^k C_{33}^k} - \frac{C_{45}^k}{C_{44}^k}\right]}{\left[1 - \frac{C_{43}^k C_{34}^k}{C_{44}^k C_{33}^k}\right]} \Gamma_7^k \quad (4-27)$$

ε_3^k is determined by substituting **Equation 4-13** and **Equation 4-21** into **Equation 4-8** and collecting terms,

$$\varepsilon_3^k = \Gamma_{14}^k \sigma_5 + \Gamma_{15}^k \sigma_4 + \Gamma_{16}^k \sigma_3 + \Gamma_{17}^k \varepsilon_1 + \Gamma_{18}^k \varepsilon_2 + \Gamma_{19}^k \varepsilon_6 \quad (4-28)$$

where,

$$\Gamma_{14}^k = - \left[\frac{C_{34}^k}{C_{33}^k} \Gamma_8^k + \frac{C_{35}^k}{C_{33}^k} \Gamma_2^k \right] \quad (4-29)$$

$$\Gamma_{15}^k = - \left[\frac{C_{34}^k}{C_{33}^k} \Gamma_9^k + \frac{C_{35}^k}{C_{33}^k} \Gamma_3^k \right] \quad (4-30)$$

$$\Gamma_{16}^k = \left[\frac{1}{C_{33}^k} - \frac{C_{34}^k}{C_{33}^k} \Gamma_{10}^k - \frac{C_{35}^k}{C_{33}^k} \Gamma_4^k \right] \quad (4-31)$$

$$\Gamma_{17}^k = - \left[\frac{C_{31}^k}{C_{33}^k} + \frac{C_{34}^k}{C_{33}^k} \Gamma_{11}^k + \frac{C_{35}^k}{C_{33}^k} \Gamma_5^k \right] \quad (4-32)$$

$$\Gamma_{18}^k = - \left[\frac{C_{32}^k}{C_{33}^k} + \frac{C_{34}^k}{C_{33}^k} \Gamma_{12}^k + \frac{C_{35}^k}{C_{33}^k} \Gamma_6^k \right] \quad (4-33)$$

$$\Gamma_{19}^k = - \left[\frac{C_{36}^k}{C_{33}^k} + \frac{C_{34}^k}{C_{33}^k} \Gamma_{13}^k + \frac{C_{35}^k}{C_{33}^k} \Gamma_7^k \right] \quad (4-34)$$

ε_i terms can be determined from **Equation 4-13**, **Equation 4-21**, and **Equation 4-28** by volume averaging (**Equation 4-3**),

$$\sum_{k=1}^n V^k \varepsilon_3^k = \sum_{k=1}^n V^k \Gamma_{14}^k \sigma_5 + \sum_{k=1}^n V^k \Gamma_{15}^k \sigma_4 + \sum_{k=1}^n V^k \Gamma_{16}^k \sigma_3 + \sum_{k=1}^n V^k \Gamma_{17}^k \varepsilon_1 + \sum_{k=1}^n V^k \Gamma_{18}^k \varepsilon_2 + \sum_{k=1}^n V^k \Gamma_{19}^k \varepsilon_6$$

$$\sum_{k=1}^n V^k \varepsilon_4^k = \sum_{k=1}^n V^k \Gamma_8^k \sigma_5 + \sum_{k=1}^n V^k \Gamma_9^k \sigma_4 + \sum_{k=1}^n V^k \Gamma_{10}^k \sigma_3 + \sum_{k=1}^n V^k \Gamma_{11}^k \varepsilon_1 + \sum_{k=1}^n V^k \Gamma_{12}^k \varepsilon_2 + \sum_{k=1}^n V^k \Gamma_{13}^k \varepsilon_6$$

$$\sum_{k=1}^n V^k \varepsilon_5^k = \sum_{k=1}^n V^k \Gamma_2^k \sigma_5 + \sum_{k=1}^n V^k \Gamma_3^k \sigma_4 + \sum_{k=1}^n V^k \Gamma_4^k \sigma_3 + \sum_{k=1}^n V^k \Gamma_5^k \varepsilon_1 + \sum_{k=1}^n V^k \Gamma_6^k \varepsilon_2 + \sum_{k=1}^n V^k \Gamma_7^k \varepsilon_6$$

and solving for the respective σ_i in terms of only homogenized parameters (ε_i & σ_i) of the form

$$\langle \Gamma_x \rangle = \sum_{k=1}^n V^k \Gamma_x^k,$$

$$\sigma_3 = \frac{1}{\langle \Gamma_{16}^k \rangle} \varepsilon_3 - \frac{\langle \Gamma_{14}^k \rangle}{\langle \Gamma_{16}^k \rangle} \sigma_5 - \frac{\langle \Gamma_{15}^k \rangle}{\langle \Gamma_{16}^k \rangle} \sigma_4 - \frac{\langle \Gamma_{17}^k \rangle}{\langle \Gamma_{16}^k \rangle} \varepsilon_1 - \frac{\langle \Gamma_{18}^k \rangle}{\langle \Gamma_{16}^k \rangle} \varepsilon_2 - \frac{\langle \Gamma_{19}^k \rangle}{\langle \Gamma_{16}^k \rangle} \varepsilon_6 \quad (4-35)$$

$$\sigma_4 = \frac{1}{\langle \Gamma_9^k \rangle} \varepsilon_4 - \frac{\langle \Gamma_8^k \rangle}{\langle \Gamma_9^k \rangle} \sigma_5 - \frac{\langle \Gamma_{10}^k \rangle}{\langle \Gamma_9^k \rangle} \sigma_3 - \frac{\langle \Gamma_{11}^k \rangle}{\langle \Gamma_9^k \rangle} \varepsilon_1 - \frac{\langle \Gamma_{12}^k \rangle}{\langle \Gamma_9^k \rangle} \varepsilon_2 - \frac{\langle \Gamma_{13}^k \rangle}{\langle \Gamma_9^k \rangle} \varepsilon_6 \quad (4-36)$$

$$\sigma_5 = \frac{1}{\langle \Gamma_2^k \rangle} \varepsilon_5 - \frac{\langle \Gamma_3^k \rangle}{\langle \Gamma_2^k \rangle} \sigma_4 - \frac{\langle \Gamma_4^k \rangle}{\langle \Gamma_2^k \rangle} \sigma_3 - \frac{\langle \Gamma_5^k \rangle}{\langle \Gamma_2^k \rangle} \varepsilon_1 - \frac{\langle \Gamma_6^k \rangle}{\langle \Gamma_2^k \rangle} \varepsilon_2 - \frac{\langle \Gamma_7^k \rangle}{\langle \Gamma_2^k \rangle} \varepsilon_6 \quad (4-37)$$

Equation 4-35, **Equation 4-36**, and **Equation 4-37** must be solved simultaneously returning σ_i in terms of only ε_i . Substituting **Equation 4-35** into **Equation 4-36**,

$$\begin{aligned}
\sigma_4 = & \frac{\frac{1}{\langle \Gamma_9^k \rangle}}{\left[1 - \frac{\langle \Gamma_{10}^k \rangle \langle \Gamma_{15}^k \rangle}{\langle \Gamma_9^k \rangle \langle \Gamma_{16}^k \rangle}\right]} \varepsilon_4 + \frac{\left[\frac{\langle \Gamma_{10}^k \rangle \langle \Gamma_{14}^k \rangle}{\langle \Gamma_9^k \rangle \langle \Gamma_{16}^k \rangle} - \frac{\langle \Gamma_8^k \rangle}{\langle \Gamma_9^k \rangle}\right]}{\left[1 - \frac{\langle \Gamma_{10}^k \rangle \langle \Gamma_{15}^k \rangle}{\langle \Gamma_9^k \rangle \langle \Gamma_{16}^k \rangle}\right]} \sigma_5 - \frac{\frac{\langle \Gamma_{10}^k \rangle}{\langle \Gamma_9^k \rangle} \frac{1}{\langle \Gamma_{16}^k \rangle}}{\left[1 - \frac{\langle \Gamma_{10}^k \rangle \langle \Gamma_{15}^k \rangle}{\langle \Gamma_9^k \rangle \langle \Gamma_{16}^k \rangle}\right]} \varepsilon_3 \\
& + \frac{\left[\frac{\langle \Gamma_{10}^k \rangle \langle \Gamma_{17}^k \rangle}{\langle \Gamma_9^k \rangle \langle \Gamma_{16}^k \rangle} - \frac{\langle \Gamma_{11}^k \rangle}{\langle \Gamma_9^k \rangle}\right]}{\left[1 - \frac{\langle \Gamma_{10}^k \rangle \langle \Gamma_{15}^k \rangle}{\langle \Gamma_9^k \rangle \langle \Gamma_{16}^k \rangle}\right]} \varepsilon_1 + \frac{\left[\frac{\langle \Gamma_{10}^k \rangle \langle \Gamma_{18}^k \rangle}{\langle \Gamma_9^k \rangle \langle \Gamma_{16}^k \rangle} - \frac{\langle \Gamma_{12}^k \rangle}{\langle \Gamma_9^k \rangle}\right]}{\left[1 - \frac{\langle \Gamma_{10}^k \rangle \langle \Gamma_{15}^k \rangle}{\langle \Gamma_9^k \rangle \langle \Gamma_{16}^k \rangle}\right]} \varepsilon_2 \\
& + \frac{\left[\frac{\langle \Gamma_{10}^k \rangle \langle \Gamma_{19}^k \rangle}{\langle \Gamma_9^k \rangle \langle \Gamma_{16}^k \rangle} - \frac{\langle \Gamma_{13}^k \rangle}{\langle \Gamma_9^k \rangle}\right]}{\left[1 - \frac{\langle \Gamma_{10}^k \rangle \langle \Gamma_{15}^k \rangle}{\langle \Gamma_9^k \rangle \langle \Gamma_{16}^k \rangle}\right]} \varepsilon_6
\end{aligned} \tag{4-38}$$

Substituting **Equation 4-35** into **Equation 4-37**,

$$\begin{aligned}
\sigma_5 = & \frac{\frac{1}{\langle \Gamma_2^k \rangle}}{\left[1 - \frac{\langle \Gamma_4^k \rangle \langle \Gamma_{14}^k \rangle}{\langle \Gamma_2^k \rangle \langle \Gamma_{16}^k \rangle}\right]} \varepsilon_5 - \frac{\frac{\langle \Gamma_4^k \rangle}{\langle \Gamma_2^k \rangle} \frac{1}{\langle \Gamma_{16}^k \rangle}}{\left[1 - \frac{\langle \Gamma_4^k \rangle \langle \Gamma_{14}^k \rangle}{\langle \Gamma_2^k \rangle \langle \Gamma_{16}^k \rangle}\right]} \varepsilon_3 + \frac{\left[\frac{\langle \Gamma_4^k \rangle \langle \Gamma_{15}^k \rangle}{\langle \Gamma_2^k \rangle \langle \Gamma_{16}^k \rangle} - \frac{\langle \Gamma_3^k \rangle}{\langle \Gamma_2^k \rangle}\right]}{\left[1 - \frac{\langle \Gamma_4^k \rangle \langle \Gamma_{14}^k \rangle}{\langle \Gamma_2^k \rangle \langle \Gamma_{16}^k \rangle}\right]} \sigma_4 \\
& + \frac{\left[\frac{\langle \Gamma_4^k \rangle \langle \Gamma_{17}^k \rangle}{\langle \Gamma_2^k \rangle \langle \Gamma_{16}^k \rangle} - \frac{\langle \Gamma_5^k \rangle}{\langle \Gamma_2^k \rangle}\right]}{\left[1 - \frac{\langle \Gamma_4^k \rangle \langle \Gamma_{14}^k \rangle}{\langle \Gamma_2^k \rangle \langle \Gamma_{16}^k \rangle}\right]} \varepsilon_1 + \frac{\left[\frac{\langle \Gamma_4^k \rangle \langle \Gamma_{18}^k \rangle}{\langle \Gamma_2^k \rangle \langle \Gamma_{16}^k \rangle} - \frac{\langle \Gamma_6^k \rangle}{\langle \Gamma_2^k \rangle}\right]}{\left[1 - \frac{\langle \Gamma_4^k \rangle \langle \Gamma_{14}^k \rangle}{\langle \Gamma_2^k \rangle \langle \Gamma_{16}^k \rangle}\right]} \varepsilon_2 \\
& + \frac{\left[\frac{\langle \Gamma_4^k \rangle \langle \Gamma_{19}^k \rangle}{\langle \Gamma_2^k \rangle \langle \Gamma_{16}^k \rangle} - \frac{\langle \Gamma_7^k \rangle}{\langle \Gamma_2^k \rangle}\right]}{\left[1 - \frac{\langle \Gamma_4^k \rangle \langle \Gamma_{14}^k \rangle}{\langle \Gamma_2^k \rangle \langle \Gamma_{16}^k \rangle}\right]} \varepsilon_6
\end{aligned} \tag{4-39}$$

Substituting **Equation 4-38** into **Equation 4-39** and collecting and isolating ε_i terms yields,

$$\sigma_5 = C_{51} \varepsilon_1 + C_{52} \varepsilon_2 + C_{53} \varepsilon_3 + C_{54} \varepsilon_4 + C_{55} \varepsilon_5 + C_{56} \varepsilon_6 \tag{4-40}$$

where,

$$\sigma_3 = C_{31}\varepsilon_1 + C_{32}\varepsilon_2 + C_{33}\varepsilon_3 + C_{34}\varepsilon_4 + C_{35}\varepsilon_5 + C_{36}\varepsilon_6 \quad (4-54)$$

where,

$$C_{31} = -\frac{\langle \Gamma_{14}^k \rangle}{\langle \Gamma_{16}^k \rangle} C_{51} - \frac{\langle \Gamma_{15}^k \rangle}{\langle \Gamma_{16}^k \rangle} C_{41} - \frac{\langle \Gamma_{17}^k \rangle}{\langle \Gamma_{16}^k \rangle} \quad (4-55)$$

$$C_{32} = -\frac{\langle \Gamma_{14}^k \rangle}{\langle \Gamma_{16}^k \rangle} C_{52} - \frac{\langle \Gamma_{15}^k \rangle}{\langle \Gamma_{16}^k \rangle} C_{42} - \frac{\langle \Gamma_{18}^k \rangle}{\langle \Gamma_{16}^k \rangle} \quad (4-56)$$

$$C_{33} = \frac{1}{\langle \Gamma_{16}^k \rangle} - \frac{\langle \Gamma_{14}^k \rangle}{\langle \Gamma_{16}^k \rangle} C_{53} - \frac{\langle \Gamma_{15}^k \rangle}{\langle \Gamma_{16}^k \rangle} C_{43} \quad (4-57)$$

$$C_{34} = -\frac{\langle \Gamma_{14}^k \rangle}{\langle \Gamma_{16}^k \rangle} C_{54} - \frac{\langle \Gamma_{15}^k \rangle}{\langle \Gamma_{16}^k \rangle} C_{44} \quad (4-58)$$

$$C_{35} = -\frac{\langle \Gamma_{14}^k \rangle}{\langle \Gamma_{16}^k \rangle} C_{55} - \frac{\langle \Gamma_{15}^k \rangle}{\langle \Gamma_{16}^k \rangle} C_{45} \quad (4-59)$$

$$C_{36} = -\frac{\langle \Gamma_{14}^k \rangle}{\langle \Gamma_{16}^k \rangle} C_{56} - \frac{\langle \Gamma_{15}^k \rangle}{\langle \Gamma_{16}^k \rangle} C_{46} - \frac{\langle \Gamma_{19}^k \rangle}{\langle \Gamma_{16}^k \rangle} \quad (4-60)$$

Remaining homogenized stiffness terms are determined from the first, second, and sixth rows of **Equation 4-4**. The first row of **Equation 4-4** can be solved for σ_1^k in terms of only homogenized parameters (ε_i and σ_i) by substitution of **Equation 4-13** (ε_5^k), **Equation 4-21** (ε_4^k), and **Equation 4-28** (ε_3^k).

$$\begin{aligned} \sigma_1^k = & [C_{11}^k + C_{13}^k \Gamma_{17}^k + C_{14}^k \Gamma_{11}^k + C_{15}^k \Gamma_5^k] \varepsilon_1 + [C_{12}^k + C_{13}^k \Gamma_{18}^k + C_{14}^k \Gamma_{12}^k + C_{15}^k \Gamma_6^k] \varepsilon_2 \\ & + [C_{13}^k \Gamma_{14}^k + C_{14}^k \Gamma_8^k + C_{15}^k \Gamma_2^k] \sigma_5 + [C_{13}^k \Gamma_{15}^k + C_{14}^k \Gamma_9^k + C_{15}^k \Gamma_3^k] \sigma_4 \\ & + [C_{13}^k \Gamma_{16}^k + C_{14}^k \Gamma_{10}^k + C_{15}^k \Gamma_4^k] \sigma_3 \\ & + [C_{16}^k + C_{13}^k \Gamma_{19}^k + C_{14}^k \Gamma_{13}^k + C_{15}^k \Gamma_7^k] \varepsilon_6 \end{aligned} \quad (4-61)$$

σ_1 is determined by substituting **Equation 4-40** (σ_5), **Equation 4-47** (σ_4), and **Equation 4-54** (σ_3) into **Equation 4-61** and applying volume averaging (**Equation 4-3**).

$$\sigma_1 = C_{11}\varepsilon_1 + C_{12}\varepsilon_2 + C_{13}\varepsilon_3 + C_{14}\varepsilon_4 + C_{15}\varepsilon_5 + C_{16}\varepsilon_6 \quad (4-62)$$

where,

$$\begin{aligned} C_{11} = & \langle C_{11}^k + C_{13}^k \Gamma_{17}^k + C_{14}^k \Gamma_{11}^k + C_{15}^k \Gamma_5^k + C_{51} [C_{13}^k \Gamma_{14}^k + C_{14}^k \Gamma_8^k + C_{15}^k \Gamma_2^k] \\ & + C_{41} [C_{13}^k \Gamma_{15}^k + C_{14}^k \Gamma_9^k + C_{15}^k \Gamma_3^k] + C_{31} [C_{13}^k \Gamma_{16}^k + C_{14}^k \Gamma_{10}^k + C_{15}^k \Gamma_4^k] \rangle \end{aligned} \quad (4-63)$$

$$C_{12} = \langle C_{12}^k + C_{13}^k \Gamma_{18}^k + C_{14}^k \Gamma_{12}^k + C_{15}^k \Gamma_6^k + C_{52} [C_{13}^k \Gamma_{14}^k + C_{14}^k \Gamma_8^k + C_{15}^k \Gamma_2^k] \\ + C_{42} [C_{13}^k \Gamma_{15}^k + C_{14}^k \Gamma_9^k + C_{15}^k \Gamma_3^k] + C_{32} [C_{13}^k \Gamma_{16}^k + C_{14}^k \Gamma_{10}^k + C_{15}^k \Gamma_4^k] \rangle \quad (4-64)$$

$$C_{13} = \langle C_{53} [C_{13}^k \Gamma_{14}^k + C_{14}^k \Gamma_8^k + C_{15}^k \Gamma_2^k] + C_{43} [C_{13}^k \Gamma_{15}^k + C_{14}^k \Gamma_9^k + C_{15}^k \Gamma_3^k] \\ + C_{33} [C_{13}^k \Gamma_{16}^k + C_{14}^k \Gamma_{10}^k + C_{15}^k \Gamma_4^k] \rangle \quad (4-65)$$

$$C_{14} = \langle C_{54} [C_{13}^k \Gamma_{14}^k + C_{14}^k \Gamma_8^k + C_{15}^k \Gamma_2^k] + C_{44} [C_{13}^k \Gamma_{15}^k + C_{14}^k \Gamma_9^k + C_{15}^k \Gamma_3^k] \\ + C_{34} [C_{13}^k \Gamma_{16}^k + C_{14}^k \Gamma_{10}^k + C_{15}^k \Gamma_4^k] \rangle \quad (4-66)$$

$$C_{15} = \langle C_{55} [C_{13}^k \Gamma_{14}^k + C_{14}^k \Gamma_8^k + C_{15}^k \Gamma_2^k] + C_{45} [C_{13}^k \Gamma_{15}^k + C_{14}^k \Gamma_9^k + C_{15}^k \Gamma_3^k] \\ + C_{35} [C_{13}^k \Gamma_{16}^k + C_{14}^k \Gamma_{10}^k + C_{15}^k \Gamma_4^k] \rangle \quad (4-67)$$

$$C_{16} = \langle C_{16}^k + C_{13}^k \Gamma_{19}^k + C_{14}^k \Gamma_{13}^k + C_{15}^k \Gamma_7^k + C_{56} [C_{13}^k \Gamma_{14}^k + C_{14}^k \Gamma_8^k + C_{15}^k \Gamma_2^k] \\ + C_{46} [C_{13}^k \Gamma_{15}^k + C_{14}^k \Gamma_9^k + C_{15}^k \Gamma_3^k] + C_{36} [C_{13}^k \Gamma_{16}^k + C_{14}^k \Gamma_{10}^k + C_{15}^k \Gamma_4^k] \rangle \quad (4-68)$$

The second row of **Equation 4-4** can be solved for σ_2^k in terms of only homogenized parameters (ε_i and σ_i) by substitution of **Equation 4-13** (ε_5^k), **Equation 4-21** (ε_4^k), and **Equation 4-28** (ε_3^k).

$$\sigma_2^k = [C_{21}^k + C_{23}^k \Gamma_{17}^k + C_{24}^k \Gamma_{11}^k + C_{25}^k \Gamma_5^k] \varepsilon_1 + [C_{22}^k + C_{23}^k \Gamma_{18}^k + C_{24}^k \Gamma_{12}^k + C_{25}^k \Gamma_6^k] \varepsilon_2 \\ + [C_{23}^k \Gamma_{14}^k + C_{24}^k \Gamma_8^k + C_{25}^k \Gamma_2^k] \sigma_5 + [C_{23}^k \Gamma_{15}^k + C_{24}^k \Gamma_9^k + C_{25}^k \Gamma_3^k] \sigma_4 \\ + [C_{23}^k \Gamma_{16}^k + C_{24}^k \Gamma_{10}^k + C_{25}^k \Gamma_4^k] \sigma_3 \\ + [C_{26}^k + C_{23}^k \Gamma_{19}^k + C_{24}^k \Gamma_{13}^k + C_{25}^k \Gamma_7^k] \varepsilon_6 \quad (4-69)$$

σ_2 is determined by substituting **Equation 4-40** (σ_5), **Equation 4-47** (σ_4), and **Equation 4-54** (σ_3) into **Equation 4-69** and applying volume averaging (**Equation 4-3**).

$$\sigma_2 = C_{21} \varepsilon_1 + C_{22} \varepsilon_2 + C_{23} \varepsilon_3 + C_{24} \varepsilon_4 + C_{25} \varepsilon_5 + C_{26} \varepsilon_6 \quad (4-70)$$

where,

$$C_{21} = \langle C_{21}^k + C_{23}^k \Gamma_{17}^k + C_{24}^k \Gamma_{11}^k + C_{25}^k \Gamma_5^k + C_{51} [C_{23}^k \Gamma_{14}^k + C_{24}^k \Gamma_8^k + C_{25}^k \Gamma_2^k] \\ + C_{41} [C_{23}^k \Gamma_{15}^k + C_{24}^k \Gamma_9^k + C_{25}^k \Gamma_3^k] + C_{31} [C_{23}^k \Gamma_{16}^k + C_{24}^k \Gamma_{10}^k + C_{25}^k \Gamma_4^k] \rangle \quad (4-71)$$

$$C_{22} = \langle C_{22}^k + C_{23}^k \Gamma_{18}^k + C_{24}^k \Gamma_{12}^k + C_{25}^k \Gamma_6^k + C_{52} [C_{23}^k \Gamma_{14}^k + C_{24}^k \Gamma_8^k + C_{25}^k \Gamma_2^k] \\ + C_{42} [C_{23}^k \Gamma_{15}^k + C_{24}^k \Gamma_9^k + C_{25}^k \Gamma_3^k] + C_{32} [C_{23}^k \Gamma_{16}^k + C_{24}^k \Gamma_{10}^k + C_{25}^k \Gamma_4^k] \rangle \quad (4-72)$$

$$C_{23} = \langle C_{53} [C_{23}^k \Gamma_{14}^k + C_{24}^k \Gamma_8^k + C_{25}^k \Gamma_2^k] + C_{43} [C_{23}^k \Gamma_{15}^k + C_{24}^k \Gamma_9^k + C_{25}^k \Gamma_3^k] \\ + C_{33} [C_{23}^k \Gamma_{16}^k + C_{24}^k \Gamma_{10}^k + C_{25}^k \Gamma_4^k] \rangle \quad (4-73)$$

$$C_{24} = \langle C_{54} [C_{23}^k \Gamma_{14}^k + C_{24}^k \Gamma_8^k + C_{25}^k \Gamma_2^k] + C_{44} [C_{23}^k \Gamma_{15}^k + C_{24}^k \Gamma_9^k + C_{25}^k \Gamma_3^k] \\ + C_{34} [C_{23}^k \Gamma_{16}^k + C_{24}^k \Gamma_{10}^k + C_{25}^k \Gamma_4^k] \rangle \quad (4-74)$$

$$C_{25} = \langle C_{55}[C_{23}^k \Gamma_{14}^k + C_{24}^k \Gamma_8^k + C_{25}^k \Gamma_2^k] + C_{45}[C_{23}^k \Gamma_{15}^k + C_{24}^k \Gamma_9^k + C_{25}^k \Gamma_3^k] + C_{35}[C_{23}^k \Gamma_{16}^k + C_{24}^k \Gamma_{10}^k + C_{25}^k \Gamma_4^k] \rangle \quad (4-75)$$

$$C_{26} = \langle C_{26}^k + C_{23}^k \Gamma_{19}^k + C_{24}^k \Gamma_{13}^k + C_{25}^k \Gamma_7^k + C_{56}[C_{23}^k \Gamma_{14}^k + C_{24}^k \Gamma_8^k + C_{25}^k \Gamma_2^k] + C_{46}[C_{23}^k \Gamma_{15}^k + C_{24}^k \Gamma_9^k + C_{25}^k \Gamma_3^k] + C_{36}[C_{23}^k \Gamma_{16}^k + C_{24}^k \Gamma_{10}^k + C_{25}^k \Gamma_4^k] \rangle \quad (4-76)$$

The sixth row of **Equation 4-4** can be solved for σ_6^k in terms of only homogenized variables by substitution of **Equation 4-13** (ε_5^k), **Equation 4-21** (ε_4^k), and **Equation 4-28** (ε_3^k).

$$\begin{aligned} \sigma_6^k = & [C_{61}^k + C_{63}^k \Gamma_{17}^k + C_{64}^k \Gamma_{11}^k + C_{65}^k \Gamma_5^k] \varepsilon_1 + [C_{62}^k + C_{63}^k \Gamma_{18}^k + C_{64}^k \Gamma_{12}^k + C_{65}^k \Gamma_6^k] \varepsilon_2 \\ & + [C_{63}^k \Gamma_{14}^k + C_{64}^k \Gamma_8^k + C_{65}^k \Gamma_2^k] \sigma_5 + [C_{63}^k \Gamma_{15}^k + C_{64}^k \Gamma_9^k + C_{65}^k \Gamma_3^k] \sigma_4 \\ & + [C_{63}^k \Gamma_{16}^k + C_{64}^k \Gamma_{10}^k + C_{65}^k \Gamma_4^k] \sigma_3 \\ & + [C_{66}^k + C_{63}^k \Gamma_{19}^k + C_{64}^k \Gamma_{13}^k + C_{65}^k \Gamma_7^k] \varepsilon_6 \end{aligned} \quad (4-77)$$

σ_6 is determined by substituting **Equation 4-40** (σ_5), **Equation 4-47** (σ_4), and **Equation 4-54** (σ_3) into **Equation 4-77** and applying volume averaging (**Equation 4-3**).

$$\sigma_6 = C_{61} \varepsilon_1 + C_{62} \varepsilon_2 + C_{63} \varepsilon_3 + C_{64} \varepsilon_4 + C_{65} \varepsilon_5 + C_{66} \varepsilon_6 \quad (4-78)$$

where,

$$C_{61} = \langle C_{61}^k + C_{63}^k \Gamma_{17}^k + C_{64}^k \Gamma_{11}^k + C_{65}^k \Gamma_5^k + C_{51}[C_{63}^k \Gamma_{14}^k + C_{64}^k \Gamma_8^k + C_{65}^k \Gamma_2^k] + C_{41}[C_{63}^k \Gamma_{15}^k + C_{64}^k \Gamma_9^k + C_{65}^k \Gamma_3^k] + C_{31}[C_{63}^k \Gamma_{16}^k + C_{64}^k \Gamma_{10}^k + C_{65}^k \Gamma_4^k] \rangle \quad (4-79)$$

$$C_{62} = \langle C_{62}^k + C_{63}^k \Gamma_{18}^k + C_{64}^k \Gamma_{12}^k + C_{65}^k \Gamma_6^k + C_{52}[C_{63}^k \Gamma_{14}^k + C_{64}^k \Gamma_8^k + C_{65}^k \Gamma_2^k] + C_{42}[C_{63}^k \Gamma_{15}^k + C_{64}^k \Gamma_9^k + C_{65}^k \Gamma_3^k] + C_{32}[C_{63}^k \Gamma_{16}^k + C_{64}^k \Gamma_{10}^k + C_{65}^k \Gamma_4^k] \rangle \quad (4-80)$$

$$C_{63} = \langle C_{53}[C_{63}^k \Gamma_{14}^k + C_{64}^k \Gamma_8^k + C_{65}^k \Gamma_2^k] + C_{43}[C_{63}^k \Gamma_{15}^k + C_{64}^k \Gamma_9^k + C_{65}^k \Gamma_3^k] + C_{33}[C_{63}^k \Gamma_{16}^k + C_{64}^k \Gamma_{10}^k + C_{65}^k \Gamma_4^k] \rangle \quad (4-81)$$

$$C_{64} = \langle C_{54}[C_{63}^k \Gamma_{14}^k + C_{64}^k \Gamma_8^k + C_{65}^k \Gamma_2^k] + C_{44}[C_{63}^k \Gamma_{15}^k + C_{64}^k \Gamma_9^k + C_{65}^k \Gamma_3^k] + C_{34}[C_{63}^k \Gamma_{16}^k + C_{64}^k \Gamma_{10}^k + C_{65}^k \Gamma_4^k] \rangle \quad (4-82)$$

$$C_{65} = \langle C_{55}[C_{63}^k \Gamma_{14}^k + C_{64}^k \Gamma_8^k + C_{65}^k \Gamma_2^k] + C_{45}[C_{63}^k \Gamma_{15}^k + C_{64}^k \Gamma_9^k + C_{65}^k \Gamma_3^k] + C_{35}[C_{63}^k \Gamma_{16}^k + C_{64}^k \Gamma_{10}^k + C_{65}^k \Gamma_4^k] \rangle \quad (4-83)$$

$$C_{66} = \langle C_{66}^k + C_{63}^k \Gamma_{19}^k + C_{64}^k \Gamma_{13}^k + C_{65}^k \Gamma_7^k + C_{56}[C_{63}^k \Gamma_{14}^k + C_{64}^k \Gamma_8^k + C_{65}^k \Gamma_2^k] + C_{46}[C_{63}^k \Gamma_{15}^k + C_{64}^k \Gamma_9^k + C_{65}^k \Gamma_3^k] + C_{36}[C_{63}^k \Gamma_{16}^k + C_{64}^k \Gamma_{10}^k + C_{65}^k \Gamma_4^k] \rangle \quad (4-84)$$

4.4 Discrete Undulated Composite Modeling: Validation

Homogenization methods for any RVE configuration require a detailed physical description of the lamina boundaries. An example five-lamina undulated heterogeneous RVE can be seen in

Figure 4-16. Laminate stacking sequence, $[\theta_1/\theta_2/\theta_1/\theta_2/\theta_1]$, was defined at $x=L_u/2$ for which only θ_2 was undulated. The laminate transitions from $[\theta_1/\theta_2]_s$ at $x=0$ to $[\theta_2/\theta_1]_s$ at $x=L_u$. A symmetric half-sine wave undulation waveform was assumed. The RVE of thickness, h_t , and length, L_u , contains an undulating lamina of thickness, h_f , at an undulation amplitude height of h_u . The undulating lamina thickness and amplitude were equal. Individual lamina thickness, $h_i(x)$, can be calculated as a function of the position along the longitudinal direction of the RVE (x -direction) (Equation 4-85). If h_u were set to zero, the resulting geometry would be a simple non-undulated composite.

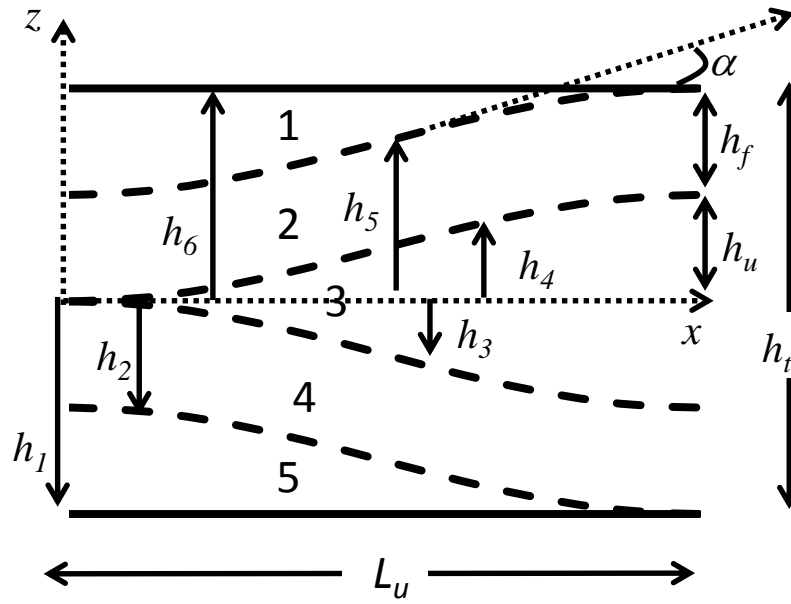


Figure 4-16. Example undulated heterogeneous RVE, $[\theta_1/\theta_2/\theta_1/\theta_2/\theta_1]$

$$\begin{aligned}
h_1(x) &= -\frac{h_t}{2} \\
h_2(x) &= -\frac{h_t}{4} - \frac{h_f}{2} - \frac{h_u}{2} \sin\left(\frac{\pi}{L_u}\left(x - \frac{L_u}{2}\right)\right) \\
h_3(x) &= -\frac{h_t}{4} + \frac{h_f}{2} - \frac{h_u}{2} \sin\left(\frac{\pi}{L_u}\left(x - \frac{L_u}{2}\right)\right) \\
h_4(x) &= \frac{h_t}{4} - \frac{h_f}{2} + \frac{h_u}{2} \sin\left(\frac{\pi}{L_u}\left(x - \frac{L_u}{2}\right)\right) \\
h_5(x) &= \frac{h_t}{4} + \frac{h_f}{2} + \frac{h_u}{2} \sin\left(\frac{\pi}{L_u}\left(x - \frac{L_u}{2}\right)\right) \\
h_6(x) &= \frac{h_t}{2} \\
\alpha(x) &= \text{atan}\left\{\frac{\pi h_u}{2L_u} \cos\left(\frac{\pi}{L_u}\left(x - \frac{L_u}{2}\right)\right)\right\}
\end{aligned} \tag{4-85}$$

The orthotropic lamina stiffness matrix at each discrete longitudinal location was rotated through angles θ (in-plane rotation) and α (out-of-plane rotation) using well known transformation equations (yielding **Equation 4-1** if both θ and α are non-zero). The preceding three-dimensional anisotropic homogenization can then be implemented, making use of the homogenized laminate stiffness equations at discrete locations (dx) along the longitudinal direction. The homogenized stiffness of the RVE depends on the choice of assumption, iso-strain (averaging the individual stiffness terms) or iso-stress (averaging the individual inverse stiffness terms, also known as compliance), along the longitudinal direction of the RVE for which the homogenized stiffness (or compliance) at discrete locations have been calculated. This averaging of the three-dimensional homogenized elastic properties (x - y - z frame) of the RVE generates upper (iso-strain) and lower (iso-stress) bounds. The homogenized compliance matrix S_{ij} (**Equation 4-86**) of the RVE can then be used to predict effective elastic constants. For a non-undulated RVE, the upper and lower bounds will be identical due to assumed symmetry along the longitudinal direction (mirrored about the laminate vertical centerline, z direction).

$$\begin{aligned}
E_x &= \frac{1}{S_{11}} \\
E_y &= \frac{1}{S_{22}} \\
E_z &= \frac{1}{S_{33}} \\
\nu_{xy} &= -\frac{S_{21}}{S_{11}} \\
\nu_{xz} &= -\frac{S_{31}}{S_{11}} \\
\nu_{yz} &= -\frac{S_{23}}{S_{22}} \\
G_{xy} &= \frac{1}{S_{66}} \\
G_{xz} &= \frac{1}{S_{55}} \\
G_{yz} &= \frac{1}{S_{44}}
\end{aligned} \tag{4-86}$$

Validation of the proposed three dimensional homogenized RVE elastic predictions was performed by comparison with Chou et al. (1972) and Ishikawa and Chou (1982). The method of Chou et al. (1972) predicts the three-dimensional homogenized elastic properties (**Equation 4-86**) for a RVE consisting of monoclinic lamina having only in-plane undulation. Stiffness components that arise from rotations out-of-plane were simply averaged ($C_{ij} = \sum_{k=1}^n V^k C_{ij}^k$). Ishikawa and Chou (1982) developed a method for predicting the two-dimensional homogenized elastic properties of an RVE consisting of anisotropic lamina with both in- and out-of-plane fiber orientation. Geometric constants used for validation include: $h_f = 0.2$ mm, $L_u = 1.0$ mm, $h_u = 0.2$ mm (zero if laminated), and $h_t = 4h_f$. Material properties (**Table 4-3**) for the various material systems were taken from Henry (2012). These material properties differ from those used in driveshaft optimization work in that the properties are quasi-static instead of dynamic and based on non-undulated testing. E_1 was found experimentally using a unidirectional bend test (Henry et al., 2014) and scaled to $V_f = 50$ %). The use of non-undulated properties was permitted by the inclusion of the undulation geometry in the derived equations.

Table 4-3. Lamina elastic material properties: discrete undulation (Henry, 2012)

Parameter	LF750	30917	EPON 862	Parameter	LF750	30917	EPON 862
$*E_1$, GPa	125	125	125	ν_{23}	0.87	0.74	0.58
E_2 , GPa	1.57	4.73	8.56	G_{12} , GPa	1.07	1.88	6.64
E_3 , GPa	1.57	4.73	8.56	G_{13} , GPa	1.07	1.88	6.64
ν_{12}	0.30	0.32	0.32	G_{23} , GPa	0.42	0.54	2.71
ν_{13}	0.30	0.32	0.32				

*Henry et al. 2014

The homogenized properties for an undulated laminate were dependent on the number and position of discrete longitudinal locations used in the analysis. Longitudinal locations which contain lamina undulation (all those except $x=0, L_u$) experience stiffness reduction. As with any discretization analysis, the number of nodes used to describe the laminate will affect the predicted results. In particular, when a larger number of longitudinal locations are considered, the stiffness of the homogenized RVE was lower due to convergence of the discrete elements. Therefore, a convergence study was conducted for an EPON 862 [90/0/90/0/90] laminate to determine the number of uniformly distributed longitudinal locations needed to predict the homogenized RVE modulus E_x (**Figure 4-17**). The two- (Ishikawa and Chou, 1982) and three-dimensional anisotropic (**Section 4.3**) homogenized solutions for the undulated laminate show convergence for at least 100 discrete steps for the given laminate configuration, supporting use of 100 steps in this research.

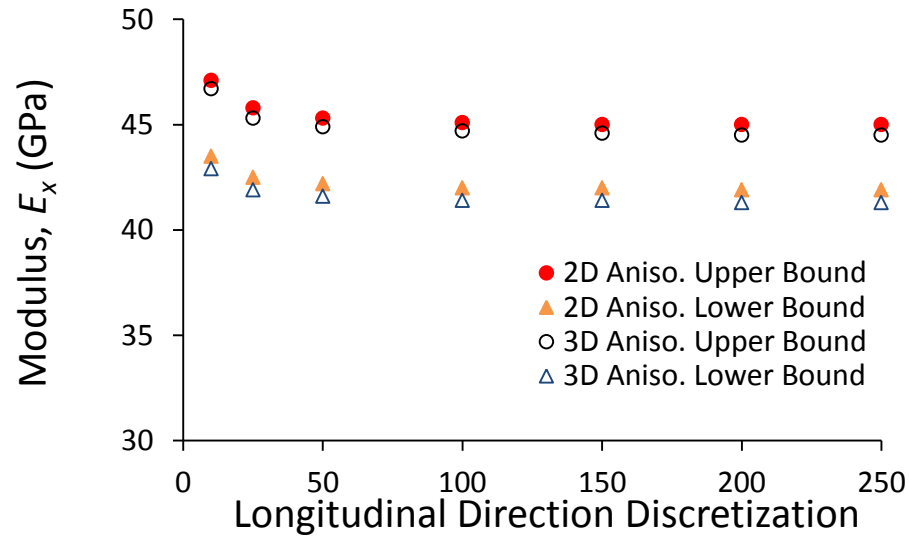


Figure 4-17. Homogenized modulus convergence vs. longitudinal discretization: EPON 862

Multiple EPON 862 laminates were evaluated for validation with no undulation (monoclinic lamina, only in-plane rotation θ), a specially orthotropic laminate, [90/0/90/0/90], as well as [60/10/60/10/60] and [45/45/45/45/45] laminates (**Table 4-4**). When there was an absence of out-of-plane undulation, the three-dimensional homogenized elastic predictions can be seen to be identical whether the laminas were assumed to be monoclinic or anisotropic. The homogenized elastic properties predicted utilizing the two-dimensional anisotropic method (Ishikawa and Chou, 1982) were also identical to those predicted using both three-dimensional methods. The three-dimensional anisotropic homogenization can therefore be said to accurately predict the elastic properties necessary for three-dimensional stress analysis of a non-undulated laminate.

Table 4-4. Homogenized elastic predictions: EPON 862 non-undulated

Value		[90/0/90/0/90]			[60/10/60/10/60]			[45/45/45/45/45]		
		Ref. [2D]	3D ANISO	Ref. [3D]	Ref. [2D]	3D ANISO	Ref. [3D]	Ref. [2D]	3D ANISO	Ref. [3D]
E_x ,	Upper	67.1	67.1	67.1	53.5	53.5	53.5	14.8	14.8	14.8
GPa	Lower	67.1	67.1	67.1	53.5	53.5	53.5	14.8	14.8	14.8
E_y ,	Upper	67.1	67.1	67.1	22.4	22.4	22.4	14.8	14.8	14.8
GPa	Lower	67.1	67.1	67.1	22.4	22.4	22.4	14.8	14.8	14.8
E_z ,	Upper	-	11.9	11.9	-	10.1	10.1	-	8.60	8.60
GPa	Lower	-	11.9	11.9	-	10.1	10.1	-	8.60	8.60
ν_{xy}	Upper	0.04	0.04	0.04	-0.16	-0.16	-0.16	0.11	0.11	0.11
	Lower	0.04	0.04	0.04	-0.16	-0.16	-0.16	0.11	0.11	0.11
ν_{xz}	Upper	-	0.53	0.53	-	0.66	0.66	-	0.52	0.52
	Lower	-	0.53	0.53	-	0.66	0.66	-	0.52	0.52
ν_{yz}	Upper	-	0.53	0.53	-	0.62	0.62	-	0.52	0.52
	Lower	-	0.53	0.53	-	0.62	0.62	-	0.52	0.52
G_{xy} ,	Upper	6.64	6.64	6.64	7.68	7.68	7.68	7.70	7.70	7.70
GPa	Lower	6.64	6.64	6.64	7.68	7.68	7.68	7.70	7.70	7.70
G_{xz} ,	Upper	-	3.85	3.85	-	4.24	4.24	-	3.85	3.85
GPa	Lower	-	3.85	3.85	-	4.24	4.24	-	3.85	3.85
G_{yz} ,	Upper	-	3.85	3.85	-	3.52	3.52	-	3.85	3.85
GPa	Lower	-	3.85	3.85	-	3.52	3.52	-	3.85	3.85
[2D] – [Ishikawa and Chou, 1982], [3D] – [Chou et al., 1972]										

The same EPON 862 laminate configurations were evaluated with out-of-plane undulation as in (Table 4-5). Lamina undulation was only present in the θ_2 lamina of the $[\theta_1/\theta_2/\theta_1/\theta_2/\theta_1]$ laminate (Figure 4-16). The homogenized elastic predictions for the RVE underestimate the degenerative effect of the lamina undulation on longitudinal modulus, E_x , when the three-dimensional approach of Chou et al. (1972) was used. The underestimation was due to coupling terms that were not included in the Chou et al. (1972) analysis, although being simply averaged through the laminate thickness here. Neglecting coupling terms due to rotation out-of-plane was a source of significant error. When the undulating lamina has lower longitudinal modulus due to in-plane rotation, for example 45-deg. ([45/45/45/45/45]) instead of 0-deg. ([90/0/90/0/90]), the homogenized elastic properties were more accurately predicted by the Chou et al. (1972) model when compared to the other two models. The homogenized elastic predictions for each laminate containing out-of-plane undulation for three-dimensional anisotropic homogenization were within

5% of that predicted by Ishikawa and Chou (1982). This excellent correlation supports the use of the three-dimensional anisotropic homogenization analysis for determining the three-dimensional homogenized stiffness and elastic properties in an undulated composite.

Table 4-5. Three-dimensional homogenized elastic predictions: EPON 862 undulated

Value		[90/0/90/0/90]			[60/10/60/10/60]			[45/45/45/45/45]		
		Ref. [2D]	3D ANIS O	Ref. [3D]	Ref. [2D]	3D ANIS O	Ref. [3D]	Ref. [2D]	3D ANIS O	Ref. [3D]
E_x	Upper	45.0	44.5	59.6	39.0	38.5	47.8	14.6	14.6	14.6
GPa	Lower	41.9	41.3	59.0	36.9	36.4	47.4	14.6	14.6	14.6
E_y	Upper	67.1	67.1	67.4	21.8	21.9	22.7	14.6	14.8	14.9
GPa	Lower	67.0	67.1	67.4	21.7	21.8	22.7	14.6	14.8	14.9
E_z	Upper	-	11.8	11.8	-	10.2	10.2	-	8.6	8.7
GPa	Lower	-	11.7	11.7	-	10.1	10.2	-	8.6	8.7
ν_{xy}	Upper	0.05	0.05	0.26	-0.01	-0.03	-0.17	0.14	0.12	0.12
	Lower	0.06	0.05	0.25	0.02	-0.01	-0.16	0.14	0.12	0.12
ν_{xz}	Upper	-	0.51	0.67	-	0.57	0.76	-	0.51	0.51
	Lower	-	0.51	0.68	-	0.55	0.76	-	0.51	0.51
ν_{yz}	Upper	-	0.51	0.51	-	0.59	0.59	-	0.51	0.51
	Lower	-	0.50	0.51	-	0.59	0.60	-	0.51	0.51
G_{xy}	Upper	6.44	6.44	6.55	7.56	7.54	7.66	7.47	7.57	7.82
GPa	Lower	6.44	6.44	6.55	7.55	7.54	7.66	7.44	7.56	7.82
G_{xz}	Upper	-	4.26	4.29	-	4.73	4.77	-	4.00	4.01
GPa	Lower	-	4.25	4.28	-	4.71	4.74	-	4.00	4.00
G_{yz}	Upper	-	4.02	4.02	-	3.67	3.67	-	4.05	4.06
GPa	Lower	-	4.02	4.02	-	3.67	3.67	-	4.05	4.05
[2D] – [Ishikawa and Chou, 1982], [3D] – [Chou et al., 1972]										

The three-dimensional anisotropic and two-dimensional anisotropic (Ishikawa and Chou, 1982) homogenization techniques predict identical values of longitudinal modulus for a non-undulated [90/0/90/0/90] composite (for which the upper and lower bound were also the same). **Table 4-4** and **Table 4-5** show that when θ_2 contributed greatly to longitudinal modulus (a relatively low in-plane angle), lamina undulation highly influences the homogenized longitudinal modulus, E_x . Lamina undulation also causes the homogenized longitudinal modulus upper and lower bound to become increasingly divergent for larger ratios of undulation amplitude/length, h_u/L_u . The degree to which the homogenized longitudinal modulus prediction was affected by the undulation (h_u/L_u) also depends on the material system (**Figure 4-18**). A stiff material

system like EPON 862 (dark points) experiences a 50 % reduction in longitudinal modulus at $h_u/L_u \sim 0.3$ which contrasts greatly with a compliant resin system such as LF750 (light points), which experiences the same reduction at $h_u/L_u \sim 0.1$ compared to the non-undulated case. For the material systems and undulation variation considered, the homogenized longitudinal modulus prediction error between the two- and three-dimensional anisotropic results was between 1-10 %. The largest discrepancies occur at relatively large h_u/L_u for more compliant resins systems.

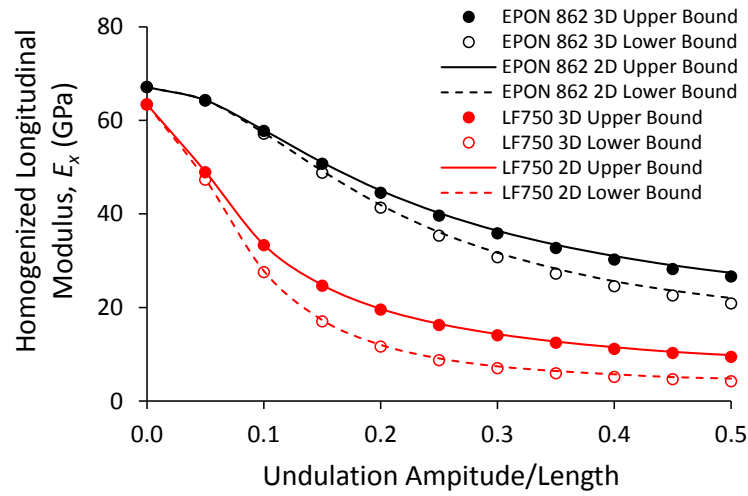


Figure 4-18. Homogenized longitudinal modulus vs. undulation height/ length: $[90/0/90/0/90]$ laminate, anisotropic solutions

4.5 Discrete Undulation Modulus and Strength Prediction

Longitudinal modulus, E_x , was calculated using the three dimensional homogenization of **Section 4.3** as well as the two dimensional method of Ishikawa and Chou (1982). The analytical predictions were compared to experimental results for discrete $[0_n/90_n]_s$ and $[30_n/-60_n]_s$ laminates. Previously in **Section 4.4** the modulus predictions for two and three dimensional analysis were shown to be in very good agreement; therefore, only the three dimensional approach was shown here. The range of the theoretical modulus bounds for $[0_n/90_n]_s$ increases with increasing resin

compliance and undulation amplitude with the experimental scatter measured in testing falling within the theoretical bounds (**Figure 4-19a**).

The theoretical modulus range (between iso-strain and iso-stress) was smaller for $[30_n/-60_n]_s$ specimens compared to $[0_n/90_n]_s$ specimens. The predictions for $[30_n/-60_n]_s$ laminates as well as the experiments show little correlation between specimen modulus and undulation amplitude/length (**Figure 4-19b**). This analytical and experimental result supports the statement that the reinforcement inclination in the plane of the lamina from 0-30 deg. reduces the modulus more than the additional inclination out-of-plane.

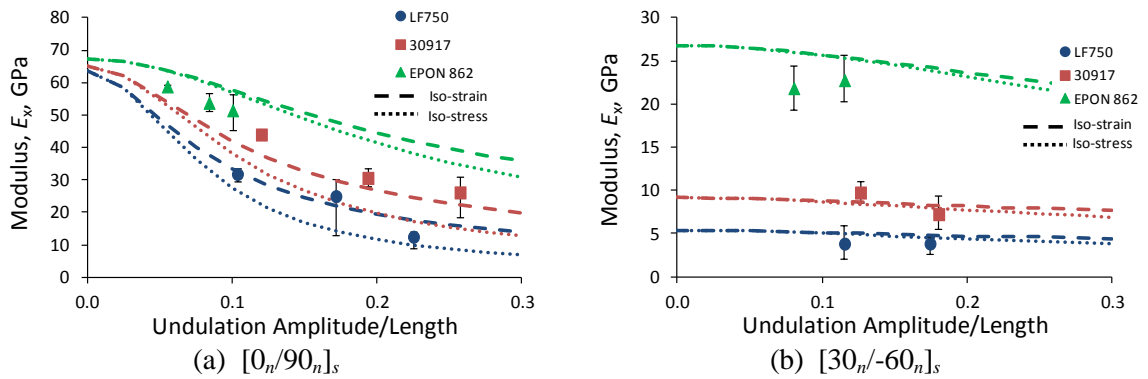


Figure 4-19. Flat undulated three dimensional modulus experimental and theoretical results

A sensitivity study was conducted to determine the major factors for which changes in inputs will change the analytically predicted modulus. The sensitivity to any input was determined by perturbing the input by 10 % and then calculating the percent change in the modulus for an undulation amplitude/length of 0.15. The vertical axis of **Figure 4-20** is the modulus prediction percent change divided by the input (horizontal axis) percent change. A sensitivity of one on the vertical axis means that a 1 % change in the particular input causes a 1 % change in the modulus.

The sensitivity of the two and three dimensional predictions of modulus was determined to be approximately identical (**Figure 4-20a** and **Figure 4-20c**, or **Figure 4-20b** and **Figure 4-20d**). This result was not a surprise due to the strong prediction correlation between these two models

shown in **Section 4.4**. Modulus predictions for $[0_n/90_n]_s$ were primarily influenced by the undulation geometry (amplitude, length), as well as the fiber direction modulus E_1 and longitudinal shear modulus G_{12} . The analysis in this investigation assumed that G_{12} was equal to G_{13} which has been shown to be important as undulation amplitude increases and the shear behavior of the lamina becomes more influential to modulus response (Bogetti et al., 1994). EPON 862 was much more influenced by E_1 and less influenced by the undulation geometry and shear modulus compared to softer composites. The modulus predictions for $[30_n/-60_n]_s$ specimens was only greatly influenced by G_{12} . The undulation amplitude, undulation length, and E_1 slightly affect modulus prediction. As mentioned, the in-plane alignment of the fibers at 30-60 deg. was more detrimental to the modulus response of the composite compared to additional inclination out-of-plane.

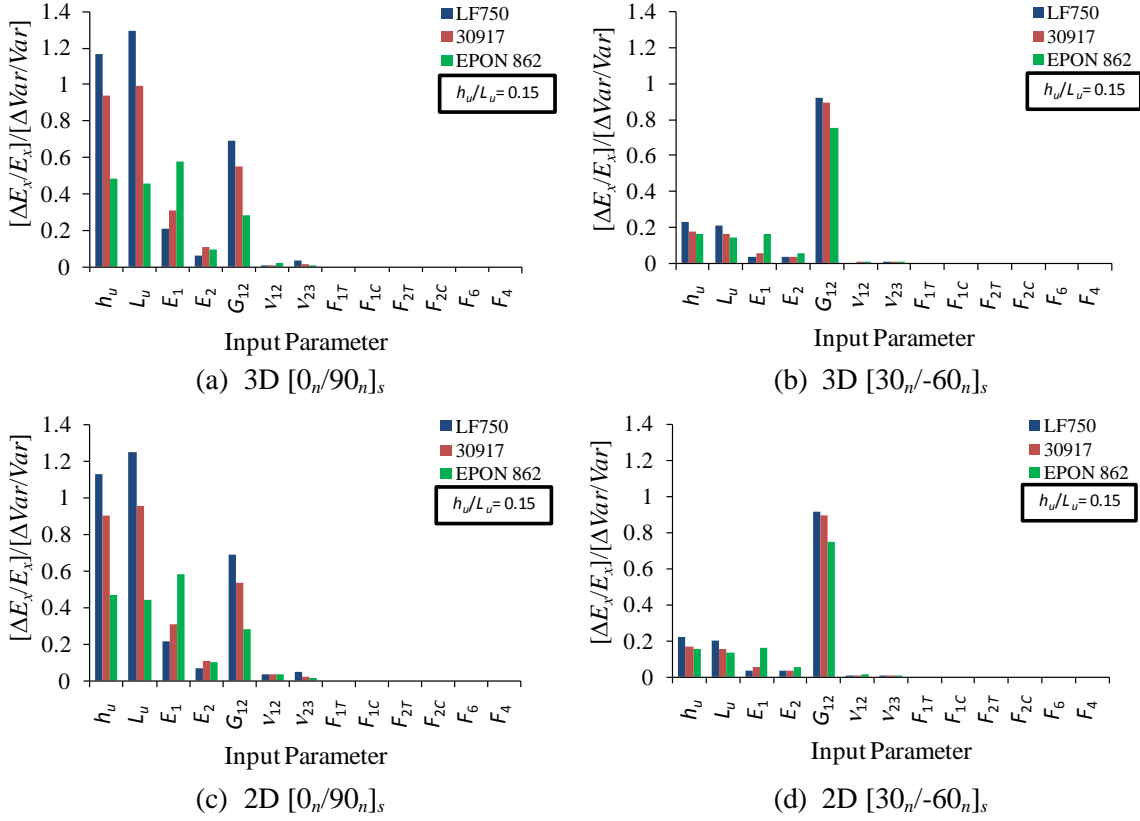


Figure 4-20. Flat undulation two and three dimensional sensitivity: longitudinal modulus

The failure envelope for discrete undulated specimens was calculated using CLT (**Figure 4-21**). Lamina stresses were determined by applying longitudinal compressive stress to the homogenized material (dark outline). The resultant lamina (light outline) strains are applied to the lamina stiffness to determine the xyz -frame stresses. The xyz -frame stresses are then rotated into the 1-2 coordinate system using well known transformation equations. Out-of-plane stresses are not introduced until the lamina stress is rotated out-of-plane by the transformation $T_{ij}^k(\alpha)$ for the 2D method. The 3D method includes many more material couplings, resulting in a “higher order” expression for each stress component (**Figure 4-21**).

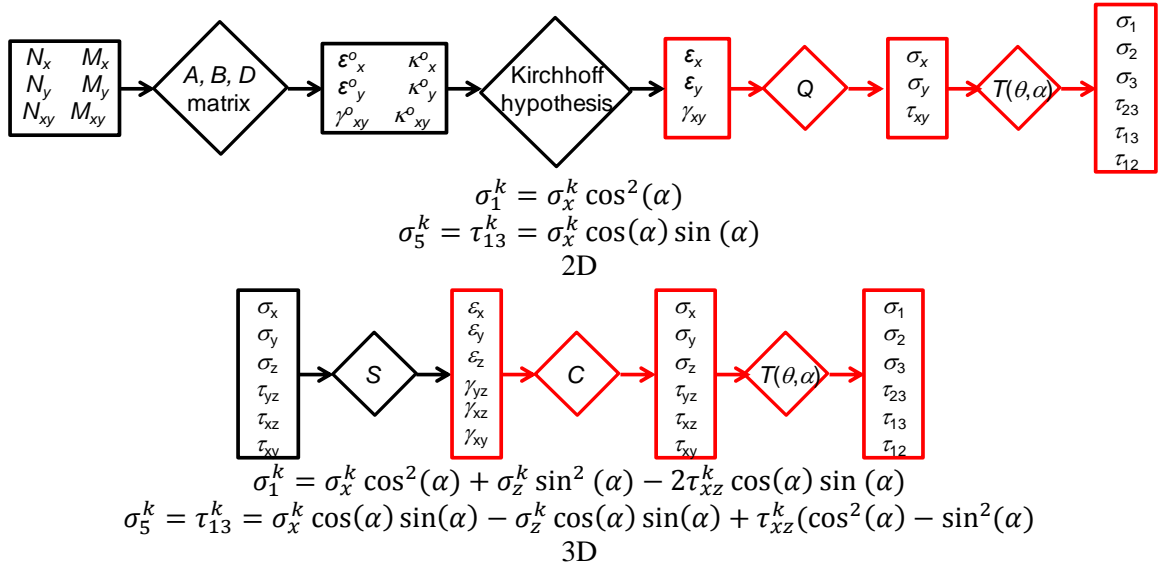


Figure 4-21. Lamina level stress calculation diagram

Lamina strengths were taken from Henry (2012) (**Table 4-6**). Fiber direction compressive strength was scaled to $V_f = 50\%$. Transverse isotropy was assumed so that properties in the 2-direction may be assumed equal to properties in the 3-direction. The shear strength in the 2-3 plane F_4 was assumed to be equal to 80 % of F_6 (Bogetti et al., 1992).

Table 4-6. Lamina strength properties: discrete undulation (Henry, 2012)

Parameter	LF750	30917	EPON 862	Parameter	LF750	30917	EPON 862
F_{1T} , MPa	2250	2250	2270	$*F_{1C}$, MPa	259	698	1034
F_{2T} , MPa	10.1	23.0	46.7	F_{2C} , MPa	27.5	50.3	131
F_{3T} , MPa	10.1	23.0	46.7	F_{3C} , MPa	27.5	50.3	131
F_4 , MPa	11.8	19.1	43.8	F_6 , MPa	14.8	23.9	54.8
F_5 , MPa	14.8	23.9	54.8				

*Henry et al. (2014)

MST (**Equation 4-87**), Tsai-Wu (TW) (**Equation 4-88**), and Henry et al., 2014 (H) (**Equation 4-89**) failure criteria were used to predict longitudinal compressive failure stress (**Figure 4-22**).

$$1 > \frac{\sigma_i^k}{F_i} \quad (4-87)$$

$$1 > \left[\sum_{i=1}^3 \left\{ \left(\frac{1}{F_{iT}} - \frac{1}{F_{iC}} \right) \sigma_i^k + \frac{1}{F_{iT}F_{iC}} (\sigma_i^k)^2 - \frac{1}{2} \left(\frac{1}{\sqrt{F_{iT}F_{iC}F_{(i+1)C}F_{(i+1)T}}} \right) \sigma_i^k \sigma_{(i+1)}^k \right. \right. \\ \left. \left. - \frac{1}{2} \left(\frac{1}{\sqrt{F_{iT}F_{iC}F_{(i+2)C}F_{(i+2)T}}} \right) \sigma_i^k \sigma_{(i+2)}^k \right\} + \sum_{j=4}^6 \frac{1}{F_j^2} \sigma_j^2 \right] \quad (4-88)$$

$$1 > \left(\frac{\sigma_1}{F_{1C}} \right)^2 + \sum_{i=5}^6 \left(\frac{\sigma_i}{F_i} \right)^2 \quad (4-89)$$

For the range of neat resin modulus and undulation amplitude/length investigated there was little difference in the strength prediction for $[0_n/90_n]_s$ laminates using any of the failure criteria when considering a singular method, 2D or 3D. The predicted failure mode for $[0_n/90_n]_s$ laminates was primarily σ_1 for the three dimensional approach and σ_5 for the two dimensional approach. The out-of-plane stress terms in the xyz frame for the 3D method decrease σ_5 and increase σ_1 compared to the 2D method. The two and three dimensional failure mechanisms are grouped in brackets “[2D/3D]” (**Table 4-7**). The undulation amplitude/length which causes a transition in the failure mode from the laminated case is also listed.

$[0_n/90_n]_s$ specimen failure was observed experimentally to be highly concentrated at the region where the undulation starts to sub-duct in the specimen. Analytically the failure was always predicted to occur at the center of the undulation where the material was most oriented out-of-plane. Experimental strength measurements considering scatter were observed to generally fall within the predicted bounds. The 2D approach provided lower predictions of composite strength due to the ratio of stress F_5 being proportionally lower than F_{1C} . Prediction correlation to experimental results is sensitive to the half-sine assumed shape of the undulation and anti-symmetry of the undulation shape about the laminate centerline and through the width, which would contribute additional coupling terms.

The major stress component of $[30_n/-60_n]_s$ specimen testing was σ_6 with LF750 providing a exception at high undulation amplitude in **Table 4-7**. The measured experimental failure strengths largely fall near the various theories, with the exception of EPON 862. This result will be commented on later when discussing strength prediction sensitivity.

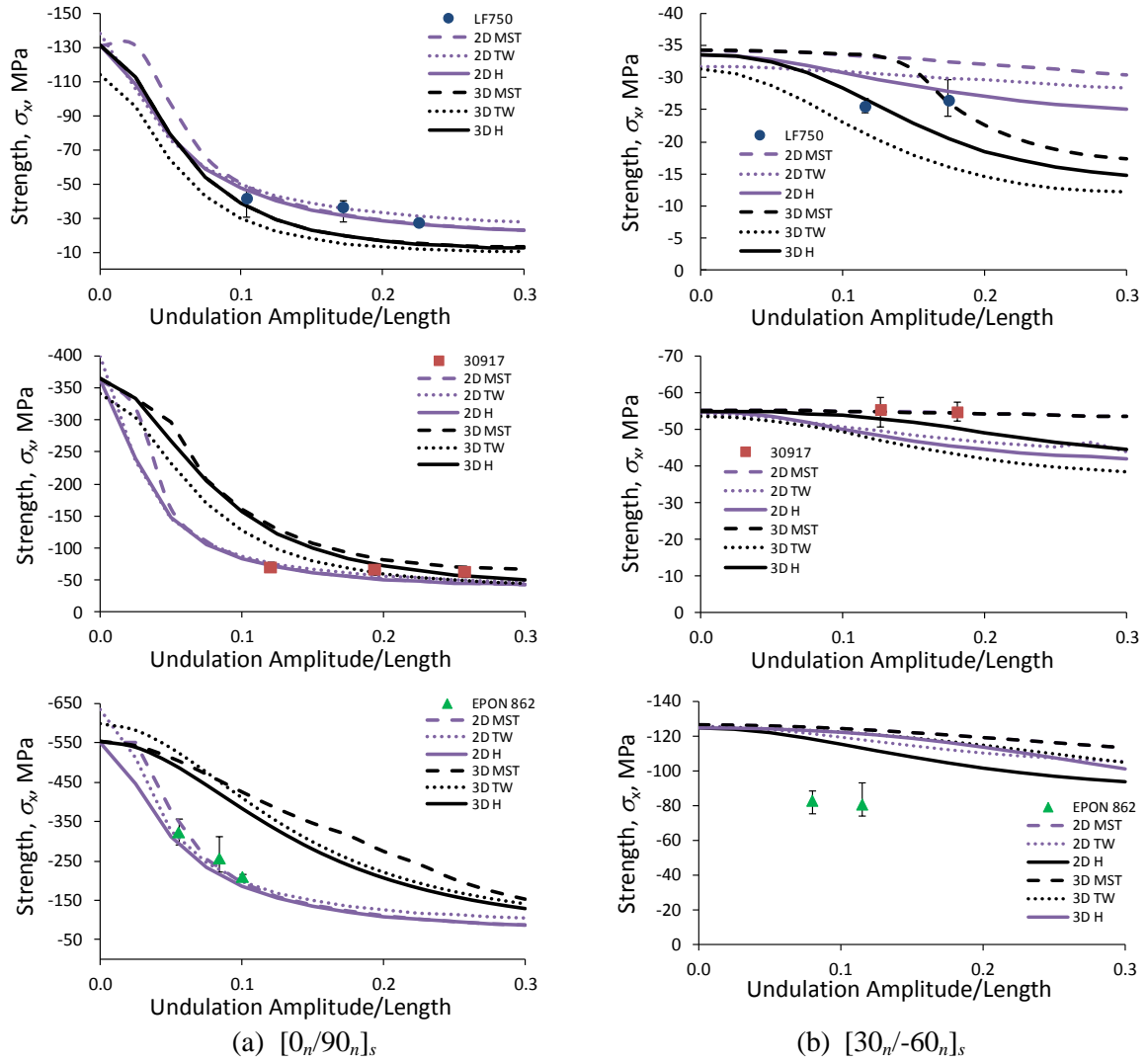


Figure 4-22. Flat undulated longitudinal strength experimental and theoretical results

Table 4-7. Flat undulated failure mode and transition undulation amplitude over length:
[2D/3D]

Material System	Laminate Stacking Sequence					
	[0 _n /90 _n] _s			[30 _n /-60 _n] _s		
	Non-undulated failure mode	Transition h_u/L_u	Large h_u/L_u failure mode	Non undulated failure mode	Transition h_u/L_u	Large h_u/L_u failure mode
Adiprene LF750	$[\sigma_1/\sigma_1]$	[0.025/-]	$[\sigma_5/\sigma_1]$	$[\sigma_6/\sigma_6]$	[0.25/0.15]	$[\sigma_5/\sigma_1]$
Conathane DPRN 30917	$[\sigma_1/\sigma_1]$	[0.025/-]	$[\sigma_5/\sigma_1]$	$[\sigma_6/\sigma_6]$	[-/-]	$[\sigma_6/\sigma_6]$
EPON 862	$[\sigma_1/\sigma_1]$	[0.025/-]	$[\sigma_5/\sigma_1]$	$[\sigma_6/\sigma_6]$	[-/-]	$[\sigma_6/\sigma_6]$

The strength failure theory chosen to represent flat undulated specimens was MST to maintain self-consistency in this research. The two and three dimensional MST approaches yielded a lower and upper bound respectively to the strength prediction of the undulated RVE with each assuming a different failure mode **Figure 4-23**. The experiment was well represented by the theory as the experimentally measured points fall largely within the bounds excluding EPON [30_n/-60_n]_s. This result validates the use of the homogenization theory in the prediction of the strength and modulus of undulated composites.

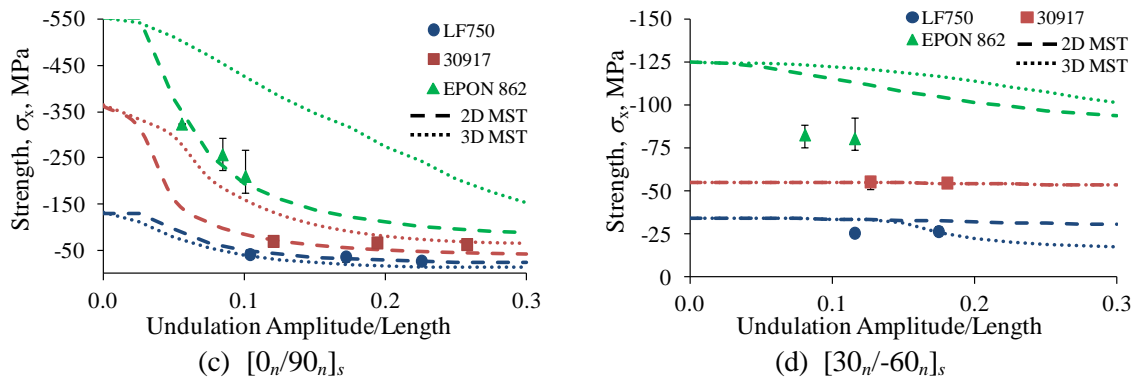


Figure 4-23. Flat undulated longitudinal experimental strength and MST predictions

The sensitivity of the two and three dimensional predictions of strength was found to be very different for $[0_n/90_n]_s$ specimens and very similar for $[30_n/-60_n]_s$ specimens (**Figure 4-24**). The strength prediction of $[0_n/90_n]_s$ specimens was very strongly influenced by the undulation geometry. The input parameters E_1 , G_{12} , and F_{1C} were additionally important with the 3D method; while for the 2D method, only F_6 was additionally important. The stress component σ_1 from three dimensional theory equals,

$$\sigma_1 = [C_{11}\varepsilon_x + C_{13}\varepsilon_z] \cos(\alpha)^2 + [C_{31}\varepsilon_x + C_{33}\varepsilon_z] \sin(\alpha)^2 - 2[C_{51}\varepsilon_x + C_{53}\varepsilon_z] \cos(\alpha) \sin(\alpha)$$

illustrating the extensive elastic coupling related to E_1 (C_{1x} terms) and G_{12} ($=G_{13}$, C_{5x} terms). A larger value of F_{1C} influenced the three dimensional laminate failure strength because it is the predicted failure mode. A higher value of F_{1C} will increase the laminate strength by increasing the allowable value of σ_1 before failure. The 2D predicted failure mode is $\sigma_5 = Q_{11}\varepsilon_x \cos(\alpha) \sin(\alpha)$. A stiffer laminate with a larger Q_{11} will require a smaller applied strain (ε_x) to yield the same σ_5 , therefore only the geometry and the allowable stress for that component F_5 (equal to F_6) were influential to the two dimensional strength of the laminate.

The strength predictions for $[30_n/-60_n]_s$ specimens were only greatly influenced by F_6 , the predicted failure mode **Table 4-7**. The prediction inaccuracy for EPON 862 specimens of this type can be attributed to a combination of previously mentioned concerns, such as poor undulation shape compared to the assumed sinusoid, and poor symmetry about the laminate centerline caused by low resin viscosity which “flows” when subjected to heat and pressure, leading to poor undulation shape control and uniformity through the laminate width. A lower experimental strength would be expected if the undulating lamina at sub-duction showed a “dog-leg” or step-wise, change instead of a gradual continuous sinusoid path increasing strain concentrations and out-of-plane inclination angles. An effective F_6 which takes into account these effects would yield better longitudinal strength predictions. Such a value could be determined through empirical testing similar to Henry et al. (2014).

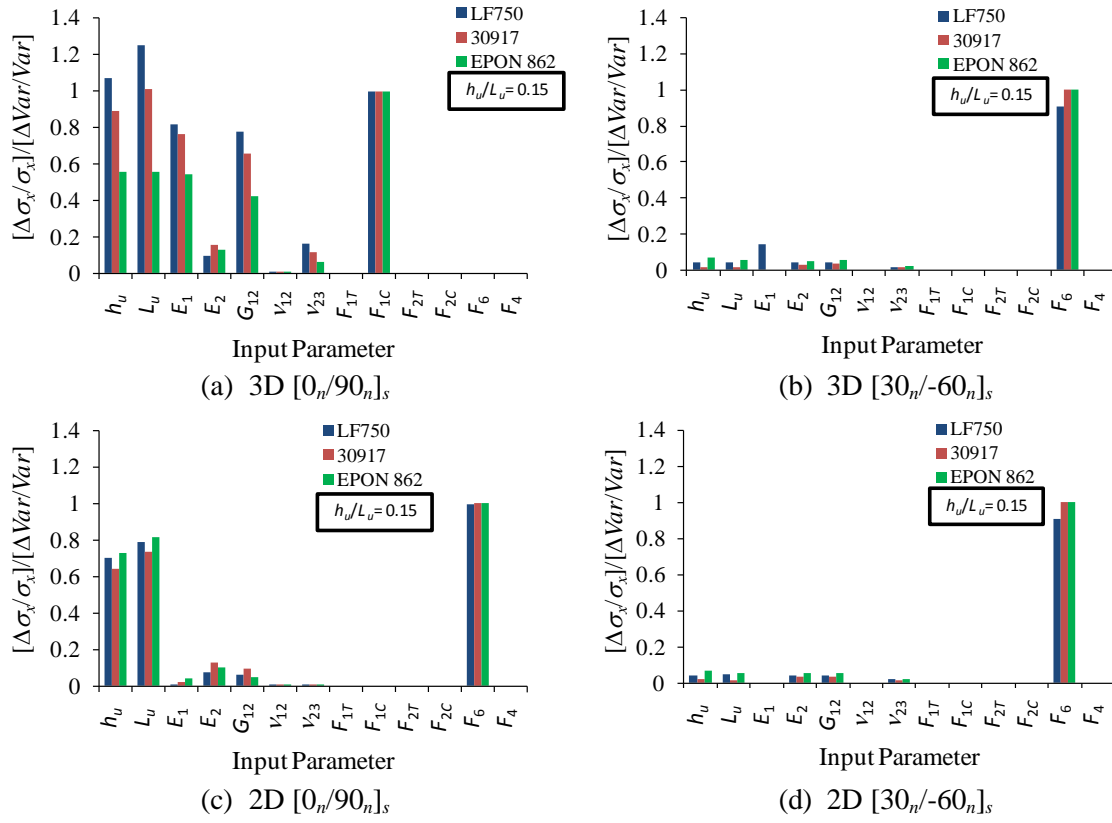


Figure 4-24. Flat undulation two and three dimensional sensitivity: longitudinal strength by MST

Chapter 5

Filament Wound Cylinder Three Dimensional DIC

This chapter focuses on the observation of the effects of filament winding parameters and matrix modulus of elasticity on full-field strain and structural behavior of composite cylinders under longitudinal compression. Fiber direction compressive strength (σ_{1c}) was shown to be a common limiting factor in driveshaft design (**Chapter 3**) with in-situ measured values dependent on the undulation architecture (**Chapter 4**). The strain distributions and failure mechanism of more geometrically complicated structures compared to discrete undulation shows a lack of understanding in the literature. Three dimensional digital DIC was used to measure in- and out-of-plane displacements on compressively loaded cylinders, which in turn are used to calculate in-plane strains and radial displacement changes with respect to applied stress. Based on these measurements, the onset of fiber microbuckling could be observed in many cases. Two material systems were evaluated in this chapter, 30917 (FMC) and EPON 862 (RMC) with varying FWP and winding angle.

A local-global homogenization approach was developed to calculate the modulus and strength of filament wound cylinders. The homogenization scheme utilizes the validated three dimensional RVE method of **Section 4.3**. Several RVEs were defined for the filament wound cylinder. The undulation geometry for each RVE was measured by cutting representative sections from post-tested filament wound cylinders and analyzing the sections optically with a microscope after polishing. Analytical predictions of the longitudinal modulus, Poisson's ratio, and ultimate compressive strength were compared to the experimental results for the various materials and FWPs. Predictions of failure location and mode compared favorably with the experiment.

5.1 Helically Wound Composite Cylinder Test Method

Cylinders, $[\pm\theta/89/\pm\theta]$ laminate, were compression tested at the Army Research Laboratory on a Model 1127 Instron (Norwood, MA) electromechanical universal testing machine with load voltage acquired and exported by the software Bluehill 2. The cross-head rate was set to 3.5 mm/min. A 222 kN load cell was used to measure the applied load. DIC was used to measure displacements in three dimensions (longitudinal, hoop, and radial) on the outer surface of the specimen, over an arc of about 120 deg. in the azimuthal direction. DIC measured the displacement of contrasting features in a random speckle pattern painted on the surface of the specimen (Chu et al., 1995; Sutton et al., 1983). In-plane strains were calculated from the in-plane displacements using the program Vic 3D (Correlated Solutions Inc., Columbia, SC). The speckle pattern was created using commercially available flat black and white spray paints (**Figure 5-1**). Black and white spray paints provide the largest color/brightness contrast in gray scale coloring. In this investigation, two Point Grey Research (Richmond, B.C. Canada) GRAS-20S4M digital cameras were used to acquire images simultaneously in a stereo setup, allowing the measurement of in-plane as well as out-of-plane displacements simultaneously (Bruck et al., 1989; Sutton et al., 2000).

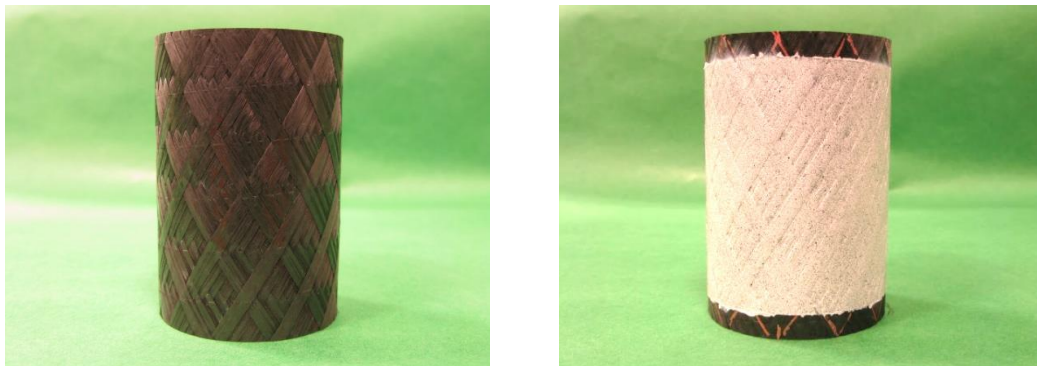


Figure 5-1. Unpainted (left) and painted (right) specimen

Prior to testing, specimens were potted in end caps to prevent the ends from “brooming” during testing (**Figure 5-2**). A hemispherical bearing was placed in the load train to minimize the transmission of moments to the specimen due to misalignment. A florescent lamp provided area illumination and a flexible head lamp provided local illumination where needed in the area of interest, AOI. Cameras were placed approximately 61 cm behind the specimen, away from walkways. Nikon 28 mm – 105 mm variable focal length lenses were used for focusing and framing the image.

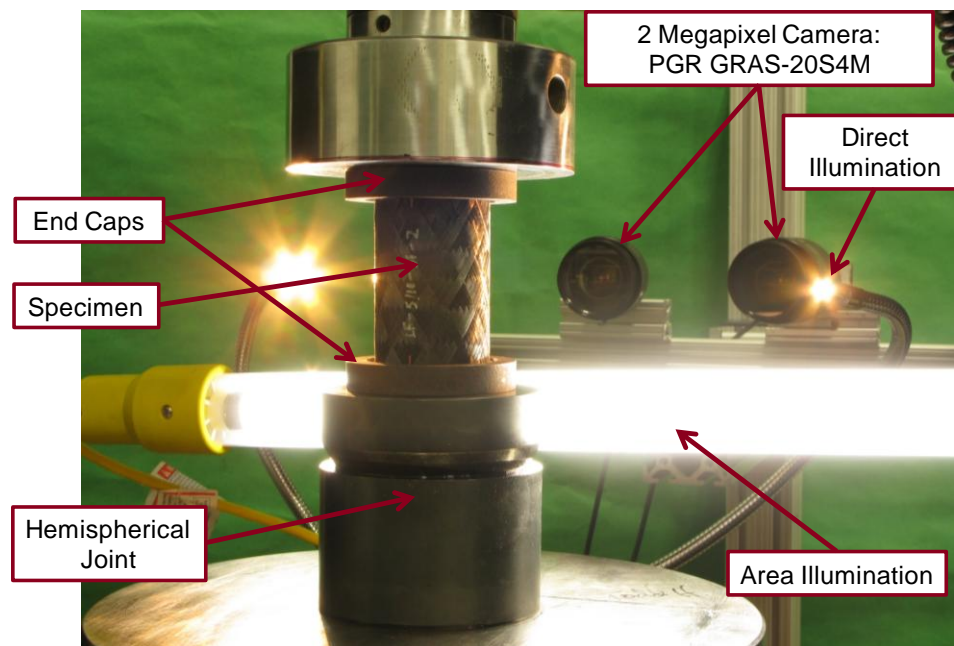


Figure 5-2. Helically wound cylinder compression test set-up

Preliminary experiments were carried out using 0.3 megapixel camera. With this camera, the FWP was observable in the radius measurement before loading, R , as well as in the increment in radius from the unloaded condition to impending failure, dR_f . On the other hand, the FWP was not observable in the in-plane strain fields. This is most certainly due to the method of strain calculation used by the DIC program, Vic-3D. Strain calculation can be controlled by resolution and noise tradeoffs of the correlated images through the use of subset and step size. The subset

size was the area of the image, in pixels, that was used to determine the displacement increment between two images (Correlated Solutions, 2010). If the subset size was too small, Vic-3D may not be able to distinguish each area during correlation due to a coarse speckle pattern or non-ideal lighting. A larger subset decreases resolution, noise, and correlation time by effectively reducing the number discrete displacements that need to be calculated. An effort was made in this investigation to create a fine speckle pattern which allowed for a subset size of 25.

The step size was the number of pixels used to generate one data point for the correlated mapping of strain, displacement, etc. If the step size was 1, a correlation was performed on every pixel in the area of interest, AOI. A step size of 7 was found to be an adequate trade-off between correlation time and resolution of the mapped field. Calculated strains were smoothed using a local filter in Vic-3D. The filter size was given in terms of data points rather than pixels. The physical size of the filter on the images also depends on the step size used during correlation. For this investigation, a strain filter size of 7 and Lagrange tensor type were used.

Increasing the spatial resolution of the AOI was the easiest solution for better visualization of FWP. This was made possible by using higher resolution cameras as was ultimately done in this investigation. The AOI was nominally 96.5 mm wide by 70.0 mm tall. For a 0.3 Mp camera (640×480 px) the spatial resolution was 6.6×6.9 px/mm, and for the GRAS-20S4M (1624×1224 px) the spatial resolution was 16.8×17.5 px/mm. For the testing done in this investigation, the resolution of the GRAS-20S4M was sufficient. Global strains discussed in the DIC results refer to the x - y coordinates (**Figure 1-1**). Transformation equations were developed for the calculation of strains in the principal coordinates of the surface lamina (with normal strains in the x and y directions of the DIC system trading places in traditional strain transformation equations) (Gibson, 2007).

5.2 Experimental Results

Specimens are described in terms of lamination arrangement in square brackets [-] and FWP in curved braces {-}. Contour plots of the outer radius of unloaded RMC and FMC specimens of type $[\pm 31/89/\pm 31] \{10/10\}$ are shown in **Figure 5-3**. The helical and circumferential crossover bands of the FWP in the outermost layer are highlighted with dashed lines. The differences seen in the outer radius are attributable to the sequence in which tow in the outermost layer was deposited with a helical winding pattern. For the first helical passage at angle θ , the carriage deposits the tow smoothly onto the previous layer. However, as the carriage returns and deposits the tow at $-\theta$, each time the fiber crosses over the previous passage it was elevated away from the surface by the small thickness of the previously laid tow. This process of incremental elevation of the tow continues with each passage of the carriage. The first passage was therefore at the smallest radial position and the last passage was at the largest radial position, with a step-wise change between passages. While the elevated tows are forced inwards and compacted to some extent by subsequently wrapped tow and shrink tape, from the results in **Figure 5-3** it is apparent that the as-cured surface maintains a small variation of height across each rhombic repeating element. In both material systems, the variation of outer radius as a function of position in the repeating rhombic pattern was approximately 0.3 mm, which is between 1% and 2% of the nominal outer radius.

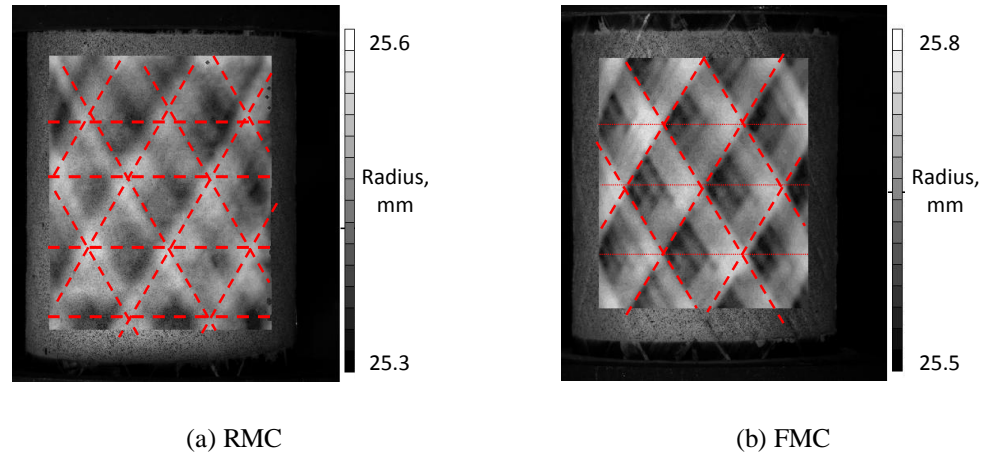


Figure 5-3. Outer radius measurement of $[\pm 31/89/\pm 31]$ $\{10/10\}$ cylinders with no applied stress.

Figure 5-4 shows representative longitudinal strain fields in RMC and FMC specimens of pattern $\{2/2\}$, $\{5/5\}$, and $\{10/10\}$ at loads prior to the initialization of microbuckling. In general, higher magnitude longitudinal strains were observed at the center of the FWP rhombus compared to the undulated material region surrounding the rhombus, which was opposite the expectation in undulated regions, according to the modeling results discussed in the introduction. These differences were roughly $5000 \mu\epsilon$ for RMC specimens (about 20-33% of the mean field value) and $2000 \mu\epsilon$ for FMC specimens (about 33-50% of the mean field value) at the applied stresses shown. Therefore, in the representative results shown, there was slightly less fractional variation in longitudinal strain for the RMC material than for the FMC material.

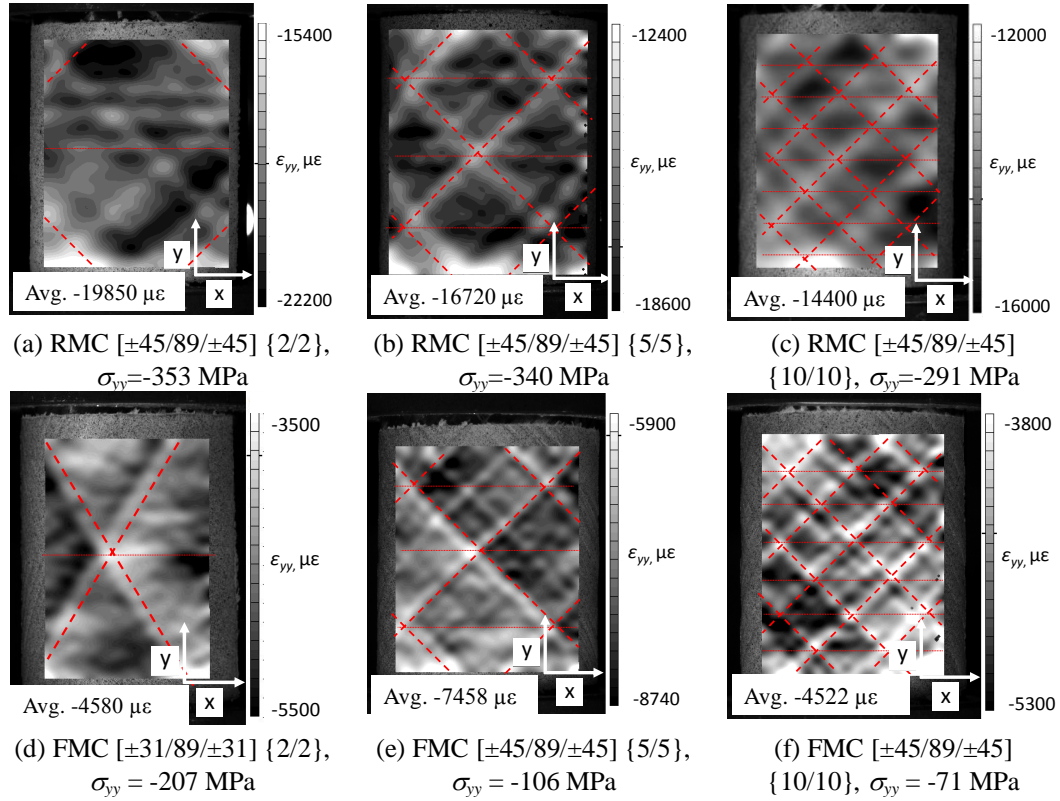


Figure 5-4. Global longitudinal strains, ϵ_{yy} , in cylinders prior to fiber microbuckling.

Figure 5-5 shows representative hoop strain fields in RMC and FMC specimens of pattern $\{2/2\}$, $\{5/5\}$, and $\{10/10\}$ prior to the initiation of microbuckling. A gradient in hoop strain was roughly $4000 \mu\epsilon$ for RMC and FMC specimens alike. In terms of proportion, this $4000 \mu\epsilon$ variation was a much larger multiple of the mean hoop strain with low helical fiber angle (16 deg.) than with the higher fiber angles (31 and 45 deg.). This result can be rationalized by considering that the hoop bending modulus was less for the smaller fiber angles than for larger fiber angles. In general, the hoop strain gradient was also a larger multiple of the mean hoop strain in the FMC material than the RMC material.

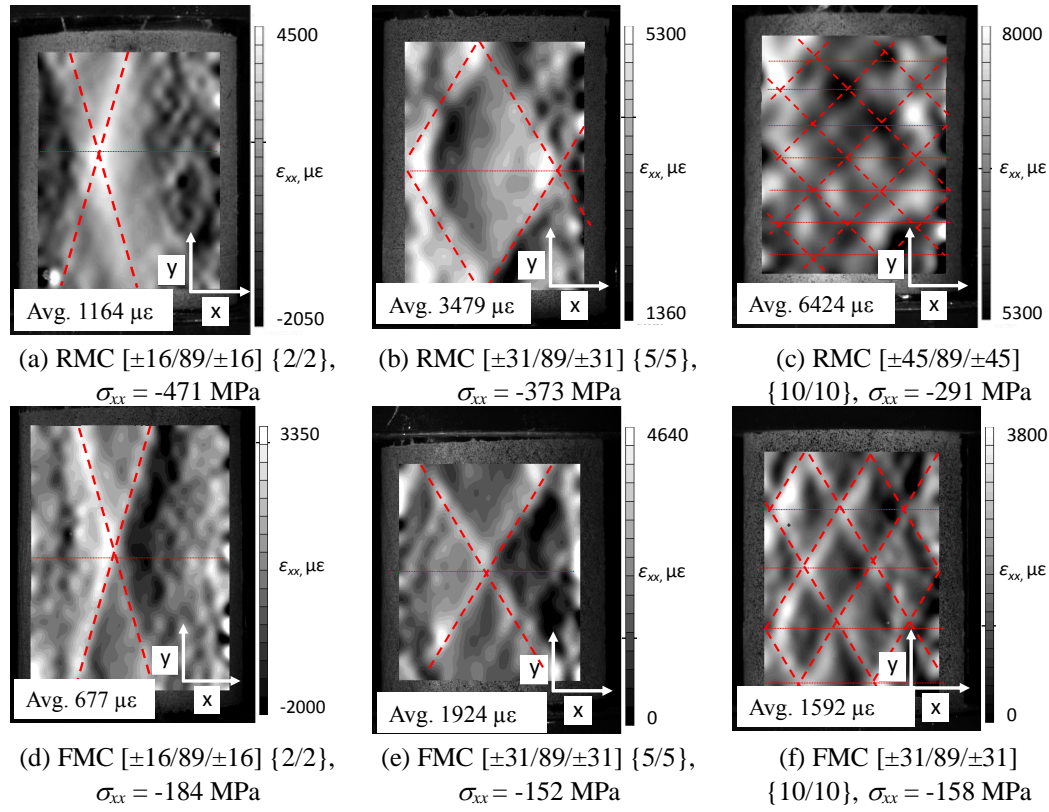


Figure 5-5. Global hoop strains, ϵ_{xx} , in cylinders prior to fiber microbuckling.

The rhombic region (dashed area in **Figure 5-6**) was seen to twist such that the positive gradient in dR_f (blue to red, **Figure 5-6a**) points in the same right-ward direction as the positive gradient in hoop strain (black to white, **Figure 5-5b**). The warping of the anti-symmetric rhombic regions contributes larger amounts of hoop strain when the warping was of higher magnitude, creating the hoop strain gradient. The warping and gradient in the hoop strain were believed to be caused by out-of-plane elastic couplings in the undulation bands and anti-symmetrically laminated regions within the rhombi. The elastic coupling effects have been modeled (Hipp and Jensen, 1992; Jensen and Hipp, 1991) and, to some extent, measured (Claus, 1994) by others in previous work with rigid matrix composite material systems, as discussed in the introduction.

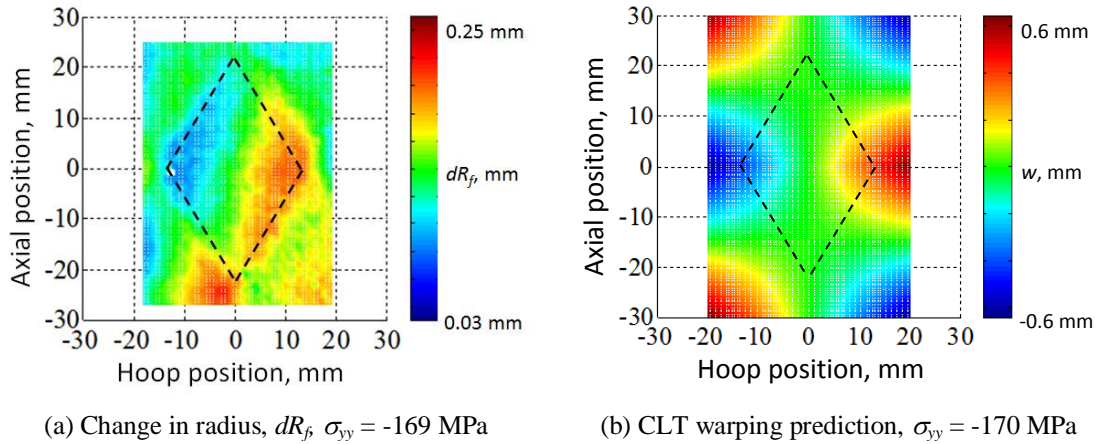


Figure 5-6. Out-of-plane displacement according to DIC data and theory for an FMC $[\pm 31/89/\pm 31]$ {5/5} specimen.

CLT was used to predict the trend in warping shape. Compressive longitudinal stress (σ_{yy}) was applied to two square laminated plates representing the stacking sequences in the upper and lower triangles of **Figure 5-6a**: $[\pm 31/89/\pm 31]$ and $[\mp 31/89/\mp 31]$, respectively. Out-of-plane displacements (w) were set equal to zero along the x and y axes passing through the middle of each plate, for convenience. The two square laminates then had matching displacements where they join together when placed end-to-end, as shown in **Figure 5-6b**. The CLT model qualitatively predicts the trend in warping seen in the experiment. In reality, the rhombic region being modeled has complicated boundary conditions (due to fiber undulation) and the surface was curved, which prevents quantitative comparisons of the experimental and theoretical results. While it was known that thin-walled cylindrical specimens can continue to carry compressive loads after buckling in modes similar to that shown in **Figure 5-6** (Hipp and Jensen, 1992; Jensen and Hipp, 1991; Claus, 1994), specimens in the current investigation failed by microbuckling and showed no evidence of post-buckled load carrying capacity (bifurcation).

The reduced longitudinal strain magnitude in the undulated region versus the laminated region of the cylinder became more apparent as the applied stress increased. To illustrate this point, **Figure 5-7** shows the longitudinal strain as a function of applied longitudinal stress, along

a vertical path in the AOI of a $[\pm 45/89/\pm 45]$ $\{5/5\}$ RMC specimen. The path A-A' passes through a junction of two helical undulation bands and one circumferential undulation band near mid-height of the AOI. The lowest magnitude longitudinal strain along the path A-A' was clearly located at the intersection of the helical and circumferential undulations.

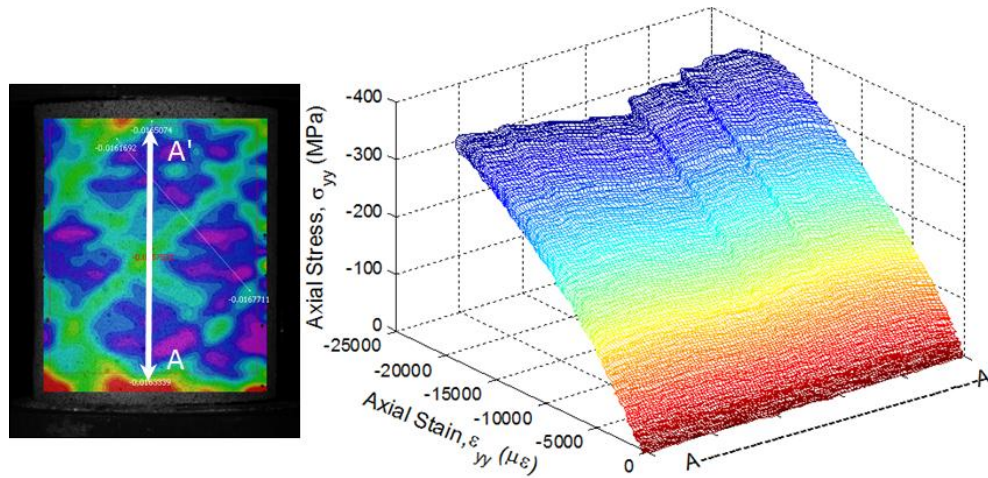


Figure 5-7. Longitudinal strain along path A-A' in an RMC $[\pm 45/89/\pm 45]$ $\{5/5\}$ specimen, highlights reduced longitudinal strain magnitude in undulated vs. laminated regions of FWP

While the failure process can initiate and localize anywhere in the tubular specimens, in a few cases it occurred within the viewed area and was able to be captured by the cameras. Mostly, this occurred in FMC specimens rather than RMC specimens, since the damage localization and failure in the latter was typically very fast. **Figure 5-8** focuses on the strain in the direction of the fibers, ϵ_{11} , at incipient failure in three different laminates of FMC material. Triangular regions of $-\theta$ fiber orientation have been shaded out to draw attention to the triangular regions with fibers at the $+\theta$ orientation, as defined in **Figure 1-1**. The concentration of fiber direction strain that leads to microbuckling failure always occurred near the intersection of the circumferential and helical undulation bands.

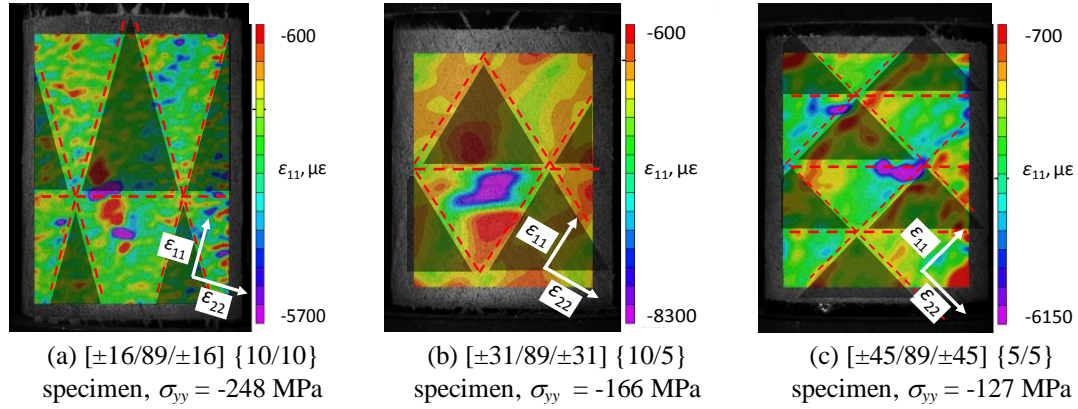


Figure 5-8. Strains in FMC specimens in the lamina longitudinal direction, ε_{11} , immediately before failure. Un-shaded regions have fibers in the 1-direction shown.

A representative set of DIC images showing microbuckling onset near the junction of helical and circumferential undulation bands is shown in **Figure 5-9** for an FMC specimen. **Figure 5-9** shows the initial outer radius measurement, which, as mentioned earlier, is sensitive to the sequence in which tows are wound on the mandrel. The area of damage localization in the upper right corner of the AOI corresponds to a position of high outer radius (**Figure 5-9a**), corresponding to the last tow wound onto the mandrel. This area also contains high strain magnitudes in the local lamina coordinate system (**Figure 5-9b-d**), and a high increment in radius relative to the initial radius (**Figure 5-9e**). The fiber microbuckling band grows circumferentially, as shown in **Figure 5-9e**. After the microbuckled band traverses a sufficient fraction of the circumference of the cylinder, failure of the specimen occurs, as seen in the photograph in **Figure 5-9f**.

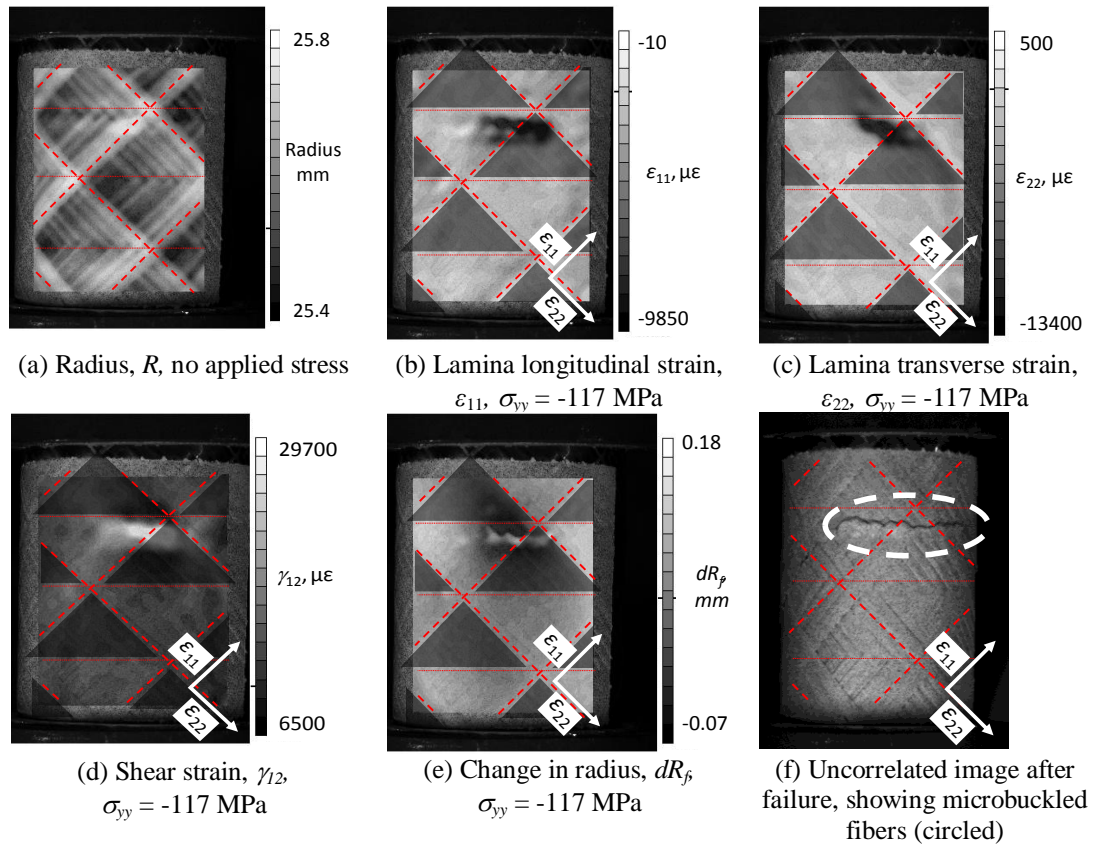


Figure 5-9. DIC data for an FMC $[\pm 45/89/\pm 45] \{5/5\}$ specimen near failure (a-e) and after failure (f). Un-shaded regions shown in (b-e) have fibers in the 1-direction shown.

Material characterization results are presented in **Table 5-1** for RMC cylinders and **Table 5-2** for FMC cylinders. Strains leading to these results were found by averaging the correlated strain map across the entire AOI. The longitudinal modulus of each cylinder was measured using a least squares fit in the 1000-2000 $\mu\epsilon$ range. Modulus and strength values were normalized for a fiber volume fraction of 58%.

Table 5-1. Normalized compression test results for RMC cylinders

Helical Angle, deg.	Pattern	Average Modulus, GPa	C_v (%)	Average Ultimate Strength, MPa	C_v (%)	Average Longitudi nal Strain @ Ultimate, $\mu\epsilon$	C_v (%)	Average Longitu dinal Poisson's Ratio	C_v (%)
16	{2/2}	90	3	449	8	5300	11	0.29	6
	{5/5}	91	6	407	6	4440	10	0.29	6
	{10/10}	92	6	428	7	4830	12	0.28	3
	{5/10}	93	5	437	8	4820	10	0.29	3
	{10/5}	87	4	468	8	5480	8	0.28	8
31	{2/2}	49	4	354	8	7740	12	0.50	4
	{5/5}	52	9	326	7	6364	12	0.49	6
	{10/10}	51	3	372	2	7780	9	0.50	4
	{5/10}	52	4	351	11	7140	15	0.48	7
	{10/5}	50	7	360	7	7470	9	0.49	2
45	{2/2}	22	2	317	3	18700	5	0.44	2
	{5/5}	23	9	301	3	18000	5	0.44	4
	{10/10}	22	2	312	5	18800	8	0.45	2
	{5/10}	22	6	309	3	18900	4	0.45	2
	{10/5}	21	3	316	2	18600	2	0.44	2

Table 5-2. Normalized compression test results for FMC cylinders

Helical Angle, deg.	Pattern	Average Modulus, GPa	C_v (%)	Average Ultimate Strength, MPa	C_v (%)	Average Longitud inal Strain @ Ultimate, $\mu\epsilon$	C_v (%)	Average Longitu dinal Poisson's Ratio	C_v (%)
16	{2/2}	83	8	234	4	2800	3	0.34	5
	{5/5}	76	7	216	8	2750	8	0.31	17
	{10/10}	81	4	221	7	2630	10	0.30	7
	{10/5}	83	4	227	2	2640	3	0.30	7
31	{2/2}	42	6	207	7	4890	7	0.57	5
	{5/5}	45	7	172	2	3870	5	0.56	5
	{10/10}	45	3	176	4	3930	6	0.55	2
	{5/10}	44	4	180	4	4172	9	0.57	5
	{10/5}	44	3	167	6	3920	9	0.56	4
45	{2/2}	16	8	155	6	10300	12	0.46	3
	{5/5}	16	10	120	10	8500	20	0.47	3
	{10/10}	17	7	126	7	9000	12	0.46	4
	{5/10}	16	4	132	5	9690	3	0.46	6
	{10/5}	16	10	130	2	9640	3	0.45	3

Test results in **Table 5-1** and **Table 5-2** are shown in bar charts for modulus (**Figure 5-10**) and ultimate strength (**Figure 5-11**) to better visualize the effect of winding pattern. The modulus results in **Figure 5-10** show little effect of winding pattern. The strength results (**Figure 5-11**) show that pattern {5/5} provides the lowest strength of all patterns. This difference was especially apparent in the FMC material, where the {5/5} pattern strength was 8-23% less than the other patterns. In the RMC material, the effect of pattern is within the range of scatter. Hybridizing the pattern to {10/5} or {5/10} produced little change to the strength of the cylinder for FMCs or RMCs.

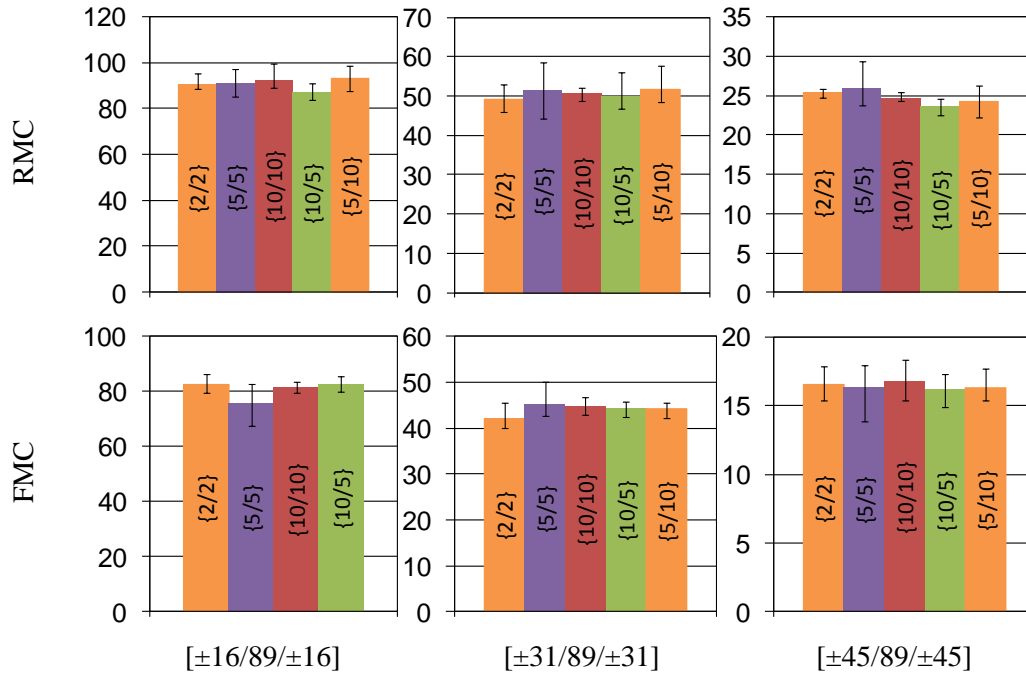


Figure 5-10. Average normalized modulus results, GPa, scatter bars indicate the range of replicate test results

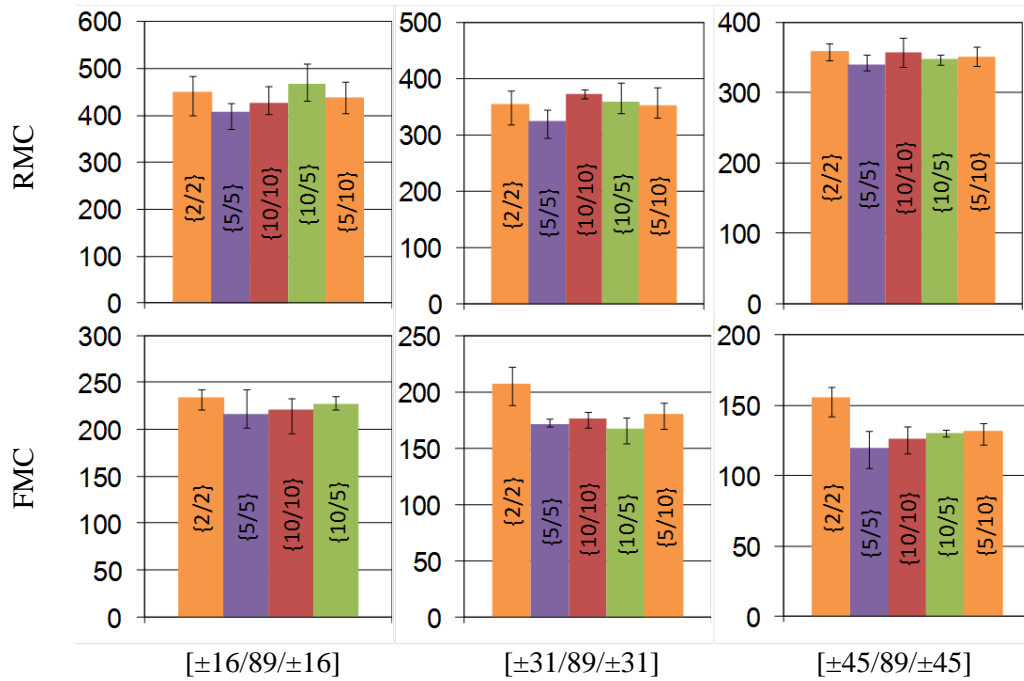


Figure 5-11. Average normalized ultimate strength results, MPa, scatter bars indicate the range of replicate test results

Localization of intense strains was observed to occur simultaneously with microbuckling onset shortly before specimen failure (**Figure 5-9b-e**). At least three FMC specimens of each fiber orientation (regardless of pattern), for which strain localization occurred in the AOI, were utilized in a statistical analysis of lamina-coordinate strains (ε_{11} , ε_{22} , and γ_{12}) immediately preceding specimen failure. Strains were calculated in a 10×10 grid of points encompassing the localized strain region (dashed rectangle, **Figure 5-12a,c**). An initial evaluation of strains in the grid area revealed that ε_{22} in the cylinders was much less than unidirectional lamina values according to Henry (2012). On the other hand, ε_{11} and γ_{12} were greater than their measured values in Henry (2012). Therefore, only ε_{11} and γ_{12} were analyzed in detail at impending failure. Discrete probability distributions of ε_{11} and γ_{12} in the 10×10 grid are represented in **Figure 5-12b,d**, respectively. Using the cumulative probability distribution, values of ε_{11} and γ_{12} corresponding to particular percentiles of the population of measurements were computed. For

example, the 20th percentile values of ε_{11} and γ_{12} were 3300 and 15,600 $\mu\epsilon$, respectively, while the 95th percentiles were 7520 and 23,700 $\mu\epsilon$, respectively, in the $[\pm 45/89/\pm 45]$ cylinder. The 95th percentile strains could be considered a measure of the highest sustained strains prior to failure, without the undue influence of noise in the measurements.

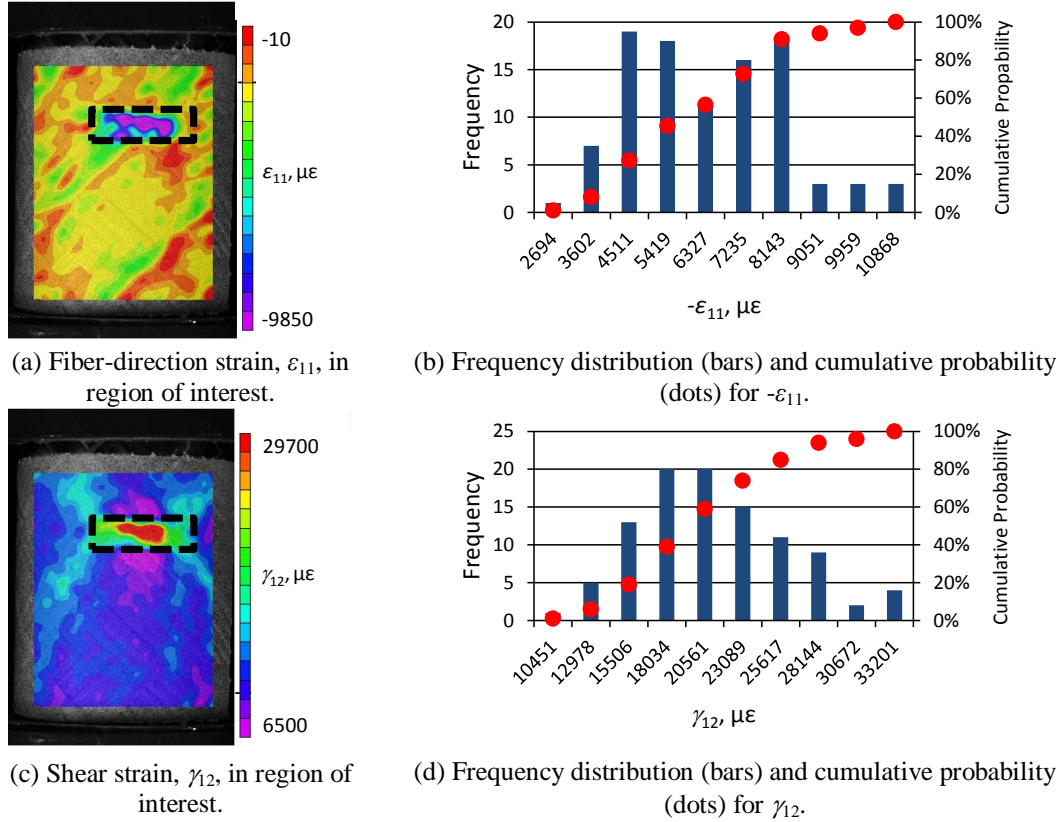


Figure 5-12. Example analysis of strain components in microbuckled region of interest in a $[\pm 45/89/\pm 45]$ {5/5} FMC cylinder

Based on a statistical analysis of lamina-coordinate strains in all FMC cylinders where failure initiated in the AOI, the 20th, 35th, 50th, 80th, and 95th percentiles of ε_{11} and γ_{12} are plotted against one another in **Figure 5-13**. Note that each percentile ($\varepsilon_{11}, \gamma_{12}$) point does not necessarily correspond to the state of strain at a single point in the grid area. For example, the 20th percentile point for ε_{11} might not be the same point in the material as the 20th percentile point for γ_{12} . Also plotted in **Figure 5-13** are the strains in the material calculated using CLT in conjunction with the

applied stress. CLT does not take into account fiber undulation and utilizes only the laminate stacking sequence, homogenized lamina properties (considering undulation) (Henry, 2012), and the applied stress at failure. The CLT points can be seen as limiting cases for the lowest percentile strains in the grid area. That is, the lower percentiles of strain in the region of strain localization approach the global strain state predicted by CLT. The 95th percentile ε_{11} is roughly 3.5 times larger than the CLT ε_{11} for $[\pm 16/89/\pm 16]$ and $[\pm 31/89/\pm 31]$ cylinders, and 4.5 times larger for $[\pm 45/89/\pm 45]$ cylinders. The 95th percentile γ_{12} is roughly 3.5 times larger than the CLT γ_{12} for $[\pm 16/89/\pm 16]$ cylinders and 2 times larger for $[\pm 31/89/\pm 31]$ and $[\pm 45/89/\pm 45]$ cylinders. These results indicate the magnitude of strain concentration existing in the cylinders immediately before failure and highlight the importance of ε_{11} and γ_{12} in the failure process.

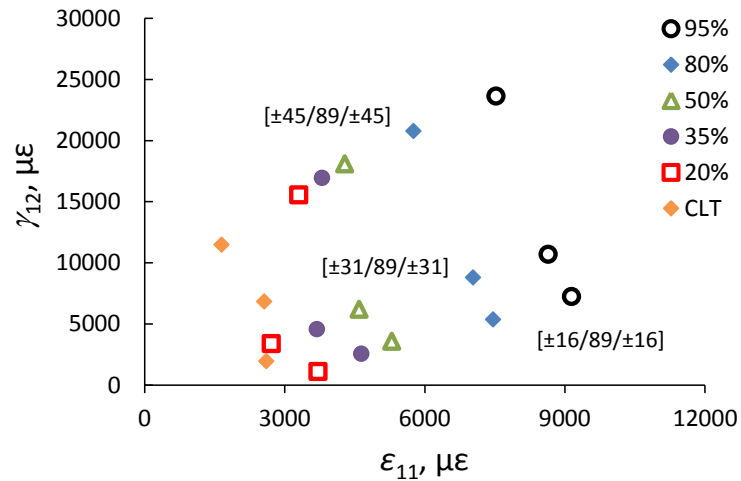


Figure 5-13. Various percentile strains, ε_{11} and γ_{12} , in FMC cylinders in the region of strain localization immediately prior to failure. Also shown are strains computed using CLT.

5.3 Analytical Methodology for Modulus and Strength

An analytical procedure was developed for homogenization of a filament wound cylinder rhombus. For an individual helically wound layer, the rhombus was divided into five smaller

RVE for which the elastic behavior was evaluated. The homogenized properties for each RVE were calculated and integrated into the larger, more geometrically complex rhombus structure. The global xy -coordinate system for the laminate was aligned such that the x -direction was oriented along the longitudinal direction of the rhombus and the y -direction was oriented along the circumferential direction of the rhombus (**Figure 5-14**). The path of the fiber reinforcement travels along θ with respect to in-plane rotation, and α with respect to out of plane rotation (**Figure 5-14a**). θ and α are zero when reinforcement is oriented along the x -direction, with each measured about the z -axis and y -axis respectively.

Three types of RVE were present in the rhombus; helical, circumferential, and non-undulated. The filament winding process creates fiber undulation which exists along the outside border of the rhombus, helical, and along the center of the rhombus, circumferential (**Figure 5-14b**). In the chosen coordinate frame, there were two helical RVE, A and B, along the positive y -direction side of the rhombus (**Figure 5-14c**). The helical RVE was created when one lamina traverses over or under another with the second lamina not undulating. A single circumferential RVE, C, was defined at the center of the rhombus where both lamina traverse over or under each other. The non-undulated area of the rhombus was defined by RVE D and RVE E which have $\mp\theta$ and $\pm\theta$ arrangements respectively.

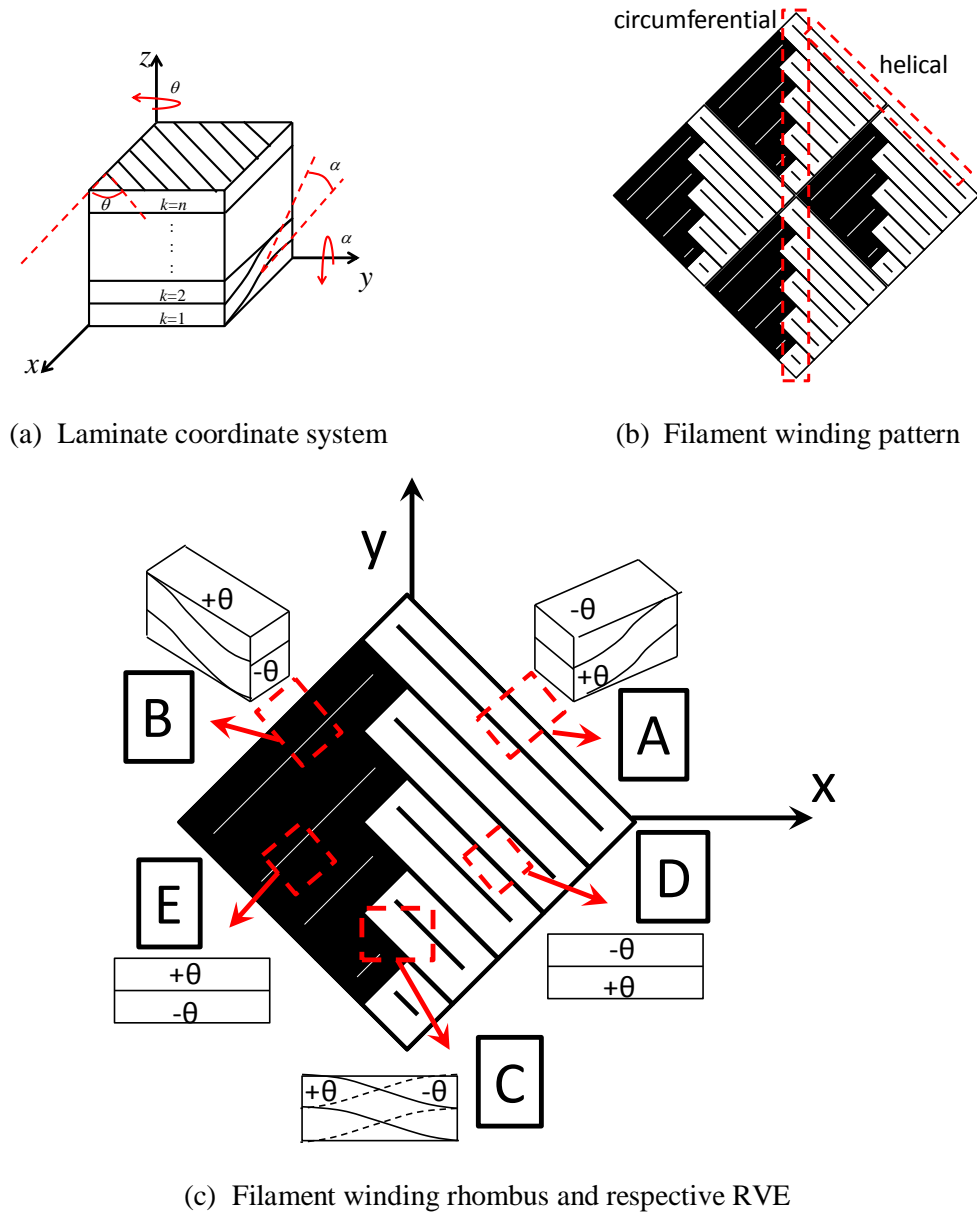


Figure 5-14. Filament wound rhombus RVE and coordinate system

Material properties (**Table 5-3**) for the various material systems were taken from Henry (2012). These material properties were identical to those of **Table 4-3** and **Table 4-6** with exception for E_1 and F_{IC} . E_1 and F_{IC} were found experimentally using a unidirectional bend test (Henry et al., 2014) and scaled to $V_f = 58\%$, the same value for the experiments.

Table 5-3. Lamina properties: filament wound cylinder (Henry, 2012)

Parameter	LF750	30917	EPON 862	Parameter	LF750	30917	EPON 862
$*E_1$, GPa	145	145	145	F_{1T} , MPa	2250	2250	2270
E_2 , GPa	1.57	4.73	8.56	F_{2T} , MPa	10.1	23.0	46.7
E_3 , GPa	1.57	4.73	8.56	F_{3T} , MPa	10.1	23.0	46.7
ν_{12}	0.30	0.32	0.32	$*F_{1C}$, MPa	259	698	1034
ν_{13}	0.30	0.32	0.32	F_{2C} , MPa	27.5	50.3	131
ν_{23}	0.87	0.74	0.58	F_{3C} , MPa	27.5	50.3	131
G_{12} , GPa	1.07	1.88	6.64	F_4 , MPa	11.8	19.1	43.8
G_{13} , GPa	1.07	1.88	6.64	F_5 , MPa	14.8	23.9	54.8
G_{23} , GPa	0.42	0.54	2.71	F_6 , MPa	14.8	23.9	54.8

*Henry et al., 2014

The geometric details of the RVE undulation were measured by extracting undulated cross-sections from post test filament wound cylinders. The region of the undulation was isolated from the cylinder, dashed box in **Figure 5-15**, with the side of intended inspection aligned with the undulating fiber. A cylindrical mold was cleaned with acetone and coated in one layer of release agent. The sample was set in EPON 8132/Jeffamine T403 (mix ratio 100:40 by weight) a clear epoxide with the double arrow side down in the cylindrical mold. The resin was then degassed at 30 inches of Hg to remove air bubbles. The molds were placed in a forced air convection oven at 116 °C (240 °F) for 8 hours. Undulated cross-sections were prepared for each winding angle (16, 31, and 45 deg.) and each material 30917 and EPON 862 (six total).

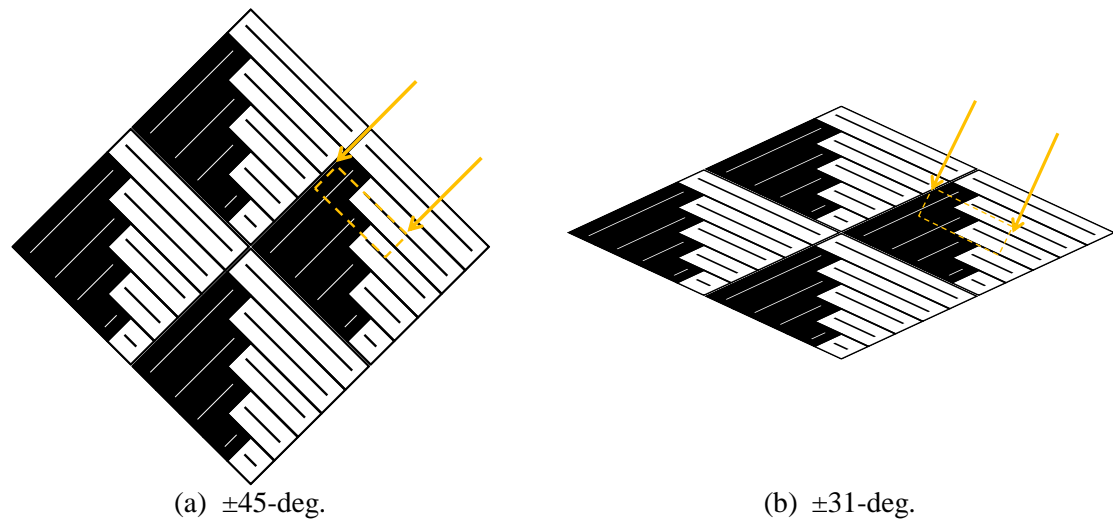


Figure 5-15. RVE undulation sample extraction

Mechanical undulated cross-section polishing was done at the Materials Research Institute (Penn State) in the Sample Preparation Laboratory. The objective of polishing was to create a smooth finish on the target side of the sample. The target side was set such that the undulated cross-section was parallel to the abrading surface (**Figure 5-16**). The sample was placed within a steel female mold (bottom), which aligns the sample perpendicular to the abrading surface. A male mold (top) was set inside the female mold, applying pressure to the top of the sample. No more pressure than the weight of a human hand was necessary. The bottom of the female mold has Teflon pads to ensure the mold was not damaged.

Sanding paper was placed on the sanding wheel and held by hydrostatic tension as water was fed onto the center of the wheel. Abrasion of the sample was conducted for approximately twenty minutes at intervals of:

- 1) 5 minutes at 180 grit sand paper (78 micron diameter)
- 2) 5 minutes at 240 grit sand paper (54 micron diameter)
- 3) 5 minutes at 320 grit sand paper (36 micron diameter)
- 4) 5 minutes at 420 grit sand paper (24 micron diameter)

At the end of each step, the target surface of the sample was observed via optical microscope to determine to start of the next step. The “grooves” from abrasion in the target surface from the prior step should be no longer visible to indicate acceptable polishing at the current step and continuance to the next step.

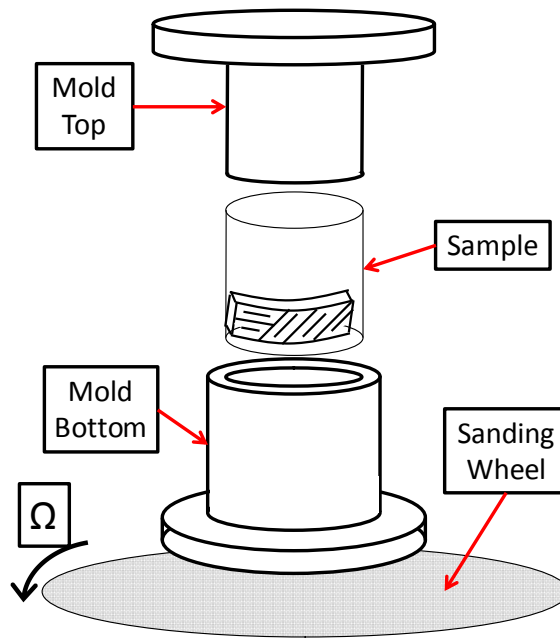
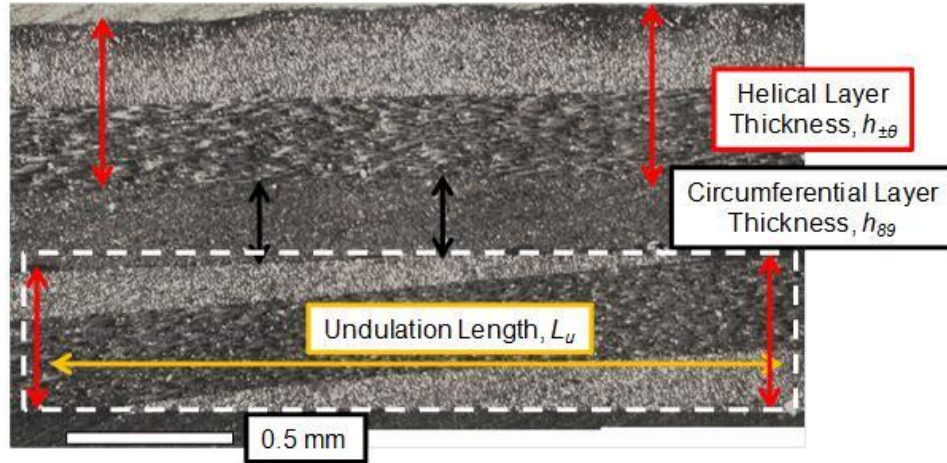


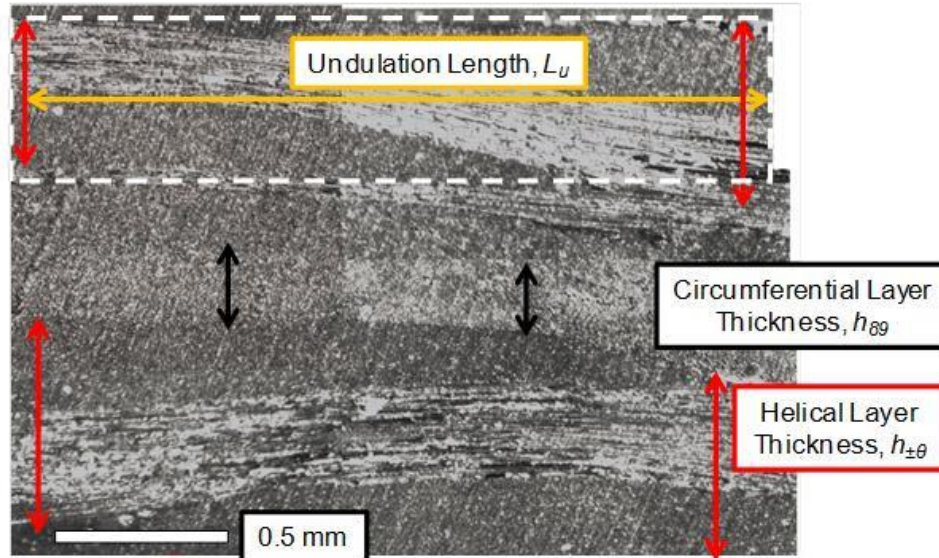
Figure 5-16. Undulation polishing

Polished specimens were evaluated by optical microscope at 50 times magnification. A composite image was created by hand from a three by three grid of images. Note the undulated cross-section target (light rectangle) in one helical layer of the composite does not necessarily align with another in the second helical layer of the composite (**Figure 5-17a**). The polished undulated cross-sections were evaluated for three parameters. For each cross-section, the helical layer thickness was measured, $h_{\pm\theta}$, the circumferential layer thickness was measured, h_{89} , and the undulation length was measured, L_u . Helical layer thickness was averaged over four locations, and circumferential layer thickness was averaged over two for each laminate. Consistent with **Chapter 4**, the undulation amplitude was assumed to be half the helical layer thickness. The

ratio of the helical layer and circumferential layer thickness to the laminate thickness, V_k , (k is the lamina number) was calculated for homogenization.



(a) EPON 862 [$\pm 16/89/\pm 16$]



(b) 30917 [$\pm 45/89/\pm 45$]

Figure 5-17. Polished undulated cross-sections highlighting measured parameters

Table 5-4 summarizes the undulation measurements taken from each laminate. Measurements in millimeters are highlighted in white. The coefficient of variation, C_v , was very low (1-9 %) for each of the parameters measured. Low variation permits the use of an average value for each parameter when defining the geometry and predicting the modulus and strength of

the laminate. Use of average values was important because it reduces the amount of testing and validation required for laminate certification. This result suggests that the undulation geometry was primarily a function of the fiber tow size, the tow tension, the tow bandwidth, and the radial compaction pressure provided by the shrink tape, which were kept identical in manufacturing.

Table 5-4. Undulation characterization measurements

Parameter	[±16/89/±16]		[±31/89/±31]		[±45/89/±45]		Avg.	C_v , %
	30917	EPON 862	30917	EPON 862	30917	EPON 862		
0.5 mm, px	195	195	195	195	195	195	195	0.0
h_u , px	133	95	121	105	130	109	115	6.0
h_u , mm	0.34	0.24	0.31	0.27	0.33	0.28	0.30	6.0
L_u , px	910	672	772	820	837	798	802	9.3
L_u , mm	2.33	1.72	1.98	2.10	2.15	2.05	2.06	9.3
h_u/L_u	0.15	0.14	0.16	0.13	0.15	0.14	0.14	4.3
$h_{\pm 0}$, px	266	190	241	210	259	218	231	6.0
$h_{\pm 0}$, mm	0.68	0.49	0.62	0.54	0.66	0.56	0.59	6.0
$V_{k,\pm q}$	0.41	0.40	0.40	0.40	0.41	0.40	0.40	0.5
h_{89} , px	122	93	118	105	119	111	111	5.4
h_{89} , mm	0.31	0.24	0.30	0.27	0.31	0.28	0.29	5.4
$V_{k,89}$	0.19	0.20	0.20	0.20	0.19	0.20	0.19	2.2
h_t , px	654	473	600	525	637.5	548	573	5.9
h_t , mm	1.68	1.21	1.54	1.34	1.63	1.40	1.47	5.9

The rhombus was divided into five RVE in **Figure 5-14c**. The physical size of each RVE was strongly dependent on the undulation length, L_u (**Figure 5-18**). Trigonometric relationships define the physical boundaries of each RVE. RVE A and RVE B as well as RVE D and RVE E were of identical size. The amount that each RVE contributes to the homogenized stiffness at any longitudinal location was related to the area ratio of each RVE to the total area at each longitudinal location (**Figure 5-18**). The “Contribution Ratio” of each RVE depends strongly on the FWP. If the FWP was small (larger rhombus) RVE D and E were a larger ratio of the rhombus area (per longitudinal location) compared to RVE A, B, and C. The reverse was true when the FWP was large (smaller rhombus) due to the undulation length (L_u) being of finite size. The ends and center of the rhombus were primarily dominated by undulated RVE (A-right, B-left,

and C-center) while the rest was influenced partially by non-undulated RVE depending on FWP and longitudinal location.

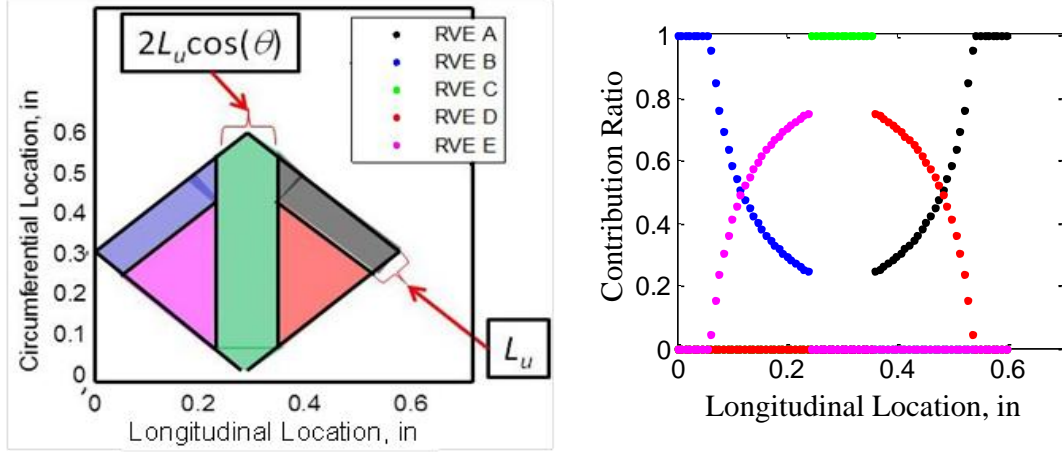


Figure 5-18. Rhombus RVE sectioning and ratio of contribution to stiffness with respect to longitudinal location: ± 45 -deg., FWP=10

The construction of the homogenized stiffness matrix starts at the RVE level (**Figure 5-19a**). The circles in **Figure 5-19** represent example discretization points where “hollow” are stiffness C_{ij} and “solid” are compliance S_{ij} . The local-global analysis was conducted by:

- (1) The homogenized stiffness matrix at the RVE level, C^{RVE} (**Section 4.3, Figure 5-19a**)
 - a. Individual lamina with respective C^{LAMINA} , rotated through the in- and out-of-plane orientations, were homogenized (3D anisotropic) and inverted to S^{UND} for each longitudinal location along the undulation
 - b. Individual longitudinal locations with respective S^{UND} were averaged (iso-stress) and inverted into a single value of C^{RVE} for the respective RVE
- (2) The homogenized stiffness matrix at the layer level, C^{LAYER} (**Figure 5-19b**)
 - a. Individual RVE with respective C^{RVE} were averaged (iso-strain) and inverted into S^{RHOM} for each longitudinal location along the rhombus

- b. Individual longitudinal locations with respective S^{RHOM} were averaged (iso-stress) and inverted into a single value of C^{LAYER} for the respective rhombus

(3) The homogenized compliance matrix at the laminate level, $S^{LAMINATE}$ (Figure 5-19c)

- a. Individual layers with respective C^{LAYER} were homogenized (3D anisotropic, Section 4.3) and inverted into $S^{LAMINATE}$

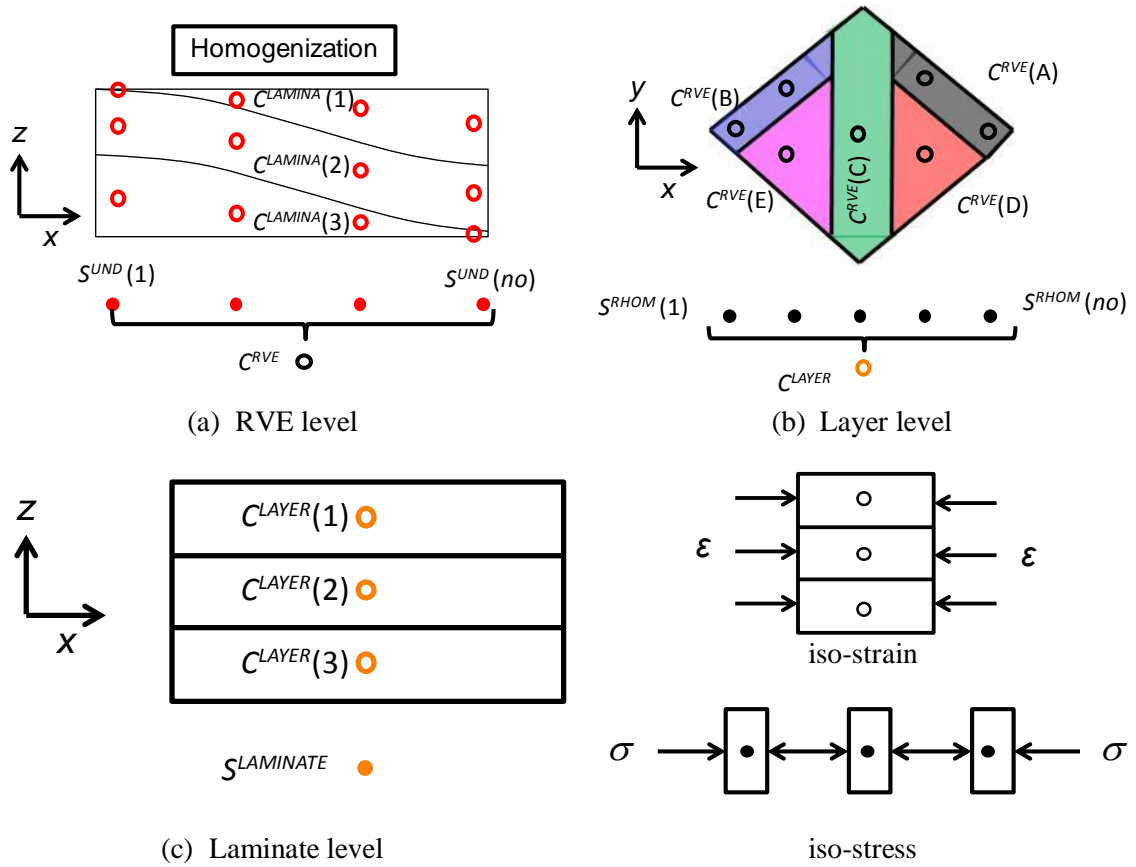


Figure 5-19. Local-global laminate stiffness construction mixed boundary conditions, laminate $[\pm\theta/89/\pm\theta]$

The devised local-global approach was only self-consistent on average at differing levels of analysis. The homogenized stiffness of a filament wound “layer level” was assumed to be equal to that of the filament wound rhombus as described above with no consideration given to alignment of the rhombi in different helically wound layers $\pm\theta$. $C^{LAYER}(2)$ was that of a 89-deg. unidirectional lamina. The upper limit on stiffness was calculated by averaging stiffness at every

level (iso-strain), and the lower limit was calculated averaging compliance at every level (iso-stress).

Laminate failure was calculated using MST at the lamina level for every discretization location in every lamina. The lamina principal coordinate stresses **Equation 5-1** (12-frame) were calculated from a laminate level applied longitudinal stress, $\sigma = \{\sigma_x, 0, 0, 0, 0, 0\}$,

$$\sigma^{12} = T(\theta)T(\alpha)C^{LAMINA}S^{UND}C^{RVE}S^{RHOM}C^{LAYER}S^{LAMINATE}\sigma \quad (5-1)$$

MST was improved with mechanisms for composites containing stress concentrations. Whitney and Nuismer (1974) created and validated two concentration based failure criterion. The criterion were created after noting that the stress concentration factor under predicts the failure strength of a composite plate subjected to tension with a circular hole. It is well known that a plate with a large hole has a lower strength than a plate with a relatively small hole, as the stress concentration is more localized in the latter. Whitney and Nuismer (1974) hypothesized that failure occurs when the (1), stress at a distance, d_o , away from the concentration, or (2), average stress from the concentration over a distance, a_o , exceeds the strength of the material. The advantage of such an approach was that the empirical critical distance was assumed to be independent of laminate construction or stress distribution as a property of the material.

Material failure was defined when $\phi > 1$, where ϕ was the largest of all stress components divided by the corresponding strength components. Analytical three dimensional strength predictions were fit using the point stress criterion, d_o , and average stress criterion, a_o , to the experimental results. “Best fit” values of d_0 or a_0 were chosen by eye for each angle and for each material. A singular value for each material was then determined by minimizing the error between experiment and the theory for a singular material with the “best fit” by eye as a starting point, this process lead to an identical fit value for 30917 and EPON 862. Analytically, the failure location was commonly RVE C where both lamina are undulating, depending on the material and filament winding angle. Example stress concentrations along the undulation in RVE

C are given in **Figure 5-20**. The point stress criterion is visualized in **Figure 5-20a**, and the average stress criterion **Figure 5-20b**, where at a distance of 0.45 mm or 0.82 mm away from the undulation center $\phi = 1$ for d_0 or $\phi = 1$ on average for a_0 .

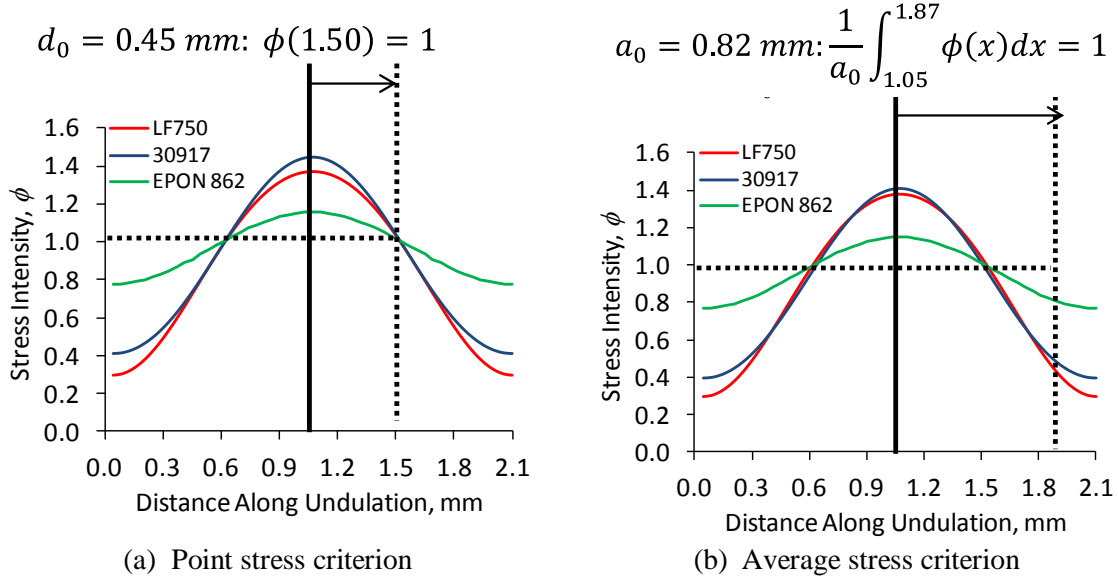


Figure 5-20. MST stress intensity profile along RVE C, laminate $[\pm 31/89/\pm 31] \{5/5\}$

5.4 Analytical Predictions for Modulus and Strength

Homogenized modulus predictions for 30917 (**Figure 5-21a**) and EPON 862 (**Figure 5-21b**) were plotted against FWP. E_x and ν_{xy} were calculated using **Equation 4-86** utilizing the homogenized laminate $S^{LAMINATE}$. E_x was slightly sensitive to FWP, decreasing from $\{2/2\}$ to $\{10/10\}$. As with discrete undulation testing, more compliant material systems such as 30917, and lower angles such as 16-deg., were more sensitive to undulation. E_x predictions with mixed boundary conditions generally fall within the experimental scatter. As expected, the mixed boundary conditions exist between iso-strain and iso-stress assumptions. The average modulus prediction error for 30917 was 6.8 %, and the average error for EPON 862 was 9.7 %, with the prediction bias high. Typical predictions in the literature range from 2% (Hipp and Jensen,

1992), 5-25 % (Zindel and Bakis, 2009), and 9-29 % (Jensen and Hipp, 1991) trend high for experiments and analysis of filament wound cylinders of various lamination arrangements and filament winding pattern. ν_{xy} was better captured for EPON 862 than for 30917. The theoretical bias was low with 20.6 % error for 30917 and 14.1 % error for EPON 862.

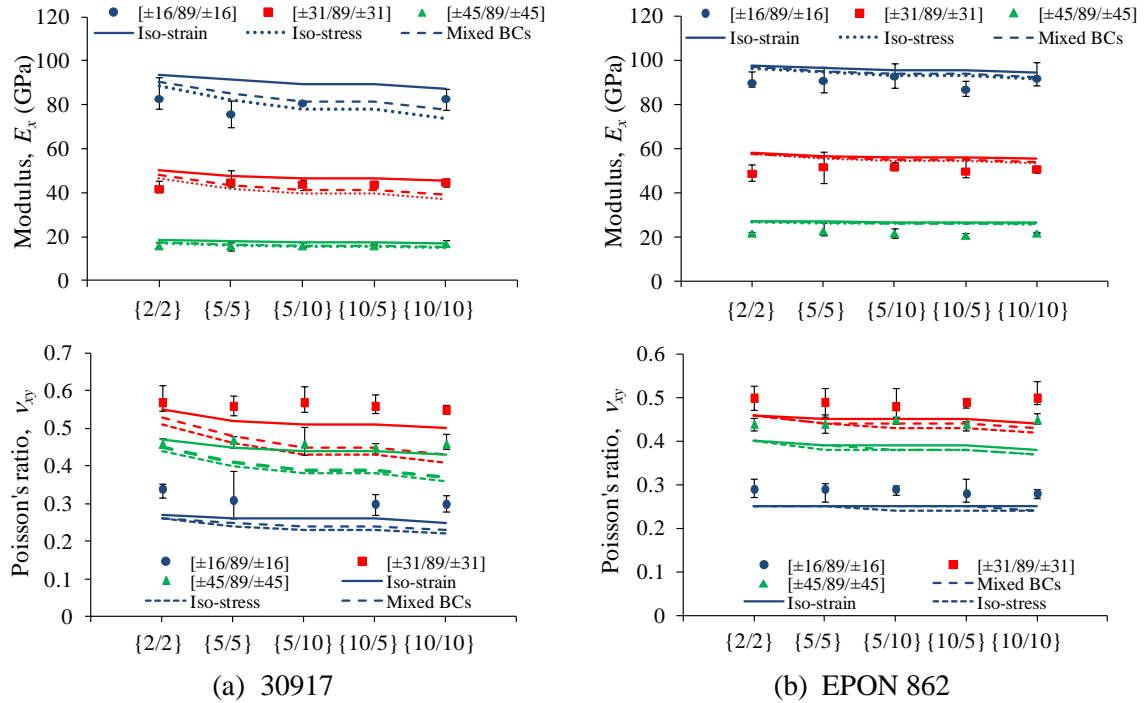


Figure 5-21. E_x and ν_{xy} predictions for $[\pm\theta/89/\pm\theta]$ cylinders various FWP

Laminate strength was predicted by incrementally calculating the stress concentration caused by σ with convergence of 0.04 % for all test materials and laminates to determine the d_o or a_o that provides the best accuracy. Failure prediction location and corresponding major stress component are listed in **Table 5-5**. For filament winding angles above 16-deg. the failure location was always RVE C, and the largest stress component was σ_6 . This result was similar to the failure mode predicted analytically for $[30_n/-60_n]_s$ flat specimens, as well as observed experimentally in both flat undulated specimens and filament wound cylinders.

Table 5-5. Analytical failure location prediction and major stress component

Material System	[$\pm\theta/89/\pm\theta$], RVE, σ_i		
	$\theta=16$	$\theta=31$	$\theta=45$
Conathane DPRN 30917	RVE C, σ_1	RVE C, σ_6	RVE C, σ_6
EPON 862	RVE A/B, σ_5	RVE C, σ_6	RVE C, σ_6

The critical distance criterion applied to a filament wound cylinder converged to $d_o = 0.45$ mm and $a_o = 0.82$ mm when fit to all laminates and both materials. The laminate strength F_x was not very sensitive to FWP (**Figure 5-22**). The strength prediction error was 7.6 % and 7.9 % for 30917 using $d_o = 0.45$ mm and $a_o = 0.82$ mm respectively. The strength prediction error was 23.4 % and 24.7 % for EPON 862, using $d_o = 0.45$ mm and $a_o = 0.82$ mm respectively. This result suggests that the point stress criterion and average stress criterion work approximately as well with the former performing marginally better.

There was no value of d_o , which would increase F_x large enough to well represent the experimental strength of EPON 862 at angles over 31-deg. It is hypothesized that the in-situ shear strength F_6 was much larger than the measured result of a 10-deg. off-axis tension used by Henry (2012). In-situ material was woven to a high degree, potentially increasing F_6 . This source of error could be mitigated using a value for F_6 that better represents a filament wound cylinder. As a basis for this hypothesis, previous filament wound cylinder testing analysis with CLT has shown that σ_6 can be potentially much higher than F_6 , measured using a 10-deg. off axis test without specimen failure for EPON 862 (Henry et al., 2014).

Typical prediction accuracy in the literature for strength ranges from 65% (Card, 1966), 42-59 % (Claus, 1991), 25-41 % (Jensen and Hipp, 1991), and 2-27 % (Pai and Jensen, 2001) trend high for experiments and analysis of filament wound cylinders. The literature predictions were, however, for global buckling of thin-walled filament wound cylinders, for which bifurcation of the stress-strain behavior was not observed in this testing. The longitudinal buckling instability

of filament wound cylinders of the type tested in this research was predicted to occur at stress levels exceeding those measured in testing as well.

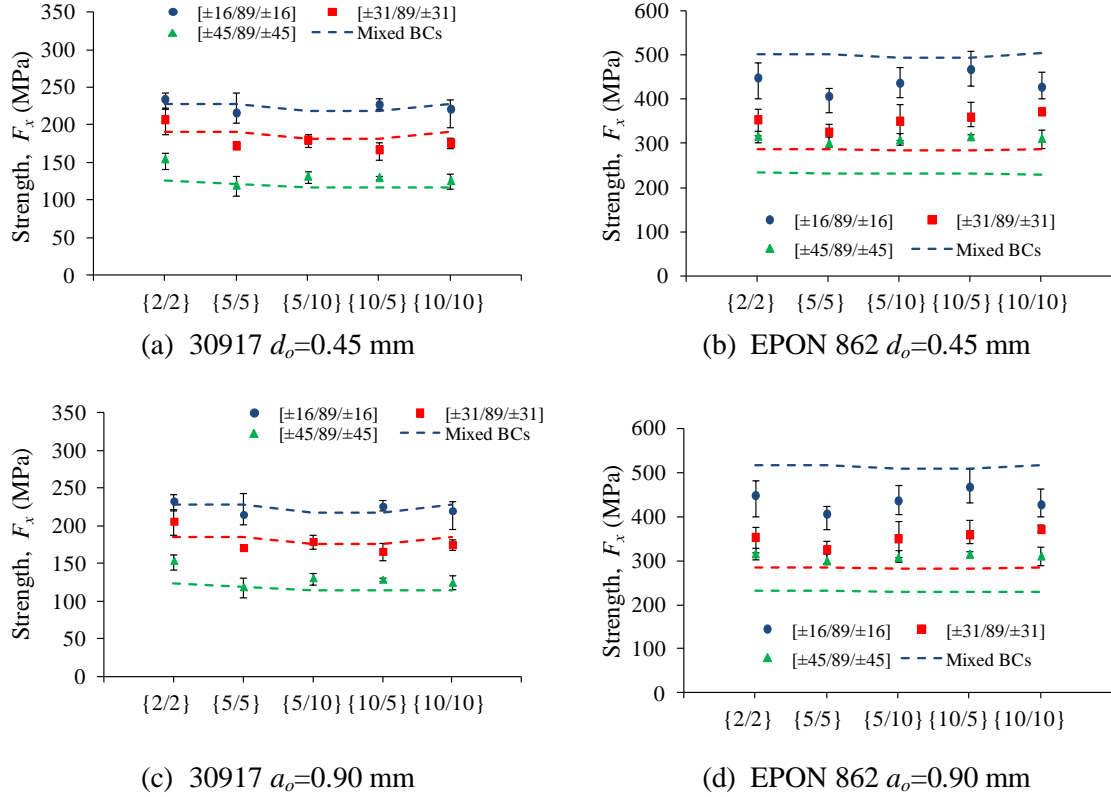


Figure 5-22. F_x predictions for $[\pm\theta/89/\pm\theta]$ cylinders various FWP

E_x and F_x for LF750 filament wound cylinders tested by Henry et al. (2014) were also analyzed. The cylinders were made with the same manufacturing conditions as in this research, motivating the use of the same undulation geometry with respect to undulation height and length. The cylinders were of the same size and laminate variation with, however, only a pattern of {10/5}. The average E_x prediction error was 11.8 %, and the average F_x prediction error was 8.9 % using a fit d_o of 0.82 mm (**Figure 5-23**).

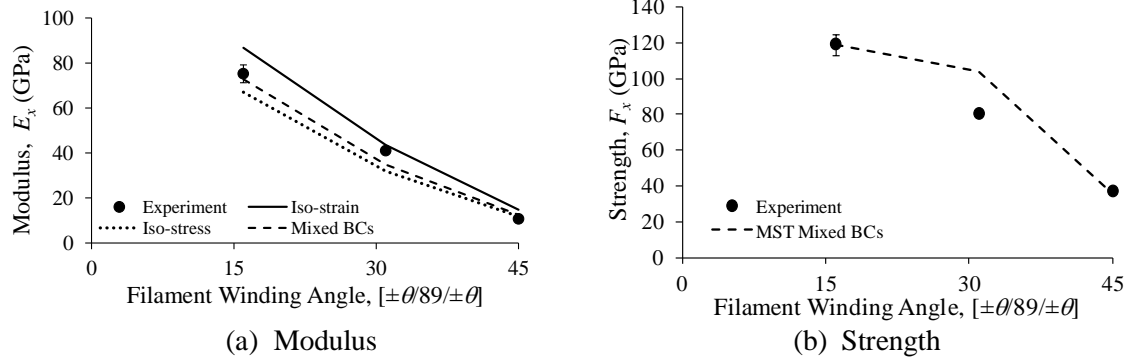


Figure 5-23. E_x and F_x predictions for $[\pm\theta/89/\pm\theta]$ LF750 cylinders

The absolute value of the average prediction error for E_x , F_x , and ν_{xy} was 14 % for all materials and laminates. The [minimum, maximum, average] percent error for E_x prediction was [0.1, 20, 9.5] %, for F_x prediction was [0.6, 37, 14] %, and for ν_{xy} prediction was [7.6, 30, 17] %.

Table 5-6. Filament wound cylinder prediction error, (theory-experiment)/theory*100

Helical Angle, deg.	Pattern	30917			EPON 862		
		Modulus Error, %	Strength Error, %	ν_{xy} Error, %	Modulus Error, %	Strength Error, %	ν_{xy} Error, %
16	{2/2}	8.26	-2.63	-30.8	7.06	10.6	-16.0
	{5/5}	10.7	5.26	-24.0	4.21	18.9	-16.0
	{5/10}				0.64	11.5	-16.0
	{10/5}	-2.09	-4.13	-25.0	7.05	5.26	-12.0
	{10/10}	-4.54	3.07	-30.4	0.22	15.1	-16.7
31	{2/2}	12.8	-8.95	-7.55	15.0	-23.3	-8.70
	{5/5}	-3.62	9.47	-16.7	6.84	-13.6	-11.4
	{5/10}	-6.64	0.55	-26.7	5.25	-24.0	-9.09
	{10/5}	-6.54	7.73	-24.4	8.89	-27.2	-11.4
	{10/10}	-15.3	7.37	-27.9	5.43	-30.1	-16.3
45	{2/2}	9.45	-24.0	-2.22	18.9	-35.5	-10.0
	{5/5}	3.73	0.83	-14.6	13.6	-30.3	-12.8
	{5/10}	-0.06	-12.8	-18.0	16.4	-33.8	-18.4
	{10/5}	-0.06	-11.1	-15.4	20.2	-36.8	-15.8
	{10/10}	-11.0	-8.62	-24.3	15.3	-35.7	-21.6

5.5 Average Stress Criterion As Applied to DIC Imaging

The Whitney-Nuismer critical distance criterion was related to physical d_0 or a_0 away from the concentration center. The light color box in **Figure 5-24** is of the size $2a_0$, extending from the center of the circumferential undulation (RVE C) or helical undulation (RVE A/B) in both normal directions, and was projected upon the DIC images at a stress level immediately preceding failure. In general the strain concentration size in the fiber direction was comparable to $2a_0$.

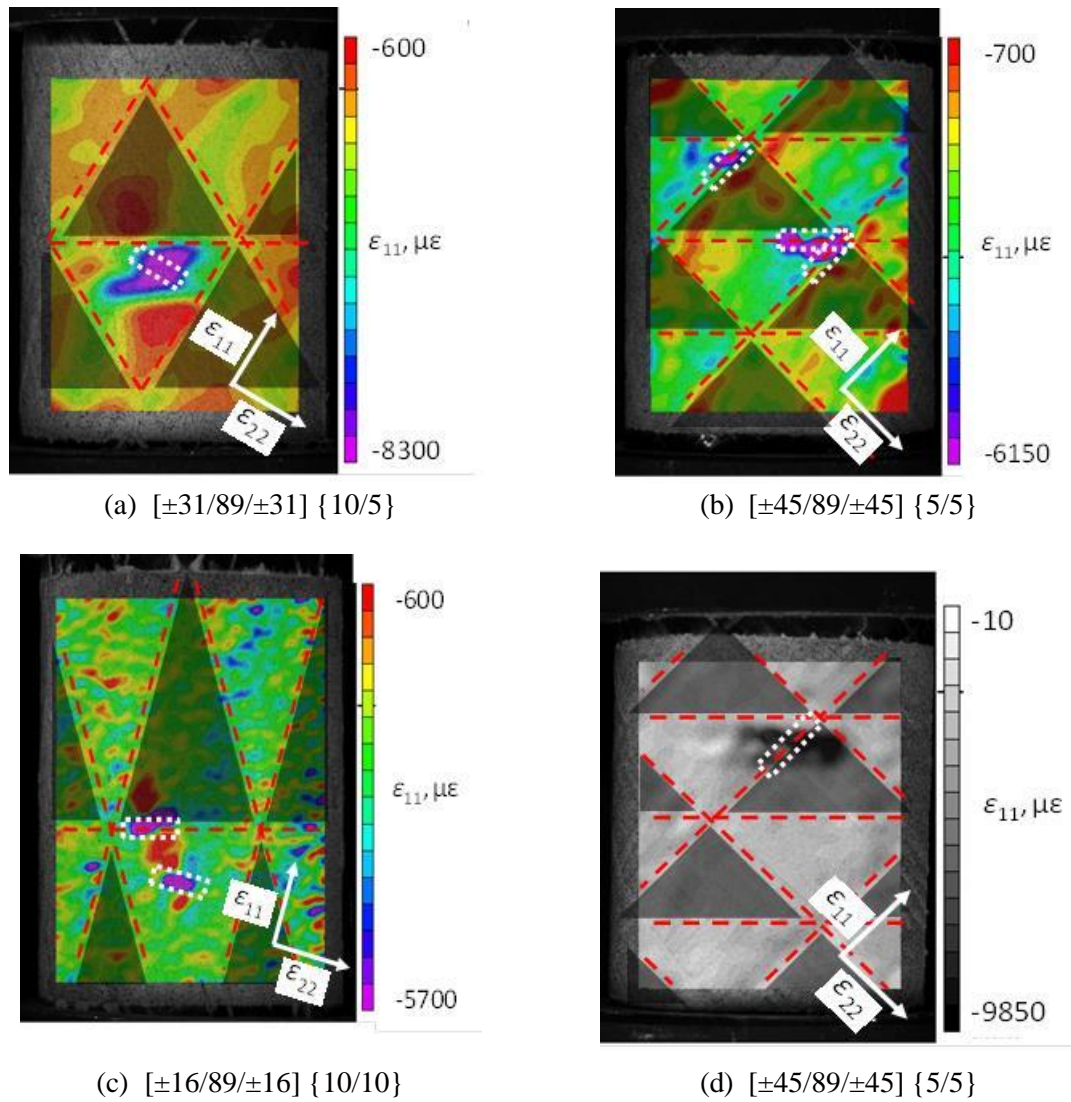


Figure 5-24. Physical size of $2a_0$ with respect to strain concentrations in 3D DIC: 30917

As may be recalled, the strains in the material measured using DIC at a region of strain concentration were considerably higher than those calculated using CLT. The in-situ ε_1 strain at failure for 30917 was approximately 5300 $\mu\epsilon$ using a unidirectional bend test (Henry et al., 2014). For comparison, the peak strain was on average 7400 $\mu\epsilon$ (between 5700 $\mu\epsilon$ and 9900 $\mu\epsilon$, **Figure 5-24**) for various filament wound cylinder tests. The average DIC strain intensity (peak strain at failure over unidirectional strain at failure) was 7400/5300, or approximately 1.4, which correlates well with the fit value of a_0 (**Figure 5-25**)

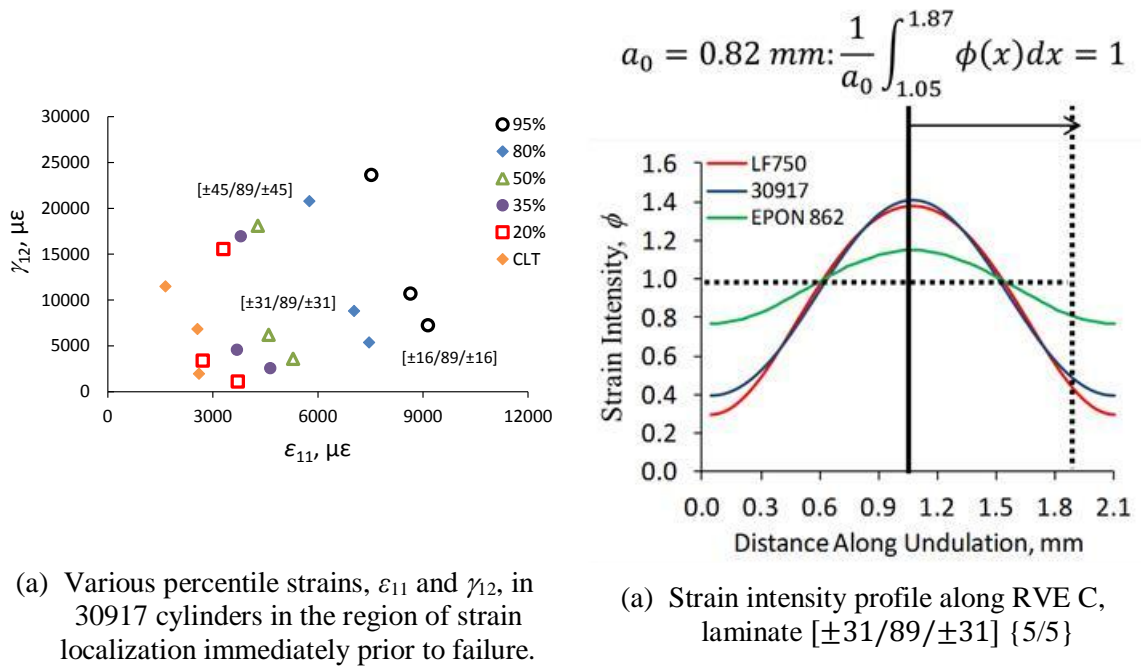


Figure 5-25. Strain intensity comparison of cylindrical specimens with a_0

The critical distance criterion a_0 does not correlate well with flat undulated specimens. **Figure 5-26** shows two $[0_n/90_n]_s$ specimens just prior to failure with a light square outline of an area equal to $2a_0$. The contour shows that the strain intensity at failure is considerably higher than that seen in filament wound cylinders. Note, however, that **Figure 5-26** shows ε_{xx} and not ε_1 and as such ε_1 may be slightly higher or lower than the value of the contour, considering the 0 deg. orientation of the lamina of interest in-plane with additional inclination out-of-plane. The

strain intensity for LF750 (**Figure 5-26a**) is 31000/2500 (2500 $\mu\epsilon$ is the unidirectional value measured in Henry et al., 2014) equals 12.4, and the intensity for 30917 (**Figure 5-26b**) is 14600/5300 equals 2.8. A strain intensity of 1.4 is approximately green in **Figure 5-26b**.

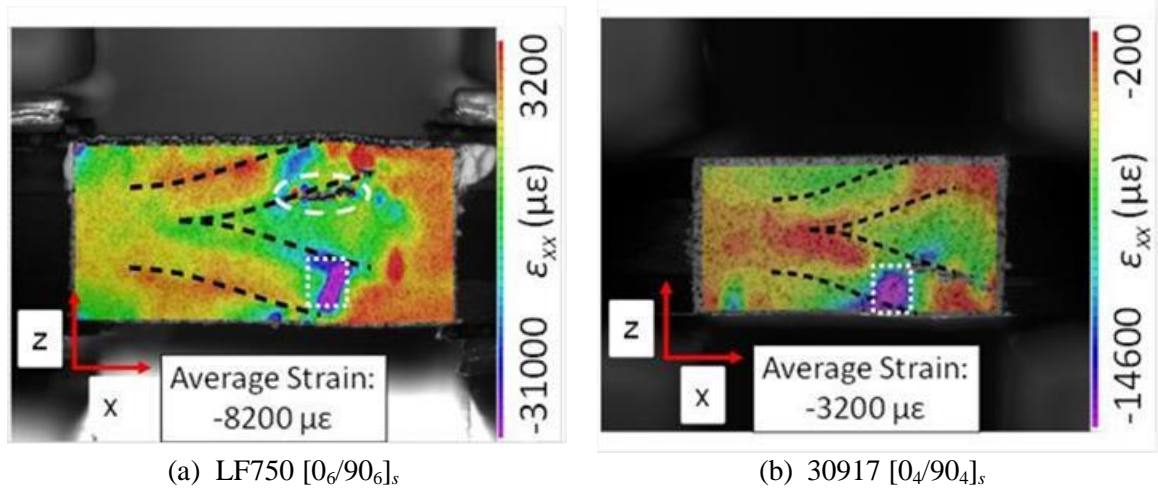


Figure 5-26. Strain intensity comparison of flat undulated specimens with a_0

The critical distance criterion should not be applied to flat undulated specimens. This was hypothesized to be due to the undulated region in flat specimens not effectively redistributing the strain around the concentration. The interwoven nature of filament wound cylinders affords better strain redistribution around the circumference for which flat undulated specimens were unable to replicate through their width. The strain intensity need only propagate the short distance through-the-thickness of the undulated lamina to cause failure in flat, undulated specimens, in contrast to filament wound cylinders where the concentration must encompass a sufficient amount of the circumference of the cylinder. The strain intensity was, therefore, comparatively smaller and of higher intensity in flat specimens, while larger and of lower intensity for filament wound cylinders.

Chapter 6

Conclusions

6.1 Composite Helicopter Driveshaft Design

Lamina level composite strength was found to be dependent on neat resin modulus, which in turn was observed to be affected by temperature. Validated empirical strength-temperature relationships were integrated into an optimization strategy. The optimization strategy focused on the design of a single piece filament wound composite driveshaft with an emphasis on reduction of weight and maximization of the minimum factor of safety. Design tradeoffs involve interactions between driveline weight and shaft self-heating, whirling stability, torsional buckling stability, and micromechanical failure. Parameters dealing directly with weight, number of bearings and number of laminas, when diminished, directly reduce whirling stability and torsional buckling stability respectively. Both values can be increased through laminate variation where increased longitudinal modulus increases whirling stability and reduces buckling stability (reducing longitudinal modulus results in the opposite effect). Low angles (which contribute high longitudinal modulus) experience high fiber direction compressive stress from driveshaft misalignment, while high angles experience the same stress response from applied torque. Fiber direction compressive stress is a known limiting factor for polymer composites loaded in compression, leading to tradeoffs between whirling stability, torsional buckling stability, and micromechanical failure.

Two helicopter design models were investigated under many operating conditions. For a given operating condition (misalignment, temperature), the largest neat resin modulus material at the operating temperature returns the lightest Pareto optimized design. Self-heating behavior was

on the order of 2-8 °C depending on operating conditions, which is much smaller than the ambient temperature ranges investigated 20-60 °C. For all cases investigated, the best Pareto optimized design used EPON 862, eliminating one bearing for a weight reduction of 15.15 kg (minimum factor of safety equals 1.41 Blackhawk), and eliminating two bearings for a weight reduction of 30.3 kg (minimum factor of safety equals 1.24 Chinook).

FMC materials were observed to soften excessively at elevated temperatures, losing up to 60% of their strength at 60°C. The stiffest polyurethane resin at elevated temperatures was 30757, which was able to generate a design eliminating one bearing for a weight reduction of 12.65 kg (minimum factor of safety equals 1.18 Blackhawk), and eliminating no bearings for a weight reduction of 11.1 kg (minimum factor of safety equals 1.10 Chinook). Many FMC materials were too low in modulus and strength at elevated temperatures to generate a viable design; while in compression providing weight savings for the Chinook, which operates at higher torque than the Blackhawk. S_w was observed to very often be a limiting factor for all investigated design spaces.

A constant power trade study was conducted varying torque and operating speed for the Blackhawk helicopter. Allowing for a slower operating driveshaft speed facilitated additional weight reduction; eliminating two bearings for a weight reduction of 18 kg (minimum factor of safety equals 1.36), and eliminating two bearings for a weight reduction of 15 kg (minimum factor of safety equals 1.13) considering EPON 862 and 30757, respectively. If applicable in practice, flexibility in driveshaft operating speed and torque would be desirable from a weight and part reduction point of view.

6.2 Discrete Undulation Two Dimensional DIC

Lamina undulation was detrimental to the longitudinal compressive modulus and strength of FMC and RMC $[0_n/90_n]_s$ specimens. FMC materials were more sensitive to fiber undulation compared to RMC. Fiber undulation induces moderate non-linearity in the compressive stress strain curves for FMCs, but not significantly so for the RMC. An undulation with an amplitude/length ratio of 0.1 reduces the longitudinal modulus of elasticity in the undulation region by approximately 43%, 28%, and 3% in specimens with LF750, 30917, and EPON 862 resins, respectively, relative to specimens without undulation. Specimens without undulations were observed to have approximately the same modulus regardless of the matrix material. For the range of undulation amplitude/length investigated, both polyurethane resins showed little change in longitudinal strength.

The $[30_n/-60_n]_s$ specimens were more strongly dominated by in-plane shear properties of the composite which, depending on the matrix material, were very different. Modulus and strength of the $[30_n/-60_n]_s$ specimens were largely independent of undulation amplitude. This result suggests that the introduction of fiber undulation more critically affects fiber dominated properties (modulus and strength of $[0_n/90_n]_s$ specimens) than matrix dominated properties (modulus and strength of $[30_n/-60_n]_s$ specimens). $[30_n/-60_n]_s$ specimens of the same undulation size and fiber volume fraction have a positive correlation between neat resin modulus and composite modulus and strength.

For both laminates, strain concentrations were of highest magnitude at the location where the undulating lamina subducts beneath the surface of the laminate. Conversely, strain concentrations were low where the undulating lamina met in the middle of the laminate. It was observed by strain measurements on the free edge of flat specimens, that the introduction of undulation itself does not greatly increase the longitudinal strain in the reinforcing fibers prior to

microbuckling where the fiber subducts from the surface to the interior. Rather, the other strain components (out-of-plane shear and out-of-plane normal strains) increase considerably where the subduction begins, eventually leading to delamination. With the out-of-plane stiffness reduced due to delamination, the misalignment of the fiber increases until microbuckling occurs. Microbuckling failure near undulations in flat specimens was consistent with that seen in filament wound cylinders.

The developed three-dimensional homogenization method accepted individual anisotropic lamina which contains in- and out-of-plane reinforcement orientation. This approach allowed for the novel prediction of all three-dimensional elastic constants of such a laminate. For several heterogeneous laminate arrangements, predictions were shown to yield identical results, compared to established two- and three-dimensional methods when individual lamina have only in-plane rotation. When evaluating an undulated composite, predictions were within 5 % for the anisotropic two- and three-dimensional methods for undulations of size undulation height/length equals 0.2. Established three-dimensional methods assuming only in-plane rotation with corrections experience significant error introduced by neglected coupling terms from out-of-plane information.

Homogenized stiffness was also observed to be highly sensitive to undulation height/length, which can be thought of as undulation severity. When undulation height/length is zero, i.e., no undulation, all methods predict identical elastic constants. Large values of undulation height/length, however, cause the upper and lower stiffness solutions to diverge, as well as to decrease. The degree to which the homogenized stiffness prediction was affected by the undulation also depends on the material system. A stiff material system such as EPON 862 experiences a 50 % reduction in longitudinal stiffness at undulation height/length equals 0.3, which contrasts greatly with a compliant resin system such as LF750 that does so at undulation height/length equals 0.1. For the material systems and undulation variation considered, the

homogenized longitudinal stiffness prediction error between the previous two- and three-dimensional anisotropic methods and the proposed methodology was 1-10 %. The largest discrepancies occur at relatively large (0.5) undulation height/length for more compliant resins (LF750), due to increased influence of out-of-plane components, which are partially accounted for in the two dimensional analysis.

Anisotropic homogenization was used to determine the longitudinal modulus and strength of $[0_n/90_n]_s$ and $[30_n/-60_n]_s$ specimens. The longitudinal modulus prediction range considering iso-stress and iso-strain assumptions was observed to contain the experimental scatter of various undulation amplitudes, material, and lamination, showing positive correlation. The analytical and experimental results showed that specimens of larger longitudinal modulus ($[0_n/90_n]_s$) were more sensitive to lamina undulation. A sensitivity study found that the longitudinal modulus prediction was most sensitive to undulation geometry, E_1 , and G_{12} for $[0_n/90_n]_s$, and most sensitive to G_{12} for $[30_n/-60_n]_s$.

Several failure criterion were surveyed. Little variation in accuracy was observed; therefore MST was chosen for consistency. Two and three dimensional anisotropic homogenization predicted lower and upper bounds on longitudinal strength respectively. The predicted failure mode for $[0_n/90_n]_s$ was generally σ_5 and σ_1 for two and three dimensional approaches respectively. The observed microbuckling failure mode could have been caused by either of these influences.

The predicted failure mode for $[30_n/-60_n]_s$ was generally σ_6 for both methods. The observed fiber splitting failure mode was hypothesized to be caused by σ_6 , supporting the analytical result. The sensitivity for the two and three dimensional strength predictions was very different for $[0_n/90_n]_s$ and very similar for $[30_n/-60_n]_s$. The strength prediction of $[0_n/90_n]_s$ was very strongly influenced by the undulation geometry. Three dimensionally, E_1 , G_{12} , and F_{1C} were also

important, while two dimensionally only F_6 was substantial. This is due to extensive coupling from three dimensional theory being absent in the two dimensional approach.

6.3 Filament Wound Cylinder Three Dimensional DIC

Through extensive experimental testing it was determined that the FWP does have a clear effect on the in-plane strains and out-of-plane displacements in cylindrical specimens subjected to longitudinal compressive loading. Higher magnitude longitudinal strain was observed at the center of the repeating rhombic element where the composite was non-undulated, compared to the border of the rhombus where the material was undulated. This difference in longitudinal strain was larger in the FMC material than the RMC material, on the basis of a percentage of the mean longitudinal strain.

Within the rhombic regions, repeatable gradients in hoop strain were observed. These gradients can be correlated with the out-of-plane warping patterns observed in the rhombic elements. It is believed that compression-twist coupling of the laminated regions of the rhombi and other out-of-plane couplings created by the undulations, as published by others mentioned in the introduction, are the cause of this behavior. Further investigation is required to confirm this hypothesis.

Failure of the cylinders occurred by a coalescence of fiber microbuckling, which was signified by large concentrated strains and out of plane displacement on the surface of the cylinders. The location of fiber microbuckling initiation was coincident with locations of undulated fiber reinforcement introduced by the filament winding process—often where the circumferential and helical undulation bands intersect. Cylinders made with a flexible matrix exhibited a more gradual fiber microbuckling process in comparison to cylinders made with a conventional epoxy matrix, facilitating the visual observation of the failure process.

The longitudinal modulus of RMC and FMC specimens with various fiber orientations was unaffected by FWP. The ultimate strength and corresponding strain were minimum when the pattern was {5/5} compared to other single pattern laminates, particularly in FMC cylinders. Hybridizing the pattern had little effect on the specimen strength for FMC or RMC cylinders.

A statistical analysis of lamina-coordinate strains in the region of FMC cylinders involved in failure revealed that the 95th percentile fiber- and shear-direction strains (ε_{11} and γ_{12}) were two to four times greater than their global counterparts computed using homogeneous lamina properties. These results indicate the magnitude of strain concentration existing in the cylinders immediately before failure, and highlight the importance of ε_{11} and γ_{12} in the failure process.

An analytical procedure was developed for homogenization of a filament wound cylinder rhombus. The homogenized properties for several RVE were calculated using the three-dimensional anisotropic approach and integrated into the more complex rhombus structure. Pertinent undulation measurements were made on polished undulated cross-sections. The coefficient of variation between several samples of varying material and in-plane angle were small, suggesting uniform application in analysis.

A novel local-global approach to filament wound cylinder application was augmented with empirical critical distance factors. The average E_x and ν_{xy} prediction error for 30917 was 6.8 % and 21 %, and the average error for EPON 862 was 9.7 % and 14 % respectively. Critical distance d_0 and a_0 were fit to the experiment, converging to 0.45 mm and 0.82 mm respectively. The strength prediction error was approximately 7.7 % and 24 % for 30917 and EPON 862, with failure location typically at the circumferential undulation by mode σ_6 . The failure mode prediction was consistent with experimental observations from filament wound cylinders and flat-undulated specimens of similar lamination arrangement. The failure location was the circumferential undulation in both experiment and theory. Theoretically the failure occurs at the

exact center of the circumferential undulation but visual accuracy in the experiment leaves this detail un-validated. Additional comparison with previous LF750 filament wound cylinder testing produced prediction error of 11.8 % and 8.9 % for longitudinal modulus and strength respectively. The average absolute value of the error for modulus, strength, and Poisson's ratio was 14 %. Application of stress concentration factors to flat undulated specimens was deemed unadvisable due to considerably higher strain intensity at failure compared to filament wound cylinders.

6.4 Recommendations for Future Work

The single-piece helicopter driveshaft concept outlined in this research experiences bending (through constant curvature) and applied torque (power transmission). Future work should focus on experimental validation of the torsional and bending stiffness of composite shafts, as well as, the associated strength predictions. Optimized composite specimens of the materials and associated lamination arrangements in this research should be fabricated. Driveshaft specimens can then be loaded in pure torsion or bending to provide confidence in torsional and bending stiffness predictions, as well as, the torsional buckling and lamina failure predictions provided analytically by the driveshaft analysis. Additional combined loading tests of specimens under bending and torque would culminate the final round of testing.

Temperature dependent strengths were integrated into the driveshaft designs at temperatures ranging from 21 °C to 65 °C. Certification of laminates for use in aviation, however, also requires testing at sub-ambient temperatures (-50 °C). The glass transition temperature of flexible matrix composites is known to be below ambient temperature. As such, lamina strength should be evaluated at sub-ambient temperatures to characterize the increased strength, stiffness, and brittleness of the composite. Similar to the transverse testing done in this research,

temperature controlled composite testing at sub-ambient temperatures should yield insight into these effects. A temperature chamber, equipped for sub-ambient testing through liquid nitrogen cooling, should be used. In this research composite strength was assumed to follow empirical relationships validated for the transverse direction only. The fidelity of the assumption would be increased using additional resins and composite strength testing (in addition to the transverse direction).

The fatigue response of candidate resins should be investigated for the optimized laminates. The response of a single piece driveshaft to the cyclic tensile-compressive loading associated with operating misaligned has not been extensively investigated. Available information suggests that the resin systems investigated here will not experience fatigue failures or overheating at misalignment strains under $1500\ \mu\epsilon$, at least for a few million cycles. Composites fabricated with resins of a relatively high neat resin modulus were observed to fail quickly by overheating when subjected to more than $2000\ \mu\epsilon$. Unstable self-heating was specifically a problem for RMC materials where, at strains exceeding $1500\ \mu\epsilon$, localized regions eventually resulted in temperatures in excess of $90\ ^\circ\text{C}$ and composite failure. Although expensive, certifying shafts of various resins for fatigue response in fully reversed bending is a necessary step towards fielding a single-piece composite driveshaft. Test cylinders of optimized laminates should be operated misaligned for each of the candidate resins to investigate fatigue response. Thermal measurements of the specimen surface can be used in support of self-heating predictions.

The constraint on the driveshaft design space was such that each factor of safety could be no lower than 1.1. The sensitivity of each, however, with respect to ballistic tolerance or transient loading is not well documented in the literature, and is likely to be proprietary information. The degree to which heating, whirling, buckling, and strength must be over designed to avoid failure of the shaft in the event of ballistic damage during operation should be investigated thoroughly. Due to the cost associated with full or semi-scale ballistic testing, a simple test should be chosen

which likely excludes misalignment. A simple test could be to damage a shaft of an optimized laminate and then load it to failure by torsion to gauge an appropriate knockdown. With this new information, different design constraints could be implemented for torsional buckling and lamina strength, depending on the failure mode of the shaft. If the test was repeated on a composite laminate with ballistic constraints in place, the new shaft should not fail when damaged under load. Different material systems are likely to require different safety factors.

APPENDIX

Table A-1. Discrete undulation modulus and ultimate strength test results: LF750, $[30_n/-60_n]_s$

Specimen	Laminate	E_x , GPa	Avg.	Cv, %	σ_u , MPa	Avg.	Cv, %	ν_{xz}	Avg.	Cv, %
AO1-1	$[30/-60]_s$	4.3	3.8	10	-26	-26	3.6	0.62	0.70	10
AO1-2	$[30/-60]_s$	4.1			-25			0.76		
AO1-3	$[30/-60]_s$	3.8			-27			0.71		
AO1-4	$[30/-60]_s$	3.5			-26					
AO1-5	$[30/-60]_s$	3.4			-25					
AO2-1	$[30/-60]_s$	3.7	3.8	19	-24	-26	7.3	0.68	0.69	9.4
AO2-2	$[30/-60]_s$	3.7			-27			0.61		
AO2-3	$[30/-60]_s$	4.5			-27			0.76		
AO2-4	$[30/-60]_s$	4.6			-26			0.73		
AO2-5	$[30/-60]_s$	2.7			-30					
AO2-6	$[30/-60]_s$	3.4			-25					

Table A-2. Discrete undulation modulus and ultimate strength test results: 30917, $[30_n/-60_n]_s$

Specimen	Laminate	E_x , GPa	Avg.	Cv, %	σ_u , MPa	Avg.	Cv, %	ν_{xz}	Avg.	Cv, %
CO1-1	$[30/-60]_s$	10.5	9.7	9.1	-59	-55	5.2	0.45	0.42	6.3
CO1-2	$[30/-60]_s$	8.6			-58			0.42		
CO1-3	$[30/-60]_s$	9.1			-54			0.41		
CO1-4	$[30/-60]_s$	9.2			-58			0.42		
CO1-5	$[30/-60]_s$	9.2			-55			0.46		
CO1-6	$[30/-60]_s$	11.1			-51			0.40		
CO1-7	$[30/-60]_s$	10.1			-53			0.39		
CO2-1	$[30/-60]_s$	7.3	7.2	18	-56	-55	2.9	0.50	0.45	7.9
CO2-2	$[30/-60]_s$	6.2			-55			0.42		
CO2-3	$[30/-60]_s$	7.7			-58			0.46		
CO2-4	$[30/-60]_s$	6.2			-55					
CO2-5	$[30/-60]_s$	5.5			-54					
CO2-6	$[30/-60]_s$	9.3			-55			0.41		
CO2-7	$[30/-60]_s$	8.0			-52			0.44		

Table A-3. Discrete undulation modulus and ultimate strength test results: LF750, $[0_n/90_n]_s$

Specimen	Laminate	E_x , GPa	Avg.	Cv, %	σ_u , MPa	Avg.	Cv, %	ν_{xz}	Avg.	Cv, %
AU1-1	$[0/90]_s$	32			-45			0.85		
AU1-2	$[0/90]_s$	31			-43			0.70		
AU1-3	$[0/90]_s$	35			-42			0.77		
AU1-4	$[0/90]_s$	33	32	17	-47	-42	12	0.75	0.77	7.3
AU1-5	$[0/90]_s$	33			-42			0.80		
AU1-6	$[0/90]_s$	37			-31					
AU1-7	$[0/90]_s$	20			-43					
AU2-1	$[0/90]_s$	26			-28			1.17		
AU2-2	$[0/90]_s$	24			-41			0.70		
AU2-3	$[0/90]_s$	26	25	9	-39	-37	14	0.72	0.89	24
AU2-4	$[0/90]_s$	21			-35			1.06		
AU2-5	$[0/90]_s$	27			-40			0.78		
AU3-1	$[0/90]_s$	9			-26			0.77		
AU3-2	$[0/90]_s$	13			-29			1.15		
AU3-3	$[0/90]_s$	12			-26			1.02		
AU3-4	$[0/90]_s$	16	12.3	20	-29	-28	5	1.16	0.99	18
AU3-5	$[0/90]_s$	11			-26			0.85		
AU3-6	$[0/90]_s$	15			-29					
AU3-7	$[0/90]_s$	10			-28					
AL1-1	$[0/90]_s$	58			-66			0.41		
AL1-2	$[0/90]_s$	54			-66			0.57		
AL2-1	$[0/90]_s$	50	56	8.6	-91	-82	18.1	0.50	0.47	14
AL2-2	$[0/90]_s$	60			-93			0.41		
AL2-3	$[0/90]_s$	62			-95			0.46		

Table A-4. Discrete undulation modulus and ultimate strength test results: 30917, $[0_n/90_n]_s$

Specimen	Laminate	E_x , GPa	Avg.	Cv, %	σ_u , MPa	Avg.	Cv, %	ν_{xz}	Avg.	Cv, %
CU1-1	$[0/90]_s$	42	44	5.2	-78	-70	8.2	0.66	0.66	1.6
CU1-2	$[0/90]_s$	45			-67			0.65		
CU1-3	$[0/90]_s$	47			-70			0.66		
CU1-4	$[0/90]_s$	45			-76			0.65		
CU1-5	$[0/90]_s$	41			-65			0.67		
CU1-6	$[0/90]_s$	43			-65			0.64		
CU2-1	$[0/90]_s$	26	30	14	-68	-67	6.9	0.69	0.87	47
CU2-2	$[0/90]_s$	23			-62			0.57		
CU2-3	$[0/90]_s$	34			-66			0.59		
CU2-4	$[0/90]_s$	32			-72			0.55		
CU2-5	$[0/90]_s$	35			-71			0.53		
CU2-6	$[0/90]_s$	32			-70			1.55		
CU2-7	$[0/90]_s$	33			-58			1.24		
CU2-8	$[0/90]_s$	29			-69			1.26		
CU3-1	$[0/90]_s$	28	26	12	-69	-63	9	0.76	0.76	8.1
CU3-2	$[0/90]_s$	30			-54			0.78		
CU3-3	$[0/90]_s$	27			-68			0.78		
CU3-4	$[0/90]_s$	27			-69			0.86		
CU3-5	$[0/90]_s$	27			-66			0.73		
CU3-6	$[0/90]_s$	25			-64			0.67		
CU3-7	$[0/90]_s$	21			-58					
CU3-8	$[0/90]_s$	23			-58					
CL1-1	$[0/90]_s$	60	61	1.5	-242	-244	0.9	0.40	0.40	5.9
CL1-2	$[0/90]_s$	60			-243			0.42		
CL1-3	$[0/90]_s$	62			-246			0.38		

Table A-5. Discrete undulation modulus and ultimate strength test results: EPON 862

Specimen	Laminate	E_x , GPa	Avg.	Cv, %	σ_u , MPa	Avg.	Cv, %	ν_{xz}	Avg.	Cv, %
EO1-1	[30/-60] _s	23	22	8.0	-84	-83	6.2	0.35	0.41	56
EO1-2	[30/-60] _s	21			-88			0.41		
EO1-3	[30/-60] _s	24			-88			0.48		
EO1-4	[30/-60] _s	22			-80					
EO1-5	[30/-60] _s	21			-80					
EO1-6	[30/-60] _s	19			-75					
EO2-1	[30/-60] _s	21	23	9.8	-74	-81	8.2	0.35	0.38	8
EO2-2	[30/-60] _s	21			-83			0.43		
EO2-3	[30/-60] _s	20			-78			0.38		
EO2-4	[30/-60] _s	22			-75					
EO2-5	[30/-60] _s	23			-78					
EO2-6	[30/-60] _s	26			-84			0.39		
EO2-7	[30/-60] _s	26			-93			0.38		
EU1-1	[0/90] _s	58	59	3.5	-331	-324	8.0	0.56	0.49	11
EU1-2	[0/90] _s	62			-295			0.44		
EU1-3	[0/90] _s	57			-291			0.55		
EU1-4	[0/90] _s	61			-308			0.49		
EU1-5	[0/90] _s	56			-359			0.47		
EU1-6	[0/90] _s	57			-342			0.42		
EU1-7	[0/90] _s	59			-341			0.49		
EU2-1	[0/90] _s	53	54	6.7	-222	-258	13.4	0.45	0.49	5
EU2-2	[0/90] _s	55			-238			0.49		
EU2-3	[0/90] _s	53			-278			0.50		
EU2-4	[0/90] _s	48			-231			0.50		
EU2-5	[0/90] _s	54			-263			0.50		
EU2-6	[0/90] _s	59			-314					
EU3-1	[0/90] _s	52	51	1.9	-219	-211	4.9	0.44	0.46	7
EU3-2	[0/90] _s	51			-199			0.50		
EU3-3	[0/90] _s	51			-215			0.44		
EL1-1	[0/90] _s	60	59	1.6	-463	-490	7.7	0.23	0.27	21
EL1-2	[0/90] _s	59			-517			0.31		

REFERENCES

- Adams, D.F., and J.S. Welsh. 1997. "The Wyoming Combined Loading Compression (CLC) Test Method," *Journal of Composites Technology and Research*, 19(3):123-133.
- Adams, D.O., and S.J. Bell. 1995. "Compression Strength Reductions in Composite Laminates due to Multiple-Layer Waviness," *Composites Science and Technology*, 53:207-212.
- Adams, R.D., and D.G.C. Bacon. 1973. "The dynamic properties of unidirectional fibre reinforced composites in flexure and torsion," *Journal of Composite Materials*, 7: 53-67.
- ASTM Standard D 695, 2003, "Standard Test Method for Compressive Properties of Rigid Plastics," ASTM International, West Conshohocken, PA.
- ASTM Standard D 3410, 2003, "Standard Test Method for Compressive Properties of Polymer Matrix Composite Materials with Unsupported Gage Section by Shear Loading," ASTM International, West Conshohocken, PA, DOI: 10.1520/D3410_D3410M-03R08
- ASTM Standard D 6641, 2009, "Standard Test Method for Compressive Properties of Polymer Matrix Composite Materials Using a Combined Loading Compression (CLC) Test Fixture," ASTM International, West Conshohocken, PA, DOI: 10.1520/D6641_D6641M-09
- Bagley, R.L., and P.J. Torvik. 1979. "A generalized derivative model for an elastomeric damper," *Shock and Vibration Bulletin*, 49:135-143.
- Bakis, C.E., E.C. Smith, and S.G. Sollenberger. 2011. "Development and validation of a self-heating model for thick, mixed angle ply composite shafts under rotating bending load," *Proc. 26th Technical Conference*, American Society for Composites.
- Bert, C.W. and C.D. Kim. 1995a. "Whirling of Composite-Material Driveshafts including Bending-Twisting Coupling and Transverse Shear Deformation," *Journal of Thermoplastic Composite Materials*, 117(1):17-21.
- Bogetti, T.A., J.W. Gillespie, and M.A. Lamontia. 1993. "Influence of Ply Waviness on the Stiffness and Strength Reduction on Composite Laminates," *Army Research Laboratory*, ARL-TN-110, Aberdeen Proving Ground, MD.
- Bruck, H. A., S. R. McNeill, S. S. Russell, and M. A. Sutton. 1989. "Use of Digital Image Correlation for Determination of Displacements and Strains," in *Non-Destructive Evaluation for Aerospace Requirements*, GL Workman, ed., New York: Gordon and Breach, pp. 99-111.
- Card, M. F., 1966, "Experiments to Determine the Strength of Filament-Wound Cylinders Loaded in Longitudinal Compression," NASA TN D-3522, Langley Station, Hampton, VA.
- Cheng, S., and B.P.C. Ho. 1963. "Stability of Heterogeneous Aelotropic Cylindrical Shells under Combined Loading," *AIAA Journal*, 1(4):892-898.
- Chu, T. C., W. F. Ranson, M. A. Sutton, and W. H. Peters. 1995. "Applications of Digital-Image-Correlation Techniques to Experimental Mechanics," *Experimental Mechanics*, 25(3):232-244.
- Chou P.C., J. Carleone, and C.M. Hsu. 1972. "Elastic Constants of Layered Media," *Journal of Composite Materials*, 6:80-93.
- Claus, S. J. 1994. "Manufacture-Structure-Performance Relationships for Filament-Wound Composite Shells," PhD Dissertation, Department of Engineering Science and Mechanics, The Pennsylvania State University, University Park, PA.

Cohen, D. 1997. "Influence of Filament Winding Parameters on Composite Vessel Quality and Strength," *Composites Part A*, 28A:1035-1047.

Correlated Solutions, 2010. "Vic-3D 2010 Reference Manual" www.CorrelatedSolutions.com, 2010.

Crane, R.M., and C. Ratcliffe. July 1993. "Graphite/Polyurethane Flexible Composites – Mechanical and Vibration Damping Properties," *Survivability, Structures, and Materials Directorate Research and Development Report*

Crouzeix, L., M. Torres, B. Douchin, J.N. Périé, F. Collombet, and H. Hernández. 2009. "Assessment of the Winding Pattern Effects on the Behaviour of Filament Wound Pipes by Using Full Field Measurements and the Equilibrium Gap Method," in *Proc. 17th International Conference on Composite Materials, ICCM-17*, Edinburgh, Scotland.

Daniel, I., and O. Ishai. 2006. *Engineering Mechanics of Composite Materials*, 2nd Edition, New York: Oxford University Press

Darlow, M. S., and J. Creonte. 1995. "Optimal Design of Composite Helicopter Power Transmission Shafts with Longitudinal Varying Fiber Layup." *Journal of the American Helicopter Society*, 40(2):50-56.

Ferry, J.D., 1970, *Viscoelastic properties of polymers*, 2nd Edition, Wiley, NY.

Gibson, R. F. 2007. *Principles of Composite Material Mechanics*, 2nd Edition, CLC Press, Boca Rotan, FL.

Guynn, E.G., O.O. Ochoa, and W.L. Bradley. 1992a. "A Parametric Study of Variables That Affect Fiber Microbuckling Initiation in Composite Laminates: Part 1-Analyses," *Journal of Composite Materials*, 26:1594-1616.

Guynn, E.G., O.O. Ochoa, and W.L. Bradley. 1992b. "A Parametric Study of Variables That Affect Fiber Microbuckling Initiation in Composite Laminates: Part 2-Experiments," *Journal of Composite Materials*, 26:1617-1643.

Hannibal, A.J., B.P. Gupta, J.A. Avila, and C.H. Parr. 1985. "Flexible Matrix Composites Applied to Bearingless Rotor Systems," *Journal of the American Helicopter Society*, 30(1):21-27.

Hillburger, M. W., and J. H. Starnes Jr. 2002. "Effects of Imperfections on the Buckling Response of Compression-Loaded Composite Shells," *International J. of Non-Linear Mech.*, 37:623-643.

Henry, T.C. 2012. "Static and Dynamic Characterization of Composite Materials for Future Driveshaft Design," MS Thesis, Department of Aerospace Engineering, The Pennsylvania State University, University Park, PA.

Henry, T.C., C.E. Bakis, and E.C. Smith. 2014. "Determination of Effective Ply-level Properties of Filament Wound Composite Tubes Loaded in Compression," *Journal of Testing and Evaluation*, Accepted, DOI: 10.1520/JTE20130159.

Herakovich, C. T., Post, D., Buczek, M. B., and Czarnek, R. 1985. "Free Edge Strain Concentrations in Real Composite Laminates: Experimental-Theoretical Correlation," *Journal of Applied Mechanics*, 52: 787–793.

Hipp P., and D. Jensen. 1992. "Design and Analysis of Filament-Wound Cylinders in Compression," *33rd AIAA/ASME/ASCE/AHS/ASC Structures, Structural Dynamics and Material Conference*, Dallas, Texas. Paper AIAA-92-2307-CP, pp. 2442–2452.

Hetherington, P., R. Kraus, and M. Darlow. 1990. "Demonstration of a supercritical composite helicopter power transmission shaft," *Journal of American Helicopter Society*, 35(1):23-28

Hur, H.K. 1994. "Computational Modeling and Impact Analysis of Textile Composite Structures," PhD Dissertation, Department of Aerospace Engineering, Virginia Polytechnic Institute and State University, Blacksburg, VA

Ishikawa, T., and T. Chou. 1982. "Stiffness and Strength Behavior of Woven Fabric Composites," *Journal of Materials Science*, 12:3211-20.

Jensen, D. W., and P. A. Hipp. 1991. "Compression Testing of Filament-Wound Cylinders," *Proc. 8th International Conference on Composite Materials*, Honolulu, Hawaii, July 15-19, 1991.

Jensen, D., and S. Pai. 1993. "Influence of Local Fiber Undulation on the Global Buckling of Filament-Wound Cylinders," *Journal of Reinforced Plastics and Composites*, 12:865-875.

Jolicœur, C., and A. Cardou. 1994. "Analytical solution for bending of colongitudinal orthotropic cylinders," *Journal of Engineering Mechanics*, 120(12): 2556-2574.

Kurashiki, T., H. Nakai, S. Hirose, M. Imura, M. Zako, I. Verost, and S. Lomov. 2007. "Mechanical Behaviors for Textile Composites by FEM based on Damage Mechanics," *Key Engineering Materials*, 334,335:257-260.

Lekhnitskii, S.G. 1981. *Theory of elasticity of an anisotropic body*, Mir Publishers, Moscow, Russia.

Lim, J.W. and M.S. Darlow. 1986. "Optimal Sizing of Composite Power Transmission Shafting," *Journal of the American Helicopter Society*, 31(1): 75-83.

Lo, K.H. and E.S.M. Chim. 1992. "Compressive Strength of Unidirectional Composites," *Journal of Reinforced Plastics and Composites*, (11):838-896.

Mayrides, B., K.W. Wang, and E.C. Smith. June 2005. "Analysis and Synthesis of Highly Flexible Helicopter Drivelines with Flexible Matrix Composite Shafting," *Proc. 61st Forum*, Grapevine, Texas, American Helicopter Society. pp. 1-3.

Mertiny, P., F. Ellyin, and A. Hothan. 2004. "An Experimental Investigation on the Effect of Multi-Angle Filament Winding on the Strength of Tubular Composite Structures," *Composites Science and Technology*, 64(1):1-9.

Miao, Y., E. Zhou, Y. Wang, and B.A. Cheeseman. 2008. "Mechanics of textile composites: Micro-geometry," *Composites Science and Technology*, 68:1671-1678.

Moon, C.J., I.H. Kim, B.H. Choi, J.H. Kweon, and J.H. Choi. 2010. "Buckling of Filament-Wound Composite Cylinders Subjected to Hydrostatic Pressure for Underwater Vehicle Applications," *Composite Structures*, 92:2241-2251.

Morozov, E.V. 2006. "The Effect of Filament-Winding Mosaic Patterns on the Strength of Thin-Walled Composite Shells," *Composite Structures*, 76:123-129.

Ocalan, M. March 2002. "High Flexibility Rotorcraft Driveshafts Using Flexible Matrix Composites and Active Bearing Control," M.S. Thesis, The Pennsylvania State University, University Park, PA.

Pai, S. P., and D. W. Jensen. 2001. "Influence of Fiber Undulations on Buckling of Thin Filament-Wound Cylinders in Longitudinal Compression," *Journal of Aerospace Engineering*, 14(1):12-20.

Price, K., R. Storn, and J. Lampinen. 2005. *Differential evolution – A Practical Approach to Global Optimization*, Springer-Verlag, Berlin, Germany

Roos, C., and C.E. Bakis. 2011. "Multi-Physics Design and Optimization of Flexible Matrix Composite Driveshafts," *Composite Structures* 93:2231-2240

Roos, C. 2010. "Multi Physics Design and Optimization of Flexible Matrix Composite (FMC) Driveshafts," MS Thesis, Institute for Mechanical Systems, Swiss Federal Institute of Technology, Zurich, Switzerland

Rosen, B. W. 1965. "Mechanics of Composite Strengthening," *Fiber Composite Materials*, Society for Metals Seminar, pp. 37-75.

Rousseau, J., D. Perreux, and N. Verdiere. 1999. "The Influence of Winding Patterns on the Damage Behavior of Filament-Wound Pipes," *Composites Science and Technology*, 59:1439-1449.

Scheuer, R., P. Mertiny, and D. Bormann. 2009. "Analysis of Surface Strains and Leakage Behavior in Composites Pipes and Vessels using Digital Image Correlation Technique," Paper PVP2009-77522, in *Proc. Pressure Vessels and Piping Conference*, ASME, New York, 5:449-455.

Shan, Y., and C.E. Bakis. 2009. "Viscoelastic Characterization and Self-Heating Behavior of a Flexible Matrix Composite Driveshaft," *Journal of Composite Materials*, 43(12):3053-306.

Shin, E., K.W. Wang, and E.C. Smith. May 2003. "Characterization of Flexible Matrix Composite Rotorcraft Driveshafts," *Proc. 59th Forum*, American Helicopter Society

Singh, S. P., H.B.H. Grubran, and K. Gupta. 1997. "Developments in Dynamics of Composite Material Shafts," *International Journal of Rotating Machinery*, 3(3):189-198.

Sollenberger, S. 2010. "Characterization and Modeling of a Flexible Matrix Composite Material for Advanced Rotorcraft Drivelines," MS Thesis, Department of Engineering Science and Mechanics, The Pennsylvania State University, University Park, PA.

Sollenberger, S. G., J. L. Bail, L. Kohlman, C. R. Ruggeri, C. E. Bakis, G. D. Roberts, and E. C. Smith. 2010. "Ballistic Impact Tolerance of Filament-Wound Composite Cylinders with Rigid and Flexible Matrix Material," in *Proc. 25th Technical Conference*, American Society for Composites, DEStech Publications, Lancaster, PA, (CD ROM).

Stump, G., S. Lego, M. Yukish, T.M. Simpson, and J.A. Donndelinger. 2009. "Visual Steering Commands for Trade Space Exploration: User-Guided Sampling With Example," *Journal of Computing and Information Science Engineering*, 9(4):1-10.

Sutton, M. A., W. J. Wolters, W. H. Peters, W. F. Ranson, and W. R. McNeill. 1983. "Determination of Displacements Using an Improved Digital Image Correlation Method," *Computer Vision*, 1(3):133-139.

Sutton, M. A., S. R. McNeill, J.D. Helm, and Y.J. Chao. 2000. "Advances in Two-Dimensional and Three-Dimensional Computer Vision," *Photomechanics*, 77:323-372.

Sun, C., and S. Li. 1988. "Three-Dimensional Effective Elastic Constants for Thick Laminates," *Journal of Composite Materials*, 22:629-639.

Torres, M., L. Crouzeix, B. Douchin, F. Collombet, H. Hernández, and J. González. 2010. "Strain Field Measurement of Filament-Wound Composites at $\pm 55^\circ$ Using Digital Image Correlation: An Approach for Unit Cells Employing Flat Specimens," *Composite Structures*, 92:2457–2464.

Wang, Y., Y. Miao, D. Swenson, B.A. Cheeseman, C.F. Yen, and B. LaMattina. 2010. "Digital element approach for simulating impact and penetration of textiles," *International Journal of Impact Engineering*, 37:552-560.

Whitney, J. M. and R. J. Nuismer. 1974. "Stress Fracture Criteria for Laminated Composites Containing Stress Concentrations," *Journal of Composite Materials*, 8: 253-265.

Xu, Y.L. and K.L. Reifsnider. 1993. "Micromechanical Modeling of Composite Compressive Strength," *Journal of Composite Materials*, 27:572-588.

Yurgartis, S.W. 1987. "Measurement of Small Angle Fiber Misalignments in Continuous Fiber Composites," *Composite Science and Technology*, 30:279-293.

Zhang, Y., Z. Xia, and F. Ellyin. 2008. "Two-Scale Analysis of a Filament-Wound Cylindrical Structure and Application of Periodic Boundary Conditions," *International Journal of Solids and Structures*, 45:5322-5336.

Zhou, E., D. Mollenhauer, and E. Iarve. 2009. "A Realistic 3-D Textile Geometric Model," *ICCM International Conference on Composite Materials*, ICCM-17.

Zinberg, H. 1970. "The Development of an Advanced Composite Tail Rotor Driveshaft," *Proc. 26th Forum*, American Helicopter Society, pg. 1-14

Zindel, D., and C. E. Bakis. 2011. "Nonlinear Micromechanical Model of Filament-Wound Composites Considering Fiber Undulation," *Mechanics of Composite Materials*, 47(1):73-94

VITA

Todd Henry

Todd Henry was born on June 15, 1988 in the city of Latrobe, Pennsylvania. He graduated in May 2010, with a Bachelor of Science degree from The Pennsylvania State University in Aerospace Engineering. During the course of his undergraduate junior and senior years, he worked in the Composite Manufacturing Technology Center on research involving, but not limited to, testing of suitable materials for use in crashworthiness devices. After graduation, he continued at The Pennsylvania State University in the Aerospace Department working on a Master of Science degree, which he completed in May 2012. In May 2011, he was awarded the SMART fellowship which funded his further schooling and research in exchange for employment upon graduation with a Doctor of Philosophy degree. Master's level research focused on characterizing several prospective polymers for their suitability as a resin material for a single piece composite driveshaft. Most of the completed work was in the areas of manufacturing, quasi-static, and dynamic testing.

He began his Doctor of Philosophy work in May 2012 with research focused on modeling undulated composites as may be applied to a filament wound driveshaft. Since that time, he has completed two summer internships at the Army Research Lab, Vehicle Technology Directorate. Scholarly publications, while working in the Composites Manufacturing Technology Center, include three conference papers and one journal paper. He is currently a member of the American Helicopter Society (AHS), American Society for Composites (ASC), American Institute of Aeronautics and Astronautics (AIAA), and Society for the Advancement of Material and Process Engineers (SAMPE).